MODELING AND SCALING LIMITATIONS OF SIGE HBT LOW-FREQUENCY

NOISE AND OSCILLATOR PHASE NOISE

Except where reference is made to the work of others, the work described in this dissertation is my own or was done in collaboration with my advisory committee. This dissertation does not include proprietary or classified information.

_____
Jin Tang

Certificate of Approval:

_____
Richard C. Jaeger
Distinguished University Professor
Electrical and Computer Engineering

_____
Guofu Niu, Chair
Professor
Electrical and Computer Engineering

_____
Foster Dai
Associate Professor
Electrical and Computer Engineering

_____
Stuart Wentworth
Associate Professor
Electrical and Computer Engineering

_____
Stephen L. McFarland
Dean
Graduate School

MODELING AND SCALING LIMITATIONS OF SiGe HBT LOW-FREQUENCY

NOISE AND OSCILLATOR PHASE NOISE

Jin Tang

A Dissertation

Submitted to

the Graduate Faculty of

Auburn University

in Partial Fulfillment of the

Requirements for the

Degree of

Doctor of Philosophy

Auburn, Alabama
August 7, 2006

MODELING AND SCALING LIMITATIONS OF SIGE HBT LOW-FREQUENCY

NOISE AND OSCILLATOR PHASE NOISE

Jin Tang

_____
Signature of Author

_____
Date of Graduation

Jin Tang, daughter of Shuren Tang and Siping Zhu, was born on 14 November, 1977, in Deyang, Sichuan Province, P. R. China. She received her B.S. degree from Huazhong University of Science and Technology in 2000, majoring in Communication Engineering, and her M.S. degree from Auburn University in 2003, majoring in Microelectronics. In August 2003, she was accepted into the Electrical and Computer Engineering department of Auburn University, Auburn, Alabama, where she has been pursuing her PhD degree. She married Yen-Kang Liu, son of Young-Chin Liu and Lan-Mei Y. Liu, on August 27, 2005.

DISSERTATION ABSTRACT

MODELING AND SCALING LIMITATIONS OF SIGE HBT LOW-FREQUENCY

NOISE AND OSCILLATOR PHASE NOISE

Jin Tang

Doctor of Philosophy, August 7, 2006
(M.S., Auburn University, 2003)
(B.S., Huazhong University of Science and Technology, 2000)

193 Typed Pages

Directed by Guofu Niu

This dissertation presents modeling of SiGe HBT low-frequency noise and oscillator phase noise, and examines their limitations posed by technology scaling. A new method of extracting low-frequency noise, inverse circuit simulation based low-frequency noise extraction, is proposed to enable noise measurement of devices operating under high current density and voltage, which are typical for modern SiGe HBTs. Traps physically located at collector-base junction are found to not only generate recombination current, but also contribute significant $1/f$ noise when high-injection occurs. The $1/f$ noises that originated from the emitter-base and collector-base junctions are separated, and shown to be two distinct processes. The noise dependence on total base current, however, is still approximately the same before and after high-injection occurs. This is good news for compact modeling, since no extra effort is needed to model $1/f$ noise generated by collector-base junction traps as long as the recombination current in the collector-base junction is correctly modeled. The $1/f$ noise at a given base current increases with technology scaling from 50 to 120 GHz, but decreases with scaling from 50 to 210 GHz. However, because of the increased current gain, scaling to 120 GHz does not necessarily increase the $1/f$ noise for a given collector current, which is more relevant for circuit operation.

v

Using frequency sensitivity method in ADS and impulse sensitivity function method, we examine the upconversion of individual transistor noise source to phase noise as a function transistor sizing, biasing, technology scaling and oscillation frequency. In ADS, $1/f$ noise in an oscillating transistor depends on the *dc* component of the oscillating noise generating current only. While in impulse sensitivity method, we consider $1/f$ noise as modulated stationary noise as supported by the experimental data. Comparison is made with the results in ADS. Phase noise from the modulated stationary model is usually more than 10 dB higher. Optimal phase noise is found in a medium sized transistor with a maximum oscillating collector current below the severe high-injection region. With technology scaling, the phase noise due to base current shot noise is reduced as a result of higher speed and the ability to operate at higher current density without inducing severe high-injection and quasi-saturation. The fundamental limit is set by the collector current shot noise. Technology scaling leads to an improvement of the far-off phase noise which is dominated by white noise contributions. The $1/f$ noise increase in the 120 GHz HBT is found to degrade only the close-in phase noise. All of the technologies investigated are excellent choices for low phase noise oscillators provided that transistor size and bias are optimized. With increasing oscillation frequency, $1/f$ noise becomes less important, and the dominant phase noise source is the collector current shot noise.

The results show that corner offset frequency defined by the intersect of the $1/f^3$ and $1/f^2$ phase noises has little to do with the traditional $1/f$ noise corner frequency. $1/f$ noise corner frequency should not be used alone to evaluate the capability of a certain technology in low phase noise oscillator application. A methodology to identify the maximum tolerable $1/f$ noise K factor for frequency synthesizers, the threshold K, is established and demonstrated for the HBTs used. Using the model that relates $1/f$ noise to the *dc* component of the noise generating current only, the actual K is lower than the respective threshold K. While the actual K is higher than the threshold K if the modulated stationary noise model is applied to $1/f$ noise.

Style manual or journal used <u>IEEE Transactions on Electron Devices (together with the style known</u> <u>as "aums"). Bibliography follows van Leunen's *A Handbook for Scholars*.</u>

Computer software used <u>The document preparation package TeX (specifically LaTeX) together with</u> <u>the departmental style-file `aums.sty`. The plots were generated using VossPlot®, MATLAB®and</u> <u>Microsoft Visio®.</u>

TABLE OF CONTENTS

LIST OF FIGURES

SiGe HBT technology has come-of-age as an important semiconductor technology for both wired and wireless telecommunications applications because of its superior analog and RF performance, together with its CMOS integration capability [1]. By employing bandgap engineering, SiGe HBTs outperform Si BJTs in nearly every important performance metric, and in several areas, provide improved performance over the III−V HBTs. One of the areas in which SiGe HBTs exceed GaAs HBTs is $1/f$ noise [2], making them an excellent choice for voltage controlled oscillators (VCOs) [3]. This thesis investigates the modeling and scaling limitations of SiGe HBT low-frequency noise and oscillator phase noise. This introductory chapter briefly reviews the SiGe HBT technology, $1/f$ noise in bipolar transistors, mechanisms of oscillator phase noise, characterization of oscillator phase noise as well as system phase noise, and gives an overview of the contributions of the thesis.

1.1 SiGe HBT Technology

1.1.1 SiGe HBT Basics

This section gives an overview of the performance capabilities of SiGe HBTs. Basic device physics, *dc* and *ac* performance advantages over Si BJTs are addressed. For brevity, only the final results are included. The interested reader is referred to [4] for complete derivations. SiGe HBT is essentially a Si bipolar junction transistor with the base region material being SiGe alloy instead of Si. The basic operation principle of SiGe HBT can be best understood by considering the band diagram shown in Figure 1.1. The Ge mole fraction is graded from the emitter towards the collector, creating an accelerating electric field in the neutral base. The important *dc* consequence of adding Ge into the base lies with the collector current density (J_C). The Ge-induced band offset exponentially increases the intrinsic carrier
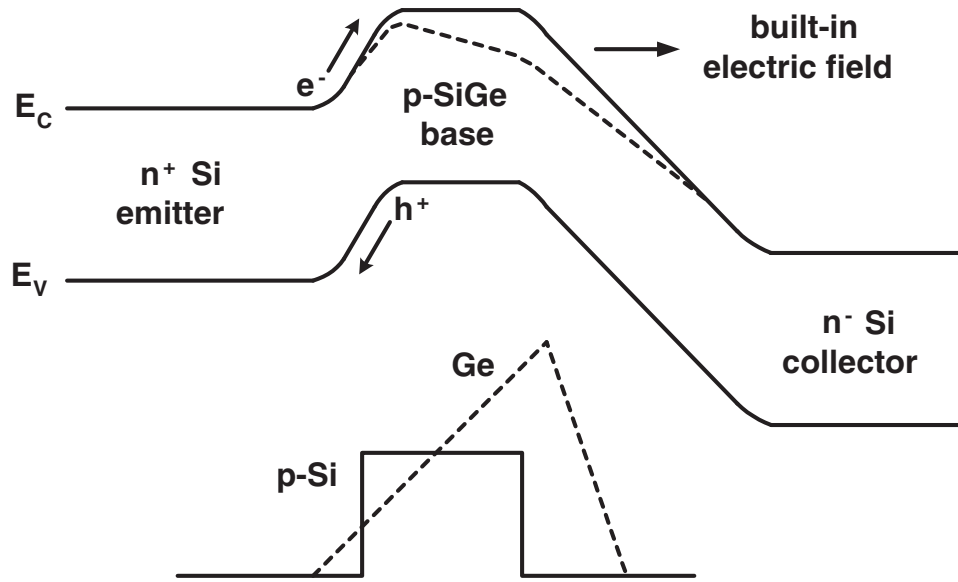
Figure 1.1: Energy band diagram of a graded-base SiGe HBT compared to a Si BJT [4].

density in the base which, in turn, decreases the effective Gummel number, and hence increasing J_C. Because emitter region is the same, base current density (J_B) is roughly the same for SiGe HBT and Si BJT. Figure 1.2 compares the Gummel characteristics for a SiGe HBT and a Si BJT which has been processed identically to allow unambiguous comparison. The J_C of the SiGe HBT is much higher than that of the Si BJT, while the J_B of these two devices are similar. As a result, current gain β, defined as J_C/J_B, is higher in the SiGe HBT.

Another beneficial effect of using a graded-Ge profile in a SiGe HBT is an enhancement in the Early voltage (V_A) which yields an improved output conductance in the device. The output conductance is a measure of how much the neutral base profile can be depleted with reverse bias on the collector-base junction, and is manifested in the rise of J_C with collector bias at fixed V_{BE}. The base profile is effectively "weighted" by the increasing Ge content on the collector side of the neutral base, making it harder to deplete the neutral base for a given applied V_{CB}, all else being equal. This effectively increases the Early voltage.
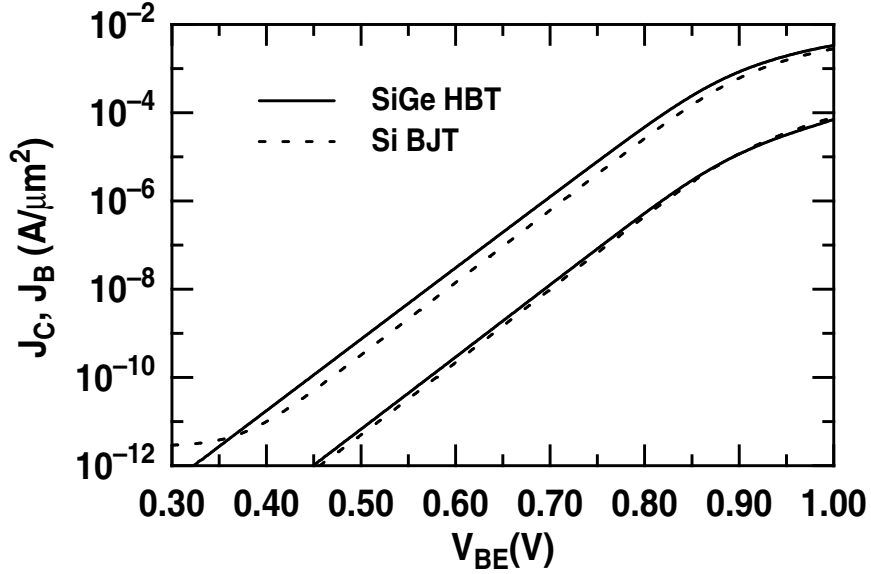
Figure 1.2: Comparison of Gummel characteristics for a SiGe HBT and a Si BJT.

In most RF and microwave circuit applications, it is the transistor frequency response that limits system performance. An important frequency response figure-of-merit is the unity-gain cutoff frequency (f_T), which is given by

$$\frac{1}{2\pi f_T} = \tau_b + \tau_e + \tau_c + \frac{1}{g_m}(C_{te} + C_{tc}),\tag{1.1}$$

where τ_b, τ_c and τ_e are base, collector and emitter transit time, respectively. g_m is the transconductance. C_{te} and C_{tc} are EB and CB junction depletion capacitances. In conventional Si BJTs, τ_b typically limits the maximum f_T. The built-in electric field induced by the Ge grading across the neutral base aids the transport of minority carriers (electrons) from emitter to collector, leading to faster base transit and thus higher f_T. Figure 1.3 compares the f_T characteristics for a SiGe HBT and a comparably constructed Si BJT. Observe that the transit time reductions due to the Ge grading increase the peak f_T from 35 GHz to 50 GHz, a factor of about 1.4 ×.

Another figure-of-merit for RF applications is the maximum oscillation frequency, f_{max}:

$$f_{max} = \sqrt{\frac{1}{8\pi C_{tc}} \frac{f_T}{r_b}},\tag{1.2}$$

3
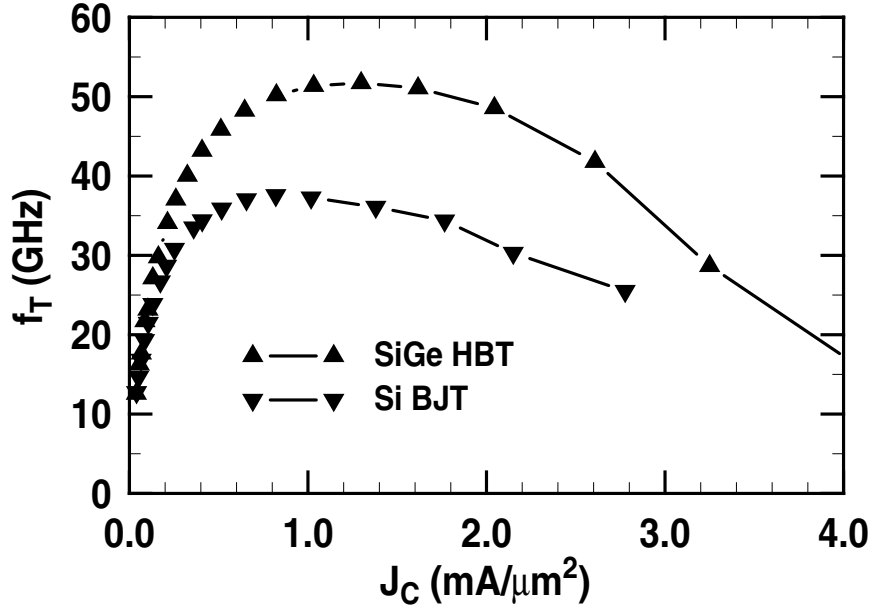
Figure 1.3: Comparison of f_T characteristics for a SiGe HBT and a Si BJT.

which indicates that the f_T/r_b ratio must be increased to improve f_{max} or transistor power gain. The base resistance r_b can be partitioned into two parts, the intrinsic and extrinsic base resistances (r_{bx} and r_{bi}), as illustrated in Figure 1.4. The total base resistance is given by the sum of the two components. r_{bx} is the resistance between the edge of the active transistor area and the base contact, and can be estimated from the transistor geometry and the extrinsic base sheet resistance $R_{S,bx}$:

$$r_{bx} = \frac{R_{S,bx}\frac{b_b}{l_b} + R_{contact}}{n_B},$$
(1.3)

where $R_{contact}$ is the base contact resistance, n_B is the number of base contacts, $n_B = 1 - 2$, and b_b and l_b are defined in Figure 1.4.

r_{bi} is the resistance of the active base region, which is the region located beneath the emitter. It can be estimated from the transistor geometry and the intrinsic base sheet resistance $R_{S,bi}$:

$$r_{bi} = C\frac{R_{S,bi}\frac{b_e}{l_e}}{n_B^2}.$$
(1.4)

4
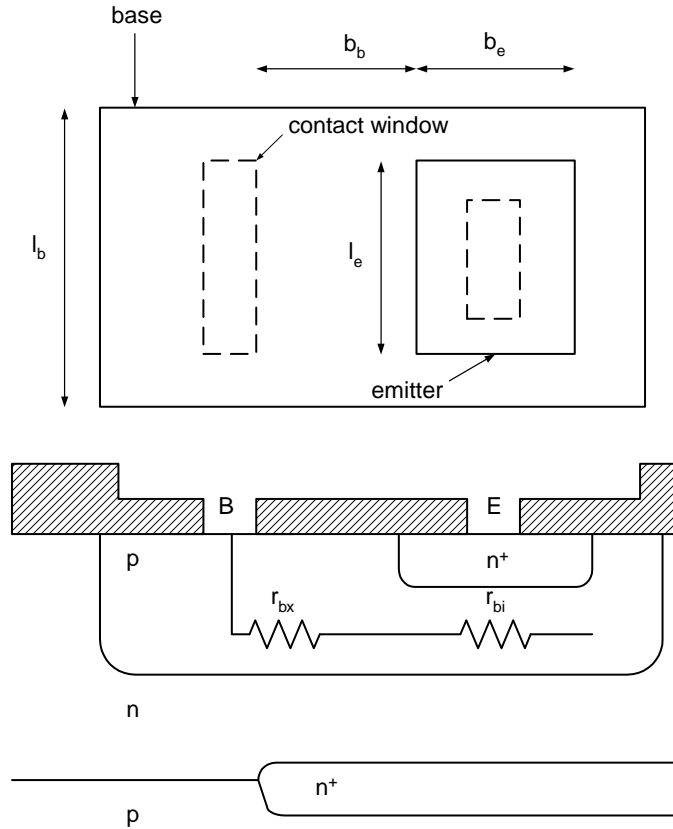
Figure 1.4: Layout and cross-section views of a basic bipolar transistor. The layout view shows base, emitter and contact window masks. The cross-section view shows the components of base resistance.

C is a constant that takes a value of $1/3$ at low currents [5], b_e and l_e are emitter width and length, as shown in Figure 1.4. The explanation for the n_B^2 term is as follows. If the transistor has only one base contact, the base current enters from only one side of the emitter and hence the path length for the current flow is the complete emitter width. If the transistor has two base contacts, the base current enters from both sides of the emitter, so the path length for the current flow is halved. A further halving arises because the two base contacts are in parallel. Assuming constant base doping (N_B) and lateral mobility of holes in the base (μ_p), r_{bi} for double base contact is simplified to

$$r_b = \frac{1}{12} \frac{1}{q\mu_p} \frac{b_e}{l_e} \frac{1}{N_B W_B},$$ (1.5)

where W_B is the base width.

Base resistance is one of the most important electrical parameters of a bipolar transistor. r_b limits transistor power gain and noise performance. Thermal noises due to the extrinsic and intrinsic base resistances are the major phase noise sources. Minimization of the various components of the base resistance is a major challenge in bipolar transistor structural design, fabrication and process integration. With bandgap engineering, r_{bi} can be reduced by increasing base doping N_B without compromising β, because β can be increased by Ge-induced band offset exponentially. However, the reduction of r_{bx} requires careful optimization of the extrinsic base structure, and is difficult to achieve.

1.1.2 SiGe Process

While the idea of using SiGe alloys to bandgap-engineer Si devices dates back to the 1960's, the synthesis of "defect-free" SiGe films proved quite difficult, and device-quality SiGe films were not successfully produced until the early to mid-1980's. Although Si and Ge can be combined to produce a chemically stable alloy ($Si_{1-x}Ge_x$ or simply SiGe), their lattice constants differ by roughly 4% and, thus, SiGe alloys grown on Si substrate are compressively strained. These SiGe strained layers are subject to a fundamental stability criterion, limiting their thickness for a given Ge concentration.

Epitaxy has been used to form the active layers in Si based devices, e.g., the base region of a SiGe HBT. The high temperature needed for film growth in the conventional Si epitaxy technique, however, may cause the strained SiGe epi-layer to relax. A number of techniques have been developed over the past two decades, with a demonstrated capability to produce device-quality SiGe film. The ultrahigh vacuum/chemical vapor deposition (UHV/CVD) [6] and atmospheric pressure chemical vapor deposition (APCVD) [7] are two techniques widely used in the commercial SiGe HBT products.

Even with the advanced techniques, traps may still be induced near the SiGe/Si growth interface. When integrated into CMOS process to form BiCMOS, the strained SiGe films inevitably experience the high thermal cycle needed in CMOS fabrication. The high thermal cycle may induce traps at the SiGe/Si retrograding layer. Although different approaches have been implemented in scaled devices to decouple the CMOS thermal cycle from the bipolar, the risk is not reduced. With technology scaling, the peak Ge concentration is increased, and the retrograding layer is steeper in order to keep the total

Figure 1.5: Schematic cross-section of the 50 GHz SiGe HBTs used in this work.

Ge concentration within thermal stability limit. The more severe mismatch at retrograding layer makes it vulnerable to relaxation at a relatively low temperature. In Chapter 3, we demonstrate the existence of those traps and investigate the impact on $I - V$ characteristics and low-frequency noise.

Figure 1.5 shows a schematic cross-section view of the 50 GHz SiGe HBT used in this work. The SiGe HBT has a planar, self-aligned structure with a conventional polysilicon emitter contact, silicided extrinsic base, and deep and shallow trench isolation. The extrinsic resistive and capacitive parasitics are intentionally minimized to improve the maximum oscillation frequency (f_{max}) of the transistor. Details of the fabrication process can be found in [8]. The SiGe base was grown using the UHV/CVD technique.

Si devices are defined by implants and not by a pre-grown epi-structure, common in the III-V HBTs, therefore it is possible to have both high cut-off frequency and high breakdown voltage devices in the same technology offering. This allows some flexibility in tuning the breakdown voltage of the high breakdown voltage device in the technology. In the 50 GHz SiGe HBT technology, the high f_T transistor has both a deep and shallow collector implant. By dropping the shallow collector implant, an additional high breakdown voltage device is obtained along with the high f_T device. Table 1.1 compares the key parameters of the standard (high f_T) SiGe HBT and high breakdown voltage SiGe HBT in the 50 GHz

7

Table 1.1: Parameters comparison for a high f_T and a high breakdown voltage SiGe HBTs from the IBM 50 GHz peak f_T technology [9]. $A_E = 0.5 \times 2.5 \ \mu m^2$. All *ac* parameters were measured at $V_{CB} = 1.0$ V and f_{max} was extracted using maximum available gain (MAG).

Parameter	Standard SiGe HBT	High-BV_{CEO} SiGe HBT
peak β	113	97
V_A (V)	61	132
peak f_T (GHz)	48	28
peak f_{max} (GHz)	69	57
BV_{CEO} (V)	3.3	5.3
BV_{EBO} (V)	4.2	4.1
r_b@peak f_T (Ω)	80	N/A

peak f_T technology. The emitter area is $0.5 \times 2.5 \ \mu m^2$. The high f_T device has a peak f_T of 50 GHz ($BV_{CEO} = 3.3$ V). The high breakdown voltage device has a peak f_T of 35 GHz ($BV_{CEO} = 5.3$ V). High breakdown voltage devices are useful in applications that require a large voltage handling capability, such as oscillators. Phase noise is an important concern in oscillator, therefore it is necessary to understand how collector doping affects low-frequency $1/f$ noise which directly upconverts to close-in phase noise. We will investigate this issue in Chapter 3.

1.1.3 Technology Scaling

As communications progress toward ubiquitous connectivity, faster transistors are needed to satisfy the demand for higher operational speed and wider bandwidth. Higher f_T performance is principally achieved through vertical scaling of dopants and device dimensions. Such scaling involves base doping increase, base width reduction, Ge ramp increase, and collector doping increase, as illustrated in Figure 1.6. Base doping increase reduces base resistance r_b. Base width reduction and the Ge ramp increase result in an decrease of base transit time τ_b, and thus a higher f_T. Increasing collector doping reduces the collector-base space charge region width and hence reduces transit time across this region. With the higher collector doping comes the added benefit that the device may be operated at higher collector current densities, and thus achieve higher f_T, due to a delayed Kirk effect.
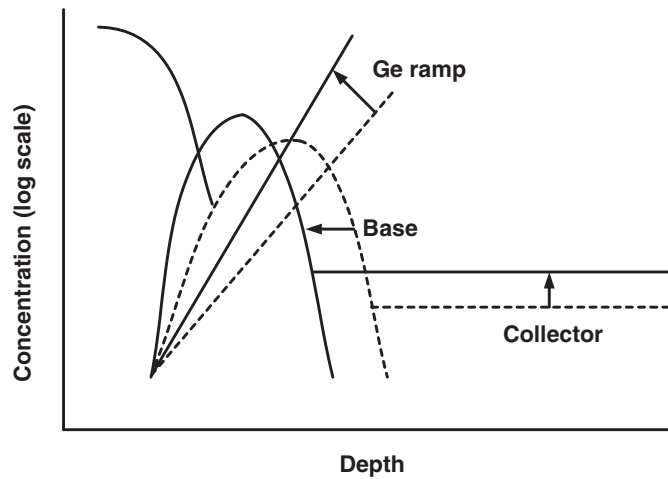
Figure 1.6: Vertical dimension and SiGe profile scaling involves increasing the base doping, reducing the base width, increasing the Ge ramp, and increasing the collector dopant concentration.

The key to vertical scaling is minimization of thermal cycles in post-base deposition processing. Previous IBM SiGe BiCMOS processes used an integration approach that shared layers and thermal cycles to reduce the structural complexity. This approach is called base-during-gate (BDGate). This approach became problematic as SiGe BiCMOS was developed across multiple generations of CMOS which also had significantly different thermal cycles. In a new process approach, the CMOS is formed before the bipolar elements are formed, without sharing silicon layers or thermal cycles; hence, it is referred to as the base-after-gate (BAGate) approach [1]. An emerging trend in base width reduction is the incorporation of carbon into the base epitaxy. At $< 10^{20}$ cm^{-3} concentrations, carbon incorporation has been shown to significantly reduce boron outdiffusion [10]. Figure 1.7 compares f_T as a function of J_C for the 50 GHz, 120 GHz and 210 GHz HBTs. S-parameters were measured from 0.5 to 40 GHz using a HP8510C vector network analyzer, from which f_T was extracted. The f_T curve is moved upward for a given J_C as a result of transit time reduction, the f_T rolloff is also delayed to higher collector current density due to higher collector doping.

Wherein transit time performance improvements are obtained through vertical profile scaling, a separate but similarly important set of performance metrics are improved through making the device smaller. Thermal noise due to base resistance is an important phase noise source. The intrinsic base
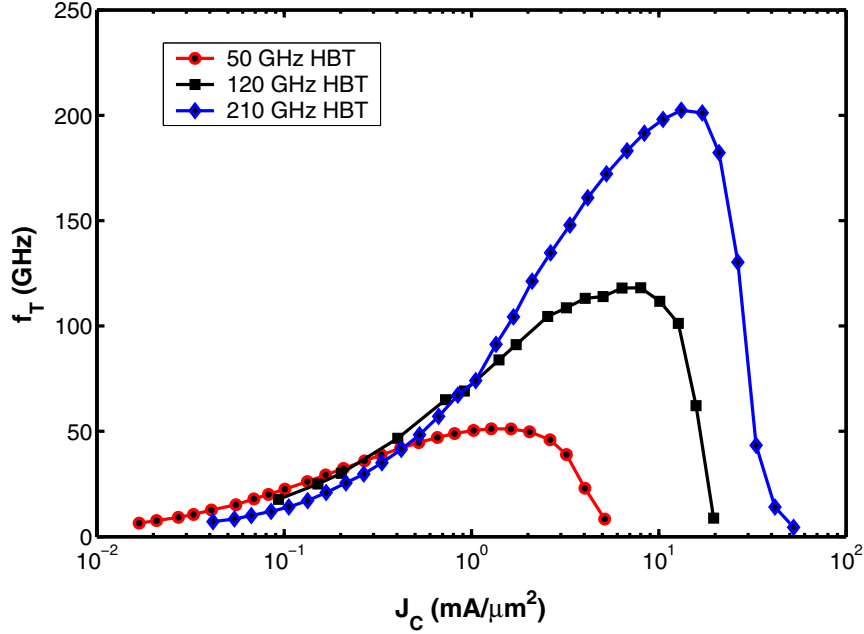
Figure 1.7: f_T comparison for the 50, 120 and 210 GHz HBTs.

resistance can be reduced by increasing base doping and decrease emitter width. The extrinsic base resistance, however, strongly depends on the extrinsic base structure. A raised extrinsic base structure is used in the 210 GHz technology [11]. The extrinsic base resistance is reduced by minimizing the resistance of the extrinsic base polysilicon and narrowing the emitter and the emitter to extrinsic base spacer dimension. Table 1.2 compares the HBT characteristics across three IBM SiGe HBT generations, featuring 50 GHz [9], 120 GHz [12] and 210 GHz [11] peak f_T. The 120 and 210 GHz technologies achieve a much higher f_T by introducing carbon into the base expitaxy as well as further optimizing Ge and collector doping profiles. These three technologies will be used in this work.

1.2 Low-Frequency Noise in Bipolar

It is well established that the major low-frequency noise source in typical SiGe HBT's is the base current noise [2] [13]. The low-frequency noise behavior can be described using a noise current source (i_{bn}) placed between the internal base and emitter, as shown in Figure 1.8. The power spectral density of

Table 1.2: Comparison of SiGe HBT Characteristics Across Three Generations.

Technology	50 GHz	120 GHz	210 GHz
A_E (μm^2)	0.5×2.5	0.2×6.4	0.12×12
β	100	200	400
V_A (V)	65	120	150
BV_{CEO} (V)	3.35	2.5	1.7
BV_{CBO} (V)	10.5	7.5	5.5
r_b@100μA	124	60	22
f_T (GHz)	50	120	210
f_{max} (GHz)	65	90	285

base current $1/f$ noise (S_{I_B}) is a function of base current I_B and is modeled by

$$S_{I_B} = \frac{K}{A_E} I_B^\alpha \frac{1}{f},$$

(1.6)

where K is the low-frequency $1/f$ noise factor, A_E is emitter area. K/A_E corresponds to the flicker noise

constant KF in SPICE. α corresponds to the AF model parameter used in SPICE. The α value provides

information on the physical origins of the $1/f$ noise. First order theory predicts $\alpha = 1$ for carrier

mobility fluctuations, and $\alpha = 2$ for carrier number fluctuations [14]- [16]. The α for typical SiGe HBTs

is close to 2, and varies only slightly with SiGe profile, collector doping profile and geometry. Even

though $1/f$ noise appears in virtually all electronic devices, the exact origin of $1/f$ noise is not well

understood. One of the theories, proposed by McWhorter [17], describes $1/f$ noise as a superposition of

individual generation-recombination (GR) noise. Our experimental data support the GR superposition

origin of $1/f$ noise. The detailed discussion of this theory and experimental results will be presented in

Sections 4.1.4 and 4.3.4.

1.3 Oscillator Phase Noise

An important issue for integrated transceiver design is to minimize voltage controlled oscillator

(VCO) phase noise, and ultimately frequency synthesizer phase noise. Ideally, we desire a purely sinu-

soidal output, the spectrum of which is a perfect delta function. In reality, transistor noises cause random
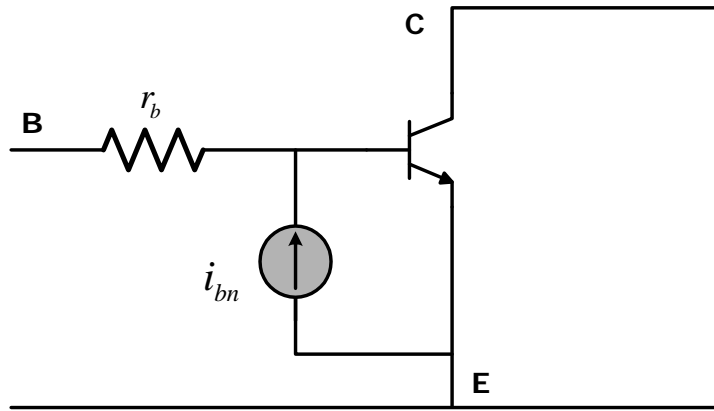
Figure 1.8: Low-frequency noise behavior can be described using a noise current source i_{bn} placed between the base and emitter.

variations in both the amplitude and the phase. The amplitude noise is suppressed by the oscillator's built-in amplitude limiting mechanisms, and is negligible. The phase noise, however, shows up as random variations in oscillation period or sidebands around the carrier frequency in the output spectrum. The time domain representation is often used in digital applications since it affects the maximum achievable frequency of operation. For RF applications, the frequency domain representation is mostly used, as phase noise degrades RF system spectral purity and limits minimum channel spacing. In this section, we only discuss the frequency domain representation.

1.3.1 Upconversion From Transistor Noises

The exact mechanism of phase noise is complicated. The basic behavior of upconversion of physical transistor noise to phase noise can be understood as following using a simplified version of the time domain model proposed in [18]. Consider injecting a unity impulse perturbation current into an oscillator. The resulting amplitude shift dies away due to the built-in amplitude limiting mechanisms, while the phase shift remains as any time-shifted version of the solution remains a solution. The response can be approximated using a step function $s(t)$ as we are not concerned with short term responses. We further assume that $s(t)$ is independent of the injection time instant for simplicity. For an arbitrary noise μ, the

12
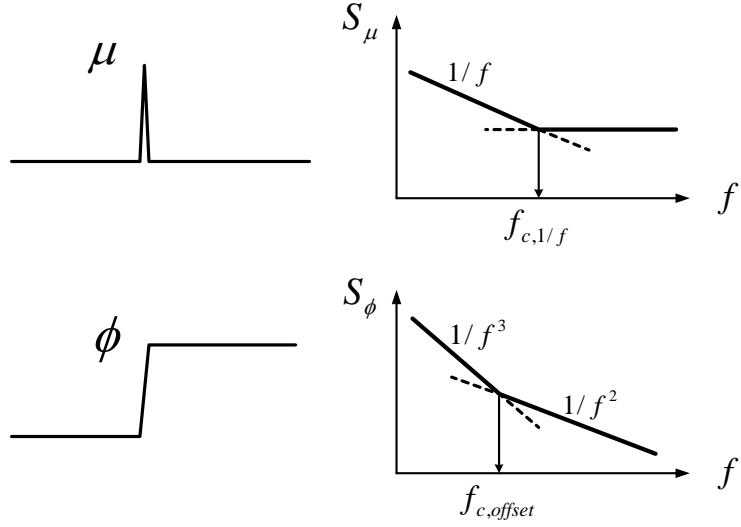
Figure 1.9: A simplified time domain model for upconversion of transistor physical noises to oscillator phase noise.

accumulated phase shift is:

$$\phi(t) \propto \int_{-\infty}^{\infty} \mu(\tau)s(t-\tau)d\tau \propto \int_{-\infty}^{t} \mu(\tau)d\tau. \tag{1.7}$$

Near the carrier frequency, the power spectral density (PSD) of ϕ is related to the PSD of the physical noise μ by:

$$S_\phi(f) \propto \frac{S_\mu}{(2\pi f)^2}. \tag{1.8}$$

For noise with a frequency independent PSD, also known as white noise, $S_\phi \propto 1/f^2$. Base resistance thermal noise and shot noise belong to this category. For $1/f$ noise, $S_\phi \propto 1/f^3$, as shown in Figure 1.9. One may attempt to apply this simple theory to transistor base current noise, and conclude that the $1/f^3$ and $1/f^2$ phase noises due to base current $1/f$ noise and shot noise intersect at an offset frequency equal to the $1/f$ noise corner frequency. This cannot be farther from the truth, as we will show in Chapters 5 and 6, primarily because of the large signal operating nature of transistor in oscillators, which makes the phase noise upconversion process much more complicated.

13

1.3.2 Phase Noise Characterization

In the previous section, it was shown that oscillators tend to convert perturbations from any source into phase variations at the output. The power spectral density of the phase variations is denoted as S_ϕ. S_ϕ is not directly observable and often difficult to measure. Therefore oscillator phase noise is often characterized by the voltage noise S_V. In this section, we first investigate how S_ϕ and S_V are related, then derive the most commonly used description of phase noise, single-sideband phase noise ($\mathcal{L}$).

An oscillation waveform with phase noise can be written as [19]

$$v(t) = x \left(t + \frac{\phi(t)}{2\pi f_0} \right), \tag{1.9}$$

where $x(t)$ represents the unperturbed periodic output voltage. f_0 is the oscillation frequency. Assume that the transistor noise source μ is white and define a such that

$$S_\phi(f) = a \frac{f_0^2}{f^2}. \tag{1.10}$$

The single-sided power spectral density of $v(t)$ is given by [19]

$$S_V(f) = 2 \sum_{i=1}^{\infty} X_i X_i^* \frac{ai^2 f_0^2}{a^2 \pi^2 i^4 f_0^4 + (f + i f_0)^2}, \tag{1.11}$$

where "2" comes from the single-sided power spectral density representation. X_i's are the Fourier coefficients of $x(t)$

$$x(t) = \sum_{i=-\infty}^{\infty} X_i e^{j2\pi i f_0 t}. \tag{1.12}$$

The total power in $S_V(f)$ is

$$P_{total} = \int_0^\infty S_V(f) df = 2 \sum_{i=1}^{\infty} |X_i|^2. \tag{1.13}$$

Note that the total power in the periodic signal $x(t)$ equals to the expression in (1.13) (excluding the power in the dc). This indicates that phase noise does not affect the total power in the signal, it only affects its distribution. Without phase noise, $S_V(f)$ is a series of impulse functions at the harmonics of f_0. With phase noise, the impulse function spreads, becoming wider and shorter but retaining the same total power.

In practice, we are usually interested in the power spectral density (PSD) around the first harmonic, i.e., $S_V(f)$ for f around f_0, because noise around higher order harmonics can be filtered. Neglecting the PSD around higher order harmonics and plotting S_V as a function of the frequency offset from the first harmonic (Δf),

$$S_V(\Delta f) = 2\left|X_1\right|^2 \frac{af_0^2}{a^2\pi^2 f_0^4 + \Delta f^2}. \tag{1.14}$$

This spectrum is Lorentzian. The corner frequency f_Δ is known as the linewidth of the oscillator and is given by $f_\Delta = a\pi f_0^2$, with

$$S_V(\Delta f) = 2\frac{\left|X_1\right|^2}{\pi} \frac{f_\Delta}{f_\Delta^2 + \Delta f^2}. \tag{1.15}$$

At $t \to \infty$, the phase of the oscillator drifts without bound, therefore $S_\phi(f) \to \infty$ as $f \to 0$. However, even as the phase drifts without bound, the excursion in the voltage is limited by the diameter of the limit cycle of the oscillator. Therefore, as $\Delta f \to 0$, the PSD of $v(t)$ flattens out and $S_V(\Delta f) \to 2\left|X_1\right|^2/(\pi f_\Delta)$, which is inversely proportional to a. Thus, the larger a, the more phase noise, the broader the linewidth, and the lower the signal amplitude within the linewidth. The relation between S_ϕ and S_V is illustrated in Figure 1.10.

We now can derive the most commonly used description of phase noise based on the PSD of the voltage noise, single-sideband (SSB) phase noise ($\mathscr{L}$). It is the ratio of the voltage noise power per unit bandwidth to carrier power

$$\mathscr{L}(\Delta f) = \frac{S_V(\Delta f)}{2\left|X_1\right|^2} = \frac{1}{\pi} \frac{f_\Delta}{f_\Delta^2 + \Delta f^2}. \tag{1.16}$$

15
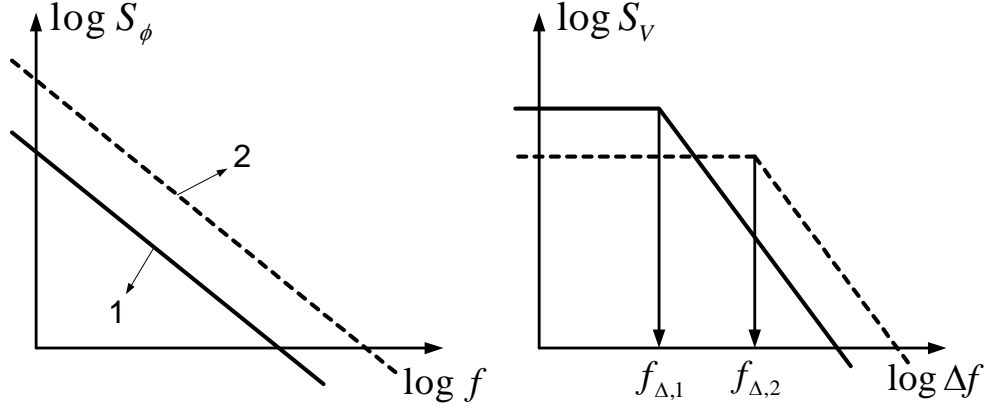
Figure 1.10: Two different ways of characterizing phase noise in the same oscillator. S_ϕ is the spectral density of the phase and S_V is the spectral density of the voltage.

$\mathscr{L}$ is specified in dBc/Hz at a given frequency offset from the carrier. For offset frequencies far way from within the linewidth ($\Delta f \gg f_\Delta$), the phase noise is approximated with

$$\mathscr{L}(\Delta f) = \frac{1}{\pi} \frac{f_\Delta}{\Delta f^2} = a \frac{f_0^2}{\Delta f^2}. \tag{1.17}$$

$\mathscr{L}$ decreases with increasing offset frequency at a rate of 20 dB/decade outside the linewidth. For double-sided S_ϕ,

$$\mathscr{L}(\Delta f) = S_\phi(\Delta f). \tag{1.18}$$

For single-sided S_ϕ,

$$\mathscr{L}(\Delta f) = \frac{1}{2} S_\phi(\Delta f). \tag{1.19}$$

The above results are derived assuming the transistor noise source is white. When significant $1/f$ noise is present, there is no solution for S_V as in the case for white noise source shown in (1.11). $\mathscr{L}$ dropping at a rate of 30 dB/decade can be observed at low offset frequency. (1.17) holds at large offset frequencies where $1/f^3$ phase noise becomes negligible.

16
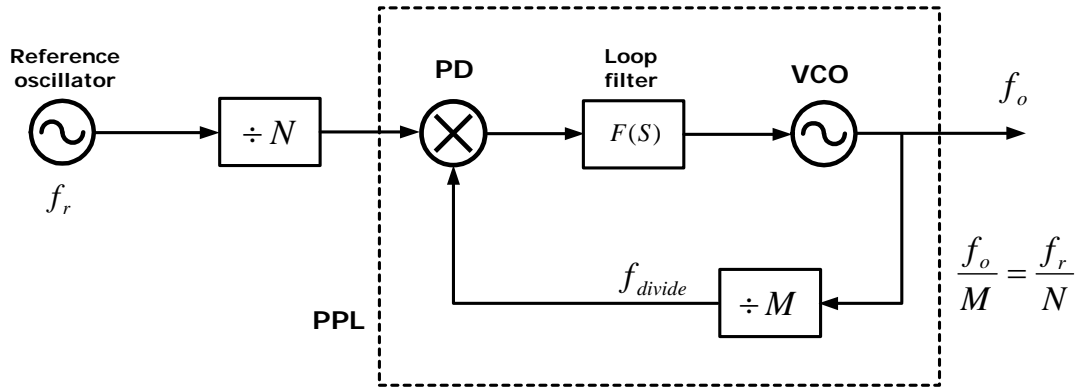
Figure 1.11: Phase locked loop (PLL) based frequency synthesizer.

1.4   System Phase Noise

Voltage controlled oscillator (VCO) is often used in a phase locked loop (PLL) to form a frequency synthesizer. A typical PLL based frequency synthesizer is shown in Figure 1.11. It contains a reference source oscillating at frequency f_r and a VCO oscillating at frequency f_0. The reference frequency is divided by an integer N and the VCO frequency is divided by M. The two divided waves are then compared in a phase detector (PD). When the two phases are equal (phase locking), $f_r/N = f_0/M$. This also means that the output frequency is locked to a rational fraction of the reference frequency. In essence, the synthesizer is capable of generating a large number of highly accurate output frequencies. Frequency selection is achieved by changing the divider ratios M and N.

PLLs are best analyzed in the phase domain. If the reference signal and the output signal are different in phase, the phase detector converts the phase difference into a charge (current). In an ideal PD, the *dc* value of the PD output current is proportional to the phase difference between the reference signal and output signal,

$$\overline{i_{pd}} = K_{pd} \times \theta_e = K_{pd} \times \left(\theta_r/N - \theta_0/M \right). \tag{1.20}$$

θ_e is the phase error. $\overline{i_{pd}}$ is the average of current flowing out of the PD. K_{pd} is the PD gain. Then $\overline{i_{pd}}$ flows into a loop filter and creates a voltage V_{lf} which serves as the control voltage for the oscillator. The oscillation frequency f_0 changes with V_{lf}, forcing θ_e to settle back to zero. f_0 is proportional to V_{lf} with

17
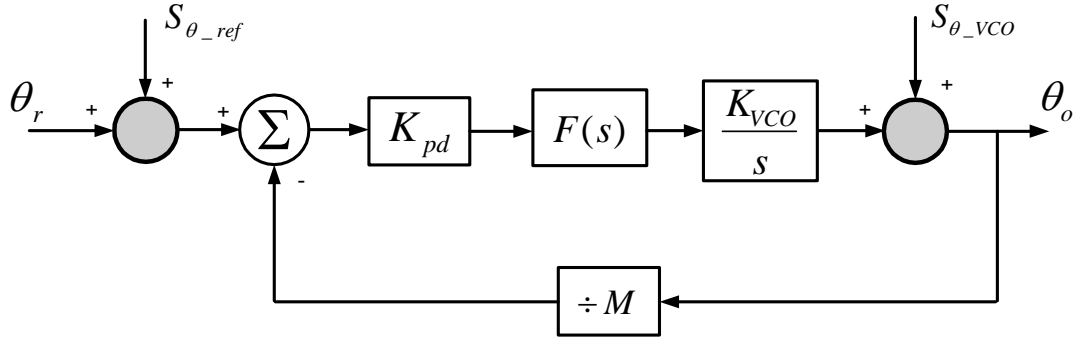
Figure 1.12: Phase locked loop modeled as a linear time invariant system. The major noise sources, reference noise and VCO noise, are included in the drawing.

a gain of K_{VCO}. Since phase is the integral of the frequency, the VCO acts as an ideal integrator for the input voltage when the output variable is phase. The frequency response of the VCO can be expressed as:

$$H_{VCO}(s) = \frac{K_{VCO}}{s}. \tag{1.21}$$

In the phase domain, the PLL can be modeled using the equivalent system shown in Figure 1.12. Also shown in Figure 1.12 are the major phase noise sources in a frequency synthesizer, VCO phase noise (S_{θ_VCO}) and reference signal phase noise (S_{θ_ref}).

To get frequency synthesizer phase noise (S_{θ_syn}), we need to know the transfer function from S_{θ_VCO} to S_{θ_syn}, denoted as $H_{n,VCO}$, as well as the transfer function from S_{θ_ref} to S_{θ_syn}, denoted as $H_{n,ref}$. Assuming the two noise sources are unrelated, S_{θ_syn} is calculated using superposition

$$S_{\theta\_syn} = \left| H_{n,VCO} \right|^2 \times S_{\theta\_VCO} + \left| H_{n,ref} \right|^2 \times S_{\theta\_ref}. \tag{1.22}$$

From classic feedback theory, we know that if the synthesizer is modeled as a linear time invariant system, then

$$H_{n,VCO}(s) = \frac{1}{1 + A(s)/M} = \frac{1}{1 + G(s)}. \tag{1.23}$$

$$H_{n,ref}(s) = \frac{A(s)}{1 + A(s)/M} = \frac{A(s)}{1 + G(s)}. \tag{1.24}$$

18

$$F(s) = \frac{V_{lf}}{i_{pd}} = \frac{1}{sRC+1}$$
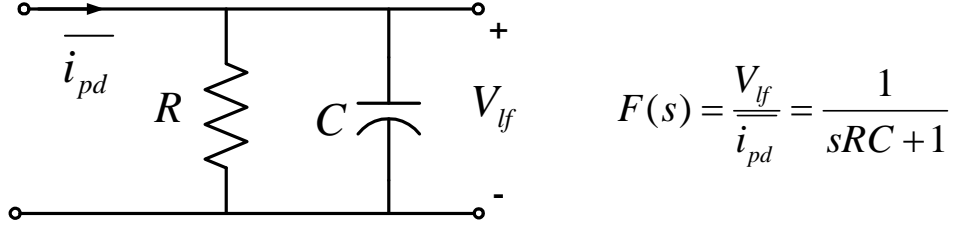
Figure 1.13: A first order RC low-pass filter.

$A(s) = K_{pd} \times F(s) \times K_{VCO}/s$ is the forward gain, M is the divider ratio, $G(s)$ is the open loop transfer function.

Consider a simple case that the PLL is implemented using a first order RC low-pass filter as shown in Figure 1.13. The transfer function of the filter is simply

$$F(s) = \frac{1}{1 + sRC}. \tag{1.25}$$

Using (1.25), it can be easily seen that (1.23) is a high-pass function, while (1.24) is a low-pass function. We should emphasize that terms like low-pass and high-pass are used with respect to the offset frequency $\Delta\omega$, the frequency offset from the oscillation frequency ω_0. For understanding purpose, we further assume that $H_{n,VCO}(s)$ and $H_{n,ref}(s)$ have the ideal high-pass and low-pass characteristics, respectively, as shown in Figure 1.14. ω_{loop} is the loop bandwidth.

To relate S_{θ_ref} and S_{θ_VCO} to S_{θ_syn}, we apply (1.22). As we have shown in Section 1.3.1, S_{θ_VCO} increases as frequency decreases. S_{θ_ref} is relatively white around ω_0 except at very small $\Delta\omega$ where S_{θ_ref} starts to rise. Figure 1.15 shows the phase noises for the VCO, reference signal and synthesizer. ω_u is the frequency where S_{θ_ref} equals S_{θ_VCO}. The choice of ω_{loop} is a matter of compromise. To make the phase locked loop (PLL) faster, ω_{loop} needs to be wider. However, besides the stability issue, there is a potential drawback to maximizing the ω_{loop}. If the reference signal is noisier than the VCO, the high bandwidth loop will reproduce this reference noise at the output. Hence, there is a tradeoff between sensitivity to noise at the input to the loop (a consideration that favors smaller ω_{loop}) and sensitivity to noise that disturbs the VCO frequency (a consideration that favors larger ω_{loop}). If lowest S_{θ_syn} is

19
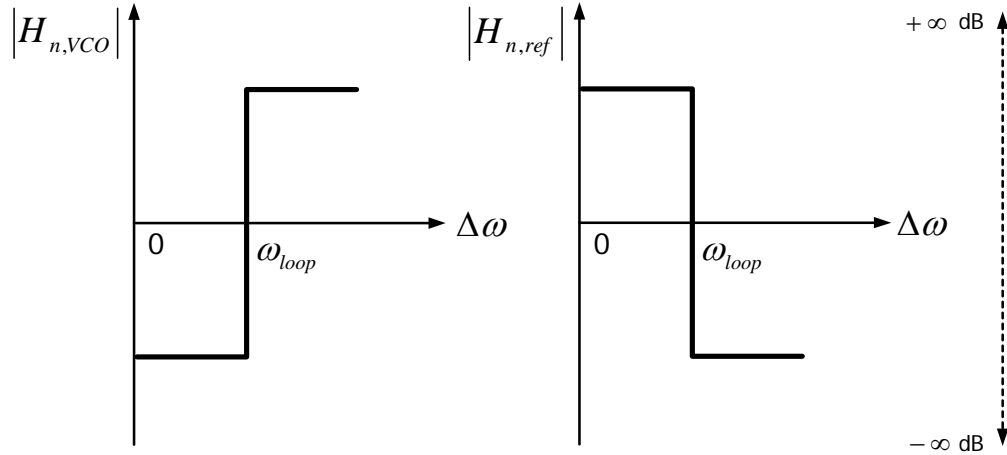
Figure 1.14: Frequency responses of the VCO noise transfer function and reference noise transfer function.

the only concern in determining the ω_{loop}, the problem is greatly simplified. To achieve the minimum integrated S_{θ_syn} (the area under S_{θ_syn}), ω_{loop} should be equal to ω_u, as shown in Figure 1.15. Within the loop bandwidth, S_{θ_ref} dominates the frequency synthesizer phase noise. Outside the loop bandwidth, S_{θ_VCO} dominates. Applying this methodology, we investigate the impact of transistor noise sources on oscillator phase noise as well as frequency synthesizer phase noise in Chapters 5 and 6.

1.5 Thesis Contributions

— **Inverse circuit simulation based low-frequency noise extraction.** The conventional low-frequency noise measurement method is based on a simple equivalent circuit which is easily violated in modern SiGe HBTs operating at high current density and voltage. To measure low-frequency noise under such condition, we propose a new method which we call inverse circuit simulation based low-frequency noise extraction. Instead of basing the noise gain calculation on the simplified circuit, we accurately simulate noise gain in a circuit simulator. The actual noise spectrum is extracted from the simulated noise gain and measured output noise. Using this method, we can investigate the noise dependence on base current and collector-base voltage.
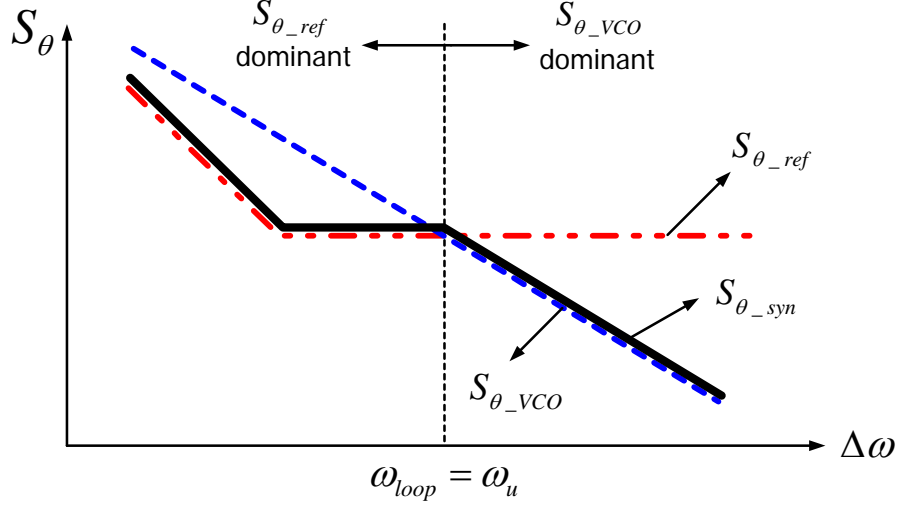
Figure 1.15: Power spectral densities of VCO noise, reference noise and the resultant synthesizer noise.

— $1/f$ **noise generated by** CB **junction traps formed during SiGe growth.** Careful SiGe profile optimization improves transistor performance greatly. However, with increased peak Ge mole fraction, traps are more likely to be induced near the SiGe/Si growth interface. Using devices with identical emitter structure but different collector doping, we prove that CB junction traps contribute to $1/f$ noise when high-injection occurs. The noises originated from EB and CB junctions are separated, and shown to be distinct processes. The similar I_B dependence of $1/f$ noise before and after high-injection indicates that the noise generated at the EB junction has similar origins as the noise generated by the CB junction traps.

— **Optimal transistor sizing and biasing for a SiGe HBT LC oscillator.** Using frequency sensitivity method in ADS and impulse sensitivity function method, we investigate the optimal transistor sizing and biasing for SiGe HBT LC oscillators. For oscillators where base current shot noise contribution is significant, the lowest $1/f^2$ phase noise is achieved in a medium sized HBT with a maximum oscillating collector current below severe high-injection region where f_T and β are significantly degraded and quasi-saturation occurs. The optimal biasing for reduced frequency synthesizer phase noise depends on the loop bandwidth. For a loop bandwidth found in typical frequency synthesizer, the optimal biasing for frequency synthesizer phase noise is the same as the optimal biasing for $1/f^2$ phase noise.

21

— **Technology scaling limitations on** $1/f$ **noise and oscillator phase noise.** The impact of technology scaling on $1/f$ noise and oscillator phase noise is investigated using SiGe technologies featuring 50, 120 and 210 GHz peak f_T. The $1/f$ noise K factor and $1/f$ noise corner frequency are found to be the highest in the 120 GHz HBT, and lowest in the 210 GHz HBT. We examine whether the $1/f$ noise "changes" with scaling translates into corresponding phase noise "changes" and how the "changes" affect RF system phase noise eventually. $1/f$ noise in oscillators is modeled as modulated stationary noise as it is supported by our experimental results. The highest $1/f$ noise K factor in the 120 GHz HBT only affects the overall phase noise at small offset frequencies. The far-off phase noise is actually the lowest in the 120 GHz HBT oscillator. We also find that contrary to the belief by many, the $1/f$ noise corner frequency should not be used alone to evaluate the importance of $1/f$ noise to phase noise. The K factor "threshold" is identified for a given technology. Once the actual K is below such "threshold", further reducing $1/f$ noise does not translate into system phase noise improvement.

— **Systematic identification of limiting phase noise sources.** The ultimate limiting phase noise is identified with technology scaling and increasing oscillation frequency. With technology scaling, phase noises due to collector and base current shot noises decrease as a result of increased current gain and transistor speed, as well as the ability to operate at higher current density. Phase noise due to intrinsic base resistance thermal noise decreases naturally as a result of intrinsic base resistance reduction. The phase noise due to extrinsic base resistance thermal noise can also be reduced by using a relatively large device and an improved extrinsic base structure. The phase noise due to collector current shot noise becomes the ultimate limiting phase noise with technology scaling. With increasing oscillation frequency, the noise power due to all noise sources decreases, except for the noise power due to collector current shot noise, which becomes the ultimate phase noise limiter.

This thesis is organized as follows. Chapter 2 presents the inverse circuit simulation based low-frequency noise extraction and its applications. Chapter 3 investigates the impact of CB junction traps on low-frequency noise and the separation of $1/f$ noises originated from EB and CB junctions. Chapter 4 reviews the small signal noise sources in bipolar junction transistors and investigates related modeling issues in oscillators. Chapter 5 investigates the impact of technology scaling on oscillator phase noise

using frequency sensitivity method analysis in ADS. Using the time domain impulse sensitivity function method, the detailed upconversion mechanisms of individual phase noise contributions is presented in Chapter 6. The limiting phase noise source is investigated as a function of technology scaling, transistor sizing and biasing, and oscillation frequency. The last chapter concludes this work and gives suggestions for future work.

CHAPTER 2

INVERSE CIRCUIT SIMULATION BASED LOW-FREQUENCY NOISE EXTRACTION

Transistor low-frequency noise is an important issue in both baseband and RF circuits of a wireless transceiver due to its conversion to phase noise. Accurate modeling of low-frequency noise is therefore important for circuit design. Different methods have been proposed for low-frequency noise measurement. However, those methods are all based on assumptions which are easily violated for modern SiGe HBTs operating at high currents or high voltage. This chapter presents a novel method of low-frequency noise measurement based on circuit simulation. Using this method, the actual low-frequency noise can be extracted as long as the transistor model used in the simulation is accurate enough.

2.1   Motivations

In a bipolar transistor, the major low-frequency noise source lies in the base current. Experimentally, it has been established that this base current noise source is located between the internal base and emitter nodes in an equivalent circuit, as discussed in Section 1.2. This base current low-frequency noise, denoted as i_{bn}, is often measured indirectly from the collector voltage noise by presenting to the transistor base a source impedance much greater than the input impedance, as shown in Figure 2.1. The measured collector voltage noise is converted to collector current noise using $S_{I_C} = S_{V_C}/R_{C,eff}^2$, which is then converted to the base current noise using $S_{I_B} = S_{I_C}/\beta_{ac}^2$ with β_{ac} being the low-frequency small signal *ac* current gain. β_{ac} is often determined from Gummel characteristics measured under a biasing condition close to that used in the noise measurement. We note that the base current noise can also be measured "directly" from the base using a high precision current amplifier with an input impedance much lower than the transistor input impedance. Each method has its advantages and disadvantages in practice, as discussed in [4]. In general, the indirect method is easier to implement, and widely used. We focus on
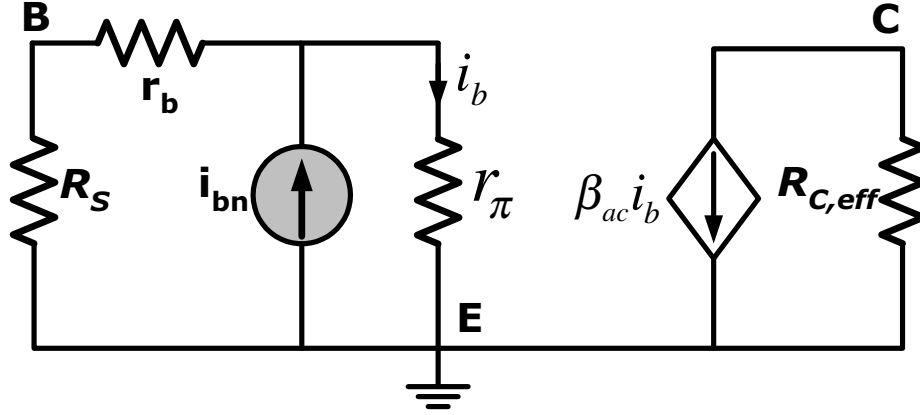
Figure 2.1: Small signal equivalent circuit assumed in the conventional method.

the indirect method in this work. Similar limitations and assumptions exist in the "direct" measurement method as well.

The widely used conventional measurement method, however, is based on a simplified equivalent circuit derived under isothermal condition. While in modern SiGe HBTs, self-heating can be significant, in part due to high operating current density. To enable high current density operation, the collector doping is increased with device vertical scaling, which then increases collector-base junction field and thus avalanche multiplication. One can therefore expect errors in the low-frequency noise measured using the conventional method in high speed SiGe HBTs. Figure 2.2 compares the $1/f$ noise spectra measured at $V_{CB} = 0$ V and 2 V. The internal I_{BE} is fixed at 10 μA. The reason why the internal base-emitter transport current I_{BE} instead of the terminal base current is fixed will be discussed later in this chapter. A big difference between spectra measured at different V_{CB}'s can be observed. A logical question is whether the observed strong V_{CB} dependence is real or just due to extraction error.

To answer this question, we develop a new method of extracting the base current low-frequency noise by taking into account higher order physical effects that are significant in modern SiGe HBTs, such as avalanche multiplication and self-heating. Instead of basing the extraction on a simplified small signal equivalent circuit, we simulate the same circuit used in noise measurement. The circuit simulator used in this work is Cadence SpectreRF [20]. For a given *internal* base current noise excitation, the
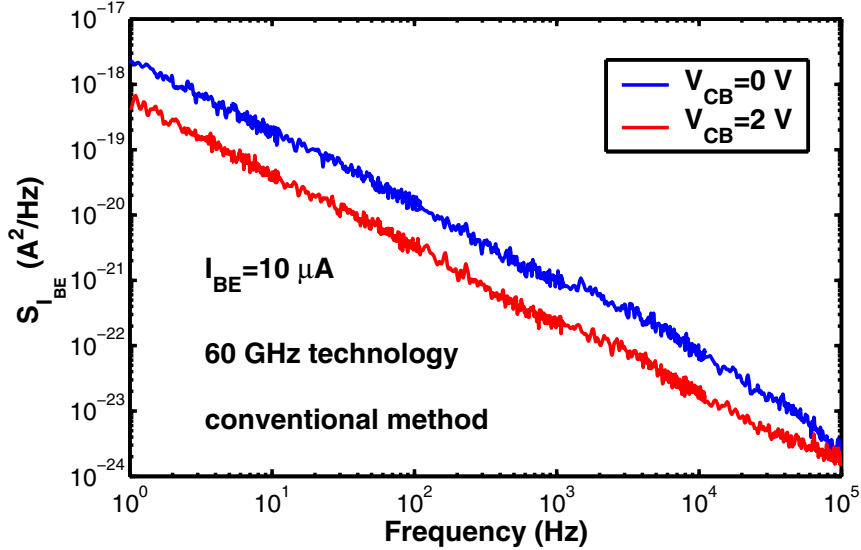
Figure 2.2: Comparison of $1/f$ noise spectra measured at different V_{CB}'s. The internal I_{BE} is fixed at 10 μA.

collector voltage noise is simulated, and thus the noise transfer function, or the noise gain G_{noise}, can be obtained from the ratio of the simulated collector voltage noise and internal base current noise excitation. We can then extract the internal base current noise from the measured collector voltage noise using $S_{I_B} = S_{V_C}/G_{noise}$. We refer to the above extraction method as inverse circuit simulation based low-frequency noise extraction, as we are essentially simulating the input base current noise from the measured output voltage noise. The VBIC bipolar transistor model [21], which takes into account self-heating and avalanche multiplication effects, is used. As a result, the impact of self-heating and avalanche multiplication on low-frequency noise extraction are automatically accounted for. Furthermore, other non-ideal effects such as Early effect, terminal parasitic resistances, and high injection effects are also accounted for.

2.2   Technical Approach

Since the built-in VBIC model does not provide access to transistor internal base and collector nodes, the first step of the proposed method is to implement the VBIC model using an analog hardware description language, such as Verilog-A [22] or Verilog-AMS [23]. In this work, the VBIC model is

26
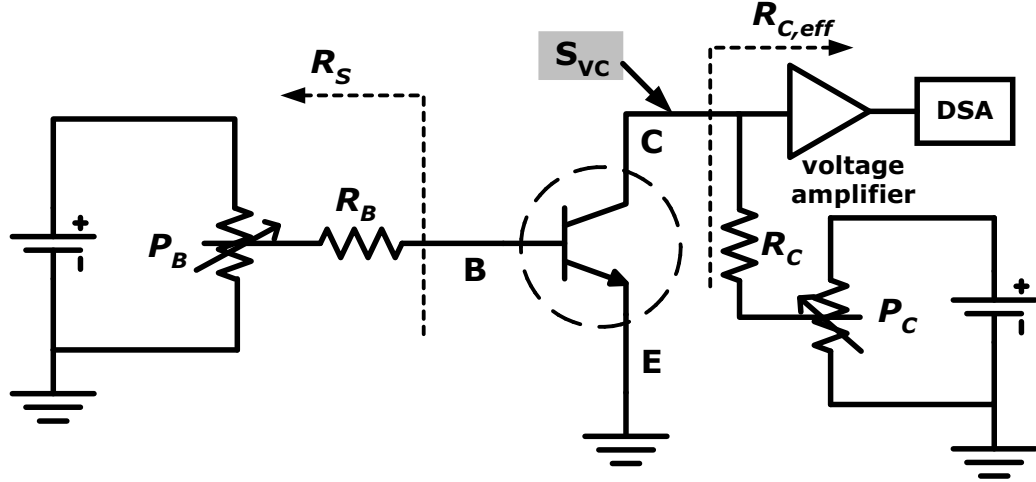
Figure 2.3: Diagram of the experimental setup.

implemented using Affirma Verilog-A [24] in SpectreRF from Cadence, the circuit simulator used in this work. Refer to Appendix B for detailed discussion on verilog-A implementation.

2.2.1 Noise Measurement Setup

Figure 2.3 shows the diagram of the measurement setup. Potentiometers P_B and P_C are used to set the *dc* biasing of the base and collector, respectively. Batteries are used as power supplies to minimize spurious noise. R_B is chosen to be much larger than the transistor input resistance r_π in order to force the base noise current to flow into the transistor instead of into the base biasing network. The collector noise voltage is further amplified by a low-noise amplifier and detected by a dynamic signal analyser (DSA). The system is controlled by a Labview program.

In the conventional method, the spectral density of the base current noise (S_{I_B}) is obtained from the spectral density of the collector voltage noise (S_{V_C}) as

$$S_{I_B} = \frac{S_{V_C}}{\left(\beta_{ac} \times R_{C,\mathit{eff}}\right)^2},$$

(2.1)

27
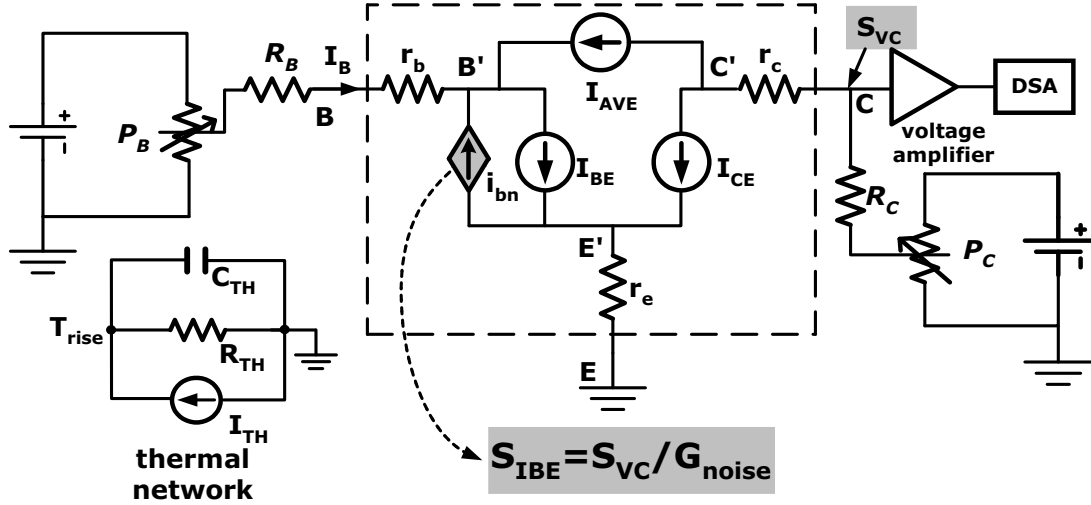
Figure 2.4: A simplified low-frequency equivalent circuit for illustration.

with $R_{C,eff}$ being the effective dynamic load resistance seen by the collector and β_{ac} being the small signal current gain. Neglecting the output resistance of the transistor, $R_{C,eff}$ is simply $R_C + P_{C,1} || P_{C,2}$ with $P_{C,1}$ and $P_{C,2}$ being the two components of P_C. β_{ac} is calculated from the simple relation [25]

$$\beta_{ac} = m\beta_{dc}, \tag{2.2}$$

where β_{dc} is the *dc* current gain given by I_C/I_B. The value of m is bias dependent

$$m = \frac{\Delta \ln I_C(V_{BE})}{\Delta \ln I_B(V_{BE})}. \tag{2.3}$$

Note I_B and I_C in β_{dc} and m are evaluated at the same V_{BE}. (2.1) neglects self-heating, avalanche multiplication, and many other higher order effects that can become significant in scaled SiGe HBTs. An alternative that includes the higher order effects is to simulate the same circuit used in the measurement using a circuit simulator, with a transistor model that accounts for these higher order effects, e.g. VBIC.

Figure 2.4 shows a simplified low-frequency equivalent circuit of the measurement setup. This drawing is simplified by leaving out the parasitic pnp transistor and capacitances, while the full circuit is used in our simulation. i_{bn} represents the base current low-frequency noise source. We denote the spectral
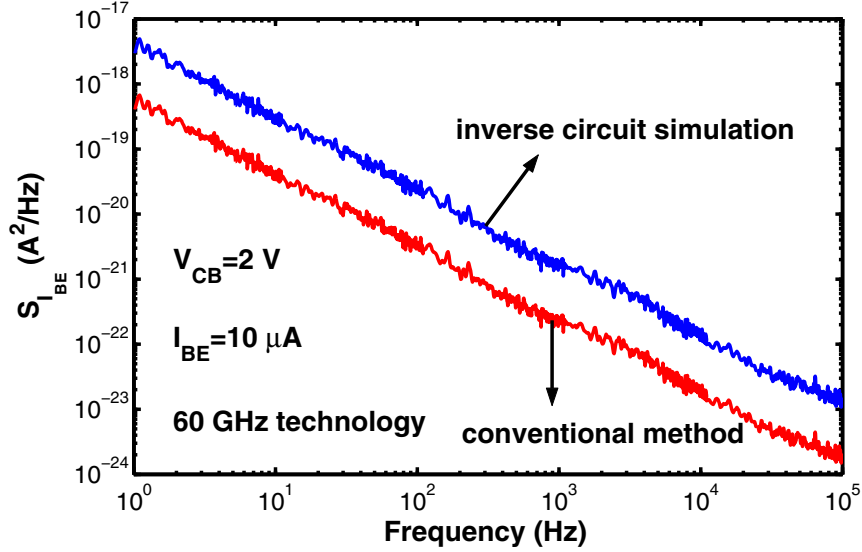
Figure 2.5: Comparison of $S_{I_{BE}}$ spectra extracted using the proposed inverse circuit simulation and the conventional measurement method. $V_{CB} = 2$ V, $I_{BE} = 10$ μA.

density of i_{bn} as $S_{I_{BE}}$, as it relates to the base current injected into the emitter (I_{BE}). I_{CE} represents the electron current transported from the emitter to the collector. I_{AVE} represents the avalanche current. The base terminal current I_B relates to I_{BE} by $I_{BE} = I_B + I_{AVE}$. The thermal network accounts for self-heating effect. I_{TH} is computed as the sum of the current and voltage product for all branches of non-energy storage elements. I_{BE}, I_{CE}, and I_{AVE} are all temperature dependent.

2.2.2 Noise Extraction

In the conventional method, the noise gain is simply assumed to be $R^2_{C,eff} \times \beta^2_{ac}$. This noise gain calculation is based on a simple equivalent circuit shown in Figure 2.1. The assumptions behind the simple model can be easily violated. Therefore, in this work, we simulate the noise gain for all frequencies measured. By placing a unity magnitude small signal noise current between the internal base and emitter nodes, the resulting collector voltage noise gives the noise gain. Next the measured collector voltage noise is divided by the simulated noise gain for all frequencies to obtain the internal base current noise spectrum, i.e. $S_{I_{BE}} = S_{V_C}/G_{noise}$. Figure 2.5 compares the $S_{I_{BE}}$ spectra extracted using the conventional method and the proposed inverse circuit simulation method. $V_{CB} = 2$ V, $I_{BE} = 10$ μA, terminal base
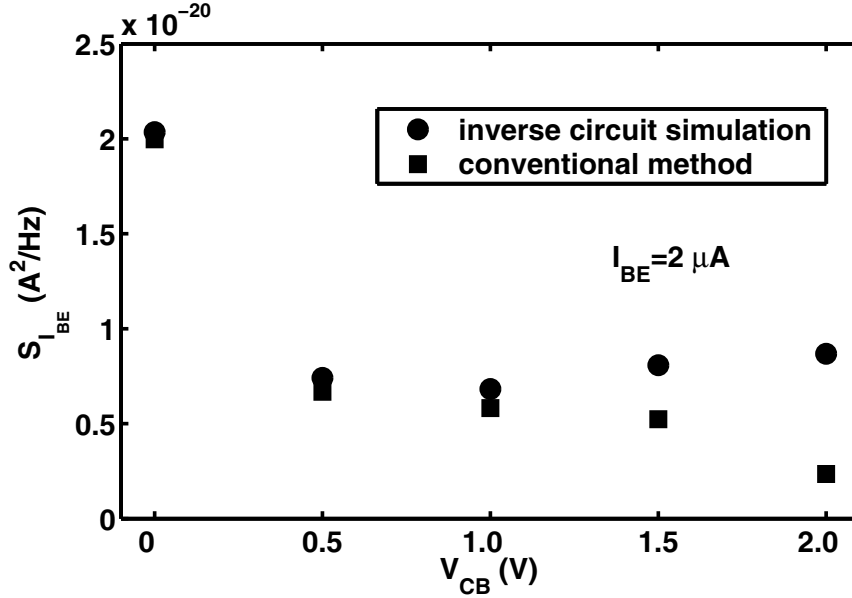
Figure 2.6: Comparison of $S_{I_{BE}}$ spectra extracted using conventional method and inverse circuit simulation as a function of V_{CB} for $I_{BE} = 2\ \mu A$. Frequency is 10 Hz.

current I_B is 8.1 μA. The $S_{I_{BE}}$ extracted from inverse circuit simulation is almost 10 times higher than that from the conventional method.

2.3 Application of the Method

The proposed method enables the investigation of a whole range of noise problems we could not investigate using conventional methods, which was mainly due to the over simplified circuit model used in base current noise extraction. In this section, we investigate the dependence of low-frequency noise on the collector-base voltage (V_{CB}) and the transport base current (I_{BE}).

2.3.1 V_{CB} Dependence

The base current noise is typically assumed to be only a function of the base current, or more precisely, the emitter injection and neutral base recombination components of the base current, which is denoted as I_{BE} in the simplified equivalent circuit shown in Figure 2.4. This is typically assumed in circuit simulators without experimental justification. Experimentally, the main difficulty with measuring
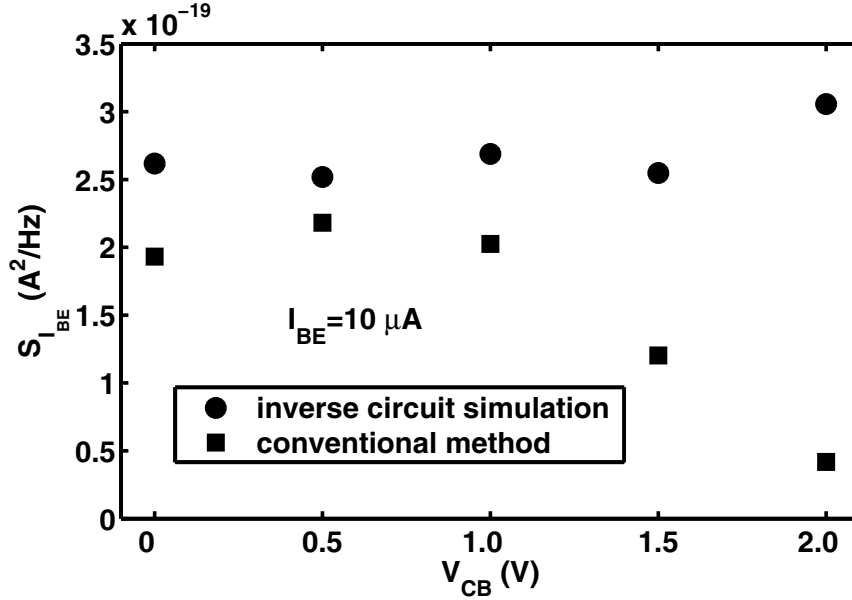
Figure 2.7: Comparison of $S_{I_{BE}}$ spectra extracted using conventional method and inverse circuit simulation as a function of V_{CB} for $I_{BE} = 10 \ \mu A$. Frequency is 10 Hz.

the V_{CB} dependence of noise has been the avalanche multiplication effect and self-heating effect, neither of which can be handled by the conventional method.

To examine V_{CB} dependence of $1/f$ noise, we first vary V_{CB} for a low biasing current. For each V_{CB}, the biasing circuit is adjusted such that the internal base current I_{BE} as opposed to the terminal base current I_B is kept the same for a fair comparison. According to Figure 2.4,

$$I_{BE} = I_B + I_{AVE}. \tag{2.4}$$

Since I_{AVE} increases with increasing V_{CB}, I_{BE} will be higher at higher V_{CB} if I_B is kept the same. This is undesired, as the physical $1/f$ noise process is associated with the EB junction base current component, and does not have anything to do with the avalanche process. For example, if I_B is kept at 2 μA for $V_{CB} = 0$ and 2 V, the resulting internal I_{BE} are 2 and 2.615 μA, respectively. The error introduced will be significant.
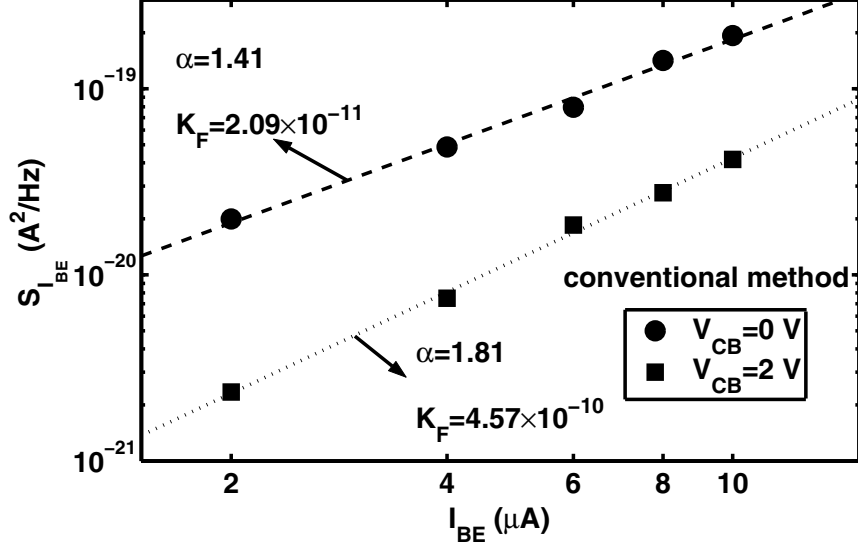
Figure 2.8: $S_{I_{BE}}$ vs I_{BE} extracted using the conventional method. $V_{CB} = 0$ and 2 V. Frequency is 10 Hz.

Figure 2.6 shows the $S_{I_{BE}}$ at 10 Hz as a function of V_{CB} measured using the inverse simulation method and the conventional method. V_{CB} is varied from 0 V to 2 V, with I_{BE} kept at 2 μA. A decrease of $S_{I_{BE}}$ with increasing V_{CB} can be clearly identified at V_{CB} close to 0 V. The conventional method underestimates the amount of $1/f$ noise at higher V_{CB} because of the incorrect noise gain. At a higher I_{BE} of 10 μA, however, the $1/f$ noise measured using the inverse simulation method is virtually independent of V_{CB}, as shown in Figure 2.7. The error introduced by the conventional method becomes larger. The $S_{I_{BE}}$ measured using conventional method decreases rapidly with increasing V_{CB}, which is clearly unphysical. The fundamental reason for the failure of the conventional method is the incorrect overestimation of the noise gain using small signal *ac* gain, which approaches infinity when base current reversal occurs.

2.3.2 Base Current Dependence

The base current $1/f$ noise in bipolar transistors is generally modeled by

$$S_{I_{BE}} = K_F \frac{I_{BE}^{\alpha}}{f^{\gamma}}, \tag{2.5}$$

32
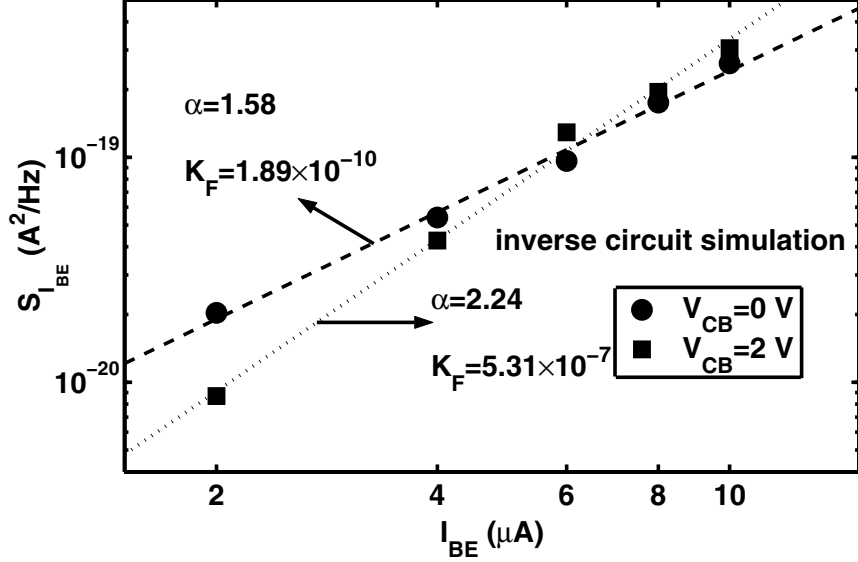
Figure 2.9: $S_{I_{BE}}$ vs I_{BE} extracted using the proposed method. $V_{CB} = 0$ and 2 V. Frequency is 10 Hz.

where K_F and α are the *KF* and *AK* factors in SPICE, respectively. γ is close to 1. Successful modeling of $1/f$ noise relies on accurate experimental extraction of *KF* and *AF* factors. We now examine the I_{BE} dependence measured using the conventional method and the proposed method.

Figure 2.8 compares $S_{I_{BE}}$ extracted using conventional method as a function of I_{BE} at $V_{CB} = 0$ V and 2 V. The conventional method gives a large reduction of $1/f$ noise with increasing V_{CB}, which is again unphysical, due to the incorrect overestimation of noise gain by the small signal current gain. Figure 2.9 plots $S_{I_{BE}}$ extracted using the inverse circuit simulation as a function of I_{BE} at $V_{CB} = 0$ V and 2 V. The extracted $S_{I_{BE}} - I_{BE}$ dependence is much more weakly dependent on V_{CB} compared to that extracted using the conventional method. In the lower I_{BE} range, the $S_{I_{BE}}$ at $V_{CB} = 0$ V is only slightly higher than at $V_{CB} = 2$ V. In the higher I_{BE} range, $S_{I_{BE}}$ is nearly the same at $V_{CB} = 0$ V and 2 V. One may still fit $S_{I_{BE}}$ as a unified function of I_{BE} using (2.5) for each V_{CB}.

We have developed an inverse circuit simulation based method for extraction of base current noise spectra in advanced SiGe HBTs. A key difference from the conventional method is that the noise gain is obtained much more accurately by accounting for higher order effects such as avalanche multiplication and self-heating. The utility of the method is demonstrated by examining the collector-base voltage and

base transport current dependences of $1/f$ noise. The proposed method can be applied to the extraction of the correlation between base current noise and collector current noise using a double channel dynamic signal analyzer.

CHAPTER 3

IMPACT OF COLLECTOR-BASE JUNCTION TRAPS

SiGe profile optimization reduces $1/f$ noise for a given collector current density [26]. However, with increased peak Ge concentration at the retrograding SiGe/Si growth interface, traps are more likely to be induced. These traps are called "collector-base (CB) junction traps" because they are physically located inside the CB junction space charge region. Since $1/f$ noise is closely related to traps, it is logical to wonder whether the CB junction traps generate $1/f$ noise. A critical tool used is to compare the standard and high breakdown voltage device characteristics at the same base-emitter voltage [27]. However, the internal base-emitter voltage may be different, because of parasitic terminal resistances, which could be significant in these devices operating at high current density. Another closely related but unresolved issue is whether the measured $1/f$ noise originated from the base and emitter series resistances [28].

In this chapter, we examine the impact of CB junction traps on low-frequency noise, especially for the high breakdown voltage devices. By taking into account the series resistances, the standard and high breakdown voltage devices are compared at the same *internal* base-emitter voltage. The impact of series resistance $1/f$ noise is quantified by varying the source impedance. The base current component due to emitter hole injection and the base current component due to CB junction recombination are separated. The $1/f$ noises associated with the two base current components are then separated. We will show that the dependence of EB and CB junction $1/f$ noise on their respective base current component is different, despite that the dependence of the total $1/f$ noise on the total base current is approximately the same for the standard and high breakdown voltage devices.

Three SiGe profiles [29] [30], including a 10% peak SiGe control profile, a 14% peak LN1 profile, a 18% peak LN2 profile, and a silicon comparison are used. The SiGe films are unconditionally stable

35

for all of the SiGe profiles. Compared to the SiGe control, LN1 and LN2 have a higher Ge content and a larger Ge gradient in the neutral base to achieve higher β and higher f_T, but less Ge retrograding into the collector to keep the total Ge content within the thermal stability limit. For each profile, two breakdown voltages are obtained during selectively implanted collector (SIC) formation. The standard breakdown voltage (SBV) devices received both a deep and a shallow collector implant, and have a peak f_T of 50 GHz (BV_{CEO} = 3.3 V). The high breakdown voltage (HBV) devices received only the deep collector implant, and have a peak f_T of 30 GHz (BV_{CEO} = 5.3 V). The key performance metrics for the SBV and HBV devices are compared in Table 1.1. Details of the fabrication process can be found in [8]. The same experiments are conducted on the standard and high breakdown voltage SiGe HBTs from a 90 GHz [31] peak f_T technology.

3.1   Impact on Base Current

A subtle but important effect in SiGe HBTs is "neutral" base recombination (NBR), which ultimately limits the output impedance of high precision current sources [32] [33]. However, traps located in the metallurgical base cannot quantitatively explain the I_B decrease with increasing V_{CB}, which is considered to manifest "neutral" base recombination. Traps physically located near the SiGe/Si growth interface were then proposed to quantitatively explain the observed $I_B - V_{CB}$ dependence, as detailed in [34]. These traps produce a recombination current in the CB junction space charge region. Below high-injection, this recombination current is small in absolute magnitude, but strongly dependent on V_{CB}. At high-injection, the CB junction traps can cause significant amount of recombination current. The situation is particularly worse in high breakdown voltage devices due to enhanced high-injection barrier effect. This recombination process through CB junction traps affects low-frequency noise as well, as detailed below.

Figure 3.1 illustrates the various base current components for the SiGe HBTs used. The total I_B consists of an emitter hole injection current I_{pe}, a neutral base recombination current I_{nbr}, an EB space charge region (SCR) recombination current I_{ebsr}, and a CB SCR recombination current I_{cbsr}. In these
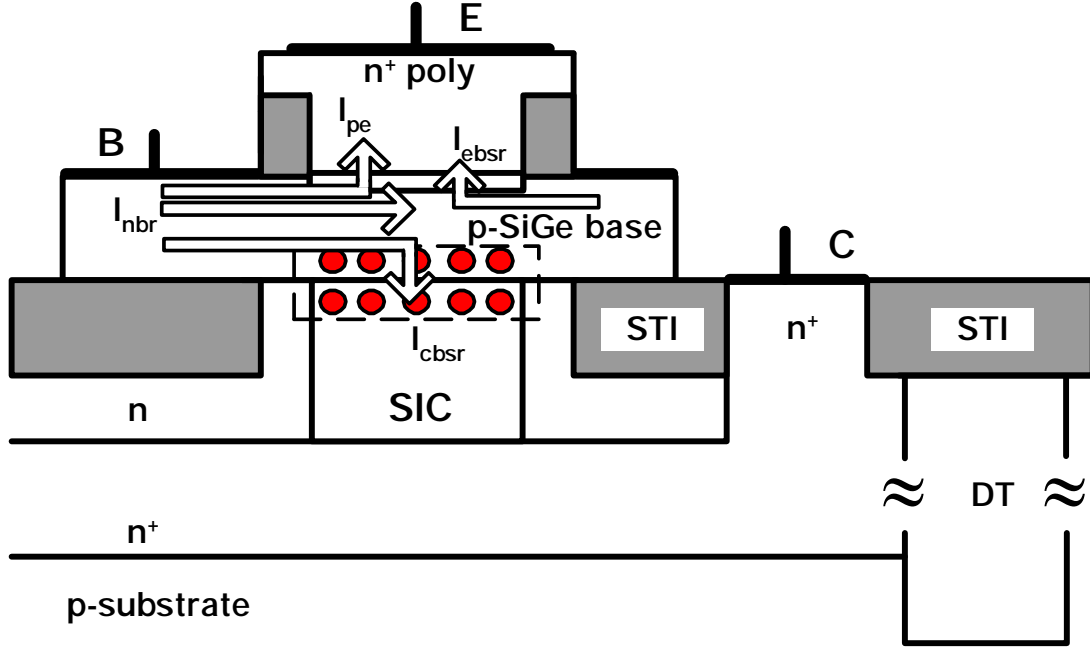
Figure 3.1: Illustration of various I_B components. CB junction traps are shown as circles.

devices, the total I_B below high-injection is dominated by I_{pe}. I_{ebsr}, I_{nbr}, and I_{cbsr} only account for a small fraction of the total I_B, as detailed in [34]. I_{cbsr} is strongly modulated by V_{CB}, and is mainly responsible for the small but measurable I_B reduction with increasing V_{CB} under low-injection. I_{cbsr}, however, can be quite significant in the high breakdown voltage devices when high-injection occurs, as detailed below. The internal base-emitter voltage V'_{BE} instead of the measured external V_{BE} is used to eliminate the impact of base and emitter series resistances. V'_{BE} is calculated as $V'_{BE} = V_{BE} - I_B r_b - I_C r_e$, where $r_b = 143.6 \ \Omega$, and $r_e = 13.7 \ \Omega$. r_b and r_e were extracted from s-parameters. Figure 3.2 compares the Gummel characteristics using the terminal V_{BE} and internal V'_{BE}. The corrections due to r_b and r_e are significant in high biasing range. In the following discussion, the internal base-emitter voltage V'_{BE} will be used unless stated otherwise.

3.1.1 $I_B - V_{CB}$ Characteristics and Trap Density

To examine the CB junction trap density difference among SiGe profiles, we first compare the I_B reduction as a function of V_{CB}. In Figure 3.3 (a), ΔI_B, defined as $I_B(V_{CB}) - I_B(V_{CB} = 0 \ \text{V})$, is plotted as

37
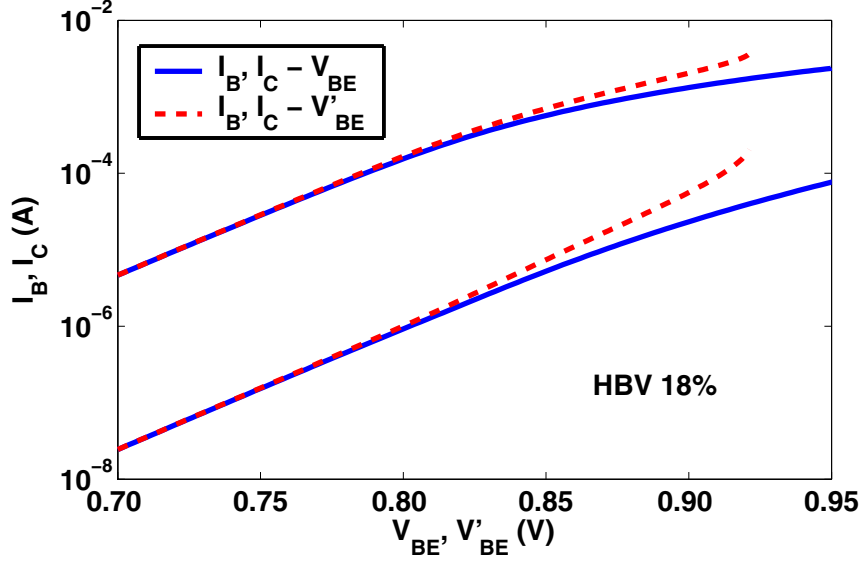
Figure 3.2: Comparison of Gummel characteristics using the terminal V_{BE} and internal V'_{BE}. The high breakdown voltage device with 18% peak Ge concentration (LN2) is used.

a function of V_{CB} for the standard breakdown voltage (SBV) devices of different SiGe profiles. The high breakdown voltage (HBV) device results are shown in Figure 3.3 (b). V_{CB} is limited to below 1.0 V for the SBV devices and 1.5 V for the HBV devices to avoid impact ionization. The internal V'_{BE} is chosen differently for each profile such that I_C is approximately the same, because I_{cbsr} is proportional to the product of I_C and trap density [34]. If the same V'_{BE} is used for different profiles, one would observe a larger I_B reduction in the SiGe devices, simply because of higher I_C.

The I_B reduction with increasing V_{CB} is strongest for LN1 and LN2, small for SiGe control, and nearly invisible for silicon control. The larger I_B reduction in the HBV devices is simply due to stronger CB depletion layer modulation by V_{CB}. This suggests that LN1 and LN2 HBTs have a higher CB junction trap density, while the Si BJTs have the lowest CB junction trap density. The higher trap density in LN1 and LN2 HBTs is attributed to the higher peak Ge content and steeper SiGe retrograding into the collector. One may question whether the higher collector implant dose in the SBV devices could have caused a lot of damages. This is unlikely, as all of the standard breakdown voltage SiGe and Si control devices show negligible I_B reduction with increasing V_{CB}.
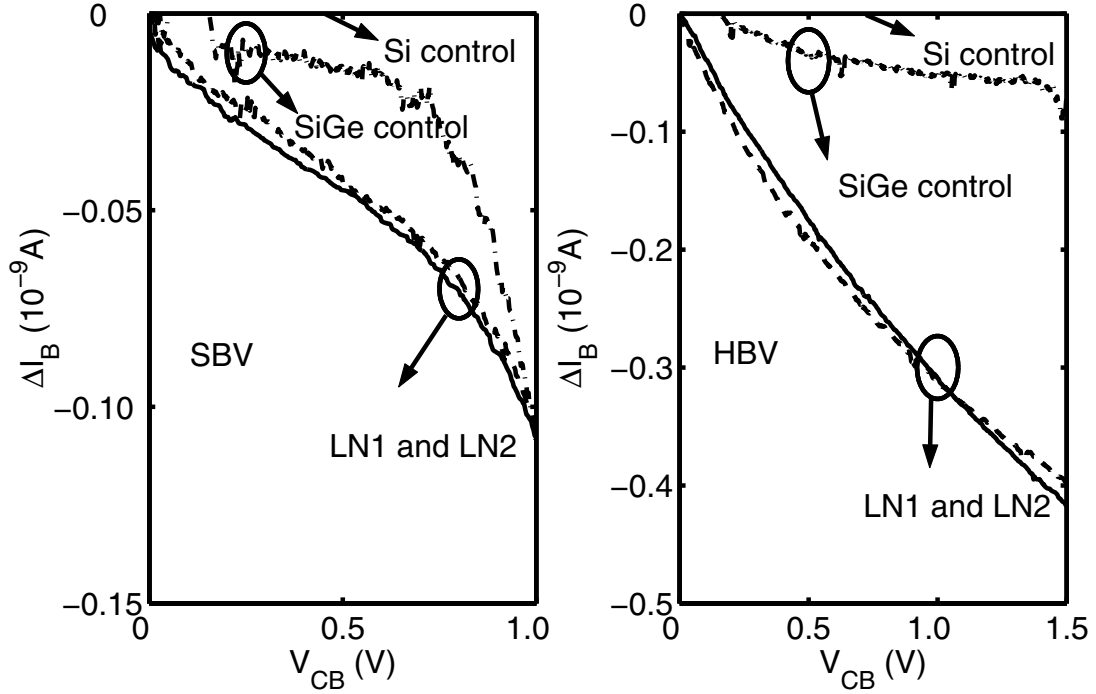
Figure 3.3: Comparison of $\Delta I_B - V_{CB}$ between different profiles, SiGe control, LN1, LN2 and Si control. (a) Standard breakdown voltage devices, (b) High breakdown voltage devices. $I_C = 0.75\ \mu A$, $A_E = 0.5 \times 2.5\ \mu m^2$.

3.1.2 Gummel Characteristics

The CB junction traps can also cause a large difference in the Gummel characteristics between the standard breakdown and high breakdown voltage devices. Figures 3.4 (a)-(d) compare the Gummel characteristics of the SBV and HBV HBTs of different SiGe profiles. $V_{CB} = 0$ V. The internal base-emitter voltage V'_{BE} instead of the external V_{BE} is used.

Collector Current I_C

For all profiles, both Si and SiGe, the I_C at low V'_{BE} is slightly lower in the HBV devices than that in the SBV devices. The difference is biggest in LN1 and LN2, smaller in SiGe control, and almost negligible in Si control. The HBV devices received only the deep collector implant, the collector doping near the collector-base junction is thus lower than the SBV devices which received both the deep and shallow collector implants. The lower collector doping near the CB junction makes the neutral base

Figure 3.4: Comparison of the Gummel characteristics between standard breakdown and high breakdown voltage devices for various SiGe profile designs. (a) LN1 with 14% peak Ge, (b) LN2 with 18% peak Ge, (c) SiGe control with 10% peak Ge, and (d) Si control. $V_{CB} = 0$ V, $A_E = 0.5 \times 2.5 \ \mu\text{m}^2$. The internal V'_{BE} is used.

width (W_B) in the HBV device larger than the SBV device of the same profile, which directly translates into lower I_C. The reason why the SiGe devices show larger difference in I_C at low V'_{BE} can be understood as follows. Collector current in a device with constant electron diffusivity (D_n) in the base region, and constant equilibrium minority carrier density (n_{p0}) can be simplified as

$$I_C = qA_E \frac{D_n n_{p0}}{W_B} e^{qV'_{BE}/kT}, \tag{3.1}$$

where A_E is the emitter area. For the same amount of W_B increase, devices with higher $D_n n_{p0}$ product experience more I_C reduction when V'_{BE} is fixed. This is the case for the SiGe devices because Ge-induced band offset exponentially increases the intrinsic carrier density in the base and hence I_C. The LN1 and LN2 devices have a higher I_C, and thus larger difference in I_C between the SBV and HBV devices at the fixed V'_{BE}.

40

With increasing V'_{BE}, the difference in I_C between the SBV and HBV devices for all of the profiles becomes larger compared to the difference at low V'_{BE}. The LN1 and LN2 devices show a even larger increase in the difference. The HBV devices reach high-injection at a smaller V'_{BE} because of lower collector doping. When the device is biased at the V'_{BE} which makes the HBV devices operate in the high-injection region while the SBV devices operate below high-injection region, the difference in I_C becomes larger because high-injection kirk effect in the HBV devices decreases I_C. For the LN1 and LN2 devices, high-injection induced heterojunction barrier effect makes the I_C reduction more serious because of the reduced Ge retrograding into the collector [4]. Therefore the difference in I_C between the SBV and HBV of the two optimized devices is much more significant than SiGe control and Si control devices.

Base Current I_B

For all profiles, both Si and SiGe, the I_B at low V'_{BE} is approximately the same for the HBV and SBV devices, because of identical emitter structure, and I_{pe} dominates the total I_B. As V'_{BE} increases, the HBV LN1 and LN2 show a higher I_B than the SBV SiGe HBTs of the same profile. We attribute the higher I_B in the HBV LN1 and LN2 to the high-injection potential barriers for electrons and holes due to Ge retrograding and the high CB junction trap density. The HBV and SBV SiGe control and Si control devices show no I_B difference, even at injection levels sufficient for base push-out. This indicates that the CB junction trap density is very low in the HBV SiGe control and Si control devices, the resulting high-injection recombination current in the CB junction still remains negligible compared to I_{pe}, the I_B due to emitter hole injection, despite high-injection.

Observe that the I_B contribution from the CB junction traps becomes quite significant at high-injection in HBV LN1 and LN2. To the first order, the CB junction recombination current in the HBV devices can be estimated as the I_B difference between the HBV and SBV devices of the same profile under the same V'_{BE}. At V'_{BE} = 0.860 V, I_{cbsr} accounts for 61.5% of total I_B for the HBV LN1 and 59.9% for the HBV LN2. This calls for accurate modeling of the I_B component due to CB junction traps in compact modeling, especially for the high breakdown voltage devices. To our knowledge, the

recombination current due to CB junction traps is not accounted for in current transistor models, e.g., VBIC [21], HICUM [35], and MEXTRAM [36].

Current Gain β

Figures 3.5 (a)-(d) compare $\beta = I_C/I_B$ as a function of internal V'_{BE} of the SBV and HBV HBTs for different SiGe profiles. $V_{CB} = 0$ V. Three regions can be identified from each β vs. V'_{BE} curve despite the difference in the onset of each region: low-injection (A), mid-injection (B) and high-injection (C), as illustrated in Figure 3.5 (c). In the mid-injection region or the ideal region, β is almost flat. β is higher in the SBV device than that in the HBV device of the same profile because of the larger W_B in the HBV device due to lower collector doping, as discussed earlier in this section. β falls off at small V'_{BE} because of the increasing importance of the EB space charge region recombination current I_{ebsr}. At high V'_{BE}, β also falls off which is caused by high-injection kirk effect, and for SiGe HBTs, heterojunction barrier effect [4], Ge grading effect [4] and CB junction recombination. The role of CB junction recombination in shaping β at high-injection region is discussed next.

As can be seen from Figure 3.5, β drops much faster and much earlier in the HBV LN1 and LN2 compared to the SBV devices of the same profile. Kirk effect, heterojunction barrier effect and Ge grading effect decrease β, however the much larger β reduction in the HBV LN1 and LN2 is not the sole result of these effects. Ge grading effect decreases collector current with increasing V'_{BE}. To the first order, for the same amount of bandgap reduction at the edge of the EB junction, SBV devices experience more I_C reduction (and thus more β reduction) because they have higher I_C to begin with. Therefore Ge grading effect is not responsible for the observed large reduction of β in the HBV LN1 and LN2. The HBV Si transistor $\left[\text{Figure 3.5 (d)}\right]$ has kirk effect, but the β reduction is not significant compared to the SBV Si transistor. The HBV SiGe control device $\left[\text{Figure 3.5 (c)}\right]$ does not show that much β decrease either compared to the SBV device, despite Kirk effect and heterojunction barrier effect. Therefore the CB junction recombination contributes significantly the observed β reduction in the HBV LN1 and LN2.
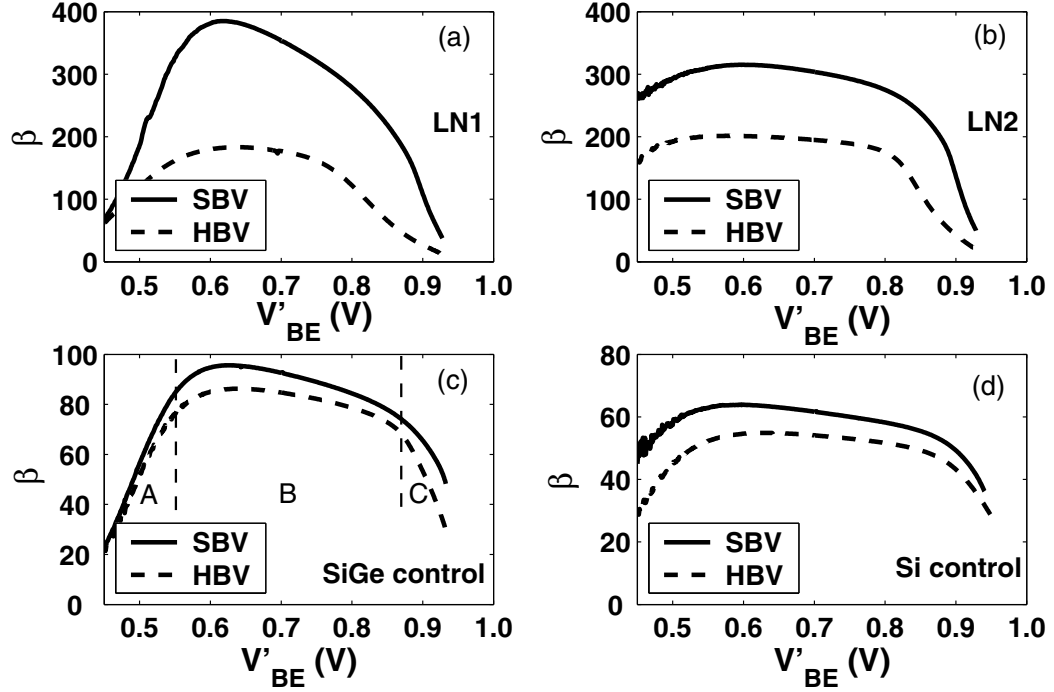
Figure 3.5: Comparison of $\beta = I_C/I_B$ as a function of internal V'_{BE} between standard breakdown and high breakdown voltage devices for various SiGe profile designs. (a) LN1 with 14% peak Ge, (b) LN2 with 18% peak Ge, (c) SiGe control with 10% peak Ge, and (d) Si control. $V_{CB} = 0$ V, $A_E = 0.5 \times 2.5$ μm^2.

3.2 Low-Frequency Noise Implications

Low-frequency noise has been a design constraint in RF applications because it can be converted to phase noise. Since low-frequency noise is sensitive to traps and defects, it is important to investigate the impact of CB junction traps on base current low-frequency noise. We use a common-emitter experimental setup identical to Figure 2.3 for low-frequency noise measurement. V_{BE} and V_{CE} are adjusted independently through the potentiometers in the biasing circuit for the base and collector, respectively. The power spectral density of the base current (S_{I_B}) can be obtained from the noise voltage measured at the collector (S_{V_C}) if S_{V_C} is dominated by the contribution from S_{I_B}.

Whether S_{V_C} is dominated by S_{I_B} or not requires careful examination. It has been shown in [28] that in modern transistors, the $1/f$ noise generated by the base series resistance r_b and emitter series resistance r_e could be significant or dominant over the $1/f$ noise of the base current, especially for

devices of small dimensions. The investigation of the impact of CB junction traps on low-frequency noise through the comparison between the SBV and HBV devices would be misleading if the measured S_{V_C} contributions from the series resistances are significant, since the HBV and SBV devices have similar series resistances. Therefore, we now examine the importance of the $1/f$ noise contributions from the series resistances.

3.2.1 Low-Frequency Noise from the Series Resistances

Figure 3.6 shows a simplified small signal equivalent circuit of the measurement setup, including all of the major $1/f$ noise sources. S_{I_B}, S_{I_C}, S_{r_b}, S_{r_e} and S_{r_c} are the $1/f$ noise spectral densities of the base current I_B, collector current I_C, base series resistance r_b, emitter series resistance r_e and collector series resistance r_c, respectively. r_π is the transistor input resistance. R_S is the equivalent source resistance. R_C is the effective load resistance. The total low-frequency noise voltage measured at the collector can be written as [28]

$$S_{V_C} = \frac{R_C^2}{Z^2} \left[\beta^2 (r_b + R_S + r_e)^2 S_{I_B} + (r_\pi + r_b + R_S + r_e)^2 S_{I_C} + \beta^2 (I_B^2 S_{r_b} + (I_B + I_C)^2 S_{r_e}) \right] . \quad (3.2)$$

Here $Z = R_S + r_b + r_\pi + (\beta+1)r_e$. Note that S_{r_c} is not in the equation because Early effect is neglected in the derivation. If the condition $R_S \gg r_b + r_\pi + (\beta+1)r_e$ is satisfied, the above equation can be simplified to

$$S_{V_C} = R_C^2 \beta^2 S_{I_B} + R_C^2 S_{I_C} + \frac{R_C^2 \beta^2 I_B^2}{R_S^2} S_{r_b} + \frac{R_C^2 (I_B + I_C)^2}{R_S^2} S_{r_e}. \quad (3.3)$$

As we can see from this equation, only the last two terms are R_S dependent. If the r_b and r_e $1/f$ noises (S_{r_b} and S_{r_e}) contribute significant amount of noise to the measured S_{V_C}, S_{V_C} should decrease with increasing R_S. However, if S_{V_C} remains invariant with different R_S, the contributions from S_{r_b} and S_{r_e} are negligible.

To find out whether S_{r_b} and S_{r_e} contributions are significant, we vary R_S. Figure 3.7 shows the measured S_{V_C} spectra for different R_S. Two representative base current values, 3 μA and 8.5 μA, are used. R_S is 607 kΩ and 375 kΩ. Both R_S values are much larger than $r_b + r_\pi + (\beta + 1)r_e$, which

44
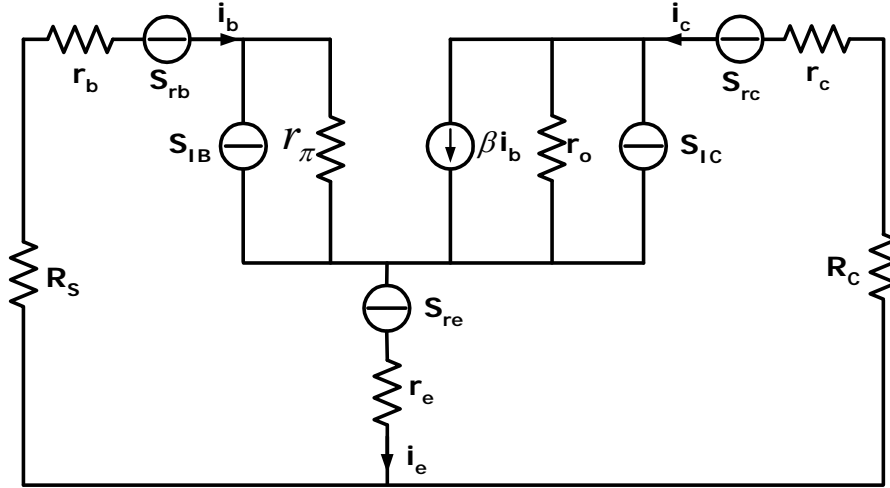
Figure 3.6: Simplified transistor model with the major $1/f$ noise sources. S_{I_B}, S_{I_C}, S_{r_b}, S_{r_e} and S_{r_c} represent the noise current densities of the base current, collector current, base series resistance, emitter series resistance and collector series resistance, respectively [37].

is 1.4 kΩ and 1.26 kΩ for I_B=3 μA and 8.5 μA, respectively. The spectra for the two different R_S are nearly identical across a wide frequency range, which indicates that S_{r_b} and S_{r_e} contributions are indeed negligible. Furthermore, since S_{I_C} is small compared to S_{I_B}, S_{I_B} can be determined using $S_{I_B} = S_{V_C}/(R_C \times \beta_{ac})^2$.

3.2.2 Impact on GR Noise

To find out whether CB junction traps generate GR noise, we measured the base current low-frequency noise for the high breakdown voltage LN1 under different biasing conditions. Figure 3.8 shows the noise spectra at representative V'_{BE} values. Since high-injection occurs when $V'_{BE} > 0.850$ V in this device, the three spectra represent the low-frequency noise behavior under low-injection ($V'_{BE} = 0.801$ V), at the onset of high-injection ($V'_{BE} = 0.848$ V), and under high-injection ($V'_{BE} = 0.879$ V), respectively. The noise spectra are "$1/f$" from 1 Hz to 10 kHz for all the biasing conditions. No GR "bump"s are observed. Therefore, the CB junction traps do not generate observable GR noise, even when they generate a large amount of recombination current at high-injection.
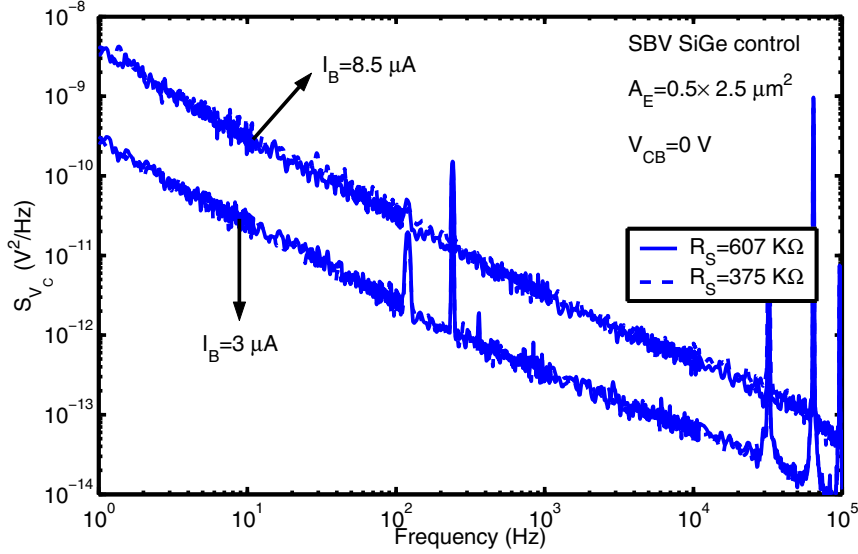
Figure 3.7: Comparison of the low-frequency voltage noise spectra measured at the collector with different source resistance R_S at two different currents.

3.2.3 Impact on $1/f$ Noise

We have shown that the low-frequency noise remains "$1/f$" in the high breakdown voltage HBTs. Since $1/f$ noise is closely related to traps, in this section, we investigate the impact of CB junction traps on the magnitude of $1/f$ noise. A new method is used, which utilizes the comparison between the standard and high breakdown voltage devices of the same SiGe profile at the same internal base-emitter voltages, as detailed below. In general, the main base current $1/f$ noise sources in modern Si BJTs and SiGe HBTs are located in the EB junction [2] [13] [38], even though there remains disagreement on the exact physical process. If EB junction is the only $1/f$ noise source, and the $1/f$ noise process is solely determined by the number of minority carriers injected into the emitter, HBV and SBV devices of the same SiGe profile should show similar $1/f$ noise level under the same V'_{BE}, or the same I_{pe} (the emitter hole injection current), because of identical emitter structure. However, if the CB junction traps also generate $1/f$ noise, the $1/f$ noise level will no longer be the same for the HBV and SBV devices across the whole biasing range. The low V'_{BE} $1/f$ noise level is expected to be the same for the HBV and SBV devices since I_B is dominated by I_{pe}. At high V'_{BE}, however, the $1/f$ noise in the HBV
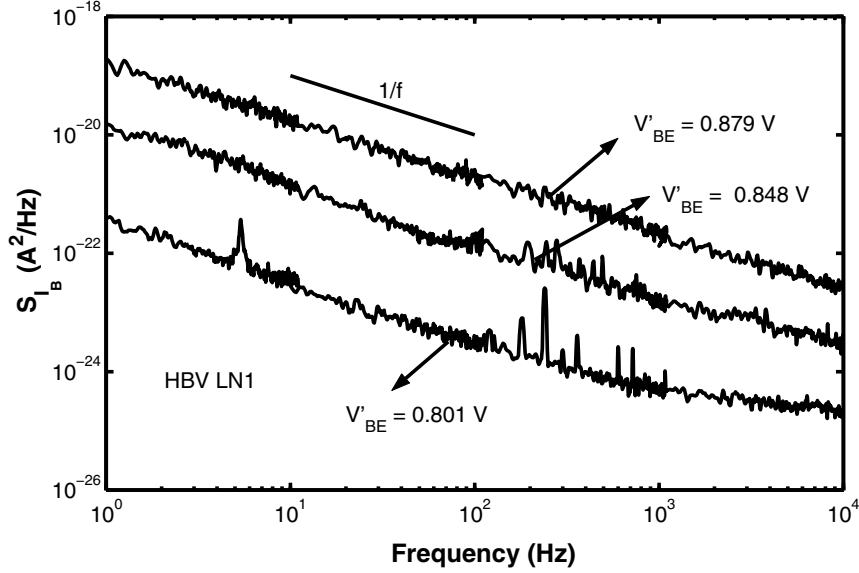
Figure 3.8: Comparison of the low-frequency noise spectra for the high breakdown voltage LN1 under different V'_{BE} (0.801 V, 0.848 V, and 0.879 V). $V_{CB} = 0$ V, $A_E = 0.5 \times 2.5$ μm^2.

devices should become higher than in the SBV devices, because of larger I_{cbsr} in the HBV devices. The difference should be a function of SiGe profile, and is expected to be larger for SiGe profiles with steeper Ge retrograding, and hence more pronounced high-injection barrier effect as well as higher CB junction trap density.

$1/f$ noise spectra were measured on HBV and SBV devices for all profiles, across a wide range of biasing current. Figure 3.9 (a) compares the base current noise spectra (S_{I_B}) of the HBV and SBV devices for LN1, at a V'_{BE} of 0.801 V. The HBV and SBV HBTs have similar S_{I_B} at this low V'_{BE}. As V'_{BE} increases to 0.879 V, at which high-injection already occurred and high-injection barriers were formed in the HBV device, the HBV S_{I_B} becomes much higher than the SBV S_{I_B}, as shown in Figure 3.9 (b). We therefore conclude that the CB junction traps also contribute to $1/f$ noise.

3.2.4 Internal Base-Emitter Voltage (V'_{BE}) Dependence

Figures 3.10 (a)-(d) compare the $S_{I_B} - V'_{BE}$ characteristics of the HBV and SBV devices for LN1, LN2, SiGe control and Si control, respectively. The S_{I_B} at 10 Hz taken from the noise spectra is used.
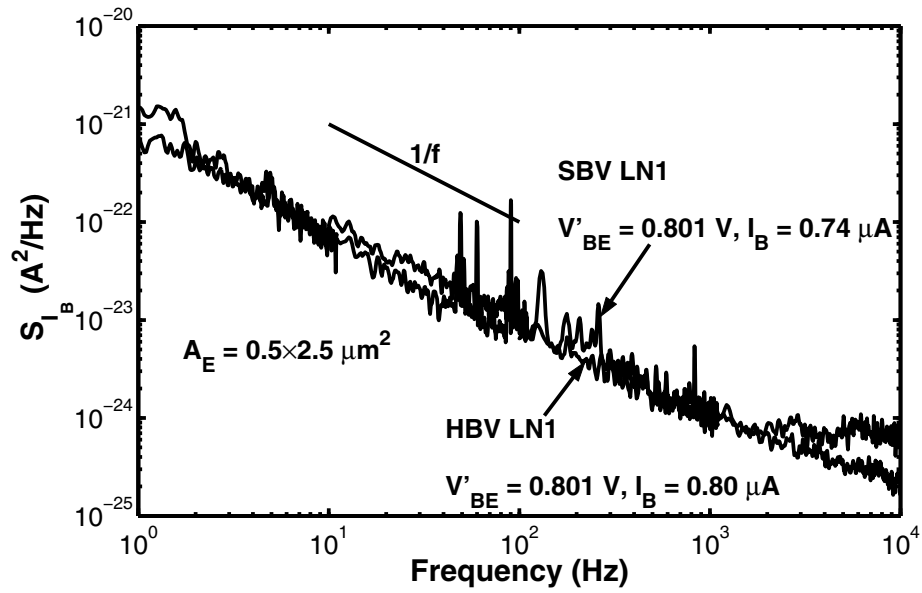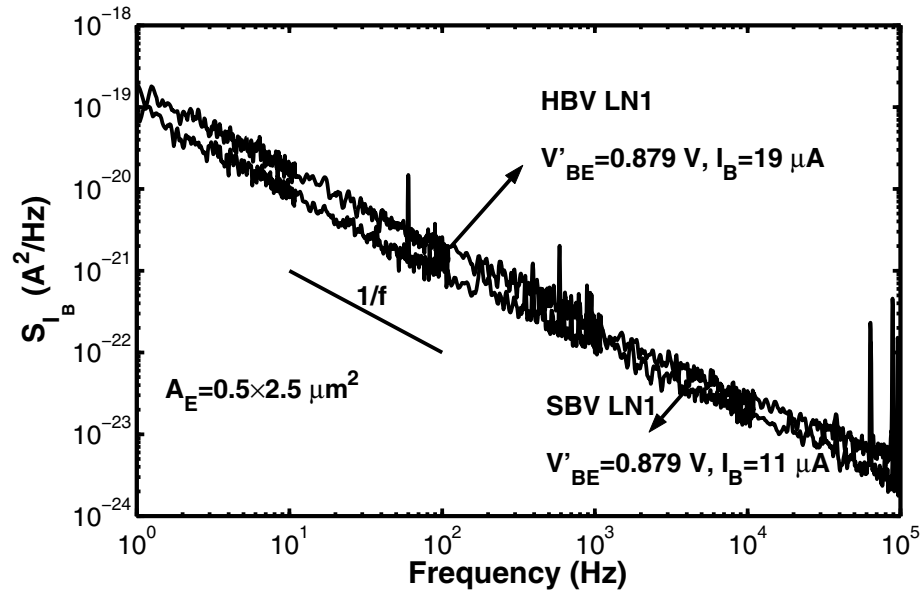
Figure 3.9: (a) Comparison of $1/f$ noise spectra for the standard and high breakdown voltage devices with $V'_{BE} = 0.801$ V on LN1 wafer. (b) Comparison of $1/f$ noise spectra for the standard and high breakdown voltage devices with $V'_{BE} = 0.879$ V on LN1 wafer.
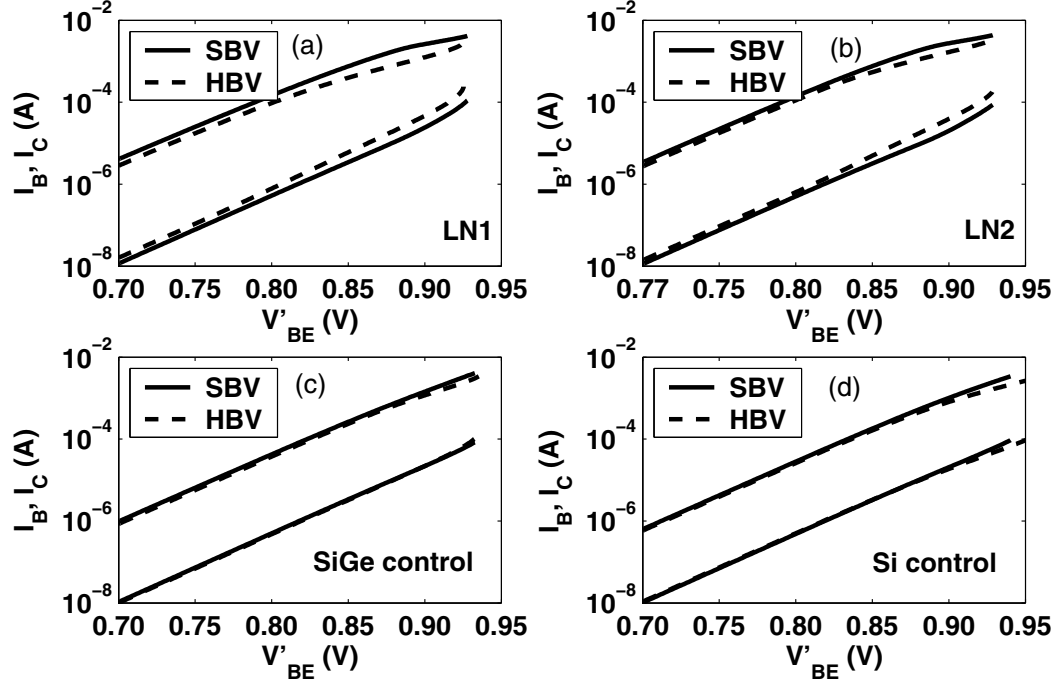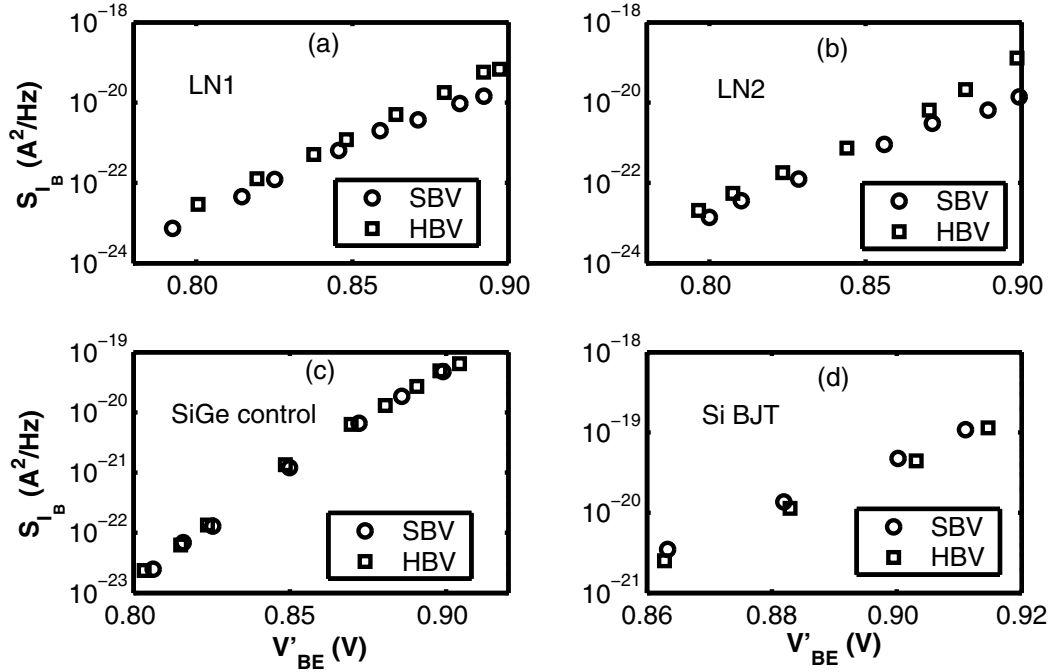
Figure 3.10: Comparison of $S_{I_B} - V'_{BE}$ between standard breakdown and high breakdown voltage devices for various SiGe profile designs. (a) LN1 with 14% peak Ge, (b) LN2 with 18% peak Ge, (c) SiGe control with 10% peak Ge, and (d) Si control. Frequency is 10 Hz, $A_E = 0.5 \times 2.5 \ \mu m^2$.

As shown in Figures 3.10 (a) and (b), the HBV LN1 and LN2 have a higher S_{I_B} than the SBV LN1 and LN2 under the same V'_{BE}. While for the SiGe control and Si control [Figures 3.10 (c) and (d)], the S_{I_B} is similar for the SBV and HBV devices for all the V'_{BE}. The $S_{I_B} - V'_{BE}$ characteristics replicate the $I_B - V'_{BE}$ characteristics shown in Figure 3.4 in terms of the difference between SBV and HBV devices. At the same V'_{BE}, the I_B difference between the SBV and HBV devices is the largest for LN1 and LN2, nearly negligible for the SiGe control and Si control. The S_{I_B} difference at the same V'_{BE} is also the largest for LN1 and LN2, and negligible for the SiGe control and Si control. The additional $1/f$ noise in the HBV devices is attributed to the $1/f$ noise generated by the CB junction traps.
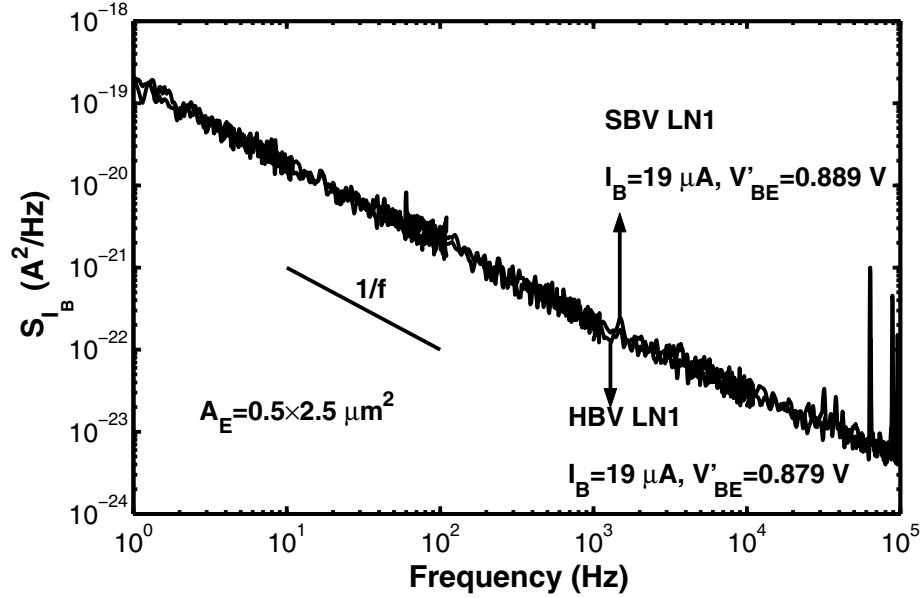
Figure 3.11: Comparison of $1/f$ noise spectra for the standard and high breakdown voltage devices with $I_B = 19$ μA on LN1 wafer.

3.2.5 Base Current Dependence

It has been shown that under low-injection condition, S_{I_B} is proportional to I_B^α for those devices, with α being close to 2 [26], indicating number fluctuation origin. The results in Section 3.2.1 also show that this I_B^α dependence does not come from the resistor $1/f$ noise. Another logical question is whether the $S_{I_B} - I_B$ dependence changes after high-injection occurs when a large part of I_B originates from recombination at the CB junction traps. To address this question, we compare the I_B dependence of $1/f$ noise for the standard and high breakdown voltage devices. Figure 3.11 shows the $1/f$ noise spectra comparison between the HBV and SBV LN1 at $I_B = 19$ μA. Interestingly, under the same I_B, the HBV and SBV devices have similar S_{I_B} despite quite different V'_{BE} (0.879 V for the HBV device versus 0.889 V for the SBV device) and thus different hole injection current I_{pe}. In Figures 3.12 (a)-(d), S_{I_B} of the SBV and HBV devices is shown as a function of I_B for all profiles. At the same I_B, the $1/f$ noise level is similar for SBV and HBV devices of the same profile.
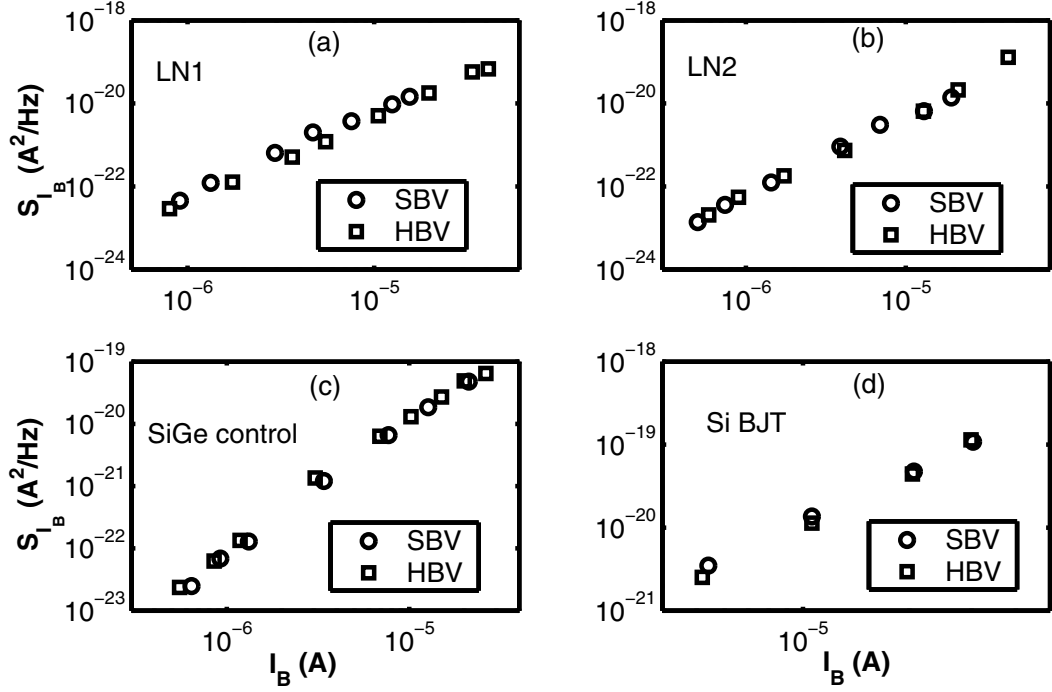
Figure 3.12: Comparison of $S_{I_B} - I_B$ between standard breakdown and high breakdown voltage devices for various SiGe profile designs. (a) LN1 with 14% peak Ge, (b) LN2 with 18% peak Ge, (c) SiGe control with 10% peak Ge, and (d) Si control. Frequency is 10 Hz, $A_E = 0.5 \times 2.5 \ \mu m^2$.

S_{I_B} can be fitted as a function of I_B for both HBV and SBV devices. For LN1,

$$S_{I_{B,SBV}} = KF_{SBV} \frac{I_{B,SBV}^{\alpha_{SBV}}}{f} = 1.35 \times 10^{-9} \frac{I_{B,SBV}^{2.06}}{f}, \tag{3.4}$$

$$S_{I_{B,HBV}} = KF_{HBV} \frac{I_{B,HBV}^{\alpha_{HBV}}}{f} = 0.54 \times 10^{-9} \frac{I_{B,HBV}^{2.02}}{f}. \tag{3.5}$$

KF_{SBV} and KF_{HBV} are the KF factors for the SBV and HBV devices, respectively. α_{SBV} and α_{HBV} are the AF factors. S_{I_B} for both the SBV and HBV devices is comparable and proportional to I_B^{α} for both low-injection and high-injection ($\alpha \approx 2$). The fact that S_{I_B} remains proportional to I_B^{α} simplifies the modeling of $1/f$ noise in the presence of significant CB junction recombination. For the HBV devices, the S_{I_B} dependence on I_B is the same with and without CB junction recombination. S_{I_B} is naturally modeled once the recombination current induced by the CB junction traps is modeled.

51

Even though the measured base current noise is approximately the same for the same amount of total base current for the SBV and HBV devices, we cannot conclude that the EB and CB noise processes are identical. The total base current in the HBV device includes a component due to hole injection into the emitter, and a component due to CB junction recombination. A separation of the two base current components and the two associated $1/f$ noises is thus necessary to gain physical insight into the difference between the two noise processes.

3.2.6 Separation of EB and CB Contributions

We have shown that when high-injection occurs, the I_B in the HBV SiGe devices has a strong component caused by recombination at the CB junction traps. These traps also generate $1/f$ noise. The total S_{I_B} is the sum of the $1/f$ noise contributions from the EB junction and CB junction, which can be written as

$$S_{I_B}(HBV) = S_{I_{pe}} + S_{I_{cbsr}}, \tag{3.6}$$

where $S_{I_{pe}}$ and $S_{I_{cbsr}}$ are the $1/f$ noise originated from the EB and CB junction, respectively. Since the SBV and HBV devices of the same profile have identical EB junction structure, the I_{pe} for the HBV devices can be assumed to equal the I_B for the SBV devices, I_{cbsr} is therefore determined from the difference between the $I_B - V'_{BE}$ characteristics of the HBV and SBV devices:

$$I_{pe,HBV} = I_{B,SBV}, \tag{3.7}$$

$$I_{cbsr,HBV} = I_{B,HBV} - I_{B,SBV}. \tag{3.8}$$

Note that the $1/f$ noise in the SBV devices is dominated by the contribution from the EB junction, $S_{I_{pe}}$ is thus simply the S_{I_B} for the SBV devices. The $S_{I_{cbsr}}$ at a given internal V'_{BE} is then obtained from the difference in S_{I_B} between the HBV and SBV devices:

$$S_{I_{pe,HBV}} = S_{I_{B,SBV}}, \tag{3.9}$$
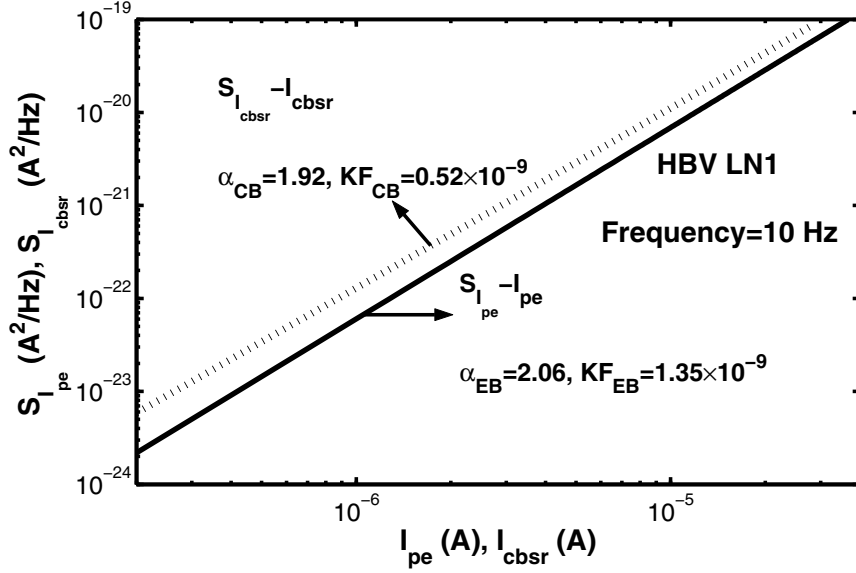
Figure 3.13: $S_{I_{pe}} - I_{pe}$ and $S_{I_{cbsr}} - I_{cbsr}$ dependences. Frequency is 10 Hz.

$$S_{I_{cbsr,HBV}} = S_{I_{B,HBV}} - S_{I_{B,SBV}}. \tag{3.10}$$

(3.7)-(3.10) must be evaluated at the same internal base-emitter voltage.

Using this method, the $1/f$ noise contributions from the EB and CB junctions are separated. Figure 3.13 plots the dependence of $1/f$ noise on the corresponding base current component for both the EB and CB noise processes. The LN1 high breakdown voltage device is used as an example. The $S_{I_{pe}} - I_{pe}$ dependence and $S_{I_{cbsr}} - I_{cbsr}$ dependences are overlaid, and fitted:

$$S_{I_{pe}} = KF_{EB} \frac{I_{pe}^{\alpha_{EB}}}{f} = 1.35 \times 10^{-9} \frac{I_{pe}^{2.06}}{f}, \tag{3.11}$$

$$S_{I_{cbsr}} = KF_{CB} \frac{I_{cbsr}^{\alpha_{CB}}}{f} = 0.52 \times 10^{-9} \frac{I_{cbsr}^{1.92}}{f}. \tag{3.12}$$

KF_{EB} and KF_{CB} represent the KF factors associated with the noise process in the EB junction and CB junction traps, respectively. α_{CB} and α_{EB} are the AF factors for the EB and CB processes. The difference in the $S_{I_{pe}} - I_{pe}$ and $S_{I_{cbsr}} - I_{cbsr}$ dependences is obvious, which indicates that the two noise
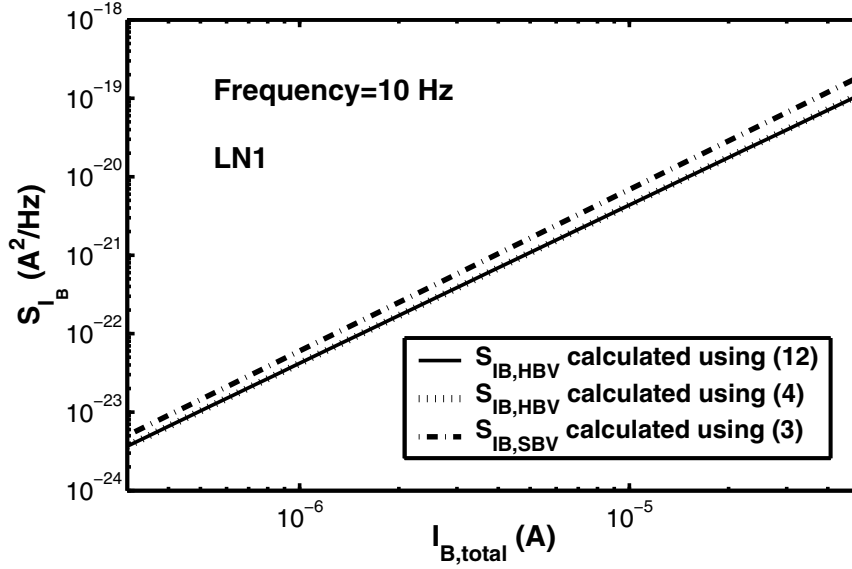
Figure 3.14: Calculated $S_{I_B} - I_B$ characteristics for the SBV and HBV LN1. S_{I_B}(HBV) is calculated using Eq. (3.13) and Eq. (3.5). S_{I_B}(SBV) is calculated using Eq. (3.4). Frequency is 10 Hz.

processes are distinctive. The KF factors are similar, therefore neither $S_{I_{cbsr}}$ nor $S_{I_{pe}}$ can be neglected when high-injection occurs as both I_{pe} and I_{cbsr} account for an significant amount of I_B.

Using (3.6), (3.11) and (3.12), the total S_{I_B} is obtained as the sum of the two noise contributions,

$$S_{I_B}(HBV) = 1.35 \times 10^{-9} \frac{I_{pe}^{2.06}}{f} + 0.52 \times 10^{-9} \frac{I_{cbsr}^{1.92}}{f}. \tag{3.13}$$

According to (3.5), S_{I_B}(HBV) can also be written as a function of the total I_B. Figure 3.14 compares the calculated $S_{I_B} - I_B$ characteristics for the HBV and SBV LN1. The S_{I_B}(HBV) is calculated using (3.13) and (3.5), the S_{I_B}(SBV) is calculated using (3.4). The two S_{I_B}(HBV) curves are nearly identical, as expected. The S_{I_B}(SBV) is comparable with S_{I_B}(HBV) across the biasing range used. Despite the introduction of a new $1/f$ noise process after high-injection, the dependence of the total S_{I_B} on the total I_B remains approximately the same as before high-injection occurs. The reason behind this is the slight difference in AF factors between the EB and CB noise processes (2.06 versus 1.92).

54
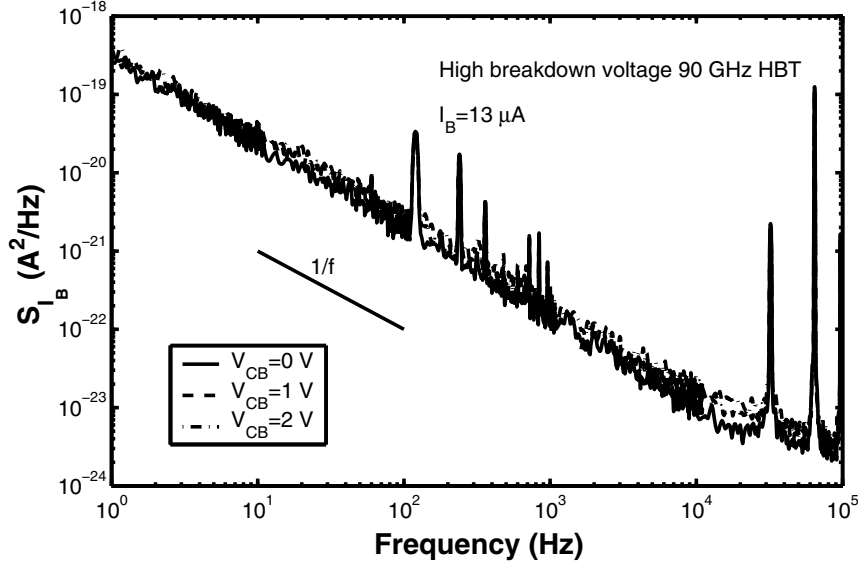
Figure 3.15: Comparison of S_{I_B} spectra for different collector-base voltages. The high breakdown voltage device from the 90 GHz technology is used. $A_E = 0.92 \times 1.6\ \mu\mathrm{m}^2$. I_B=13 μA.

3.3   Impact of Technology Scaling

The same investigation is also conducted on the standard breakdown and high breakdown voltage devices from a 90 GHz peak f_T technology. Figure 3.15 shows the comparison of base current $1/f$ noise spectra for the HBV devices under different collector-base voltage V_{CB}. I_B is fixed at 13 μA. S_{I_B} level remains invariant as V_{CB} increases from 0 V to 2 V, indicating that recombination in the CB junction indeed contributes to the total base current $1/f$ noise. We also compare S_{I_B} as a function of V'_{BE} and I_B. The SBV device has a 90 GHz peak f_T ($BV_{CEO} = 2.7$ V), and the HBV device has a 25 GHz peak f_T ($BV_{CEO} = 5.5$ V) [31]. The measurement results are consistent with what we observed for the 50 GHz technology. Under the same V'_{BE}, the HBV device shows a higher S_{I_B} when high-injection occurs, as shown in Figure 3.16 (a). Under the same I_B, the HBV and SBV devices have similar S_{I_B} and $S_{I_B} \propto I_B^{\alpha}$ holds for both low-injection and high-injection conditions with $\alpha \approx 2$ $\left[\text{Figure 3.16 (b)}\right]$.

We have investigated the impact of CB junction traps on low-frequency noise in high breakdown voltage SiGe HBTs for a 50 GHz peak f_T technology. The impact of series resistances on Gummel characteristics is eliminated by using the internal base-emitter voltage. The series resistance $1/f$ noise
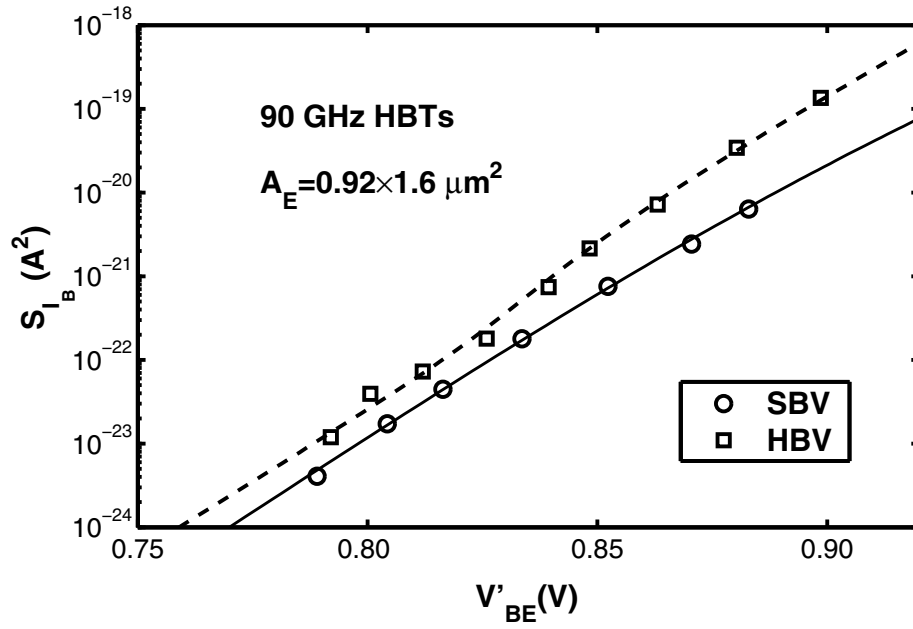
(a)
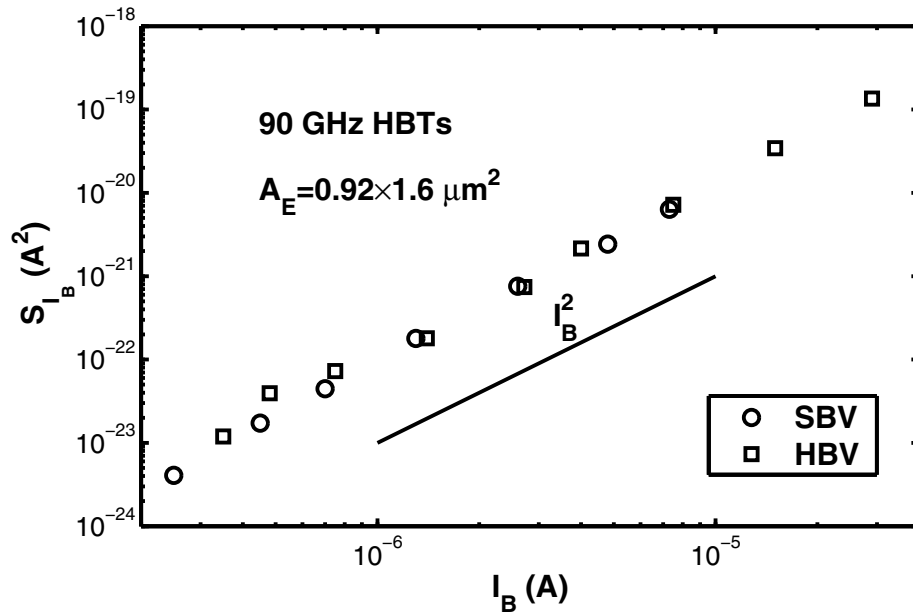
(b)

Figure 3.16: (a) Comparison of $S_{I_B} - V'_{BE}$ between standard breakdown and high breakdown voltage devices for the 90 GHz HBTs. (b) Comparison of $S_{I_B} - I_B$ between standard breakdown and high breakdown voltage devices for the 90 GHz HBTs. Frequency is 10 Hz, $A_E = 0.92 \times 1.6\ \mu\text{m}^2$.

is found negligible. For SiGe HBTs exhibiting a larger CB junction traps induced recombination at low-injection, a larger difference in high-injection base current is observed between the standard and high breakdown voltage SiGe HBTs. This result suggests the necessity of modeling the recombination current due to the CB junction traps since it contributes significant amount of I_B when high-injection occurs. CB junction traps do not generate GR noise, but contribute $1/f$ noise when high-injection occurs. The base current components due to hole injection into emitter and CB junction recombination, as well as their $1/f$ noises are separated. The noises generated from the EB and CB junctions are distinctive. However, the dependence of total base current $1/f$ noise on the total base current for the high breakdown voltage SiGe HBTs is found to be approximately the same at both low- and high-injections, and is nearly the same as that of the standard breakdown voltage SiGe HBTs, making modeling easier. The above conclusions are also verified using standard and high breakdown voltages HBTs from a 90 GHz peak f_T technology.

NOISE IN BIPOLAR JUNCTION TRANSISTORS AND MODELING IN OSCILLATORS

In this chapter, the noise sources in bipolar junction transistors and the modeling in oscillators are addressed. Base resistance thermal noise, shot noise from the base and collector currents, and base current $1/f$ noise are the major noise sources in a bipolar junction transistor. The small signal representation of these noises will be reviewed in Section 4.1. $1/f$ noise is sensitive to defects and traps in the transistors, it is not clear how the physical changes of the emitter-base junction composition during technology scaling affect the $1/f$ noise. We investigate the impact of technology scaling on the $1/f$ K factor and $1/f$ noise corner frequency in Section 4.2. When the transistors are used in the oscillators, the small signal representation of the current dependent noise sources is no longer valid. In small signal noise measurement, the current dependent noise sources are simple functions of the terminal currents, e.g., base current shot noise and collector current shot noise depend on the terminal base current and collector current, respectively. In an oscillator, due to the charge and discharge of the junction capacitances, the noise generating currents are significantly different from the terminal currents due to the extra capacitive components. Furthermore, the noise generating currents themselves are oscillating and large signal in nature. In Section 4.3, we investigate these modeling issues.

4.1 Noise Sources in Bipolar Junction Transistors and Small Signal Representations

4.1.1 Base Resistance Thermal Noise

Thermal noise is generated by the equilibrium fluctuations of the electric current inside an electrical conductor, which happen regardless of any applied voltage, due to the random thermal motion of the charged carriers. Also referred to as "Johnson noise" (J. B. Johnson being the first to observe this phenomena at Bell Labs in 1928), the single-sided spectral density of thermal noise current is given

by [39]

$$S_{thermal}(\omega) = 4kTG. \tag{4.1}$$

This is the Nyquist theorem for the thermal noise of a resistor. k is the Boltzmann's constant. T is the temperature (in Kelvin). This theorem relates the spectral density $S_{thermal}$ of the resistor thermal noise current to its conductance G. The components in a transistor that have thermal noise are base resistance r_b, emitter resistance r_e and collector resistance r_c. r_b thermal noise is a major phase noise source as detailed in the following chapters.

4.1.2 Shot Noise

Shot noise in electronic devices consists of random fluctuations of the electric current in an electrical conductor, which are caused by the fact that the current is carried by discrete charges (electrons). The number of charged carriers at time t, $N(t)$, is a discrete random process, termed *Poisson process*. Since the mean of $N(t)$ is clearly an increasing function of time, Poisson process is not stationary. The time derivative of $N(t)$, $X(t) = dN(t)/dt$, is a stationary random process called *Poisson increments*. The collected current is therefore $i(t) = qX(t)$. The (zero average) fluctuations $\delta X(t) = X(t) - \langle X \rangle$ of the Poisson increments are a white noise process whose auto-correlation function is proportional to the increments mean [40]:

$$R_{\delta X, \delta X}(\tau) = \langle X \rangle \delta(\tau). \tag{4.2}$$

$\langle \cdot \rangle$ represents taking the expected value. The current fluctuations $\delta i(t) = i(t) - \langle i \rangle$ are characterized by the following auto-correlation function:

$$R_{\delta i, \delta i}(\tau) = q^2 R_{\delta X, \delta X}(\tau) = q^2 \langle X \rangle \delta(\tau) = q \langle i \rangle \delta(\tau). \tag{4.3}$$

The single-sided spectral density of shot noise current is therefore:

$$S_{shot} = 2q \langle i \rangle. \tag{4.4}$$

In a bipolar junction transistor, shot noise occurs at both the base and collector as the discrete charged carriers pass a potential barrier. The base current shot noise results from the flow of the base majority holes across the emitter-base (EB) junction potential barrier and is described by the spectral density of

$$S_{shot} = 2qI_B, \tag{4.5}$$

with I_B being the dc base current. Similarly, the collector current shot noise results from the flow of emitter majority electrons over the EB junction potential barrier, and has a spectral density of

$$S_{shot} = 2qI_C, \tag{4.6}$$

with I_C being the dc collector current.

4.1.3 Generation-Recombination (GR) Noise

In bipolar junction transistors, in addition to the normal diffusion transport mechanisms, generation-recombination (GR) current can also occur through trap levels located near the EB junction. The appearance and disappearance of carriers is described by a differential equation of the form

$$\frac{d\Delta N}{dt} = -\frac{\Delta N}{\tau} + H(t), \tag{4.7}$$

where

$$\frac{1}{\tau} = \frac{1}{\tau_c} + \frac{1}{\tau_e}, \tag{4.8}$$

with τ_c being the capture (trapping) time constant, and τ_e being the emission (detrapping) time constant. ΔN is the fluctuation in the number of carriers. $H(t)$ is the Langevin terms corresponding to fluctuations in the GR transition rate, whose auto-correlation is given by $R_{H,H}(t, \tau) = 2\big[G(t) + R(t)\big]\delta(\tau)$ where $G(t)$ and $R(t)$ are the generation and recombination rates [41]. Using Langevin method, the single-sided

spectral density of ΔN is solved from (4.7) as [39]

$$S_{GR}(\omega) = \frac{S_H(0)\tau^2}{1 + \omega^2\tau^2} = 4\overline{\Delta N^2}\frac{\tau}{1 + \omega^2\tau^2}. \tag{4.9}$$

Such a spectrum is called Lorentzian spectrum. A good example is trapping and detrapping of electrons by surface traps, as in the surface oxide on the base of a bipolar junction transistor, or on the surface of the space-charge region of the EB junction. In analogy to (4.9), we have for discrete, multiple levels of traps

$$S_{GR}(\omega) = 4\sum_i \overline{\Delta N_i^2}\frac{\tau_i}{1 + \omega^2\tau_i^2}. \tag{4.10}$$

ΔN_i and τ_i are the fluctuations in the number of carriers and time constant for one trap level, respectively. These spectra are called GR spectra. Such spectra are seldom observed in the devices we used. However, as we will see in Section 4.1.4, a proper distribution in time constants τ_i gives rise to the "mysterious" $1/f$ noise, and our experimental results indeed support this theory.

4.1.4 $1/f$ Noise

At low frequencies, $1/f$ noise or flicker noise, with a spectral density proportional to $f^{-\gamma}$, where $\gamma = 1.0 \pm 0.1$, is observed in all electronic devices over a wide frequency range. At high frequencies, the $1/f$ noise disappears into (white) thermal noise or shot noise. Unlike thermal noise, shot noise or GR noise, the exact origin of $1/f$ noise has not been well understood. $1/f$ noise is due to conductivity fluctuations, this is the last thing researchers have agreed on. Since conductivity $\sigma = q\mu N$ with q being the electronic charge, μ being the mobility and N being the number of carriers, conductivity fluctuations can be due to *mobility* fluctuations and *number* fluctuation, or both.

One of the theory, proposed by McWhorter [17], expressed $1/f$ noise as a superposition of GR noises. If one has a time constant distribution $g(\tau)d\tau$, by analogy with (4.10),

$$S_N(\omega) = 4\overline{\Delta N^2}\int_0^\infty \frac{\tau g(\tau)d\tau}{1 + \omega^2\tau^2}, \tag{4.11}$$

61

where

$$\int_0^\infty g(\tau)d\tau = 1. \tag{4.12}$$

In particular, if $g(\tau)$ follows a $1/\tau$ distribution between τ_1 and τ_2 with τ_1 and τ_2 widely separated

$$\begin{cases} g(\tau)d\tau = \dfrac{d\tau/\tau}{\ln(\tau_2/\tau_1)}, & \tau_1 \ll \tau \ll \tau_2 \\[2ex] g(\tau)d\tau = 0, & \text{otherwise} \end{cases} \tag{4.13}$$

a $1/f$ spectrum yields

$$S_N(f) = \frac{\overline{\Delta N^2}}{\ln(\tau_2/\tau_2)} \cdot \frac{1}{f}, \quad 1/\tau_2 \ll \omega \ll 1/\tau_1 \tag{4.14}$$

whereas

$$S_N(f) = \frac{\overline{\Delta N^2}}{\ln(\tau_2/\tau_2)} \cdot 4\tau_2, \quad \omega \ll 1/\tau_2 \ll 1/\tau_1 \tag{4.15}$$

$$S_N(f) = \frac{\overline{\Delta N^2}}{f \ln(\tau_2/\tau_2)} \cdot \frac{1}{\pi^2 \tau_1 f^2}. \quad 1/\tau_2 \ll 1/\tau_1 \ll \omega \tag{4.16}$$

$S_N(f)$ is constant for $\omega\tau_2 \ll 1$ and varies as $1/f^2$ for $\omega\tau_2 \gg 1$. In most cases, τ_2 is so long and τ_1 so short that only the $1/f$ part of the spectrum is observed. Figure 4.1 shows such an example of Lorentzian spectra (dashed lines). The superposition of Lorentizan spectra gives rise to a $1/f$ dependence, as represented by the solid line in Figure 4.1. This model is valid only when there is no interaction between trap levels at different energies. If the levels are interacting with each other, instead of a $1/f$ spectrum, a Lorentzian spectrum is observed [42]. One way to verify whether $1/f$ noise is due to GR superposition is to measure samples of very small area where not enough traps are available to produce the $1/\tau$ distribution. We will show the experimental results on small emitter area devices in Section 4.3.4.

In bipolar transistors, the major $1/f$ noise source is found to be located in the EB junction. The spectral density is found experimentally as:

$$S_{1/f} = K_F \frac{I_B^\alpha}{f}, \tag{4.17}$$
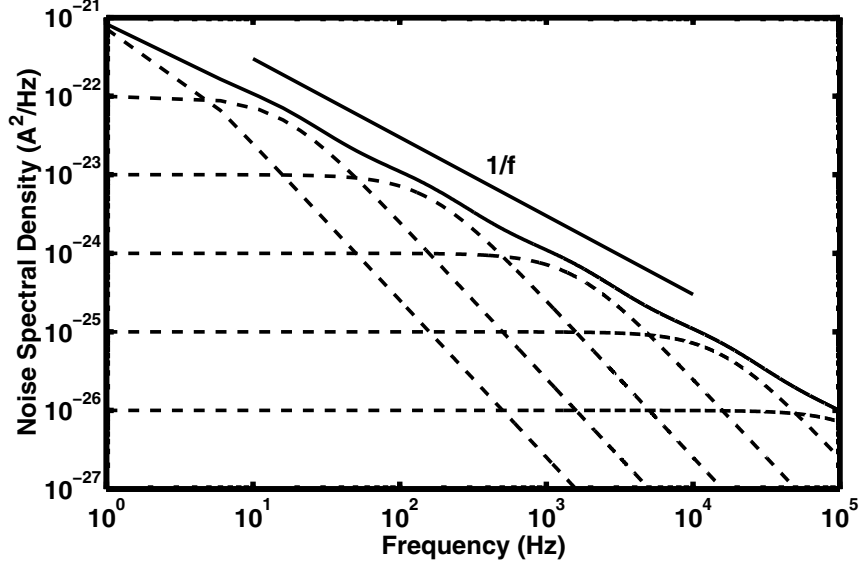
Figure 4.1: $1/f$ noise as a superposition of Lorentzians.

with I_B being the *dc* base current. K_F and α corresponds to the *KF* and *AF* parameters used in SPICE. The α value provides information on the physical origins of $1/f$ noise. First order theory predicts $\alpha = 1$ for carrier mobility fluctuations, and $\alpha = 2$ for carrier number fluctuations. The $1/f$ noise amplitude at a given I_B, measured by the K_F factor, scales inversely with the total number of carriers in the noise generating elements, according to Hooge's theory [42]. The $1/f$ noise generated by sources in the EB spacer oxide at the device periphery is inversely proportional to the emitter perimeter $P_E = W_E + L_E$ where W_E and L_E are emitter width and emitter length, respectively. While the $1/f$ noise generated by sources located at the intrinsic EB interface (i.e., the emitter polysilicon-silicon interface) across the emitter window is inversely proportional to the emitter area $A_E = W_E \times L_E$. The K_F factor is often examined as a function of A_E, P_E, or A_E/P_E as a means of locating the contributing $1/f$ noise sources. For all the SiGe HBTs used in this work, we find K_F factor is inversely proportional to A_E [26]. Furthermore $\alpha = 2$ holds for all the devices [26], indicating number fluctuation origin. Therefore (4.17) can be rewritten as

$$S_{1/f} = \frac{K}{A_E} \frac{I_B^2}{f}. \tag{4.18}$$

63

We have experimentally verified that for a given technology, K factor is independent of SiGe profiles and collector doping profile [26]. K factor is a function of technology scaling, as detailed in Section 4.2.

4.2 $1/f$ Noise versus Technology Scaling

4.2.1 $1/f$ Noise K Factor

As discussed in the previous section, the major $1/f$ noise in a SiGe HBT is located in the EB junction, and can be modeled by (4.18). K is a constant for a given technology, depending on defect level. Vertical scaling of SiGe HBT focuses on base and collector transit time reduction. Base transit time reduction can be achieved by using a narrower and more heavily doped base profile together with a lower thermal cycle for the bipolar processing and increasing the Ge ramp to create a higher accelerating electric field for minority carriers. A small amount of carbon can also be added in the base to limit boron outdiffusion so that the base doping profile can be kept in place after device fabrication.

$1/f$ noise is sensitivity to defects and traps on the devices, it is not clear how the physical changes of the emitter-base junction composition during scaling affect the $1/f$ noise K factor. Here we compare a 50 GHz 0.5 μm SiGe HBT [9], a 120 GHz 0.18 μm SiGe HBT [12] and a 210 GHz 0.12 μm SiGe HBT [11], all from BiCMOS processes. Figure 4.2 (a) compares the measured $1/f$ noise ($S_{I_B,1/f}$) spectra at I_B=10 μA. Similar emitter areas (A_E) are chosen: A_E =0.5×2.5 μm^2, 0.2×6.4 μm^2 and 0.12×12 μm^2 for the 50, 120 and 210 GHz technologies, respectively. Since $S_{I_B,1/f} \propto 1/A_E$, $S_{I_B,1/f}$ is normalized by A_E. The 120 GHz HBT has the highest $1/f$ noise for a given I_B. The noise level is the lowest in the 210 GHz HBT. The noise level in the 50 GHz HBT is comparable to the 210 GHz HBT.

For oscillators, a comparison at the same biasing I_C is more relevant, since the biasing I_C sets the amplitude of oscillation to the first order. $1/f$ noise for a given I_C is modeled as

$$S_{I_B,1/f} = \frac{K}{A_E} \frac{I_C^2}{\beta^2 f}.$$

(4.19)

Figure 4.2 (b) compares the low frequency noise spectra of the 50, 120 and 210 GHz peak f_T SiGe HBTs at I_C = 1.4 mA. The $1/f$ noise difference between the 50 and 120 GHz HBTs is only 3×. The $1/f$
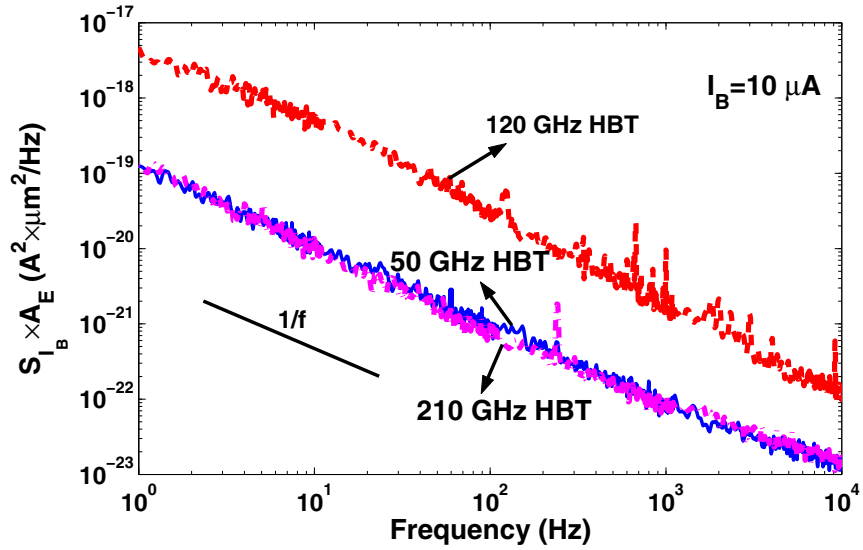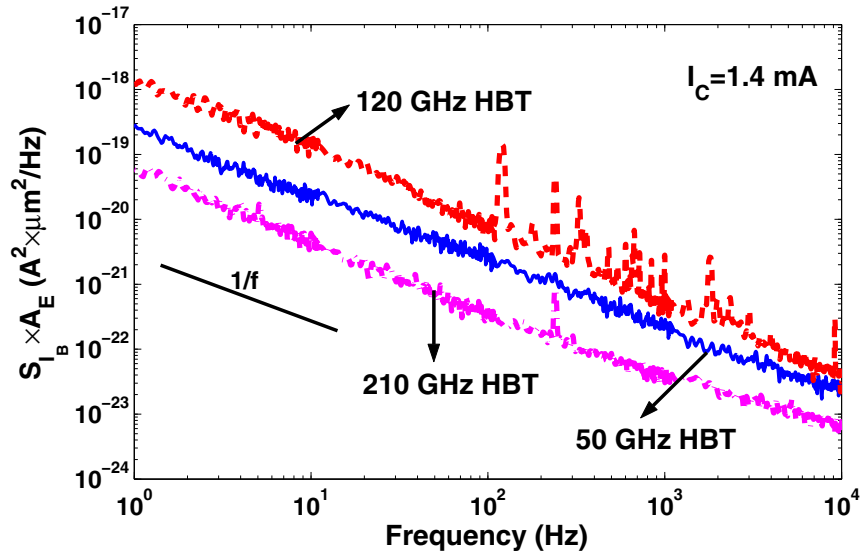
Figure 4.2: Measured $S_{I_B,1/f}$ spectra of 50, 120 and 210 GHz HBTs. $S_{I_B,1/f}$ is normalized by A_E. (a) Comparison at $I_B = 10\ \mu$A. (b) Comparison at $I_C = 1.4$ mA.

noise in the 210 GHz HBT is 5× lower than the 50 GHz HBT. The changes in the relative noise level at fixed I_C is due to the increase of β with scaling, as $S_{I_B} \propto 1/\beta^2$ for a given I_C.

Figure 4.3 (a) shows $S_{I_B,1/f}$ at 10 Hz as a function of I_B. $S_{I_B,1/f}$ is approximately proportional to I_B^2 in all of the three HBTs. The $1/f$ noise K factor, which measures $S_{I_B,1/f}$ for a given I_B, increases from 1.25×10^{-10} μm^2 to 3.84×10^{-9} μm^2 with scaling to 120 GHz, then decreases to 8.64×10^{-11} μm^2 with further scaling to 210 GHz. Figure 4.3 (b) shows $S_{I_B,1/f}$ at 10 Hz as a function of I_C. The $S_{I_B,1/f}$ at the same I_C is proportional to K/β^2. K/β^2 for the 120 GHz HBT is only 4× higher than the 50 GHz HBT, K/β^2 for the 210 GHz HBT is more than 5× lower than the 50 GHz HBT, because of the β increase with scaling.

4.2.2 $1/f$ Noise Corner Frequency

The $1/f$ noise corner frequency, $f_{c,1/f}$, at which $S_{I_{B,1/f}} = 2qI_B$ is given by [26]:

$$f_{c,1/f} = K\frac{I_B}{2qA_E} = K\frac{I_C}{2q\beta A_E} = \frac{K}{2q\beta}J_C. \tag{4.20}$$

At a fixed J_C, $f_{c,1/f}$ is proportional to $1/f$ noise K factor, and inversely proportional to β. The increase of the $1/f$ noise K factor with scaling to 120 GHz tends to increase $f_{c,1/f}$. However, depending on device design, β is often increased with scaling as well, which partially offsets the K factor increase.

Figure 4.4 shows the measured $f_{c,1/f}$ a function of J_C for the 50, 120 and 210 GHz HBTs. The nature of bipolar transistor operation necessitates a higher operating J_C to realize the high speed potential offered by scaling. A larger J_C range is thus used for the 120 and 210 GHz HBTs. For a given J_C, an increase of $f_{c,1/f}$ in the 120 GHz HBT and a decrease of $f_{c,1/f}$ in the 210 GHz HBT are observed, as expected. At $J_C = 2.5$ mA/μm^2, the 120 GHz HBT shows a $f_{c,1/f}$ of 1.6 MHz, which is relatively high compared to the 50 GHz HBT at $J_C = 1$ mA/μm^2. Such an increase of $1/f$ corner frequency in the 120 GHz HBT, however, does not necessarily cause an increase of the overall oscillator phase noise or the ultimate frequency synthesizer phase noise, due to different mechanisms of phase noise upconversion for the base current $1/f$ noise and base current shot noise, as detailed in Chapter 5 and Chapter 6.
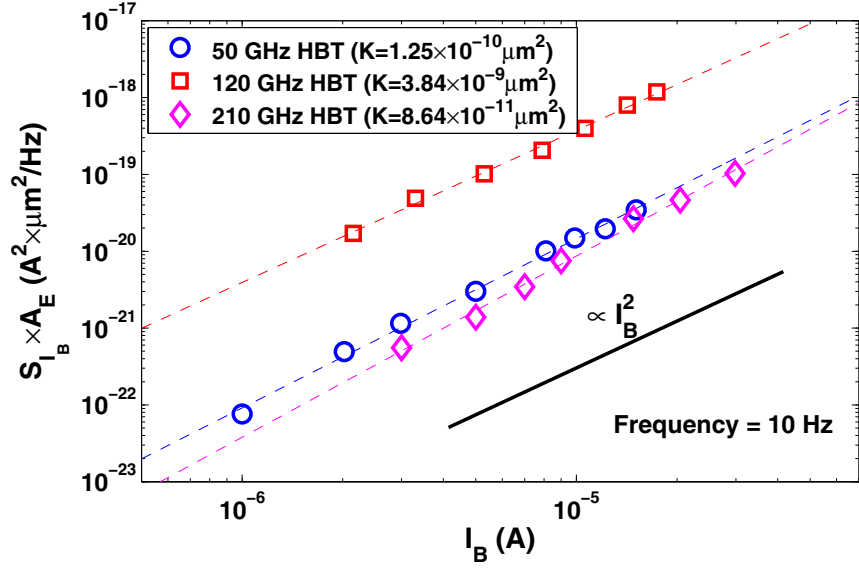
(a)
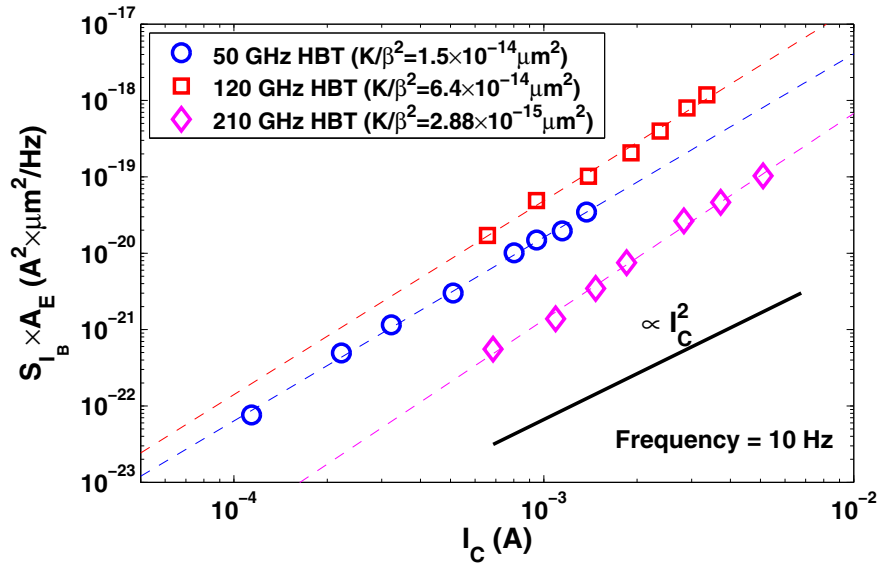
(b)

Figure 4.3: (a) Measured $S_{I_B,1/f} \times A_E$ versus I_B. (b) Measured $S_{I_B,1/f} \times A_E$ versus I_C. Frequency is 10 Hz.
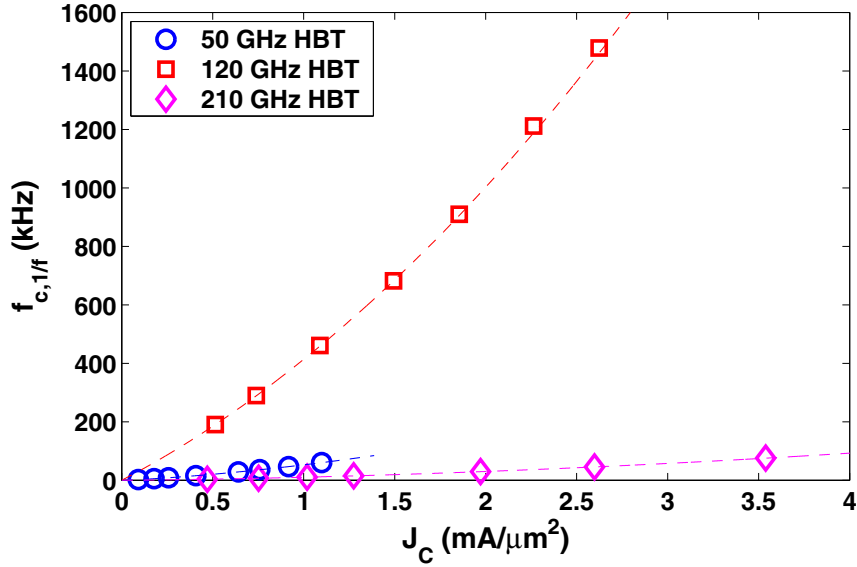
Figure 4.4: Measured $f_{c,1/f}$ versus J_C.

4.3 Noise Modeling in Oscillators

We have discussed the modeling of noise sources in bipolar junction transistors under small signal operation condition. There are several noise sources which are of particular interest to oscillators because they are converted to sideband around the fundamental oscillation frequency, known as phase noise. Intrinsic and extrinsic base resistance thermal noise (r_{bi} noise and r_{bx} noise), shot noise from the base current and collector current ($i_{b,s}$ noise and $i_{c,s}$ noise), base current $1/f$ noise ($i_{b,1/f}$ noise) are such noise sources. Figure 4.5 shows a simplified transistor model. The shaded components are the major phase noise sources. When used in oscillators, r_{bi} and r_{bx} noises are still simple functions of the respective resistances. The treatment of the biasing dependent noise sources, $i_{b,s}$ noise, $i_{c,s}$ noise and $i_{b,1/f}$ noise, requires care because the noise generating currents (i_{BE} and i_{CE}) are on longer constant, but periodically time-varying. In this section, we investigate the noise modeling issues in oscillators.

68
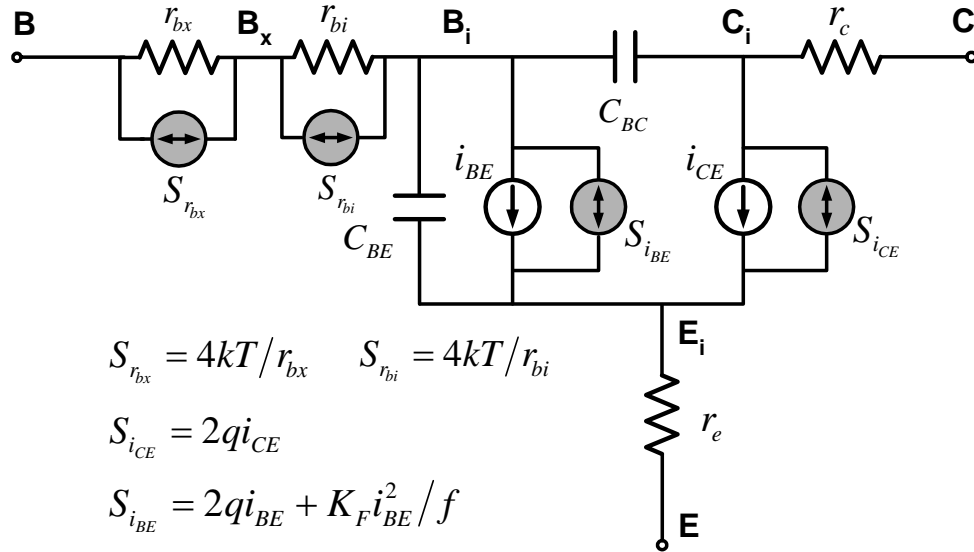
Figure 4.5: Simplified transistor model. The shaded components are the major noise sources to phase noise.

4.3.1 Noise Generating Current versus Terminal Current

In small signal noise measurement, the transistor is biased at a fixed I_B or I_C. The small signal base current $1/f$ noise and base current shot noise are simple functions of the base terminal current I_B, the collector current shot noise is simple function of the collector terminal current I_C. In an oscillator, the situation is complicated as:

1. The terminal base current I_B has a large capacitive component, which does not contribute to either $1/f$ noise or shot noise. Instead, the internal base to emitter junction current, i_{BE}, is responsible for noise generation. This is illustrated in Figure 4.6 using a simplified large signal transistor model. Similarly, the terminal I_C is different from the noise generating collector to emitter transport current i_{CE}.

2. The internal i_{BE} and i_{CE} responsible for base and collector current noise generation are periodically oscillating.

Therefore, to understand the phase noise upconversion process, we first need to separate the internal i_{BE} from the external I_B, and the internal i_{CE} from the external I_C. At present, neither Cadence SpectreRF
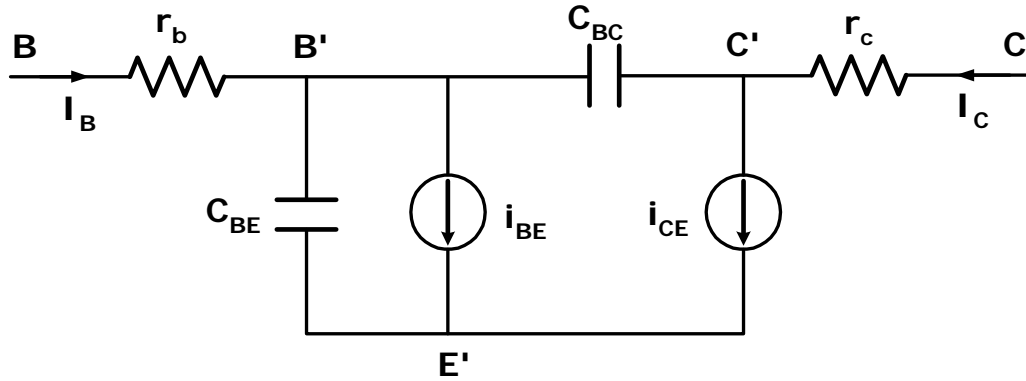
Figure 4.6: A simplified large signal transistor model.

[20] nor ADS [43] allows access of the internal nodes when the built-in transistor VBIC model is used. The internal i_{BE} and i_{CE} can be accessed by implementing the transistor model using Verilog-A [22]. Refer to Appendix B for detailed discussion on Verilog-A implementation.

Figure 4.7 shows the waveforms of the terminal I_B, the noise generating internal i_{BE}, and internal base-emitter voltage v_{BE} for an oscillator designed with the 50 GHz peak f_T SiGe HBT. The difference between I_B and i_{BE} is obvious even when the device peak f_T is much higher than the oscillation frequency (50 GHz vs 5.5 GHz). Due to the nature of oscillation, the base-emitter junction is turned on and off periodically, as shown on the right y-axis of Figure 4.7. A significant portion of the terminal base current is due to capacitive charging and discharging of the strongly nonlinear junction capacitances. The noise generating current, i_{BE}, is only a small portion of the terminal I_B.

4.3.2 System Approaches for Noise Source Modeling

In RF systems, circuits and devices often operate in large signal, (quasi-) periodic conditions, e.g., as in power amplifiers, mixers, frequency multipliers, and oscillators. This has a strong impact on the statistical properties of the stochastic processes exploited for the description of noise. Shot noise, being stationary in small signal operation condition, is no longer stationary due to the modulation by the time-varying operating point. Since shot noise results from fast microscopic scattering processes whose time constants are of the order of less than 1 ps, such a modulation can be assumed to be instantaneous.
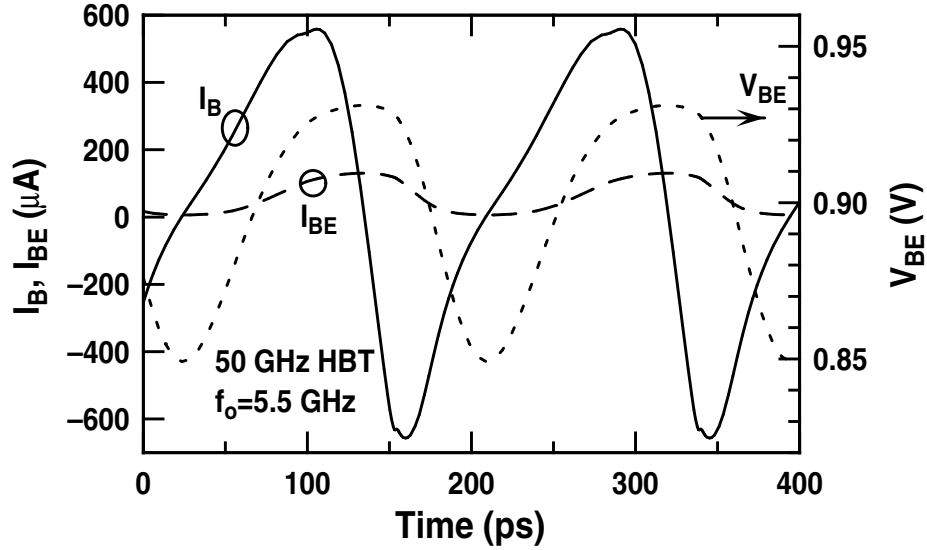
Figure 4.7: Comparison of terminal I_B and internal i_{BE} for the 50 GHz HBT. The internal v_{BE} is shown on the right y-axis.

Under large signal condition, shot noise becomes *cyclostationary*. The instantaneous modulation by the operating point converts noise at a frequency $\Delta\omega$ away from the harmonics $\omega_k = k\omega_0$ (ω_0 is the oscillation frequency) into sideband noises at $\widetilde{\omega}_l = l\omega_0 \pm \Delta\omega$. Note k and l are arbitrary integers. Figure 4.8 illustrated the frequency conversion process using an oscillatory system. $f(t)$ is the large signal operating point. $x(t)$ is the bias dependent noise. $y(t)$ is the noisy oscillator output. The frequency conversion makes noises at different sidebands correlated. The self- or cross-correlation is described by the *sideband correlation matrix* (SCM), denoted as **S**. **S** is a function of $\Delta\omega$, the frequency offset from the harmonics.

For noise sources that are colored in small signal condition, such as GR noise, system approaches for noise source modeling in large signal operation condition are provided in [44]. In [44], two correlated noise sources $\gamma_1(t)$ and $\gamma_2(t)$ are characterized, in small signal condition, by

$$S_{\gamma_i,\gamma_j}(\omega) = f^{(i)} f^{(j)} H_i(\omega) H_j^*(\omega), \tag{4.21}$$

71
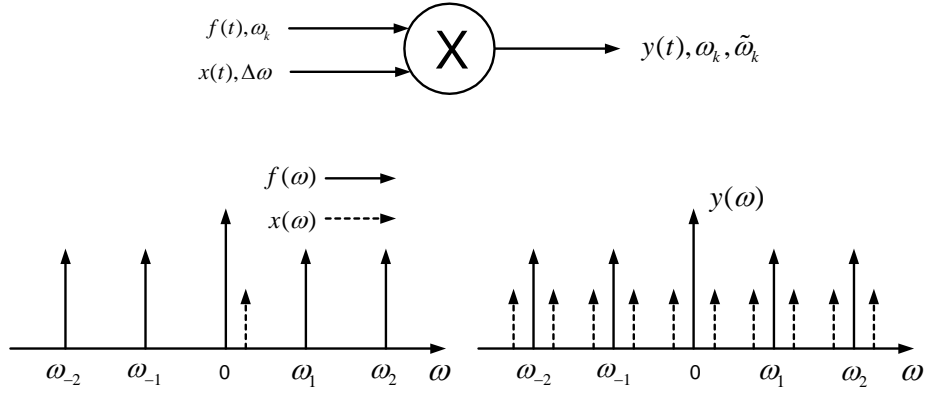
Figure 4.8: Frequency conversion in an oscillatory system.

where $i, j = 1, 2$. $H_i(\omega)$ denotes the Fourier transform of the impulse response $h_i(t)$ of a properly defined linear time invariant system, and $f^{(i)}$ contains all of the information on the operating point of the device. In large signal operation conditions, the operating point becomes periodically time-varying, and $f^{(i)}$ becomes time-dependent, thus modulating the fluctuation process. The large signal version of (4.21) can be expressed according to two possible systems as illustrated in Figure 4.9:

1. The input white process $x(t)$ is first amplitude modulated by $f^{(i)}(t)$ and then filtered by the linear system with impulse response $h_i(t)$. This approach is denoted as modulation + filtering (MF).

2. $x(t)$ is first filtered by $h_i(t)$ and then amplitude modulated by $f^{(i)}(t)$. This approach is denoted as filtering + modulation (FM).

Using the MF approach, the cross-correlation of $\gamma_1(t)$ and $\gamma_2(t)$ is given by

$$\left(S_{\gamma_{MF,1}, \gamma_{MF,2}}(\Delta\omega) \right)_{k,l} = H_1(\widetilde{\omega}_k) P_{k-l}^{(1,2)} H_2^*(\widetilde{\omega}_l), \qquad (4.22)$$

where $P_n^{(1,2)}$ is the nth Fourier coefficient of the periodic function $p^{(1,2)}(t) = f^{(1)}(t) f^{(2)}(t)$. Using the FM approach, the intermediate processes $\beta_1(t)$ and $\beta_2(t)$ are stationary with power spectral density

$$S_{\beta_i, \beta_i}(\omega) = \left| H_i(\omega) \right|^2 S_{x,x}(\omega), \qquad (4.23)$$

72
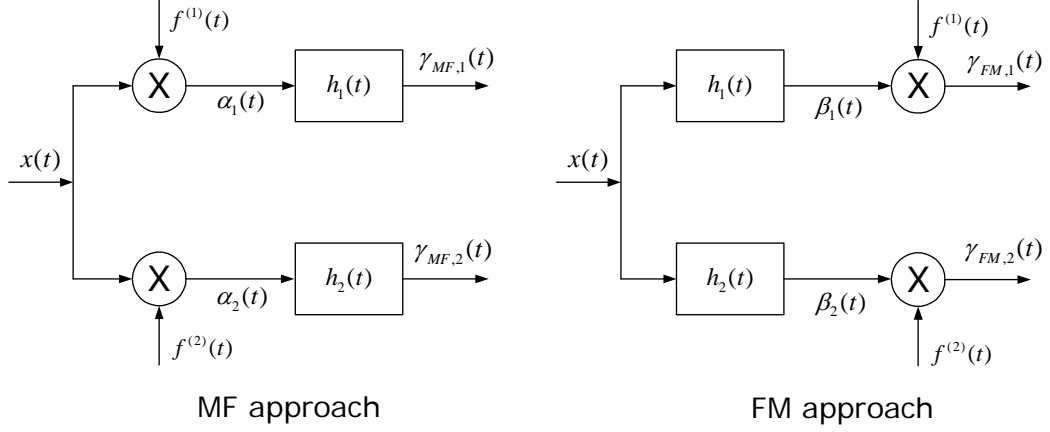
Figure 4.9: System approaches for noise source modeling in large signal operation condition: MF approach and FM approach [44].

where $S_{x,x}(\omega)$ is the power spectral density of $x(t)$. The cross-correlation of $\gamma_1(t)$ and $\gamma_2(t)$ is given by

$$\left(S_{\gamma_{FM,1},\gamma_{FM,2}}(\Delta\omega)\right)_{k,l} = \sum_{n=-\infty}^{\infty} F_n^{(1)} F_{k-l-n}^{(2)} H_1(\widetilde{\omega}_{k-n}) H_2^*(\widetilde{\omega}_{k-n}), \qquad (4.24)$$

where $F_n^{(i)}$ is the nth Fourier coefficient of the periodic function $f^{(i)}(t)$.

The two approaches give identical result in the shot noise case where $H_i(\omega) = 1$,

$$\left(S_{\gamma_{MF,1},\gamma_{MF,2}}(\Delta\omega)\right)_{k,l} = \left(S_{\gamma_{FM,1},\gamma_{FM,2}}(\Delta\omega)\right)_{k,l} = P_{k-l}^{(1,2)} = \sum_{n=-\infty}^{\infty} F_n^{(1)} F_{k-l-n}^{(2)}. \qquad (4.25)$$

We will derive this relation in Section 4.3.3. For GR noise, the two approaches lead to quite different behaviors. Due to the low-pass nature of the filtering transfer function $H_i(\omega)$, the corner frequency is, at least in RF applications, typically much lower than the operating fundamental frequency ω_0. The MF scheme leads to $\left(S_{\gamma_{MF,1},\gamma_{MF,2}}(\Delta\omega)\right)_{k,l} = 0$ unless $k = l = 0$, and in this case one has

$$\left(S_{\gamma_{MF,1},\gamma_{MF,2}}(\Delta\omega)\right)_{0,0} = H_1(\widetilde{\omega}_0) P_0^{(1,2)} H_2^*(\widetilde{\omega}_0). \qquad (4.26)$$

In other words, the noise source is a function of the *dc* component of the operating point only. The FM scheme, instead, leads to nonzero SCM component as long as $k = n$ in (4.24)

$$\left(S_{\gamma_{FM,1},\gamma_{FM,2}}(\Delta\omega)\right)_{k,l} = F_k^{(1)} F_{-l}^{(2)} H_1(\widetilde{\omega}_0) H_2^*(\widetilde{\omega}_0). \tag{4.27}$$

This is a cyclostationary noise. The noise source being modulated is $\beta_i(t)$, which is the low-pass filtered $x(t)$. The modeling of colored noise sources, e.g. *GR* noise and $1/f$ noise, is presented in Section 4.3.4.

In the following, the frequency domain quantities are summarized. We denote harmonics of the fundamental frequency as $\omega_k = k\omega_0$ $(-\infty < k < \infty)$ and sideband frequency as $\widetilde{\omega}_k = \omega_k \pm \Delta\omega$. Usually $\Delta\omega < \frac{1}{2}\omega_0$ is assumed, because noise away from the harmonics has insignificant impact on noise close to the fundamental oscillation frequency ω_0, which is of the most concern. We further define upper sideband as $\widetilde{\omega}_k^+ = \omega_k + \Delta\omega$, and similarly lower sideband as $\widetilde{\omega}_k^- = \omega_k - \Delta\omega$. This representation uses both positive and negative frequencies, and therefore it is a double-sided spectrum representation. When the signal is real, the spectral components of positive and negative frequencies are complex conjugates of each other

$$Y_{\widetilde{\omega}_k^+} = Y_{\widetilde{\omega}_{-k}^-}^*, \tag{4.28}$$

and similarly

$$Y_{\widetilde{\omega}_k^-} = Y_{\widetilde{\omega}_{-k}^+}^*. \tag{4.29}$$

Y represents the spectral component of $y(t)$ shown in Figure 4.8. Obviously only half of the frequencies in the double-sided spectrum are necessary. Therefore the single-sided spectrum representation is often used.

In the single-sided spectrum representation, the upper sideband frequency is $\widetilde{\omega}_k^+$ $(k \geqslant 0)$ and the lower sideband frequency is $\widetilde{\omega}_k^-$ $(k \geqslant 1)$. We can alternatively express the lower sideband frequency $\widetilde{\omega}_k^-$ using $\widetilde{\omega}_{-k}^+$ $(k \geqslant 1)$ according to (4.29). Now we do not need to differentiate "+" (upper sideband) or "−" (lower sideband), the sideband frequency in the single-sided spectrum representation is generalized to $\widetilde{\omega}_k$. The upper or lower sideband information is contained in the polarity of k with $k \geqslant 0$ representing

Table 4.1: Frequency Domain Quantities

ω_0	Fundamental frequency of periodic large signal
ω_k	Harmonics at $k\omega_0$
$\widetilde{\omega}_k^+ \ (-\infty < k < \infty)$	Upper sideband small signal frequency in the double-sided spectrum
$\widetilde{\omega}_k^- \ (-\infty < k < \infty)$	Lower sideband small signal frequency in the double-sided spectrum
$\widetilde{\omega}_k \ (k \geqslant 0)$	Upper sideband small signal frequency in the single-sided spectrum
$\widetilde{\omega}_k \ (k < 0)$	Lower sideband small signal frequency in the single-sided spectrum
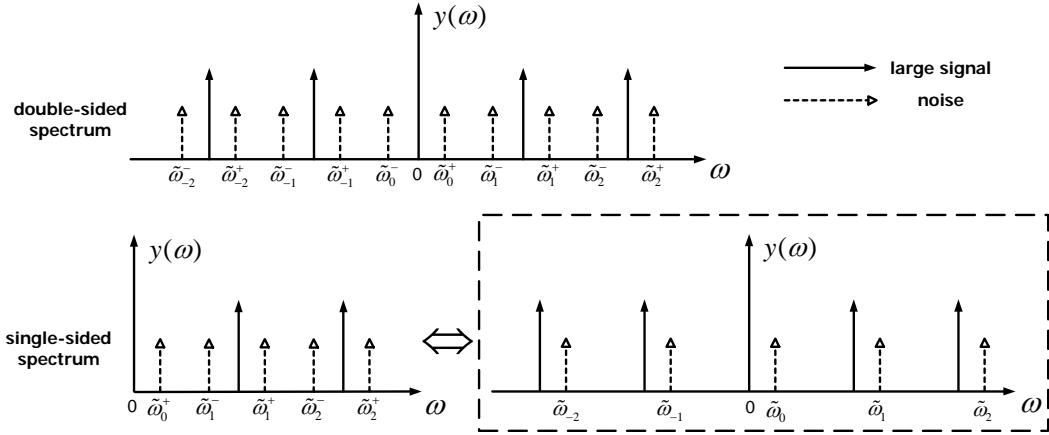
Figure 4.10: Small signal noise representations.

upper sideband and $k < 0$ representing lower sideband. Table 4.1 summarizes the frequency domain quantities. The small signal representations are illustrated in Figure 4.10. In this work, we use the unified $\widetilde{\omega}_k \ (-\infty < k < \infty)$ representation for noise, which is enclosed in the dashed box.

4.3.3 Shot Noise Modeling

As discussed in Section 4.3.2, shot noise is no longer stationary but rather cyclostationary when used in oscillators. Modulation by the periodic operating point makes noises at different sidebands correlated. The self- and cross-correlation of the sideband noises are described by the sideband correlation matrix (SCM). We derive the SCM for base current and collector current shot noises in this section. Cyclostationary noise $i_n(t)$ can be modeled as a unity white noise $x(t)$ modulated by a noise power distribution

function $f(t)$ [45]

$$i_n(t) = f(t) \cdot x(t). \tag{4.30}$$

As discussed in Section 4.3.2, only noises $\Delta\omega$ away from the harmonics of the oscillation frequency are converted to noise $\Delta\omega$ away from the oscillation frequency. When we derive $\mathbf{S}(\Delta\omega)$, the unity white noise is simplified to sinusoidal signals with randomly varying and statistically independent phase angles ϕ_k:

$$x(t) = \sum_{k=-\infty}^{\infty} e^{j\widetilde{\omega}_k t + \phi_k}, \tag{4.31}$$

where the angle ϕ_k is distributed uniformly in the range of $[0, 2\pi]$ and $\widetilde{\omega}_k = k\omega_0 + \Delta\omega$. The auto-correlation function of $x(t)$ is a delta function $R_{x,x}(t, t + \tau) = \delta(\tau)$ and therefore noises at different time instants are uncorrelated. The instantaneous noise power $p(t)$ relates to $f(t)$ by:

$$p(t) = f^2(t). \tag{4.32}$$

It can be easily seen that both $f(t)$ and $p(t)$ are instantaneous functions of the operating point, therefore they can be expressed using Fourier series:

$$f(t) = \sum_{k=-\infty}^{\infty} F_k e^{j\omega_k t}. \tag{4.33}$$

$$p(t) = \sum_{k=-\infty}^{\infty} P_k e^{j\omega_k t}. \tag{4.34}$$

Using (4.33) and (4.34), (4.32) can be rewritten using the Fourier series representation as:

$$\sum_{k=-\infty}^{\infty} P_k e^{j\omega_k t} = \sum_{l=-\infty}^{\infty} F_l e^{j\omega_l t} \sum_{m=-\infty}^{\infty} F_m e^{j\omega_m t}$$

$$= \sum_{l=-\infty}^{\infty} \sum_{m=-\infty}^{\infty} F_l F_m e^{j\omega_{l+m} t}. \tag{4.35}$$

For (4.35) to hold, $k = l + m$, thus $m = k - l$. (4.35) then becomes

$$\sum_{k=-\infty}^{\infty} P_k e^{j\omega_k t} = \sum_{k=-\infty}^{\infty} \sum_{l=-\infty}^{\infty} F_l F_{k-l} e^{j\omega_k t}. \tag{4.36}$$

Therefore

$$P_k = \sum_{l=-\infty}^{\infty} F_l F_{k-l}. \tag{4.37}$$

The cyclostationary noise current $i_n(t)$ at sideband $\widetilde{\omega}_k$ can be expressed using the Fourier series:

$$i_n(t) = \sum_{k=-\infty}^{\infty} I_{n,k} e^{j\widetilde{\omega}_k t}, \tag{4.38}$$

where $I_{n,k}$ is the magnitude of the noise current at sideband $\widetilde{\omega}_k$. Replacing $i(t)$, $f(t)$ and $x(t)$ in (4.30) using their respective Fourier series representations $\left[(4.38), (4.33) \text{ and } (4.31)\right]$, we get

$$\sum_{k=-\infty}^{\infty} I_{n,k} e^{j\widetilde{\omega}_k t} = \sum_{l=-\infty}^{\infty} F_l e^{j\omega_l t} \sum_{m=-\infty}^{\infty} e^{j\widetilde{\omega}_m t} e^{\phi_m}$$

$$= \sum_{l=-\infty}^{\infty} \sum_{m=-\infty}^{\infty} F_l e^{j\widetilde{\omega}_{l+m} t} e^{j\phi_m}. \tag{4.39}$$

Similarly $k = l + m$ must hold in the above equation, therefore $l = k - m$. (4.39) then becomes

$$\sum_{k=-\infty}^{\infty} I_{n,k} e^{j\widetilde{\omega}_k t} = \sum_{k=-\infty}^{\infty} \sum_{m=-\infty}^{\infty} F_{k-m} e^{j\widetilde{\omega}_k t} e^{j\phi_m}. \tag{4.40}$$

It can be easily seen

$$I_{n,k} = \sum_{m=-\infty}^{\infty} F_{k-m} e^{j\phi_m}. \tag{4.41}$$

The complex conjugate of $I_{n,k}$ is

$$I_{n,k}^* = \left(\sum_{m=-\infty}^{\infty} F_{k-m} e^{j\phi_m} \right)^* = \sum_{m=-\infty}^{\infty} F_{k-m}^* e^{-j\phi_m}. \tag{4.42}$$

$f(t)$ is a real function, therefore

$$F^*_{k-m} = F_{m-k}.$$ (4.43)

$I^*_{n,k}$ is then

$$I^*_{n,k} = \sum_{m=-\infty}^{\infty} F_{m-k} e^{-j\phi_m}.$$ (4.44)

$\left\langle I_{n,l} I^*_{n,k} \right\rangle$ is then

$$\left\langle I_{n,l} I^*_{n,k} \right\rangle = \left\langle \sum_{m=-\infty}^{\infty} F_{l-m} e^{j\phi_m} \sum_{s=-\infty}^{\infty} F_{s-k} e^{-j\phi_s} \right\rangle.$$ (4.45)

For the random angles

$$\left\langle e^{j\phi_m} e^{-j\phi_s} \right\rangle = \begin{cases} 1 & m = s \\ \\ 0 & m \neq s. \end{cases}$$ (4.46)

(4.45) reduces to

$$\left\langle I_{n,l} I^*_{n,k} \right\rangle = \left\langle \sum_{m=-\infty}^{\infty} F_{l-m} F_{m-k} \right\rangle.$$ (4.47)

Using the relation given by (4.37), the cross-correlation spectral density of noise current at sidebands $\widetilde{\omega}_l$ and $\widetilde{\omega}_k$ is given by the noise power at a noise generating current equal to the $(l-k)^{th}$ order of harmonic of the oscillating current

$$\left\langle I_{n,l} I^*_{n,k} \right\rangle = P_{l-k}.$$ (4.48)

For shot noise,

$$\left\langle I_{n,l} I^*_{n,k} \right\rangle = 2q I_{l-k},$$ (4.49)

where I_{l-k} is $(l-k)^{th}$ order Fourier coefficient of the noise generating current $i(t)$ (i_{BE} or i_{CE}).

4.3.4 $1/f$ Noise Modeling

For $1/f$ noise which is also a function of biasing current I in small signal measurement, it is often assumed that the $1/f$ noise associated with the oscillating i_{BE} is the same as the $1/f$ noise measured

under a base current equal to the *dc* component of i_{BE} ($I_{BE,0}$), considering the large time constant associated with $1/f$ noise [46] [47]. This method is consistent with the MF approach. Current circuit simulators, ADS and Cadence, both use this model. The above assumption, however, does not consider the physical origin of $1/f$ noise, which is still being debated. Recent work showed that the FM approach should be applied. The $1/f$ noise in an oscillating transistor should also be treated as modulated stationary noise, in the same way shot noise is treated, if the physical origin of the $1/f$ noise is GR fluctuation [44] [48].

In [44], two system theory approaches were proposed for the modeling of colored noise sources in devices and circuits driven in large signal conditions. Through the analysis of GR noise in physics-based device simulation, it was shown that the FM scheme (low-pass filtering followed by amplitude modulation), which resulted in cyclostationary noise, was consistent with the fundamental approach. In [48], the SCM was derived for a GR fluctuation in a resistor. The model was then applied to the GR noise in a bipolar junction transistor. Using 2-D device simulation, it was shown that GR noise in bipolar junction transistors should also be modeled as modulated stationary noise. These indicate that if superposition of GR events is the origin of the $1/f$ noise, $1/f$ noise should be treated as cyclostationary noise as well. In the following, we first derive the SCM for GR noise and $1/f$ noise under large signal operation condition, then show using experimental results that $1/f$ noise is SiGe HBTs is indeed due to GR noise superposition.

In the literature, $1/f$ noise and GR noise have been observed in bipolar junction transistors. For GR noise, the spectra is often observed as

$$S_{GR}(\widetilde{\omega}) = \frac{CI^2}{1 + \widetilde{\omega}^2\tau^2},$$ (4.50)

where C is the magnitude of GR noise, τ is the time constant for the trapping-detrapping process defined in (4.8). If we consider the GR fluctuations as bias independent (stationary) resistivity fluctuations, the modulated stationary model shown in (4.30) applies, except that the unity white noise source is low-pass

filtered. (4.31) then becomes

$$x(t) = \sum_{k=-\infty}^{\infty} \alpha(\widetilde{\omega}_k) e^{j\widetilde{\omega}_k t} e^{j\phi_k}, \tag{4.51}$$

where $\alpha(\widetilde{\omega}_k)$ is a function of frequency

$$\left| \alpha(\widetilde{\omega}_k) \right|^2 = \frac{C}{1 + \widetilde{\omega}_k^2 \tau^2}. \tag{4.52}$$

(4.39) becomes

$$\sum_{l=-\infty}^{\infty} I_{n,l} e^{j\widetilde{\omega}_l t} = \sum_{k=-\infty}^{\infty} F_k e^{j\omega_k t} \sum_{m=-\infty}^{\infty} \alpha(\widetilde{\omega}_m) e^{j\widetilde{\omega}_m t} e^{\phi_m}$$

$$= \sum_{k=-\infty}^{\infty} \sum_{m=-\infty}^{\infty} F_k \alpha(\widetilde{\omega}_m) e^{j\widetilde{\omega}_{k+m} t} e^{j\phi_m}. \tag{4.53}$$

This leads to

$$I_{n,l} = \sum_{m=-\infty}^{\infty} F_{l-m} \alpha(\widetilde{\omega}_m) e^{j\phi_m}, \tag{4.54}$$

and

$$I_{n,l}^* = \sum_{m=-\infty}^{\infty} F_{m-l} \alpha(\widetilde{\omega}_m) e^{-j\phi_m}. \tag{4.55}$$

The self- or cross-correlation spectral density is given by

$$\left\langle I_{n,l} I_{n,k}^* \right\rangle = \left\langle \sum_{s=-\infty}^{\infty} F_{k-s} \left| \alpha(\widetilde{\omega}_s) \right|^2 F_{s-l} \right\rangle. \tag{4.56}$$

For RF applications, $\left| \alpha(\widetilde{\omega}_s) \right|^2 \approx 0$ for $|s| > 0$, therefore (4.56) becomes

$$\left\langle I_{n,l} I_{n,k}^* \right\rangle = \left\langle \left| \alpha(\widetilde{\omega}_0) \right|^2 F_k F_{-l} \right\rangle. \tag{4.57}$$

80

Since the noise power spectral density is quadratically dependent on the current according to (4.50), the noise power distribution function is simply the noise generating current

$$f(t) = i(t). \tag{4.58}$$

Therefore (4.57) becomes

$$\left\langle I_{n,l} I_{n,k}^* \right\rangle = \left| \alpha(\widetilde{\omega}_0) \right|^2 I_k I_{-l} = \frac{C}{1 + \widetilde{\omega}_0^2 \tau^2} I_k I_l^*. \tag{4.59}$$

$1/f$ noise in small signal condition is often modeled as

$$S_{1/f} = K_F \frac{I_B^2}{f}. \tag{4.60}$$

The low-pass filter function for $1/f$ noise is

$$\left| \alpha(\widetilde{\omega}_0) \right|^2 = \frac{2\pi K_F}{\widetilde{\omega}_0}. \tag{4.61}$$

The noise power distribution function is still the noise generating current

$$f(t) = i(t). \tag{4.62}$$

Following similar derivations, we get the self- and cross-correlation of the sideband noise as

$$\left\langle I_{n,l} I_{n,k}^* \right\rangle = \left| \alpha(\widetilde{\omega}_0) \right|^2 I_k I_{-l} = \frac{2\pi K_F}{\widetilde{\omega}_0} I_k I_l^*. \tag{4.63}$$

The above cyclostationary model for $1/f$ noise is based on the assumption that $1/f$ noise is due to superposition of GR noise. We now investigate whether this is the case. If $1/f$ noise is indeed due to superposition of GR events, the $1/f$ dependence is expected to be clearly seen in device with large emitter area, where a large number of traps exist. In small devices, however, one may expect
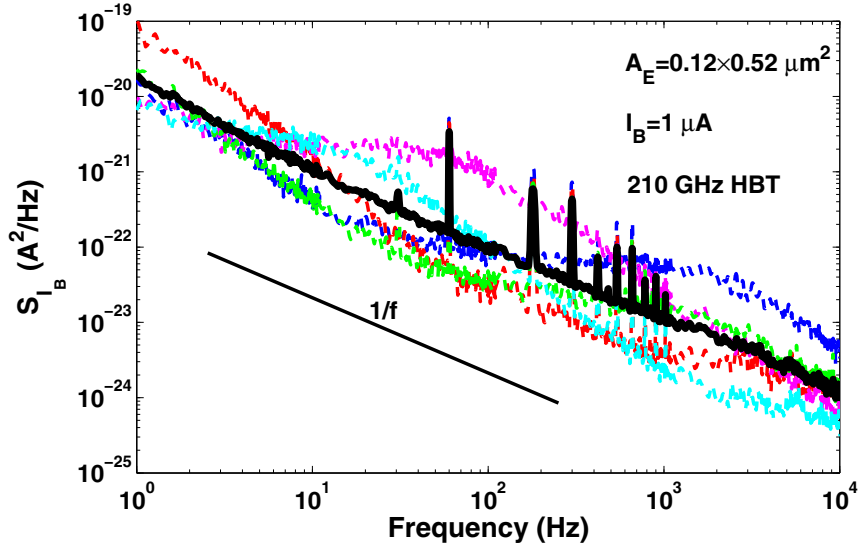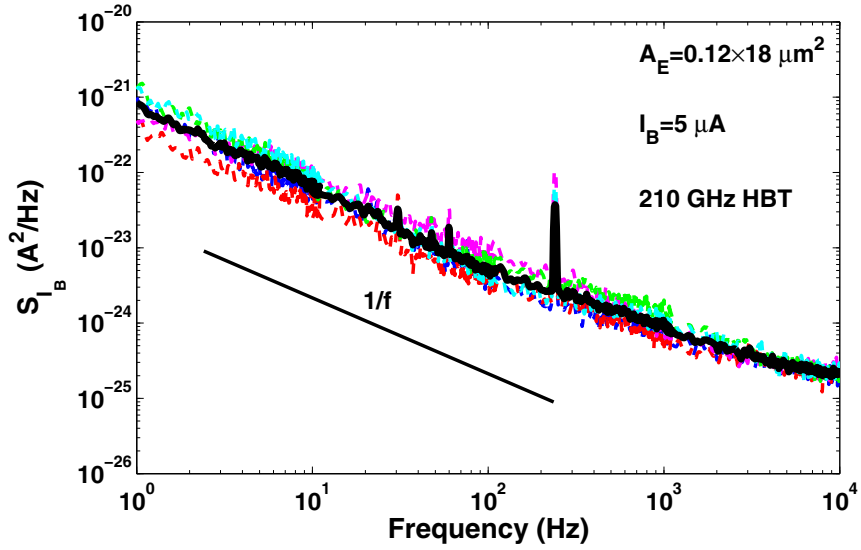
Figure 4.11: (a) Low-frequency noise spectra in five samples with emitter area 0.12×0.52 μm^2. (b) Low-frequency noise spectra in five samples with emitter area 0.12×18 μm^2. The thick black lines are the averages.

to observe the Lorentzian shape of behavior. Figures 4.11 (a) and (b) shows the low-frequency noise spectra measured in SiGe HBTs from the 210 GHz peak f_T technology with both small and large emitter areas, $A_E = 0.12 \times 0.52$ μm^2 and $A_E = 0.12 \times 18$ μm^2, respectively. For each geometry, five samples are collected. The noise spectra show a strong deviation from the "$1/f$" behavior and a large statistical scatter in the small devices, as shown in Figure 4.11 (a). The average of the five spectra (the thick black line), however, shows a clear $1/f$ dependence. All of the noise spectra from the large devices $\left[\text{Figure 4.11 (b)}\right]$ show a $1/f$ dependence. Therefore $1/f$ noise in the SiGe HBTs under investigation is indeed due to superposition of GR noises. It is very likely that $1/f$ noise in oscillators should be treated as cyclostationary noise.

PHASE NOISE ANALYSIS USING FREQUENCY SENSITIVITY METHOD

Oscillator phase noise physically results from transistor $1/f$ noise, base resistance thermal noise, shot noise, as well as any other thermal noise sources in the passives (e.g. inductors). All of the above noise sources change with technology scaling. It is therefore necessary to examine the impact of technology scaling on oscillator phase noise. Although a lower $1/f$ noise is desired to reduce phase noise, $1/f$ noise reduction in semiconductor manufacturing is very challenging as it is sensitive to defects. From a manufacturing standpoint, it is highly desired to quantitatively determine the highest $1/f$ noise level that can be tolerated for a given system phase noise requirement. An often used $1/f$ noise figure-of-merit is the so-called $1/f$ noise corner frequency, often defined by the intersect of base current $1/f$ noise and base current shot noise. The utility of the $1/f$ noise corner frequency is that it indicates whether $1/f$ noise or base current shot noise dominates for a given offset frequency. However, due to the complexity of the upconversion, the $1/f$ noise corner frequency is not a meaningful figure-of-merit for phase noise, as we will show below. Instead, we will introduce the concept of *phase noise corner offset frequency* [49], defined by the intersect of the phase noise upconverted from $1/f$ noise and the phase noise upconverted from white noise sources. A detailed analysis of phase noise upconversion is made to facilitate the understanding of the quantitative relations between $1/f$ noise measured at the *dc* biasing point and phase noise.

In this chapter, we investigate the impact of technology scaling on phase noise using SiGe technologies featuring 50 [9], 120 [12] and 210 [11] GHz peak f_T. This work is done using ADS simulation, which uses frequency sensitivity method for phase noise calculation [46]. A method of determining such "critical" or "threshold" $1/f$ noise level for a given bipolar technology is developed, whose utility is demonstrated for the SiGe HBTs used. The disconnection between $1/f$ noise corner frequency and

84

phase noise corner offset frequency is clarified. A single-ended common-base Colpitts oscillator is used in this work. In the following section, we will discuss the basic idea behind LC oscillator design.

5.1 LC Oscillator Design

An oscillator is a circuit that generates a periodic waveform whether it be sinusoidal, square, triangular, or more likely, some distorted combination of all three. Oscillators are used in a number of applications in which a reference tone is required. In most RF applications, sinusoidal references with a high degree of spectral purity (low phase noise) are needed. This section discusses the design on LC-based oscillators, as they are the most prominent form of oscillator used in RF applications.

LC Resonator

At the core of almost all integrated RF oscillators is an LC resonator that determines the oscillation frequency and often forms part of the feedback mechanism used to obtain sustained oscillations. Figure 5.1 shows a parallel resonator. Since there are two reactive components, it is a second-order system which can exhibit oscillatory behavior if the losses are low or if positive feedback is added. It is useful to find the system response to an impulse current, which in a real system could represent noise. If $i(t) = I_{pulse}\delta(t)$ is applied to the parallel resonator, the time domain response of the system is a sinusoid with exponential decay whose amplitude is inversely proportional to the value of the capacitance of the resonator and whose frequency is given by

$$\omega_0 = \sqrt{\frac{1}{LC} - \frac{1}{4R^2C^2}}.$$

(5.1)

The resulting waveform is shown in Figure 5.1. Once steady state has been reached in a real oscillator, R approaches infinity and ω_0 will approach

$$\omega_0 = \sqrt{\frac{1}{LC}}.$$

(5.2)

85

$$v_{out}(t) = \frac{\sqrt{2}I_{pulse}e^{\frac{-t}{2RC}}}{C}\cos\left(\sqrt{\left(\frac{1}{LC} - \frac{1}{4R^2C^2}\right)}\cdot t\right)$$
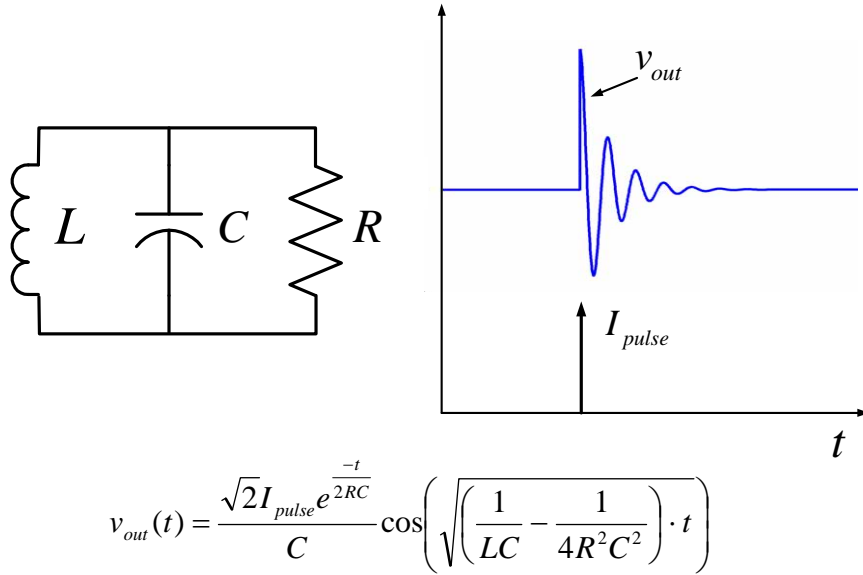
Figure 5.1: Parallel resonator and its response to an impulse current [50].

Adding Positive Feedback to the Resonator

The resonator is only part of an oscillator. As can be seen from Figure 5.1, oscillations will die away unless feedback is added in order to sustain the oscillation. The oscillator can be viewed as a linear feedback system, as shown in Figure 5.2. At the input, the resonator is disturbed by an impulse which represents a noise stimulus that starts up the oscillator. The impulse input results in an output that is detected by the amplifier. The gain of the system is given by

$$\frac{v_{out}(s)}{v_{in}(s)} = \frac{H_1(s)}{1 - H_1(s)H_2(s)}. \tag{5.3}$$

A self-sustaining mechanism arises at the frequency s_0 if $H_1(s)H_2(s) = 1$. Thus for steady oscillation, two conditions must be simultaneously met at ω_0: 1) the open loop gain, $|H_1(j\omega_0)H_2(j\omega_0)|$ must equal to unity, and 2) the total phase shift around the loop, $\angle H_1(j\omega_0)H_2(j\omega_0)$ must equal to zero or 2π. Called Barkhausen's criteria, the above conditions imply that any feedback system can oscillate if the loop gain and phase shift are chosen properly.
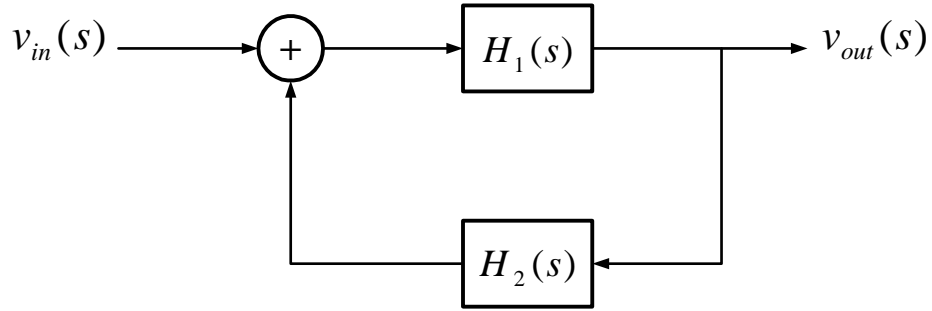
Figure 5.2: Linear model of an oscillator as a feedback system.

Colpitts Oscillator

Following the feedback model of Figure 5.2, we postulate that a single-transistor LC oscillator may include an LC parallel resonator at the collector of a bipolar transistor. Since at resonance, the impedance of the tank is real, the phase difference between its current and voltage is zero. Thus, to achieve a total phase equal to zero, the feedback signal must return to the emitter of the transistor. The connection of the tank to the emitter entails an important issue: the resistive load seen at the emitter terminal, $1/g_m$, is in parallel with the resonator. This resistance drastically reduces the Q of the resonator, dropping the loop gain to below unity and preventing oscillation. For this reason, the emitter impedance must be transformed to a higher value before it appears in parallel with the resonator.

A simple approach to transforming the emitter impedance is to use a capacitive divider. The resulting circuits is called Colpitts oscillator. The schematic of a Colpitts oscillator is shown in Figure 5.3. A common-base bias configuration provides gain from emitter to collector, which connects to the resonator. The capacitor divider (C_1 and C_2) provides positive feedback from collector to emitter, and sets oscillation frequency together with the inductor L. The transformed emitter resistance is equal to $(1 + C_2/C_1)^2/g_m$ [51].

5.2 Frequency Sensitivity Method

The detailed derivation for frequency sensitivity method is provided in Appendix C. In this section, only the final results are listed here for convenience. Frequency sensitivity method is used in ADS for
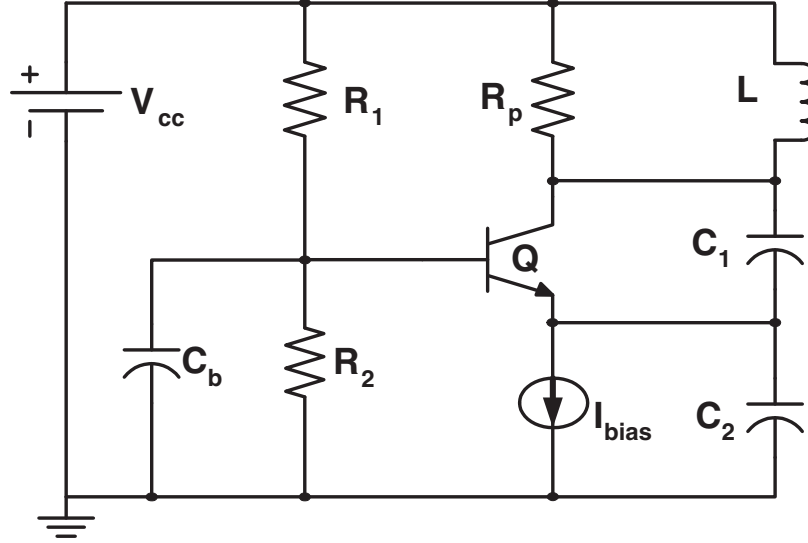
Figure 5.3: Schematic of the single-ended Colpitts oscillator.

phase noise simulation. It assumes that noise acts to randomly modulate the oscillation frequency. The phase noise at a given offset frequency $\Delta\omega$ originates from the sensitivity of the oscillation frequency ω_0 to the sideband noise at $\widetilde{\omega}_k$ with k being the harmonic index $\left(k \in [0, \infty]\right)$.

For thermal noise from a resistor R, there is no correlation between noises at different sidebands, the total phase noise due to thermal noise is therefore

$$\mathcal{L}_{thermal}(\Delta\omega) = \frac{1}{2\Delta\omega^2} \sum_{k=0}^{N} \left| \frac{\partial\omega_0}{\partial i_{n,k}} \right|^2 \frac{4kT}{R}. \tag{5.4}$$

N is the highest harmonic in question. We further define thermal noise gain G_{r_b} for comparison of base resistance noise upconversion from different devices sizes or different technologies. G_{r_b} is the ratio of phase noise to thermal noise voltage $(4kTr_b)$

$$G_{r_b} = 2\Delta\omega^2 \frac{\mathcal{L}_{thermal}(\Delta\omega)}{4kTr_b} = \frac{\sum_{k=0}^{N} \left| \frac{\partial\omega_0}{\partial i_{n,k}} \right|^2}{r_b^2}. \tag{5.5}$$

For shot noise, since the correlation time is typically much smaller than the oscillation period, the cyclostationary model applies. All the noises at $\widetilde{\omega}_k$ contribute a phase noise at $\Delta\omega$. As these noises are

correlated, the total phase noise is given by

$$\mathscr{L}_{shot}(\Delta\omega) = \frac{1}{2\Delta\omega^2} \sum_{k=0}^{N} \sum_{l=0}^{N} \frac{\partial\omega_0}{\partial i_{n,k}} 2qI_{k-l} \left(\frac{\partial\omega_0}{\partial i_{n,l}} \right)^*, \qquad (5.6)$$

where I_{k-l} is $(k-l)^{th}$ order Fourier coefficient of the noise generating current $i(t)$ (i_{BE} or i_{CE}). For $1/f$ noise, ADS assumes that only the *dc* component of the noise generating current contributes $1/f$ noise. Therefore phase noise due to $1/f$ noise is calculated as:

$$\mathscr{L}_{1/f}(\Delta\omega) = \frac{1}{\Delta\omega^2} \left| \frac{\partial\omega_0}{\partial i_{n,0}} \right|^2 S_{1/f}(I_0), \qquad (5.7)$$

where I_0 is the *dc* component of I, and $S_{1/f}(I_0)$ is the $1/f$ noise power spectral density at a biasing current equal to I_0.

5.3 Oscillator Phase Noise

In this section, we investigate the impact of technology scaling using the single-ended Colpitts oscillator described in Section 5.1. The schematic is shown in Figure 5.3. Three oscillators are designed and simulated using ADS and SpectreRF. Calibrated VBIC models that accurately reproduce measured *dc* and RF characteristics are used. The HBTs are from 50, 120, and 210 GHz peak f_T technologies. The oscillation frequency is 5.5 GHz. The inductor L quality factor Q is 7 for all of the technologies. $V_{CC} = 2.0$ V is chosen to avoid breakdown. Note that each technology is capable of operating at much higher frequencies. In Section 5.3.1, we define the phase noise corner offset frequency $f_{c,offset}$. In Section 5.3.2, the optimal transistor sizing and biasing are discussed. Using the optimal transistor size and bias for each technology, the impact of technology scaling on phase noise will be presented in Section 5.3.3. In Section 5.3.4, the ultimate limiting phase noise with scaling is examined.
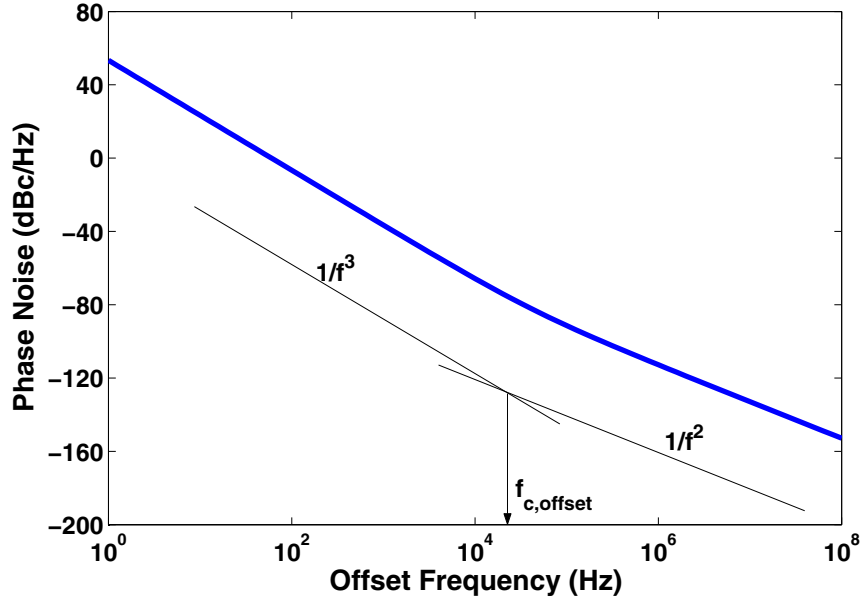
Figure 5.4: A typical phase noise spectrum simulated in ADS. $f_{c,offset}$ is the intersect of $1/f^3$ phase noise and $1/f^2$ phase noise.

5.3.1 Corner Offset Frequency $f_{c,offset}$

Figure 5.4 shows a typical simulated phase noise spectrum. A $1/f^3$ component due to $1/f$ noise upconversion and a $1/f^2$ component due to white noise upconversion can be clearly identified. The intersect of $1/f^2$ and $1/f^3$ phase noises is defined as the phase noise corner offset frequency, $f_{c,offset}$. $f_{c,offset}$ is a direct measure of the importance of the phase noise upconverted from $1/f$ noise with respect to the phase noise upconverted from the white noise sources. Note that $f_{c,offset}$ itself does not contain any information on either the $1/f^3$ or $1/f^2$ phase noise level. A higher $f_{c,offset}$ does not necessarily mean a higher phase noise level. As we will see in Section 5.3.3, the 120 GHz HBT oscillator has the highest $f_{c,offset}$. The far-off phase noise, which is dominated by $1/f^2$ phase noise, is actually the lowest. $f_{c,offset}$ is typically much lower than the intersect of base current $1/f$ noise and base current shot noise, $f_{c,1/f}$, due to different upconversion processes, as detailed in Section 5.4.

5.3.2 Optimal Transistor Sizing and Biasing

In RF integrated-circuit (RFIC) design, transistor size and bias are optimized for better circuit performance. In an oscillator, the most important characteristics are phase noise and output swing. The major phase noise sources in a transistor are: thermal noise from the base resistance, shot noise from the collector current and base current, and base current $1/f$ noise. All of the noise sources are function of transistor size and bias. For example, with increasing transistor size, base resistance thermal noise reduces due to the decrease of base resistance, base current $1/f$ noise reduces due to the decrease of $1/f$ noise K factor with increasing transistor size. Increasing transistor biasing current increases the collector current, and base current if current gain β is weakly dependent on biasing current. These affect the upconverted collector current shot noise and base current shot noise. The upconversion gains for each noise sources are also functions of bias and size. The output swing depends on transistor size and bias as well. Therefore it is reasonable to first identify the optimal transistor size and bias for each technology, and then to compare each technology using their optimized performance.

Figure 5.5 shows phase noise ($\mathscr{L}$) as a function of emitter finger number (N_E) and emitter biasing current (I_{bias}). The results are obtained from ADS simulation. The 50 GHz peak f_T HBT with an emitter finger of 0.5×2.5 μm^2 is used. Phase noise is predominant by contribution from the transistor itself. Phase noise from the inductor is negligible. In Figure 5.5 (a), the offset frequency is 100 MHz, where the $1/f^2$ phase noise upconverted from white noise sources dominates. When N_E is fixed, $\mathscr{L}$ first decreases with increasing I_{bias}, then increases with further increase of I_{bias}. There exists an optimal I_{bias} between 5 mA to 8 mA for the $1/f^2$ phase noise for all N_E's. The optimal I_{bias} increases slightly with increasing N_E. This I_{bias} dependence is consistent with the results in [52] [53]. When I_{bias} is fixed, $\mathscr{L}$ decreases with increasing N_E and eventually approaches a constant with further increase of N_E to above 8. In Figure 5.5 (b), the offset frequency is 1 Hz where the $1/f^3$ phase noise upconverted from $1/f$ noise dominates. $1/f^3$ phase noise increases with increasing I_{bias} and decreases with increasing N_E. The reduction with increasing N_E is mostly due to the decrease of $1/f$ noise K factor with increasing
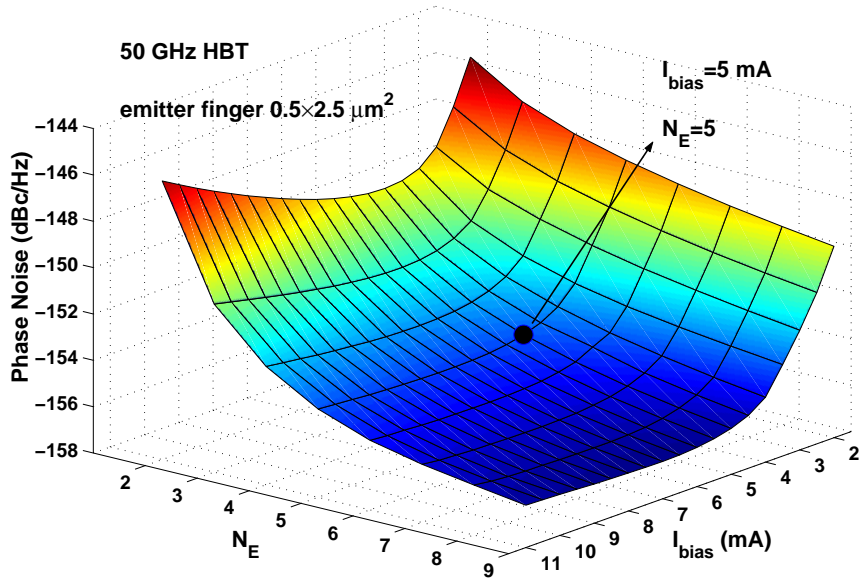
(a)
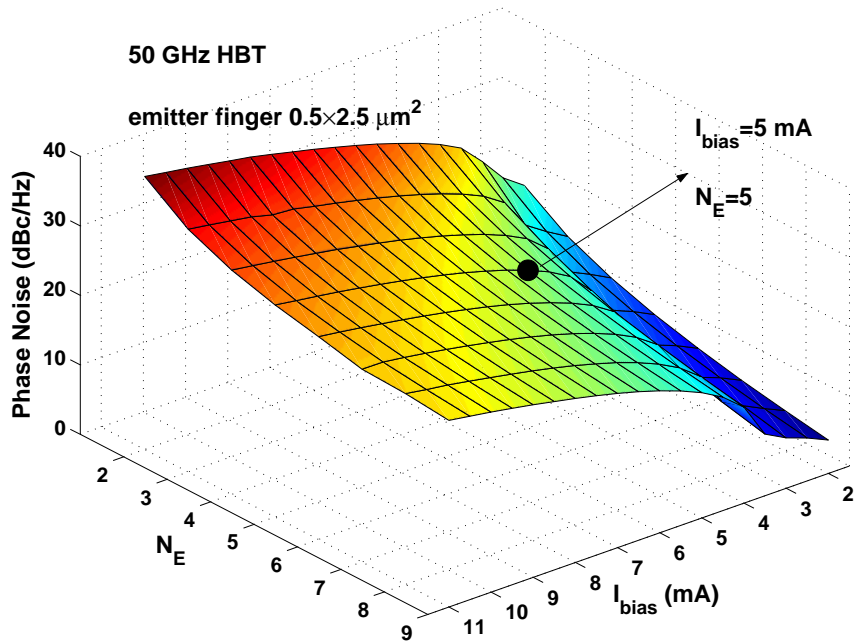
(b)

Figure 5.5: ADS Simulated phase noise as a function of N_E and I_{bias}. The 50 GHz HBT is used. The dot represents $I_{bias} = 5$ mA and $N_E = 5$. Single finger area is 0.5×2.5 μm^2. Oscillation frequency is 5.5 GHz. (a) Offset frequency is 100 MHz where $1/f^2$ phase noise dominates. (b) Offset frequency is 1 Hz where $1/f^3$ phase noise dominates.

"Noiseless" reference

S_θ

S_{θ_VCO}

S_{θ_syn}

S_{θ_ref}

$\omega_{c,offset}$ $\omega_{loop}=\omega_u$ $\Delta\omega$

"Noisy" reference

S_θ

S_{θ_VCO}

S_{θ_ref}

S_{θ_syn}

$\omega_{loop}=\omega_u$ $\omega_{c,offset}$ $\Delta\omega$
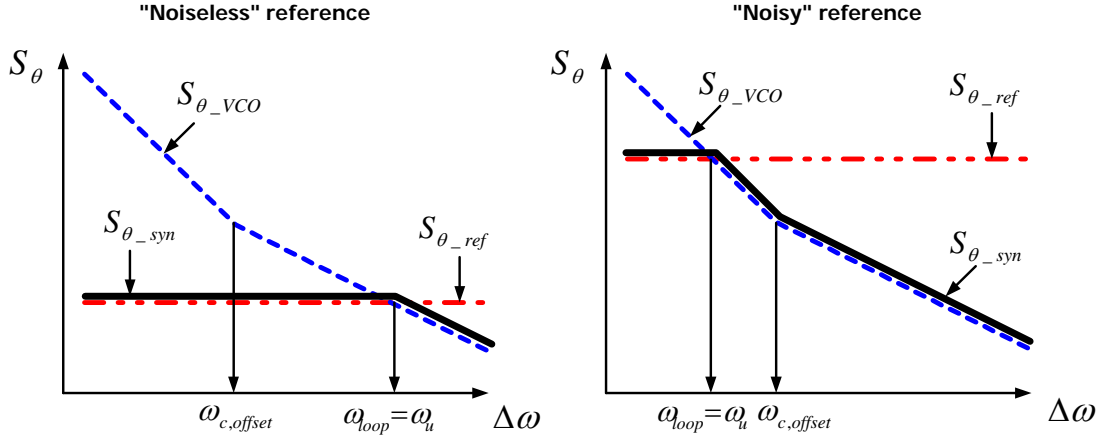
Figure 5.6: VCO phase noise S_{θ_VCO}, reference phase noise S_{θ_ref} and the resulting frequency synthesizer phase noise S_{θ_syn}. The loop bandwidth ω_{loop} is chosen to be equal to ω_u.

transistor size. The increase with increasing I_{bias} is attributed to the increase of the *dc* component of the oscillating base-emitter transport current i_{BE} ($I_{BE,0}$).

The $1/f^2$ phase noise first decreases with I_{bias}, then increases with further increase of I_{bias}, while the $1/f^3$ phase noise increases with I_{bias}. Therefore the lowest close-in and far-off phase noises can not be achieved simultaneously. The optimal I_{bias} for reduced phase noise is not obvious if oscillator phase noise is the only concern. One thing is certain: I_{bias} above the optimal $1/f^2$ phase noise I_{bias} is never a good choice because both $1/f^2$ and $1/f^3$ phase noises are high. Therefore we only consider I_{bias} no larger than the optimal $1/f^2$ phase noise I_{bias}. When the oscillator is used in phase locked loop to form frequency synthesizer, the optimal I_{bias} for system phase noise depends on the loop bandwidth, because the in-band phase noise is suppressed by the loop effect while the out-of-band phase noise directly translates into system phase noise, as discussed in Section 1.4. Assuming loop bandwidth is always chosen to be equal to ω_u (the frequency where VCO phase noise intersects with reference noise) such that the integrated frequency synthesizer phase noise is minimized, the optimal I_{bias} depends on the reference noise level.

Consider two extreme cases, as shown in Figure 5.6, the "noiseless" reference case and the "noisy" reference case. In the "noiseless" reference case, the reference noise S_{θ_ref} is so low compared to the oscillator phase noise such that $\omega_u \gg \omega_{c,offset}$ with the $\omega_{c,offset}$ ($= 2\pi f_{c,offset}$) being the oscillator phase

Table 5.1: Comparison of Parameters For the Three HBTs of Different Technologies.

technology	50 GHz	120 GHz	210 GHz
A_E (μm^2)	0.5×2.5×5	0.2×6.4×5	0.12×12×4
$\beta @ I_{bias}$	75.2	261.8	480.8
$f_T @ I_{bias}$ (GHz)	49	65	80
K_F	2.0×10^{-11}	6.0×10^{-10}	1.5×10^{-11}
r_{bx} (Ω)	5.24	4.02	4.06
r_{bi} (Ω)	24.48	1.58	1.48

noise radian corner offset frequency. The optimal I_{bias} for $1/f^2$ phase noise is the optimal for frequency synthesizer phase noise because the out-of-band phase noise is solely due to $1/f^2$ phase noise. On the other hand, in the "noisy" reference case where $\omega_u \ll \omega_{c,offset}$, the optimal I_{bias} for frequency synthesizer phase noise should be smaller than the optimal $1/f^2$ phase noise I_{bias} in order to reduce the $1/f^3$ phase noise. However, I_{bias} should still be reasonably large to maintain adequate output swing for the intended application. For instance, if the oscillator is used to drive the local oscillator (LO) switching transistors in a double-balanced mixer cell, the voltage swing must be large enough to switch the mixer. We can also understand the two cases as the "noisy" VCO and the "noiseless" VCO, respectively. In Section 5.5, we fix ω_u (thus ω_{loop}) and examine the importance of $1/f^3$ phase noise to synthesizer phase noise for the three technologies used.

Both the $1/f^2$ and $1/f^3$ phase noises decrease with increasing N_E. However, it is not the best choice to use the biggest transistor one can get. Bigger devices make the oscillator difficult or even impossible to tune due to increased device capacitances. Furthermore, the oscillator will stop oscillating due to the diminished f_T with increasing transistor size. Therefore 5 is a good choice for N_E because it is reasonably small but big enough to make both $1/f^2$ and $1/f^3$ phase noises close to their minima.

5.3.3 Oscillator Phase Noise versus Technology Scaling

The optimal transistor bias and size are found for the 120 and 210 GHz technologies as well. The phase noise dependence on bias and size is the same as the 50 GHz technology. Despite the slight difference in the optimal I_{bias} for reduced $1/f^2$ phase noise, the $1/f^2$ phase noise at 5 mA is close to
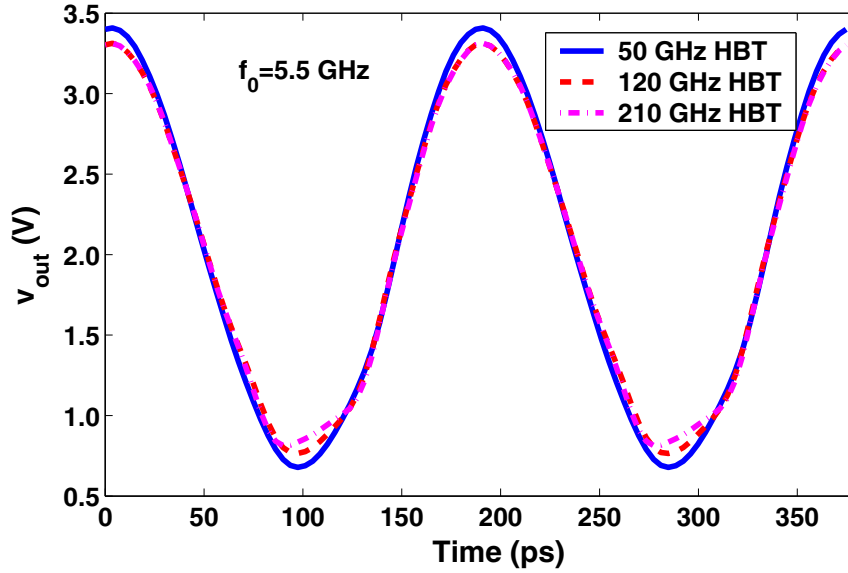
Figure 5.7: Simulated output waveforms of the 5.5 GHz single-ended Colpitts oscillators.

the minimum in all cases. Therefore the three oscillators are biased at the same I_{bias} of 5 mA for a fair comparison of output power. Table 5.1 compares the parameters for the three HBTs. Similar emitter areas are chosen for each technology for a fair comparison of $1/f$ noise. These areas are large enough to make the phase noise close to the achievable minimum phase noise at a I_{bias} of 5 mA. Current gain β increases with technology scaling. The f_T at $I_{bias} = 5$ mA also increases with scaling. The $1/f$ noise K_F is extracted from experimental result, as discussed in Section 4.2. The extrinsic base resistance r_{bx} decreases slightly with scaling to 120 GHz, then remains almost unchanged with further scaling to 210 GHz. The intrinsic base resistance r_{bi} decreases a lot in the 120 GHz HBT, then remains almost unchanged in the 210 GHz HBT.

Figure 5.7 shows the simulated output waveform. The load resistance is 50 Ω. $I_{bias} = 5$ mA. The three oscillators have similar output swing. Figure 5.8 shows simulated phase noise versus offset frequency. Phase noise is dominant by the contribution from the transistors itself. The $1/f^3$ phase noise increases by 12.0 dB with scaling to 120 GHz, while decreases by 18.0 dB with further scaling to 210 GHz, in part because of the K_F factor changes with scaling. The $1/f^2$ phase noise is the highest in the

95
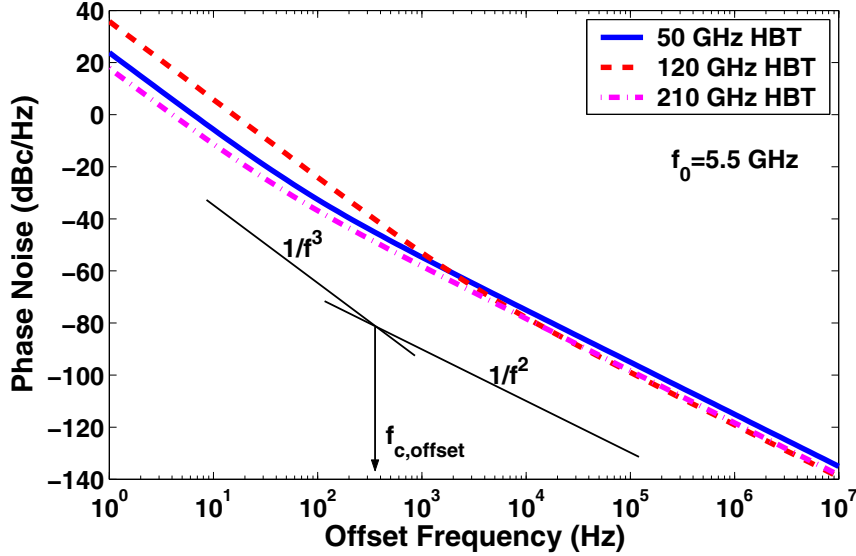
Figure 5.8: Comparison of phase noise spectra of the oscillators designed using HBTs from three technologies.

50 GHz HBT, and is similar in the 120 and 210 GHz HBTs. Scaling to 120 and 210 GHz leads to as much as 4 dB improvement in $1/f^2$ phase noise.

The phase noise corner offset frequency $f_{c,offset}$ is 76.4 Hz, 3.09 kHz and 40.8 Hz for the 50, 120 and 210 GHz technologies, respectively. All of the three technologies show small $f_{c,offset}$. The $f_{c,offset}$ for the 120 GHz HBT is nearly 42× higher than that for the 50 GHz HBT. We emphasize here that $f_{c,offset}$ does not indicate either the $1/f^2$ phase noise level or the $1/f^3$ phase noise level. It is only a measure of the relative importance of $1/f^3$ phase noise with respect to $1/f^2$ phase noise. The overall effect of scaling to 120 GHz on oscillator phase noise is a degradation at offsets below 2 kHz, but an improvement at higher offset frequencies. In a frequency synthesizer, if the loop bandwidth is greater than 2 kHz, the overall synthesizer phase noise will improve with scaling, despite the increased $f_{c,offset}$, since the oscillator phase noise below 2 kHz is removed by loop feedback, as discussed in Section 1.4.

Interestingly, $f_{c,offset}$ is significantly *lower* than the $1/f$ noise corner frequency at the *dc* biasing current for all of the three technologies. For the 50 GHz HBT, $f_{c,offset}$ =76.4 Hz, while $f_{c,1/f}$ =38.5 kHz. For the 120 GHz HBT, $f_{c,offset}$ =3.09 kHz, while $f_{c,1/f}$ =309 kHz. For the 210 GHz HBT, $f_{c,offset}$ =40.8
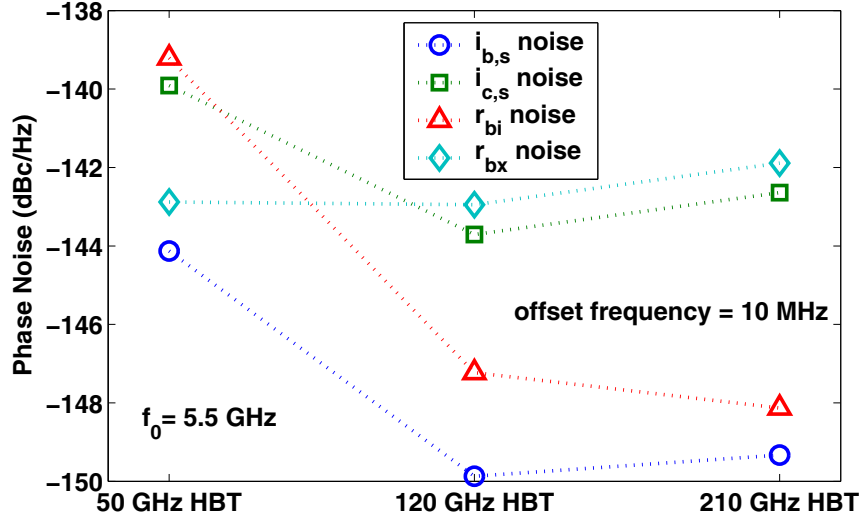
Figure 5.9: Individual $1/f^2$ phase noises at 10 MHz as a function of technology.

Hz, while $f_{c,1/f}$ =8.24 kHz. This observation has significant implications on the methodology of $1/f$ noise evaluation of a process technology. One would have disqualified the 120 GHz HBT for low phase noise oscillators if the $1/f$ noise corner frequency was used as a figure-of-merit for phase noise (309 kHz at 0.78 mA/μm^2). In Section 5.4, we investigate why the $1/f$ noise corner frequency is different from the corner offset frequency in SiGe HBT oscillators.

5.3.4 Technological Limitations

Oscillator phase noise results from various noise sources. The most important ones inside a transistor are: 1) base current $1/f$ noise ($i_{b,1/f}$ noise); 2) base and collector current shot noise ($i_{b,s}$ noise and $i_{c,s}$ noise); 3) thermal noise from the intrinsic and extrinsic base resistance (r_{bi} noise and r_{bx} noise). In this section, we investigate the upconversion of individual phase noise sources as a function of technology scaling and identify the phase noise limiters with scaling. As discussed in Section 5.3.3, $i_{b,1/f}$ noise upconversion is strongly affected by the $1/f$ noise K_F factor. Furthermore $1/f$ noise is not a concern for oscillator phase noise due to the small $f_{c,offset}$ for all technologies. Therefore we only compare individual $1/f^2$ phase noises at 10 MHz as a function of technology in Figure 5.9.

97

With scaling to 120 GHz, all of the $1/f^2$ phase noises decrease except for the r_{bx} noise, which remains almost unchanged. Further scaling to 210 GHz, except for the r_{bi} noise, all of the other $1/f^2$ phase noises increase slightly. The relative importance of the $1/f^2$ phase noises also changes with scaling. The most important $1/f^2$ phase noise contributor in the 50 GHz technology, r_{bi} noise, becomes insignificant in the 120 and 210 GHz technologies. The r_{bx} noise contribution, however, stays about the same with scaling and becomes the most dominant $1/f^2$ phase noise in the 120 and 210 GHz HBTs, followed by the $i_{c,s}$ noise contribution.

As can be seen from Figure 5.9, the intrinsic r_b noise contribution dominates in the 50 GHz HBT, while the extrinsic r_b noise contribution dominates in the 120 and 210 GHz HBTs. The thermal noise gain G_{r_b} defined in (5.5) is calculated for all of the thermal noise sources. The G_{r_b} for r_{bi} thermal noise in the 50 GHz HBT is 10× higher than the G_{r_b} for r_{bx} thermal noise. The G_{r_b} for r_{bi} thermal noise is found to *decrease* by as much as 100 × with scaling to 120 and 210 GHz. The G_{r_b} for r_{bx} thermal noise, however, remains almost unchanged with scaling. For the 120 and 210 GHz HBTs, the G_{r_b} for r_{bi} noise is about 10% of the G_{r_b} for r_{bx} noise, which indicates that, in scaled SiGe HBT technologies, for the same amount of total base resistance, a process in which r_{bi} dominates is better in terms of phase noise reduction. This result also suggests the importance of reducing extrinsic base resistance in scaled SiGe HBT technologies.

The intrinsic base resistance r_{bi} decreases dramatically from 24.48 Ω in the 50 GHz HBT to less than 2 Ω in the 120 and 210 GHz HBTs, as a result of decreased emitter width-to-length ratio, as well as decreased intrinsic base sheet resistance, according to (1.4). Therefore the observed reduction in r_{bi} thermal noise contribution is the result of decreased r_{bi} and G_{r_b}. The extrinsic base resistance r_{bx}, however, stays about the same (from 5.24 Ω in the 50 GHz HBT to 4.02 and 4.06 Ω in the 120 and 210 GHz HBTs) despite decreased width-to-length ratio. The r_{bx} normalized by emitter length increases from 65.5 Ω · μm in the 50 GHz HBT to 128.6 and 194.9 Ω · μm in the 120 and 210 GHz HBTs due to the complexities of extrinsic base scaling [54]. Since G_{r_b} for the r_{bx} thermal noise is almost the same in the three HBTs, the resultant phase noise is also the same. Although $i_{c,s}$ noise contribution is 1 dB lower than r_{bx} noise contribution in the 120 and 210 GHz HBT, $i_{c,s}$ noise sets the fundamental limit on

phase noise reduction through technology scaling. r_{bx} noise contribution can be reduced by extrinsic base structure optimization and the use of a larger device, while $i_{c,s}$ noise is hard to reduce.

5.4 $1/f$ Noise Corner Frequency versus Phase Noise Corner Offset Frequency

5.4.1 Disconnection Between $f_{c,1/f}$ and $f_{c,\text{offset}}$

To investigate the relationship between $1/f$ noise corner frequency and the phase noise corner offset frequency, we consider the phase noise upconversion process implemented in ADS. For simplicity, we will first consider the upconversion of only the base current $1/f$ noise and the base current shot noise. For shot noise, all of the noises at $\widetilde{\omega}_k$ contribute to a phase noise at an offset angular frequency $\Delta\omega$, as shown in (5.6). The $1/f$ noise contribution to phase noise at $\Delta\omega$ is from the dc component of i_{BE} ($I_{BE,0}$) only, as shown in (5.7).

Even though the $1/f^3$ phase noise is determined by the dc component of i_{BE}, the $1/f^2$ phase noise associated with the shot noise of i_{BE} has little to do with the dc component of i_{BE} in typical bipolar oscillators. For typical i_{BE} waveforms found in bipolar oscillators, $\mathcal{L}_{shot}$ is dominated by the noise sidebands near ω_0 instead of the noise sidebands near dc. $\mathcal{L}_{shot}$ is mainly determined by the noises at $\omega_0 \pm \Delta\omega$, $2qI_{BE,1}$, as well as the corresponding frequency sensitivity $\partial\omega_0/\partial i_{BE,1}$. For all practical purposes, one can safely neglect the upconversion of shot noise associated with the dc component of i_{BE}. For instance, for the 50 GHz HBT oscillator considered here, $K_F = 2 \times 10^{-11}$, $I_{BE,0} = 103.78~\mu$A. The sensitivity of ω_0 to the dc component of i_{BE}, $|\partial\omega_0/\partial i_{BE,0}|$, can be calculated from (5.7) as 1.33×10^{10} rad/A. The $\mathcal{L}_{shot}$ due to noise sidebands near dc is -165.33 dBc/Hz at 10 MHz offset frequency. The total phase noise due to i_{BE} shot noise is 21.2 dB higher than that associated with the dc component alone.

Recall that the $1/f$ noise corner frequency is defined by the intersect of the $1/f$ noise and the $2qI_B$ shot noise with I_B being the dc biasing base current. For phase noise upconversion, however, only the $1/f$ noise upconversion is related to the dc component of I_{BE} (which differs from total terminal base current I_B in oscillators). $\mathcal{L}_{1/f}$ is determined by $\partial\omega_0/\partial i_0$ and $S_{1/f}(I_{BE,0})$, while $\mathcal{L}_{shot}$ is mainly
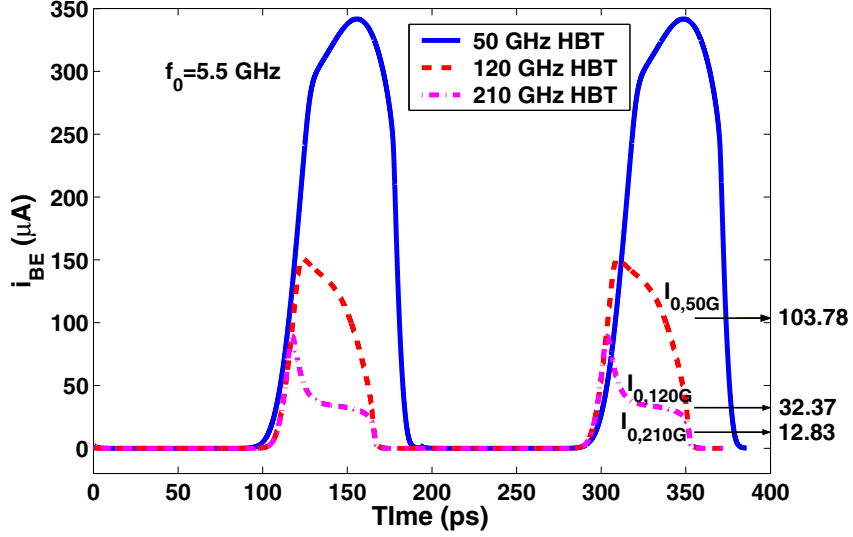
Figure 5.10: Comparison of internal i_{BE} for the 50, 120 and 210 GHz HBT oscillators.

determined by $\partial \omega_0 / \partial i_1$ and $2q I_{BE,1}$. It is therefore not surprising that the $1/f$ noise corner frequency defined using I_B and $S_{1/f}(I_B)$ at either the *dc* biasing current or the *dc* component of i_{BE} does not indicate the value of the phase noise corner frequency, $f_{c,offset}$, as observed in our simulation results.

5.4.2 Impact of Technology Scaling

Figure 5.10 compares the simulated internal i_{BE} waveforms for the three HBTs. The higher speed of the scaled 120 and 210 GHz HBTs leads to faster turn on and turn off of i_{BE}. The maximum of i_{BE} decreases with scaling due to the increase of current gain β, as shown in Table 5.1. The *dc* component of i_{BE}, $I_{BE,0}$, is 103.78, 32.37, and 12.83 μA, respectively (the *dc* biasing I_B is 66.53, 19.18 and 10.35 μA). As discussed above, $I_{BE,0}$ in the oscillator, instead of the *dc* biasing I_B, determines the amount of $1/f$ noise available for phase noise upconversion. In this case, the available $1/f$ noise for upconversion, $S_{1/f}(I_{BE,0})$, increases from 2.15×10^{-20} to 6.29×10^{-20} A^2/Hz (at 10 Hz), or 2.92× increase with scaling to 120 GHz, and decreases to 2.47×10^{-22} A^2/Hz, or 86.96× decrease with further scaling to 210 GHz.

The $i_{b,1/f}$ noise contribution, however, degrades by as much as 12 dB, or 15.9× with scaling to 120 GHz, and improves by only 6 dB, or 4× with further scaling to 210 GHz, as shown in Figure 5.11. Only

100
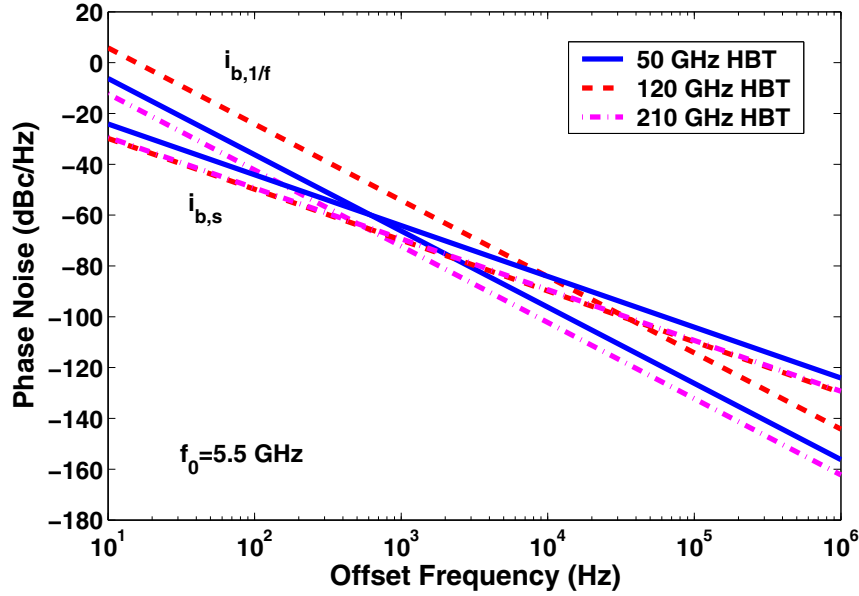
Figure 5.11: $i_{b,1/f}$ and $i_{b,s}$ contributions to phase noise.

a small part of the $i_{b,1/f}$ noise contribution change with scaling is due to the change of the $1/f$ noise available for upconversion. The primary $i_{b,1/f}$ noise contribution change is because of a *large increase of the sensitivity of oscillation frequency to* $1/f$ *noise* with scaling. Table 5.2 compares the factors affecting $1/f$ noise upconversion for the three HBTs. The factors for the 120 and 210 GHz HBTs are normalized by the numbers for the 50 GHz HBT. The sensitivity of oscillation frequency to the *dc* component of i_{BE} increases by 2.33× and 4.67× with scaling to 120 and 210 GHz, respectively.

Also shown in Figure 5.11 is the base current shot noise (denoted by $i_{b,s}$) contribution for the three HBTs. $i_{b,s}$ contribution decreases by 5.7 dB, or 3.7× with scaling from 50 GHz to 120 GHz, and 5.2 dB, or 3.3× with scaling from 50 GHz to 210 GHz. The first order harmonic of i_{BE}, ($I_{BE,1}$), decreases from 170.94 μA to 57.84 μA (2.96× reduction) and 21.99 μA (7.77× reduction) with scaling to 120 and 210 GHz, respectively. The reduction of $i_{b,s}$ noise contribution with scaling to 120 GHz is a little more than the $I_{BE,1}$ reduction, while the $i_{b,s}$ noise contribution reduction with scaling to 210 GHz is less than the $I_{BE,1}$ reduction. This indicates that the sensitivity of oscillation frequency to shot noise decreases a little with scaling to 120 GHz, while increases with further scaling to 210 GHz. Despite the sensitivity

Table 5.2: Comparison of Factors Affecting $i_{b,1/f}$ Noise Upconversion.

technology	50 GHz	120 GHz	210 GHz
K_F	2.0×10^{-11}	30×	0.75×
$I_{BE,0}$ (μA)	103.78	0.31×	0.12×
$i_{b,1/f}$ @ 10 Hz(A^2/Hz)	2.15×10^{-20}	2.92×	0.012×
$|\partial \omega_0 / \partial i_{BE,0}|$ (rad/A)	1.33×10^{10}	2.33×	4.67×
$\mathscr{L}_{1/f}$ @ 10 MHz (dBc/Hz)	-186.22	12(+)	6(-)

increase in the 210 GHz HBT, the phase noise resulting from $i_{b,s}$ noise remains low due to the low $I_{BE,1}$. For transistors operating at severe high-injection region, the phase noise resulting from $i_{b,s}$ noise may be significant because of the β degradation (thus $I_{BE,1}$ increase) at severe high-injection.

The corner offset frequency, where the $1/f^3$ phase noise and the $1/f^2$ phase noise due to $i_{b,s}$ noise intersect, is 600 Hz, 34 kHz and 550 Hz for the 50, 120 and 210 GHz technologies. These numbers are much smaller than the $1/f$ noise corner frequencies at the biasing current $I_C = I_{bias}$ (38.5 kHz, 309 kHz and 8.24 kHz), because of different upconversion mechanisms of $1/f$ noise and shot noise, as discussed above. The overall corner offset frequency is even lower because of additional contributions from other white noise sources, e.g. the base resistance thermal noise and collector current shot noise.

Based on the above discussions, we conclude that the widely used $1/f$ noise corner frequency is not a good indicator of the relative importance of phase noise upconverted from $1/f$ noise for SiGe HBTs. As we have shown, the phase noise upconverted from $1/f$ noise is important only for offset frequencies below $f_{c,offset}$, which is in general much lower than the $f_{c,1/f}$ at the biasing current. The speed increase with scaling leads to more efficient energy shuffling in oscillator, which helps reducing the amount of $1/f$ noise available for upconversion with scaling. The sensitivity of oscillation frequency to $1/f$ noise increases with scaling. The sensitivity of oscillation frequency to base current shot noise decreases with scaling to 120 GHz and increases with further scaling to 210 GHz. Base current shot noise may be a dominant factor for transistors operating at severe high-injection region.
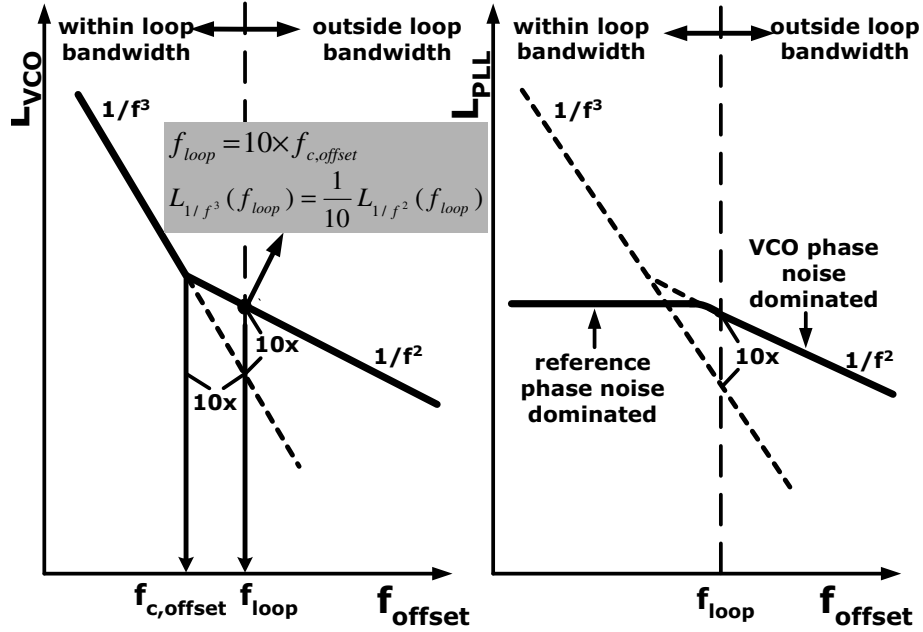
Figure 5.12: Illustration of the conversion process of VCO and reference phase noise to frequency synthesizer phase noise and the definition of K_{th}.

5.5 K_F Factor Threshold and System Phase Noise

In frequency synthesizers, the voltage controlled oscillator (VCO) phase noise within the loop bandwidth is suppressed by the loop feedback mechanism. The out-of-band phase noise of the VCO, however, directly translates into synthesizer out-of-band phase noise. From an application standpoint, if the loop bandwidth is sufficiently higher than the phase noise corner offset frequency $f_{c,offset}$, the $1/f^3$ phase noise can be completely suppressed by loop feedback. The out-of-band noise will then be the $1/f^2$ phase noise due to white noises. The $1/f$ noise K factor which makes $f_{c,offset}$ much smaller than the loop bandwidth can be identified. We call such a K factor the K factor threshold, denoted as K_{th}. Obviously, K_{th} is technology dependent as it relates to the relative importance of $1/f^2$ and $1/f^3$ phase noises. Also K_{th} is dependent on the loop bandwidth. In this section, we define K_{th} and identify the K_{th} for each technology for a given loop bandwidth.

5.5.1 K_{th} Definition

K_{th} is the K factor that makes $f_{c,offset}$ much smaller than the loop bandwidth. The definition for "much smaller" is quite arbitrary. Using 10× as a criterion, K_{th} is then the K factor that makes $f_{c,offset}$ 1/10 of the loop bandwidth. For a given oscillator, $f_{c,offset}$ increases linearly with K factor increase. Therefore the $1/f^3$ phase noise is only 1/10 of the $1/f^2$ phase noise at the offset frequency equal to the loop bandwidth, as shown in Figure 5.12. For a given process and loop bandwidth, a threshold K that makes $f_{c,offset}$ equal to 1/10 of the loop bandwidth can be defined. Once $K < K_{th}$, the synthesizer phase noise no longer decreases with further decrease of K. One can also view this threshold K as the maximum tolerable K. This is very attractive from a semiconductor technology development standpoint, because the $1/f$ noise K factor is sensitive to defect level, and very challenging to minimize.

5.5.2 Impact of Technology Scaling

With K_{th} defined, we now identify the K_{th} for each technology for a given loop bandwidth. As discussed in Section 1.4, loop bandwidth is compromised among the overall frequency synthesizer phase noise, the recovering speed of the PLL and the stability of the loop. Despite different applications, loop bandwidth used in typical frequency synthesizers falls between 30 kHz to 200 kHz [55]- [60]. We will identify the K_{th} for the 50, 120 and 210 GHz technologies using a typical loop bandwidth of 100 kHz. Figure 5.13 shows $f_{c,offset}$ versus $1/f$ noise K factor for the three technologies. K_{th} is determined as the K which makes $f_{c,offset}$ = 10 kHz, such that the $1/f^3$ phase noise is only 10% of the $1/f^2$ noise at 100 kHz. The actual K is below the K_{th} for all the technologies, even for the 120 GHz peak f_T technology which has the highest K factor. With optimized transistor sizing and biasing, $1/f$ noise is not a concern for synthesizer phase noise, since practically all of the $1/f^3$ phase noise is suppressed by loop feedback, and the in-band noise is limited by reference oscillator.

Using frequency sensitivity method, we have examined the implications of SiGe HBT scaling on phase noise of oscillators and frequency synthesizers, as well as the mechanisms of $1/f$ noise upconversion. A significant difference between the $1/f$ noise typically measured at the *dc* biasing current and the
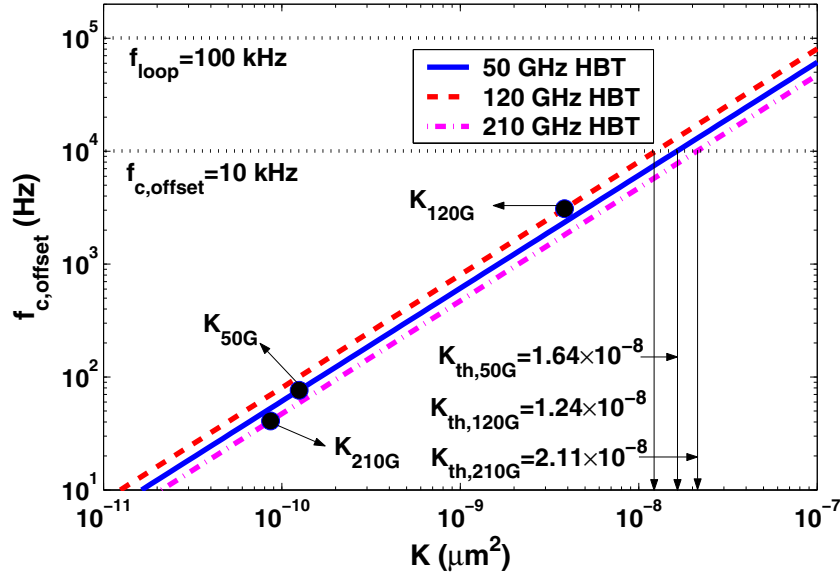
Figure 5.13: $f_{c,offset}$ versus K factor. K_{th} is determined for a loop bandwidth of 100 kHz. The actual K values are shown as circles.

$1/f$ noise available for phase noise upconversion has been identified. The increase of transistor speed with scaling has been found to significantly increase the sensitivity of oscillation frequency to $1/f$ noise. The sensitivity of oscillation frequency to base current shot noise is found to decrease with scaling from 50 GHz to 120 GHz, then increase with further scaling to 210 GHz. The contributions from extrinsic base resistance thermal noise and collector current shot noise are found to be dominant with scaling. The ultimate phase noise limiter is the collector current shot noise. For a given process, the $1/f$ noise K factor only needs to be below a certain threshold, and any further reduction of the K factor does not help reducing system phase noise. The actual K factor for all of the technologies is below their respective K_{th}. $1/f$ noise is not a concern for system phase noise provided transistor size and bias are optimized.

PHASE NOISE ANALYSIS USING IMPULSE SENSITIVITY FUNCTION

It is well known that transistor low-frequency noise is upconverted to oscillator phase noise. Various phase noise analysis methods have been developed, among which the frequency sensitivity, mixing and impulse sensitivity function (ISF) methods are widely used. An in-depth understanding of the upconversion mechanism is highly desired for both oscillator design and process technology development. In Chapter 5, We investigated technology scaling limitations on SiGe HBT oscillator phase noise using ADS simulation, which uses the frequency sensitivity and mixing methods. The underlying upconversion mechanisms, however, were not well understood, in part due to the limited user access to the frequency sensitivities, and in part due to the frequency domain based nature of phase noise simulation methods. To further investigate the underlying upconversion mechanisms, as well as optimal biasing, sizing, technology scaling and oscillation frequency dependence at the transistor level, we use the impulse sensitivity function (ISF) method [18], a time domain based method that provides better insight due to the time-varying nature of oscillation. The expense, however, is that the ISF method is very time consuming, and is not available in commercial simulators for this reason. We have implemented the ISF method with the help of verilog-A, as detailed below.

An important concern to phase noise is $1/f$ noise, which is typically measured under a given *dc* current. In oscillators, however, the noise generating currents are oscillating and large signal in nature. ADS does not consider these complexities, and simply assumes that the $1/f$ noise in an oscillating transistor is identical to the $1/f$ noise measured at a biasing current equal to the *dc* component of the oscillating current [46]. Recent work showed that the $1/f$ noise in an oscillating transistor should also be treated as modulated stationary noise, in the same way shot noise is treated, if the physical origin of the $1/f$ noise is trap-assisted GR fluctuations [44] [48]. Experimental data support the trapping origin of the

$1/f$ noise for the SiGe HBTs used, as detailed in Section 4.3.4. These two methods of handling $1/f$ noise in oscillators result in significantly different phase noise, and the difference can be as much as 10 dB or more in a typical oscillator, as we will show below. Therefore we use the complete cyclostationary modulation model for $1/f$ noise in oscillators. This chapter presents a systematic examination of the upconversions of all of the physical noise sources as a function of transistor sizing and biasing, technology scaling and oscillation frequency. Optimal transistor sizing and biasing for reduced $1/f^2$, $1/f^3$ oscillator phase noises and frequency synthesizer phase noise are investigated. The limiting phase noise sources are identified with technology scaling and the increase of oscillation frequency.

6.1 Impulse sensitivity Function and Implementations

Impulse sensitivity function characterizes phase noise from the time domain. The sensitivity of phase shift to a perturbation impulse current is calculated, which is defined as $\Gamma \triangleq \Delta\phi/\Delta q$ with Δq being the injected charge and $\Delta\phi$ being the resultant phase shift. Γ is periodic, and fundamentally characterizes phase noise upconversion. The accumulated phase shift is calculated for the noise current of interest. Through phase modulation, the noise in the phase is converted to noise in voltage. The detailed derivation on impulse sensitivity function and its application to the upconversion of thermal noise, shot noise and $1/f$ noise to phase noise is presented in Appendix D. The final results are repeated here for convenience.

The upconversion of base resistance thermal noise is determined by the *rms* (root-mean-squared) value of the Γ function and the power spectral density of the noise current:

$$\mathscr{L}_{r_b}(\Delta\omega) = \frac{4kT}{r_b} \frac{\Gamma_{rms}^2}{2\Delta\omega^2}. \tag{6.1}$$

We further define thermal noise gain G_{r_b} for comparison of base resistance noise upconversion from different devices sizes or different technologies. G_{r_b} is the ratio of phase noise to thermal noise voltage $(4kTr_b)$

$$G_{r_b} = 2\Delta\omega^2 \frac{\mathscr{L}_{r_b}(\Delta\omega)}{4kTr_b} = \left(\frac{\Gamma_{rms}}{r_b}\right)^2. \tag{6.2}$$

This is equivalent to replacing the Γ in (6.1) with Γ/R.

For shot noise with a power spectral density of $2qI$, we need to account for the time-varying nature of the noise generating current I, by modulating a white stationary noise with a modulation function [45]. A convenient though arbitrary choice is to use the maximum $2qI$ as a reference, and modulate the reference noise with a function $\alpha_{shot} = \sqrt{|I(t)/I_{max}|}$, which varies between 0 and 1 [18]. Here I_{max} is the maximum of $I(t)$. We can then equivalently use a constant noise generating current I_{max}, but replace Γ with an effective ISF $\Gamma_{eff}(\omega_0 t) = \Gamma(\omega_0 t) \times \alpha_{shot}(\omega_0 t)$. Phase noise due to shot noise is given by

$$\mathcal{L}_{shot}(\Delta\omega) = 2qI_{max}\frac{\Gamma_{eff,rms}^2}{2\Delta\omega^2}, \tag{6.3}$$

where $\Gamma_{eff,rms}$ is the *rms* value of $\Gamma_{eff}(\omega_0 t)$.

For $1/f$ noise which is also a function of biasing current I in small signal measurement, two models exist. The "*dc*" only model treats $1/f$ noise as a slow process, therefore it only depends on the *dc* component of $I(t)$, I_0. Using this model, the phase noise due to $1/f$ is

$$\mathcal{L}_{1/f}(\Delta\omega) = \pi K_F I_0^2 \frac{\Gamma_{dc}^2}{\Delta\omega^3}. \tag{6.4}$$

Γ_{dc} is the *dc* component of Γ. The cyclostationary model treats $1/f$ noise in an oscillating transistor as modulated stationary noise, the same way shot noise is treated. We still use I_{max} as a reference, the modulation function is given by $\alpha_{1/f} = I(t)/I_{max}$. The $1/f$ noise upconversion is modeled as

$$\mathcal{L}_{1/f}(\Delta\omega) = \pi K_F I_{max}^2 \frac{\Gamma_{eff,dc}^2}{\Delta\omega^3}, \tag{6.5}$$

where $\Gamma_{eff,dc}$ is the *dc* component of Γ_{eff}. As detailed in Section 4.3.4, the experimental results suggest the cyclostationary model should be used. Therefore we use (6.5) for phase noise calculation, but comparison will be made with results using (6.4).

Γ and Γ_{eff} are obtained by placing an impulse current in places of the noise currents shown in Figure 4.5 and performing transient analysis in ADS [43] or SpectreRF [20]. Neither of them allows access

of the internal nodes when the built-in VBIC model is used. To solve this problem, we implemented the VBIC model using Verilog-A [22], a hardware description language. The model implementation is compared against the built-in model in all aspects of electrical characteristics for verification. Refer to Appendix B for detailed discussion on Verilog-A implementation. The impulse current is injected at different time instants within one period. Since transient analysis is time consuming when a small time step is used, 16 equally-spaced time instants are used. The resultant phase shift is obtained after the oscillation is restablized. Computation of a single Γ takes about 12 hours on a workstation with 2G memory. The *rms* value of Γ or Γ_{eff} is calculated in MATLAB [61]. The detailed discussion on Γ calculation is presented in Appendix E. The phase noise from thermal noise, shot noise and $1/f$ noise is obtained using (6.1), (6.3) and (6.5), respectively. We compare phase noises simulated using ADS and using our ISF implementation in Appendix F, and the agreement is within 1 dB for most noises.

6.2 Optimal Transistor Sizing and Biasing

We investigated optimal transistor sizing and biasing in Chapter 5. Due to the limited user access to frequency sensitivities, the detailed upconversion mechanisms were not well understood. In this Chapter, we revisit this issue using impulse sensitivity function. The exact reason why transistor sizing and biasing affect phase noise in the observed way will be explained. We still use the same Colpitts oscillator used in Chapter 5. The schematic is shown in Figure 5.3. The three SiGe technologies used in Chapter 5, a 50, 120 and 210 GHz peak f_T technologies, are used here. Figure 6.1 shows phase noise $\mathscr{L}$ as a function of emitter finger number (N_E) and emitter biasing current (I_{bias}). The offset frequency is 100 MHz, where the $1/f^2$ phase noise dominates. The oscillation frequency is 5.5 GHz. A 50 GHz HBT [9] with 0.5×2.5 μm^2 emitter finger is used. The simulated output swing V_{out} increases with increasing I_{bias} and N_E. V_{out} can be estimated using [62]

$$V_{out} = 2R_L I_{bias}(1 - C_2/C_1),\qquad(6.6)$$

where R_L is the effective tank resistance. (6.6) was derived under the assumption that i_{CE} consists of sharp spikes of current with i_{CE} being the instantaneous collector to emitter transport current. This
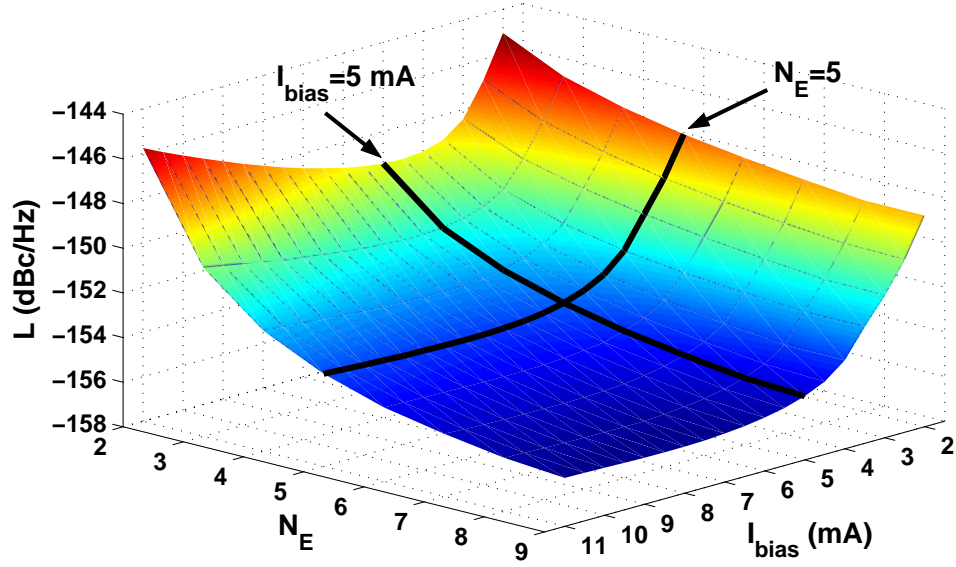
Figure 6.1: $\mathscr{L}$ as a function of N_E and I_{bias}. The 50 GHz HBT is used. Single finger area is 0.5×2.5 μm^2. Oscillation frequency is 5.5 GHz. Offset frequency is 100 MHz.

assumption fails at large I_{bias} and small N_E, as detailed below, making the actual V_{out} smaller than the number predicted by (6.6).

When N_E is fixed, $\mathscr{L}$ first decreases with increasing I_{bias}, then increases with further increase of I_{bias}. There exists an optimal I_{bias} for $1/f^2$ phase noise for all N_E's. The optimal I_{bias} increases slightly with increasing N_E. When I_{bias} is fixed, $\mathscr{L}$ first decreases with increasing N_E and eventually approaches a constant with further increase of N_E to above 8. Larger devices make the oscillator difficult to tune because of larger device capacitances. Furthermore, the oscillator will stop oscillating due to the diminished f_T with increasing transistor size. Therefore 5 is a good choice for N_E because 5 is reasonably small but large enough to make phase noise close to the minimum. The I_{bias} and N_E dependences are consistent with the results in Chapter 5. In the following, we detail the impact of transistor size on $\mathscr{L}$ using an I_{bias} of 5 mA and the impact of transistor biasing using the optimal N_E of 5.
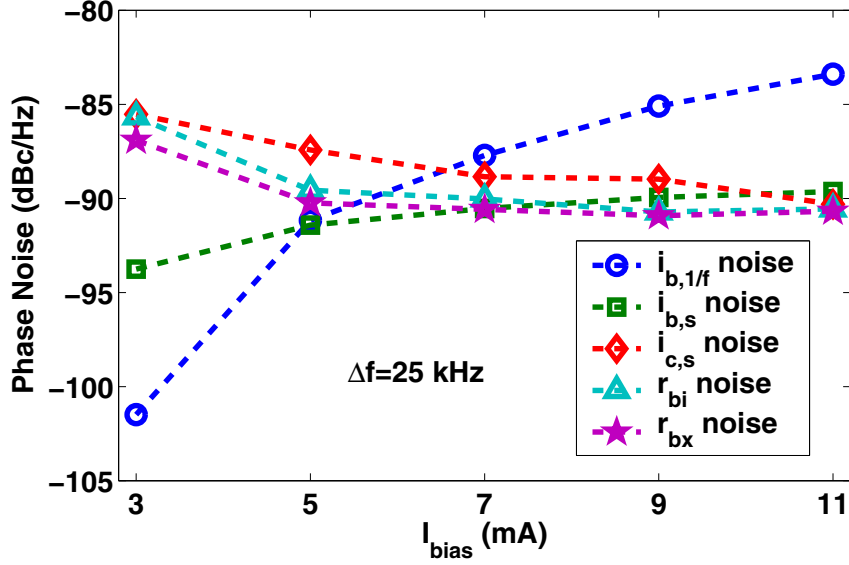
Figure 6.2: Simulated individual phase noises as a function of I_{bias}. The 50 GHz HBT is used. A_E=0.5×2.5×5 μm^2. Oscillation frequency is 5.5 GHz. Offset frequency is 25 kHz.

6.2.1 Phase Noise versus I_{bias}

To understand the I_{bias} dependence observed above, we plot the individual phase noises versus I_{bias} for the optimal $N_E = 5$ size in Figure 6.2. The offset frequency chosen is 25 kHz. The r_{bi} and r_{bx} noise contributions first decrease as increasing I_{bias} to 7 mA, then remains almost unchanged with further increase of I_{bias}. The $i_{c,s}$ noise contribution decreases with increasing I_{bias}. The $i_{b,1/f}$ and $i_{b,s}$ noise contributions increase with I_{bias}. The total $1/f^2$ phase noise is minimized at $I_{bias} = 7$ mA. The relative importance of individual white noise contributions evolves with the increase of I_{bias}. For instance, $i_{b,s}$ noise, which contributes the least $1/f^2$ phase noise at I_{bias} =3 mA, becomes the most dominant $1/f^2$ phase noise source at I_{bias} =11 mA.

Transport i_{CE} and i_{BE}

Figure 6.3 compares i_{CE} and i_{BE} waveforms for transistors at different I_{bias}. The maximum of i_{CE} ($I_{CE,max}$) increases due to I_{bias} increase. The time span during which the transistor is turned on also increases with I_{bias}. i_{CE} shows an impulse-like shape at I_{bias}=3 mA only. The deviation from the "ideal"
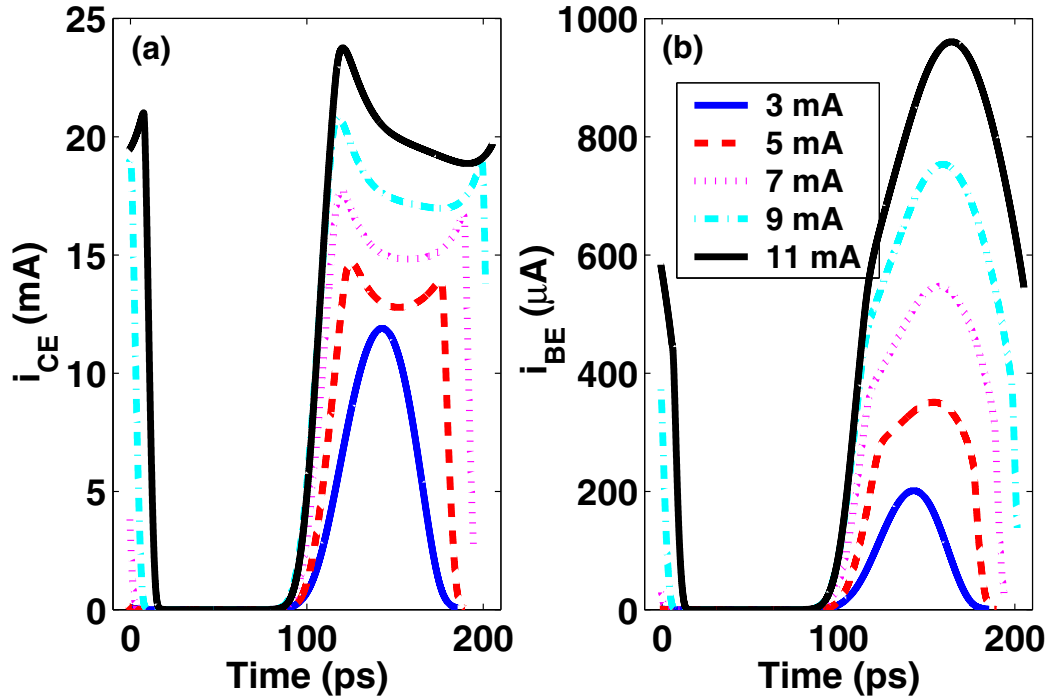
Figure 6.3: (a) i_{CE} and (b) i_{BE} for 50 GHz HBTs at different I_{bias}. $A_E = 0.5 \times 2.5 \times 5 \ \mu m^2$. The 50 GHz HBT is used. Oscillation frequency is 5.5 GHz.

impulse-like shape at higher I_{bias} is due to high-injection and quasi-saturation effects which reduce i_{CE}. This reduction becomes increasingly significant with increasing I_{bias}. To maintain the average value of I_{bias}, the width of the on-state i_{CE} must increase. The maximum of i_{BE} ($I_{BE,max}$) also increases with increasing I_{bias}. The increase is much larger because high-injection and quasi-saturation effects increase i_{BE}.

Thermal Noise Upconversion

Both r_{bx} and r_{bi} thermal noise contributions decrease with increasing I_{bias} to 7 mA, then remains almost unchanged with further increase of I_{bias}. The upconversion mechanism of r_{bx} and r_{bi} noises is similar, we use r_{bx} noise as an example. Figure 6.4 compares the Γ function of r_{bx} noise at different I_{bias}. The Γ values are all close to zero when the transistor is off. Little r_{bx} noise is upconverted to phase noise during off-state. During on-state, the magnitude of the Γ function decreases with increasing I_{bias} mostly

112
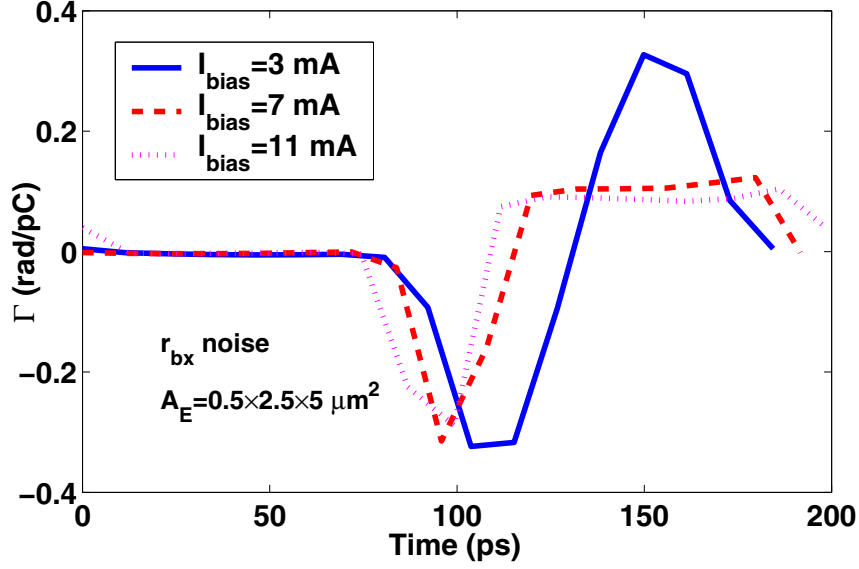
Figure 6.4: Γ of r_{bx} noise for oscillators at different I_{bias}. A_E=0.5×2.5×5 μm^2. The 50 GHz HBT is used. Oscillation frequency is 5.5 GHz.

due to the increase of V_{out}, while the width of the on-state Γ function increases with increasing I_{bias}. Since r_{bx} is the same, $\mathcal{L}_{r_{bx}}$ first decreases with increasing I_{bias} to 7 mA, then remains almost unchanged with further increasing I_{bias}.

Shot Noise Upconversion

Figure 6.5 compares the α function, Γ and Γ_{eff} of the $i_{c,s}$ and $i_{b,s}$ noises at different I_{bias}. For the $i_{c,s}$ noise [Figure 6.5 (a)], the α values are all close to zero when the transistor is turned off. When the transistors is turned on, the pulse width in α function increases with increasing I_{bias}. Since the maximum of the Γ function and the minimum of the α function occur almost simultaneously, the maximum Γ reduces to zero after modulation by α. The longer on-state at high I_{bias} does not degrade Γ_{eff} because Γ is close to zero during on-state. According to (6.3), shot noise upconversion is determined by the reference current ($I_{CE,max}$) and $\Gamma_{eff,rms}$. $\Gamma_{eff,rms}$ is 0.369, 0.210, and 0.155 rad/pC at I_{bias}=3 mA, 7 mA and 11 mA, respectively. The $\Gamma_{eff,rms}$ reduction dominates the $I_{CE,max}$ increase, therefore $\mathcal{L}_{i_{c,s}}$ decreases with increasing I_{bias}. For $i_{b,s}$ noise [Figure 6.5 (b)], the maxima of the α function and Γ function coincide.

113
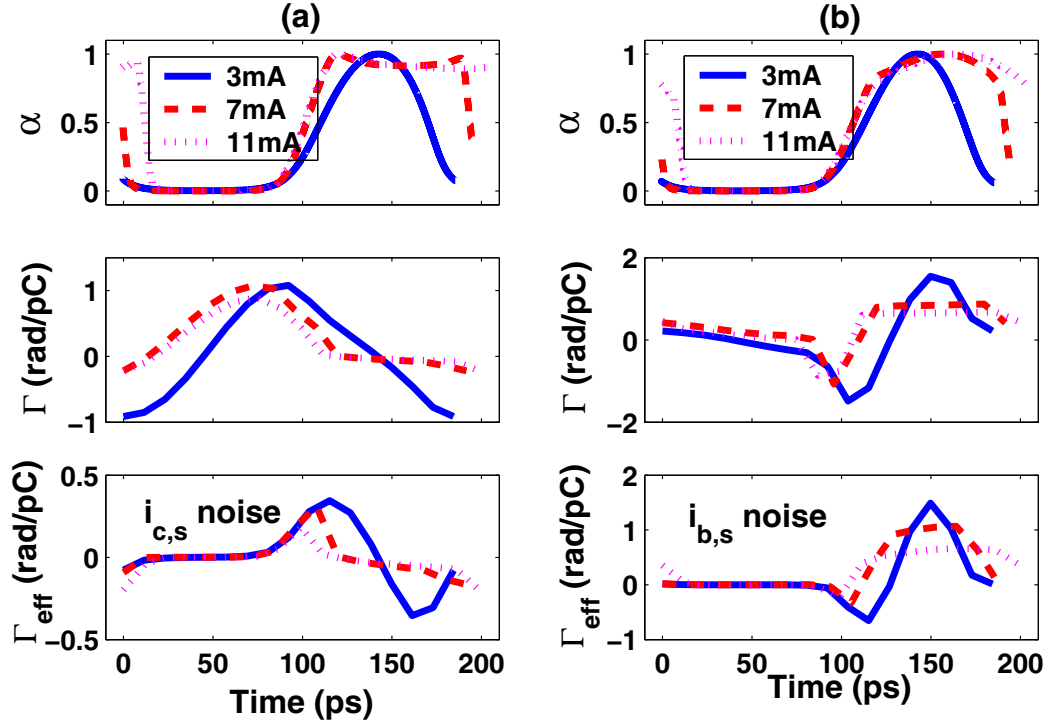
Figure 6.5: α, Γ and Γ_{eff} for the $i_{c,s}$ noise (a) and $i_{b,s}$ noise (b) at different I_{bias}. A_E=0.5×2.5×5 μm^2. The 50 GHz HBT is used. Oscillation frequency is 5.5 GHz.

The wider on-state α function at high I_{bias} results in a wider on-state Γ_{eff}. $\Gamma_{eff,rms}$ decreases only slightly with increasing I_{bias}. This reduction cannot offset the increase of $I_{BE,max}$, thus $\mathscr{L}_{i_{b,s}}$ increases.

The modulation by the oscillating currents reduces the upconverted shot noise. The reduction is much less for the $i_{b,s}$ noise compared to the $i_{c,s}$ noise. For example, at I_{bias} = 7 mA, for the $i_{b,s}$ noise, the *rms* value of the ISF function is 1.213 and 0.965 (rad/pC) before and after modulation, respectively, while it is 1.10 and 0.21 (rad/pC) for the $i_{c,s}$ noise. $\mathscr{L}_{i_{b,s}}$ becomes the limiting phase noise in transistors operating under high bias because of the reduced β (thus high $I_{BE,max}$). To reduce $\mathscr{L}_{i_{b,s}}$, the instantaneous i_{CE} of the SiGe HBT should be kept below the severe high-injection region to avoid significant β and f_T rolloff as well as quasi-saturation.

To make the above argument clearer, we show cutoff frequency f_T as a function of collector current I_C in Figure 6.6 (a), together with the i_{CE} and β waveforms for oscillator biased at 3 mA and 11 mA in Figures 6.6 (b) and (c), respectively. The waveforms are rotated by 90° for better view. At the low
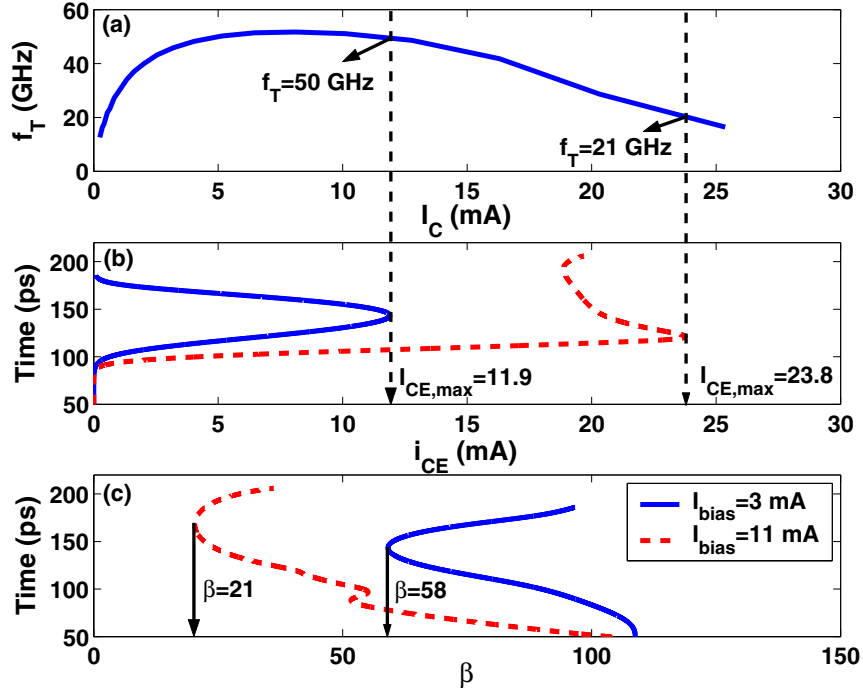
Figure 6.6: (a) Small signal current gain β as a function of I_C on the left-y axis, f_T as a function of I_C on the right-y axis. (b) i_{CE} for the 50 GHz HBT oscillator biased at 7 mA. $A_E = 0.5 \times 2.5 \times 5 \ \mu m^2$.

bias of 3 mA, $I_{CE,max}$ is 11.9 mA, where f_T =50 GHz, very close to peak f_T. At the higher bias of 11 mA, $I_{CE,max}$ is 23.8 mA, where f_T is only 21 GHz, less than 50% of the peak f_T. In Figure 6.6 (c), β waveforms are compared. β is calculated as the ratio of the instantaneous i_{CE} and i_{BE}. The minimum β at 3 mA is 58, while it is only 21 at 11 mA. β degradation caused by high-injection and quasi-saturation is quite severe in part of the cycle when biased at 11 mA. For oscillators where $i_{b,s}$ noise contribution is significant, $I_{CE,max}$ should be kept below severe high-injection and quasi-saturation region to avoid significant β reduction.

$1/f$ Noise Upconversion

As shown in Figure 6.2, $1/f^3$ phase noise increases with increasing I_{bias}. According to the cyclostationary model (6.5) used for $1/f$ noise, both $I_{BE,max}$ and $\Gamma_{eff,dc}$ affect the upconversion of $1/f$ noise. Table 6.1 compares the factors affecting $1/f$ noise upconversion at different I_{bias}. $\Gamma_{eff,dc}$ first increases

Table 6.1: Comparison of Various Factors Affecting $1/f$ Noise Upconversion at Different I_{bias}.

I_{bias} (mA)	$\Gamma_{eff,dc}$ (rad/pC)	$I_{BE,max}$ (μA)	$\mathscr{L}_{1/f}$ @ 100 kHz (dBc/Hz)
3	0.313	201.3	-99.6
5	0.589	350.9	-89.5
7	0.563	547.0	-86.0
9	0.553	753.2	-83.4
11	0.527	960.6	-81.7

with increasing I_{bias} to 5 mA, then decreases slightly with further increasing I_{bias}. $I_{BE,max}$ increases with increasing I_{bias}. The increase in $\Gamma_{eff,dc}$ and $I_{BE,max}$ is responsible for the increase of $\mathscr{L}_{1/f}$ from $I_{bias} = 3$ mA to 5 mA. The increase of $\mathscr{L}_{1/f}$ for I_{bias} greater than 5 mA is solely due to the increase of $I_{BE,max}$.

6.2.2 System Phase Noise versus I_{bias}

As we have already seen, the lowest $1/f^3$ and $1/f^2$ phase noises cannot be achieved simultaneously. As far as the reduced total oscillator phase noise is concerned, it is not clear to us what the optimal I_{bias} should be. Similar to what was discussed in Chapter 5, the optimal I_{bias} for reduced oscillator phase noise should be no larger than the optimal I_{bias} for $1/f^2$ phase noise (7 mA) for a N_E of 5, because both $1/f^2$ and $1/f^3$ phase noises increase when I_{bias} is greater than 7 mA. Without considering I_{bias} greater than 7 mA, the phase noise corner offset frequency, $f_{c,offset}$, increases with increasing I_{bias}. $f_{c,offset}$ is 25 kHz at $I_{bias} = 7$ mA.

When the oscillator is used in a frequency synthesizer, the optimal I_{bias} for system phase noise depends on the loop bandwidth as discussed in Section 1.4. In Chapter 5, we investigate the optimal I_{bias} for frequency synthesizer assuming the loop bandwidth is always chosen such that the integrated synthesizer phase noise is minimized. The highest $f_{c,offset}$ is 25 kHz. If the loop bandwidth is much larger than 25 kHz, the optimal I_{bias} for system phase noise is 7 mA. If the loop bandwidth is much smaller than 25 kHz, the optimal I_{bias} for system phase noise should be lower than 7 mA.

116
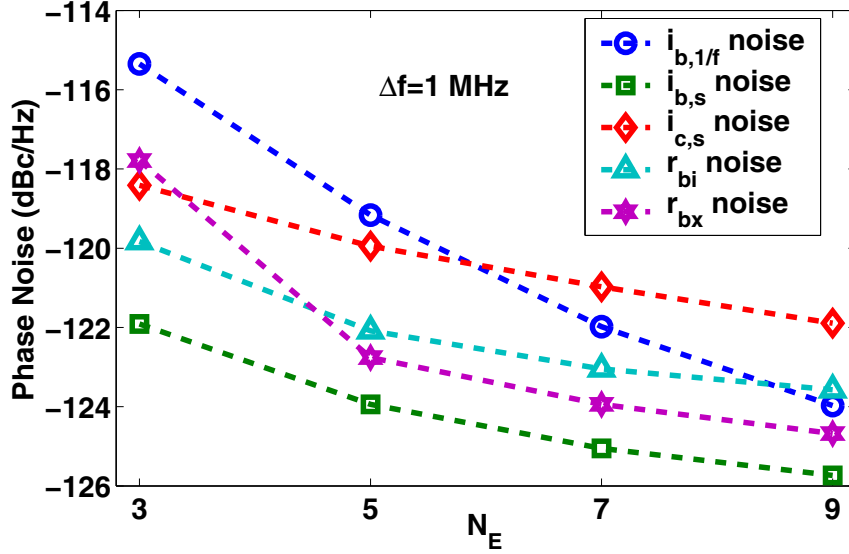
Figure 6.7: Individual phase noise at 1 MHz as a function of N_E. Single finger area is $0.5 \times 2.5 \ \mu m^2$. Oscillation frequency is 5.5 GHz. $I_{bias} = 5$ mA.

6.2.3 Phase Noise versus N_E

We now examine the impact of transistor size using a $0.5 \times 2.5 \ \mu m^2$ emitter finger, and vary N_E from 3 to 9. I_{bias} is 5 mA. Figure 6.7 shows the individual phase noise at 1 MHz as a function of N_E. All of the noises decrease with increasing N_E. The reduction of $1/f^3$ phase noise is mostly due to the decrease of the $1/f$ noise K_F factor with increasing transistor size. The reduction of r_{bx} and r_{bi} noise contributions is mainly due to the reduction of r_{bi} and r_{bx} with scaling. $i_{c,s}$ noise becomes the dominant phase noise in large devices, as detailed below.

Figure 6.8 compares i_{CE} waveforms for transistors of different N_E. Larger devices experience less severe quasi-saturation due to collector resistance reduction, and less severe high-injection due to operating collector current density reduction. Therefore $I_{CE,max}$ increases with increasing transistor size. Since i_{CE} should be averaged to 5 mA, bigger device shows a narrower pulse in i_{CE}. Figure 6.9 compares the Γ and Γ_{eff} of the $i_{c,s}$ noise. Γ's have similar shape and magnitude, while the magnitude of Γ_{eff} and thus $\Gamma_{eff,rms}$ decrease with increasing N_E. The reduction in Γ_{eff} magnitude mostly occurs during the transitions between off- and on-states, $80-120 \ ps$ and around $180 \ ps$. Despite the $I_{CE,max}$ increase
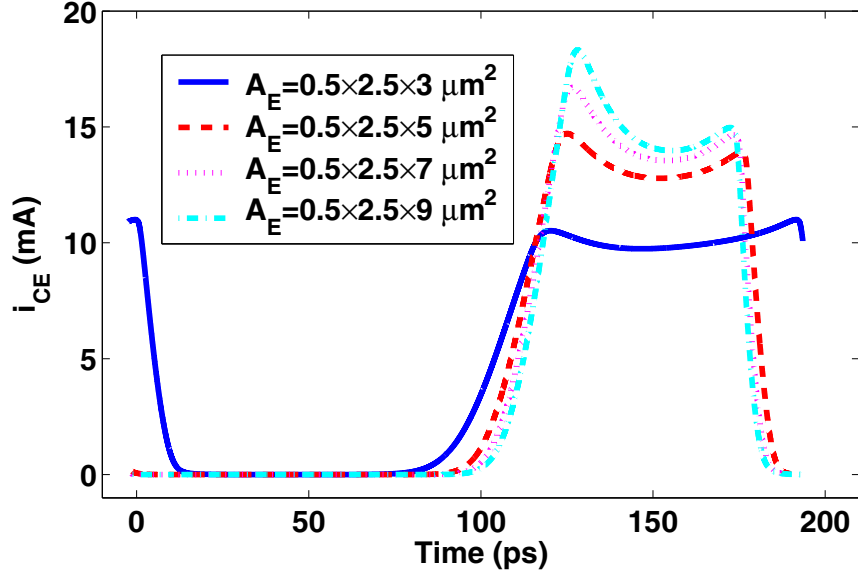
Figure 6.8: i_{CE} for transistors of different N_E. Single finger area is $0.5{\times}2.5$ μm^2. The 50 GHz HBT is used. Oscillation frequency is 5.5 GHz. I_{bias}=5 mA.

with increasing N_E, $\mathscr{L}_{i_{c,s}}$ decreases with increasing transistor size. With continuous increasing of N_E, however, i_{CE} will show an impulse-like shape. The increase of $I_{CE,max}$ will dominate the reduction in Γ_{eff} magnitude, and thus $\mathscr{L}_{i_{c,s}}$ limits the phase noise reduction with increasing transistor size.

6.3 Impact of Technology Scaling

To investigate the impact of technology scaling, we use the three Colpitts oscillators in Chapter 5. They are designed using HBTs from 50, 120 [12] and 210 GHz [11] peak f_T technologies. The transistor sizing and biasing are identical to those used in Chapter 5. I_{bias} is fixed at 5 mA because 5 mA makes makes $1/f^2$ phase noise close to its minimum achievable value. The emitter areas chosen are large enough to make the phase noise close to its minimum, and similar for a fair comparison of $1/f$ noise. The three oscillators have similar output power, as shown in Figure 5.7. Table 6.2 compares the parameters for the three HBTs. This table is similar to Table 5.1 except the $I_{CE,max}$ and $I_{BE,max}$ information is added. $I_{CE,max}$ increases with scaling. $I_{BE,max}$ decreases due to increased current gain β. K_F's are extracted
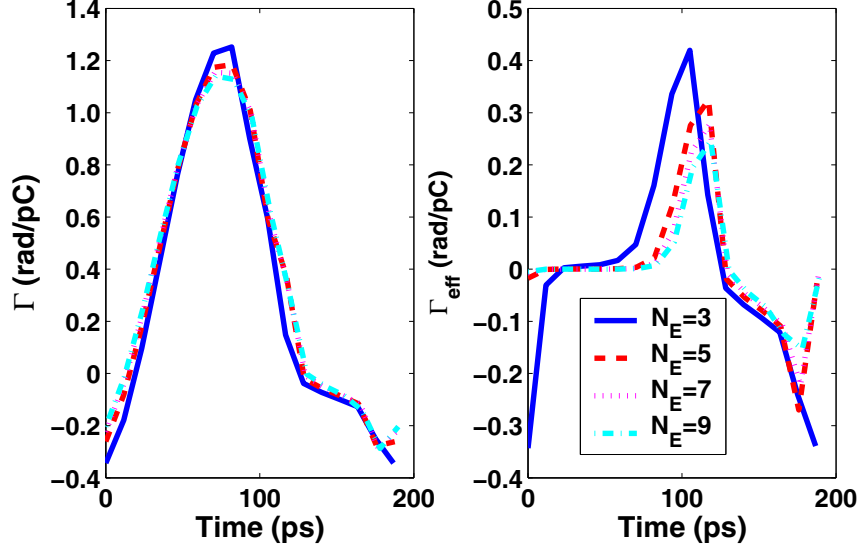
Figure 6.9: (a) Γ and (b) Γ_{eff} of the $i_{c,s}$ noise for transistors of different size. Single finger area is 0.5×2.5 μm^2. The 50 GHz HBT is used. I_{bias}=5 mA.

from the experimental results. The 120 GHz HBT has the highest K_F. r_{bx} is similar for the three HBTs. r_{bi} is much larger in the 50 GHz HBT, and similar in the 120 and 210 GHz HBTs.

Figure 6.10 (a) compares the total phase noise spectra for the three oscillators. The $1/f^3$ phase noise first increases with scaling to 120 GHz, then decreases in the 210 GHz HBT. The $1/f^2$ phase noise is the highest in the 50 GHz HBT. The 120 and 210 GHz HBTs show similar $1/f^2$ phase noise. Figure 6.10 (b) shows the individual $1/f^2$ phase noise versus technology. The offset frequency is 1 MHz. With scaling to 120 GHz, all of the $1/f^2$ phase noises decrease with scaling except r_{bx} noise contribution, which becomes the most dominant $1/f^2$ phase noise and followed by $i_{c,s}$ noise contribution. With further scaling to 210 GHz, all of the $1/f^2$ phase noises remains almost unchanged except r_{bi} noise contribution.

6.3.1 Base Resistance Thermal Noise

As discussed in Section 6.1, Γ/R better characterizes the upconversion of different resistance thermal noise sources. Figure 6.11 compares Γ/R of r_{bx} noise for the three oscillators. The normalized Γ's have similar shape and magnitude, and thus similar *rms* value. The calculated $G_{r_{bx}}$ is similar. As shown in Table 6.2, the three HBTs have similar r_{bx}, therefore $\mathscr{L}_{r_{bx}}$ is almost the same in the three oscillators

Table 6.2: Comparison of the Three HBTs from Different Technologies.

technology	50 GHz	120 GHz	210 GHz
A_E (μm^2)	0.5×2.5×5	0.2×6.4×5	0.12×12×4
$I_{BE,max}$ (μA)	350.9	150.0	87.8
$I_{CE,max}$ (mA)	14.7	29.3	31.0
$\beta @ I_{bias}$	75.2	261.8	480.8
$f_T @ I_{bias}$ (GHz)	49	65	80
K_F	2.0×10^{-11}	6.0×10^{-10}	1.5×10^{-11}
r_{bx} (Ω)	5.24	4.02	4.06
r_{bi} (Ω)	24.48	1.58	1.48

and becomes the most dominant $1/f^2$ phase noise. Using a larger device with smaller r_{bx} will naturally help reducing $\mathscr{L}_{r_{bx}}$. The penalty, however, is larger parasitic capacitances and lower oscillation frequency because of degrading f_T for a given biasing current and power consumption.

6.3.2   Shot Noise Upconversion

Figure 6.12 compares the i_{CE} waveforms for the three transistors. The 120 and 210 GHz HBTs turn on faster and stay on for a smaller portion of the oscillation period, in part due to the higher speed of the 120 and 210 GHz HBTs, and in part due to the less severe high-injection and quasi-saturation effects, similar to what was discussed in Section 6.2.3. $I_{CE,max}$ increases with scaling because of the narrower i_{CE} pulse in the 120 and 210 GHz HBTs, as i_{CE} should average to 5 mA. The higher β in the scaled devices leads to smaller $I_{BE,max}$ despite the increased $I_{CE,max}$, as shown in Table 6.2. The higher speed in the 120 and 210 GHz HBTs reduces $i_{c,s}$ noise contribution. This, together with the ability to operate at higher current density without severely degrading f_T and β, leads to significantly reduced $i_{b,s}$ noise contribution with scaling. The $i_{b,s}$ noise contribution becomes insignificant even at I_{bias} high enough to drive the transistor into severe high-injection. Therefore we focus on the $i_{c,s}$ noise below.

Figure 6.13 compares the Γ and Γ_{eff} of $i_{c,s}$ noise. Despite the largest Γ_{rms} for the 210 GHz HBT, $\Gamma_{eff,rms}$ remains smallest as a result of the strongest modulation by α. $\Gamma_{eff,rms}$ decreases a lot with scaling to 210 GHz, and remains almost unchanged with further scaling to 210 GHz. Since $I_{CE,max}$ increases by two times with scaling to 120 and 210 GHz, $\mathscr{L}_{i_{c,s}}$ decreases by 4 dB with scaling to 120 GHz, then
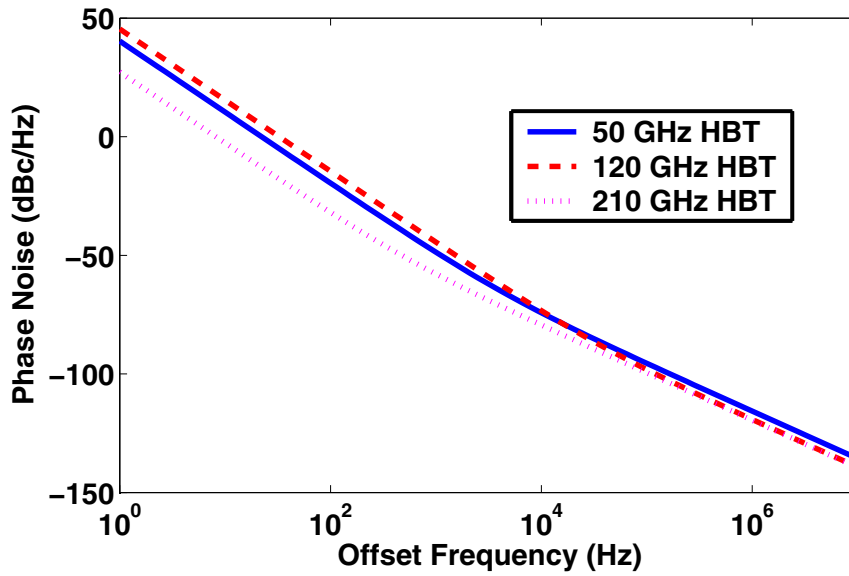
(a)
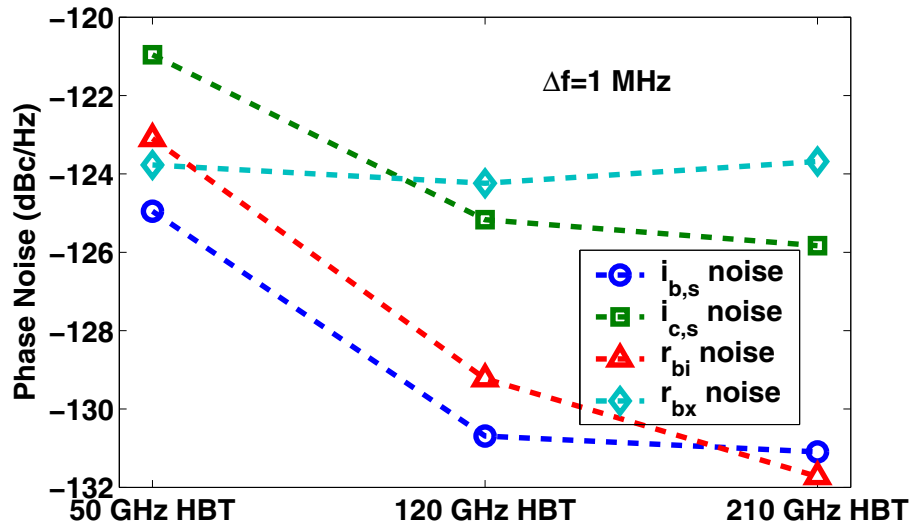
(b)

Figure 6.10: (a) Total phase noise as a function of technology. (b) Individual $1/f^2$ phase noises at 1 MHz as a function of technology.
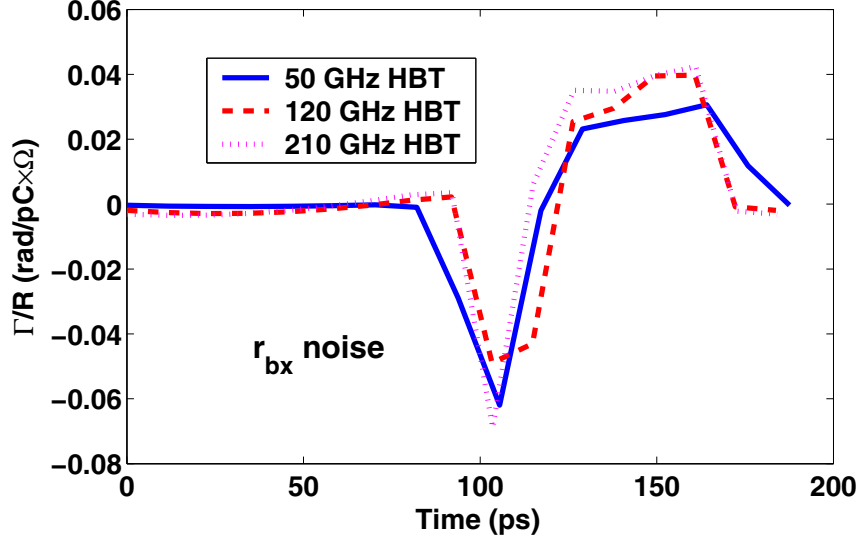
Figure 6.11: Γ/R of r_{bx} noise for the 50, 120 and 210 GHz HBTs. Oscillation frequency is 5.5 GHz. $I_{bias} = 5$ mA.

remains almost unchanged with further scaling to 210 GHz. Although $\mathscr{L}_{i_{c,s}}$ is more than 2 dB lower than $\mathscr{L}_{r_{bx}}$ in the 210 GHz HBT, $\mathscr{L}_{i_{c,s}}$ is the ultimate limiting $1/f^2$ phase noise with technology scaling. Smaller $\mathscr{L}_{r_{bx}}$ can be achieved by reducing r_{bx} through extrinsic base structure optimization or the use of a larger device, while $\mathscr{L}_{i_{c,s}}$ is difficult to reduce.

6.3.3 $1/f$ Noise Upconversion

As shown in Figure 6.10 (a), $1/f$ noise contribution increases by 5 dB with scaling from 50 GHz to 120 GHz, while decreases by 13 dB with scaling from 50 GHz to 210 GHz. According to the cyclostationary model used for $1/f$ noise as shown in (6.5), the upconversion of $1/f$ noise is determined by K_F factor, $I_{BE,max}$ and $\Gamma_{eff,dc}$. Table 6.3 compares those factors for the three HBTs. Remember in Chapter 5, we conclude that the sensitivity of oscillation frequency to $1/f$ noise increases with technology scaling. The sensitivity increases by 2.33× with scaling from 50 GHz to 120 GHz, and 4.67× with scaling from 50 GHz to 210 GHz, as shown in Table 5.2. The counterpart of the oscillation frequency sensitivity in the ISF method is $\Gamma_{eff,dc}$, which is not a strong function of technology scaling. The observed changes
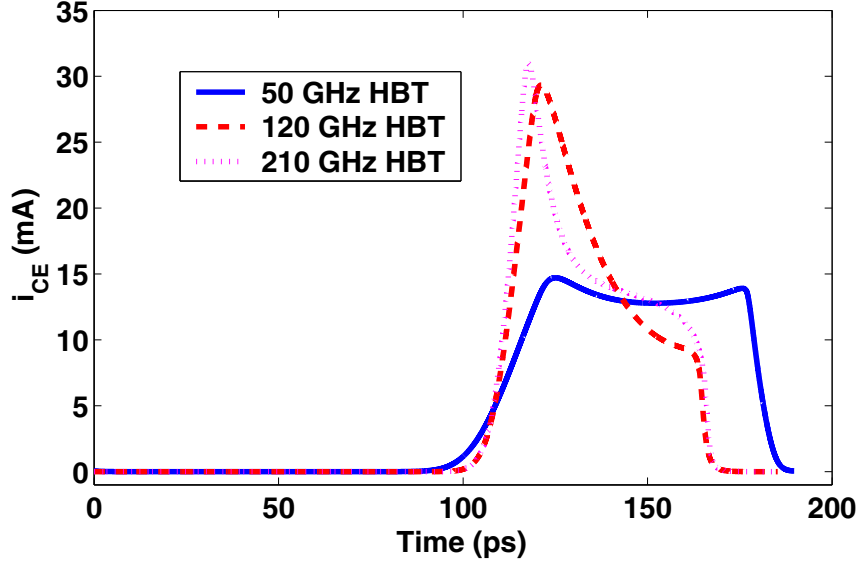
Figure 6.12: i_{CE} for the 50, 120 and 210 GHz HBTs. Oscillation frequency is 5.5 GHz. I_{bias}=5 mA.

Table 6.3: Comparison of the Factors Affecting $1/f$ Noise Upconversion Using the Cyclostationary Model. $I_{bias} = 5$ mA.

technology	50 GHz	120 GHz	210 GHz
A_E (μm^2)	0.5×2.5×5	0.2×6.4×5	0.12×12×4
K_F	2.0×10^{-11}	6.0×10^{-10}	1.5×10^{-11}
$I_{BE,max}$ (μA)	350.9	150.0	87.8
$\Gamma_{eff,dc}$ (rad/pC)	0.589	0.450	0.603
$\mathscr{L}_{i_{b,1/f}}$@10 MHz (dBc/Hz)	-169.65	-164.60	-182.74

in $1/f$ noise contribution with scaling is therefore mostly due to the changes in the available $1/f$ noise current for upconversion ($K_F I_{BE,max}^2/f$).

The corner offset frequency $f_{c,offset}$ is 1.6 kHz, 24.3 kHz and 760 Hz for the 50, 120 and 210 GHz HBT. Note that the $f_{c,offset}$ number is larger than the $f_{c,offset}$ when the frequency sensitivity method is used, as shown in Chapter 5. We will look deeper into the comparison of ISF method and frequency sensitivity method in Section 6.5. Despite the increase of $f_{c,offset}$ when the cyclostationary model is used, $f_{c,offset}$ is still lower than $1/f$ noise corner frequency, $f_{c,1/f}$, which is measured under the biasing current equal to the *dc* bias current in the oscillator (38.5 kHz, 309 kHz and 8.24 kHz for the 50, 120 and 210
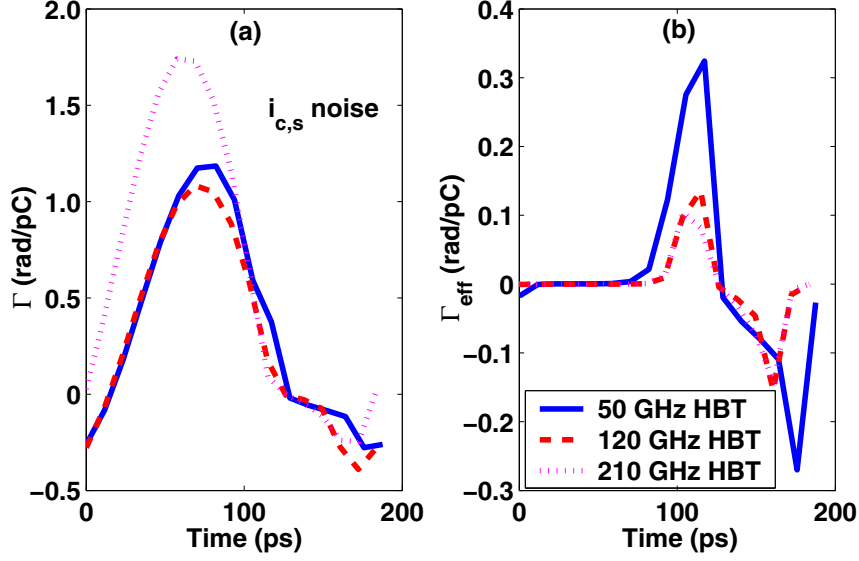
Figure 6.13: (a) Γ and (b) Γ_{eff} of the $i_{c,s}$ noise for the 50, 120 and 210 GHz HBTs. Oscillation frequency is 5.5 GHz. I_{bias}=5 mA.

GHz HBTs). This indicates that $f_{c,1/f}$ should not be used alone to evaluate the relative importance of phase noise upconverted from $1/f$ noise for SiGe HBTs.

6.4 Oscillation Frequency Dependence

We now investigate the impact of oscillation frequency (f_0) using the 210 GHz HBT as an example. Three oscillators are designed, with f_0 5.5, 20, and 40 GHz, respectively. I_{bias}=5 mA, at which $f_T = 80$ GHz and is sufficient for all of the oscillators. The emitter area is $0.12 \times 12 \times 4$ μm^2. Phase noise increases with increasing f_0, as expected. To account for ω_0 and output power P_{out} differences, the phase noise is normalized by $(\omega_0/\Delta\omega)^2/P_{out}$ for comparison [51]. Figure 6.14 compares the normalized noise power as a function of f_0. For $1/f$ noise, the offset frequency is 10 kHz. Except for $i_{c,s}$ noise, all of the noise powers decrease with increasing f_0. $i_{c,s}$ noise becomes the most dominant phase noise source.

Figure 6.15 compares the i_{CE} waveforms for the three oscillators. The time axis is normalized by the oscillating period. Since the three oscillators are biased at the same I_{bias} of 5 mA (thus the same f_T), the oscillator with larger f_0 turns on and off slower, which results in a wider pulse in i_{CE}. i_{CE} should be

124
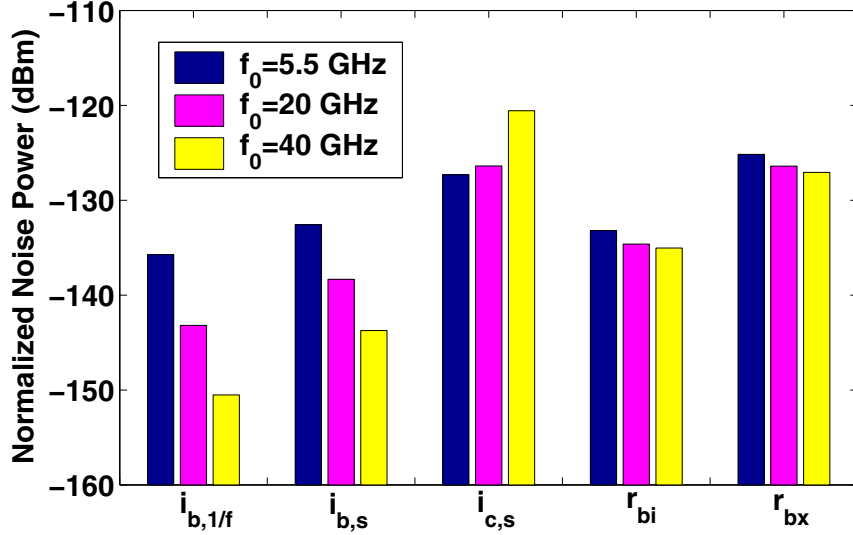
Figure 6.14: Individual noise power as a function of f_0. The noise power is normalized by $(\omega_0/\Delta\omega)^2/P_{out}$. I_{bias}=5 mA. A_E=0.12×12×4 μm^2.

averaged to 5 mA, therefore $I_{CE,max}$ decreases with increasing f_0. This effect can be clearly seen from the 20 GHz and 40 GHz oscillator comparison. For the 5.5 GHz oscillator, since the instantaneous i_{CE} is so high sometimes, quasi-saturation and high-injection occur, which decreases i_{CE} and thus increases the pulse width in i_{CE}.

Figure 6.16 compares the α, Γ and Γ_{eff} of the $i_{c,s}$ noise. The ISF functions are divided by ω_0/V_{out} for a fair comparison for different oscillators. As shown in Figure 6.16 (b), Γ moves downward with increasing f_0. The 40 GHz oscillator has a much smaller Γ value (more negative) during on-state when α is close to 1. Therefore $\Gamma_{eff,rms}$ is much larger for this oscillator, as shown in Figure 6.16 (c). Despite the decrease of $I_{CE,max}$, $i_{c,s}$ noise contribution increases with increasing f_0.

Figure 6.17 compares the normalized Γ and Γ_{eff} of the $i_{b,1/f}$ noise. Γ also moves downward with increasing f_0. The on-state Γ magnitude decreases with increasing f_0. After modulation by α, the on-state Γ_{eff} remains similar to the on-state Γ, while the off-state Γ_{eff} is close to zero. $\Gamma_{eff,dc}$ which together with $I_{BE,max}$ determine the upconversion of $1/f$ noise, decreases with increasing f_0. $I_{BE,max}$ also decreases with increasing f_0, therefore $\mathscr{L}_{i_{b,1/f}}$ decreases with increasing f_0. Since the dominant

125
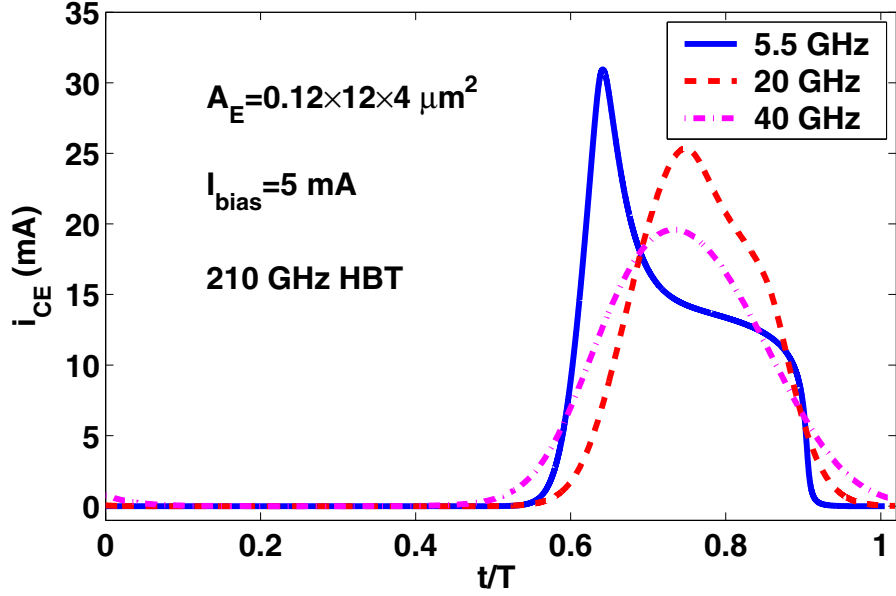
Figure 6.15: i_{CE} waveform for the 5.5, 20 and 40 GHz oscillators. I_{bias}=5 mA. The 210 GHz HBT is used. A_E=0.12×12×4 μm^2.

$1/f^2$ phase noise, $\mathscr{L}_{i_{c,s}}$, increases with increasing f_0, while $1/f$ contributions decreases with increasing f_0, $1/f$ noise is less an issue in oscillators with high f_0.

6.5 $1/f$ Noise Modeling and Impact on System Phase Noise

As we have discussed in Section 4.3.4, two models are available for $1/f$ noise modeling in oscillating transistors. The *dc* only model considers $1/f$ noise to be dependent on the *dc* component of the oscillating noise generating current only. Currently this model is implemented in the frequency sensitivity method in ADS and used in Chapter 5. The ISF method can also implement this model, the resulting $1/f^3$ phase noise is shown in (6.4). Excellent agreement is achieved between $1/f^3$ phase noise simulated using the *dc* only model in ISF method and the frequency sensitivity method, as shown in Appendix F. Therefore in the following discussion, we do not differentiate the two methods. We call them both *dc* only model. The other model is the cyclostationary model, which is used throughout this chapter since it is supported by the experimental results. In this section, we investigate the impact of $1/f$ noise modeling on oscillator phase noise as well as system phase noise. In Section 6.5.1, we investigate

126
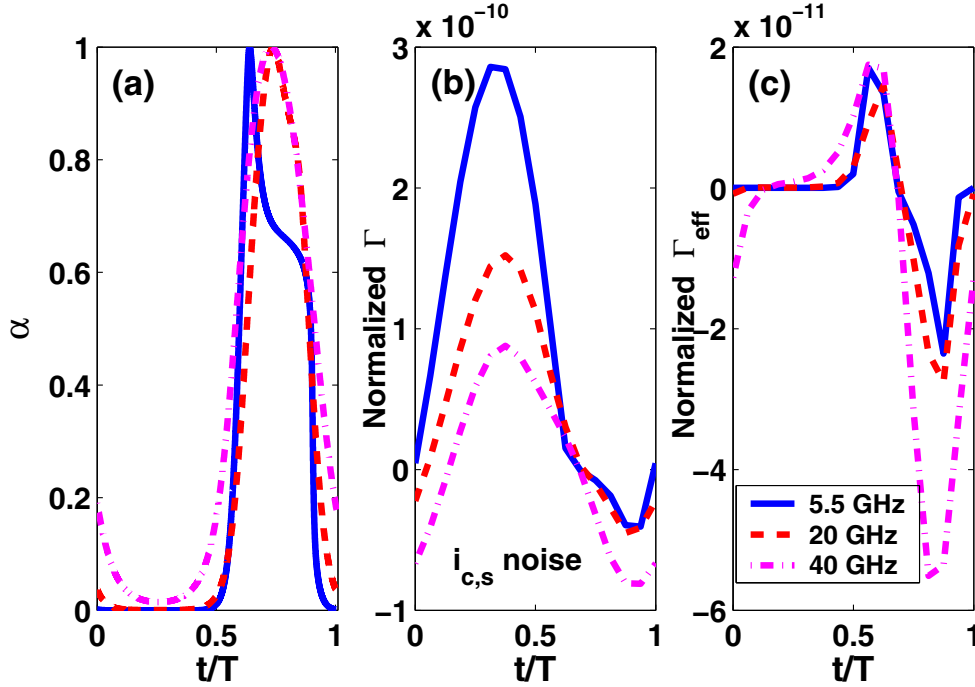
Figure 6.16: (a) α, (b) Γ and (c) Γ_{eff} of $i_{c,s}$ noise for oscillators of different f_0. Both the ISF functions and the time axis are normalized.

the impact on phase noise corner offset frequency. In section 6.5.2, the impact on system phase noise and K factor threshold is examined.

6.5.1 Impact on $f_{c,offset}$

Phase noise corner offset frequency $f_{c,offset}$ is the intersect of $1/f^3$ phase noise and total $1/f^2$ phase noise. For simplicity, we first consider the upconversion of base current $1/f$ noise and base current shot noise only. Using the *dc* only model, $f_{c,offset}$ is obtained by equating (6.3) and (6.4)

$$f_{c,offset} = \frac{K_F I_{BE,0}}{2q} \cdot \frac{I_{BE,0}}{I_{BE,max}} \cdot \frac{\Gamma_{dc}^2}{\Gamma_{eff,rms}^2} = f_{c,1/f} \cdot \frac{I_{BE,0}}{I_{BE,max}} \cdot \frac{\Gamma_{dc}^2}{\Gamma_{eff,rms}^2},$$

(6.7)

where $f_{c,1/f}$ is the $1/f$ noise corner frequency defined in (4.20). It is without doubt that $I_{BE,0} < I_{BE,max}$. Furthermore due to the weak modulation of Γ function of the $i_{b,s}$ noise by α function, as discussed in
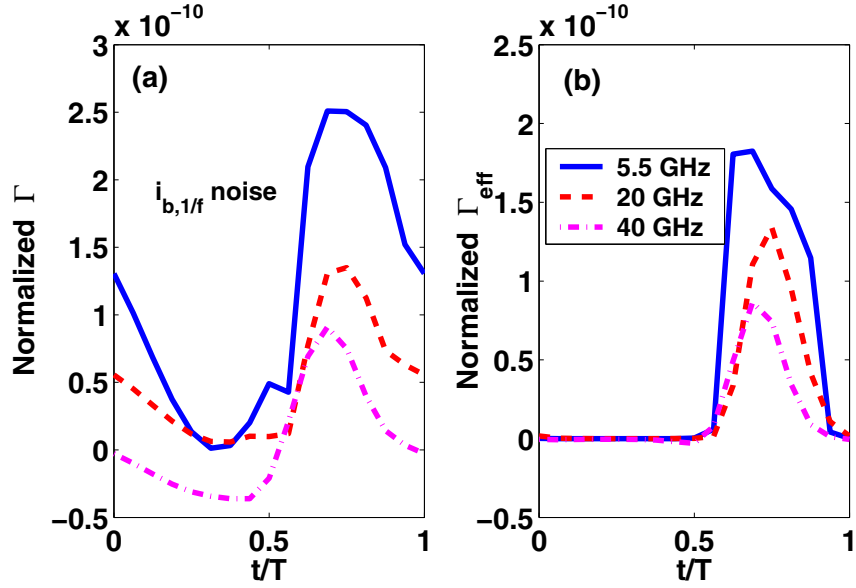
Figure 6.17: (a) Γ and (b) Γ_{eff} of $i_{b,1/f}$ noise for oscillators of different f_0. Both the ISF functions and the time axis are normalized.

Section 6.2, $\Gamma_{dc} < \Gamma_{eff,rms}$ holds for typical oscillators. Therefore it can be clearly seen that $f_{c,offset} < f_{c,1/f}$.

Using the cyclostationary model, $f_{c,offset}$ is obtained by equating (6.3) and (6.5)

$$f_{c,offset} = \frac{K_F I_{BE,max}}{2q} \cdot \frac{\Gamma^2_{eff,dc}}{\Gamma^2_{eff,rms}} = \frac{K_F I_{BE,0}}{2q} \cdot \frac{I_{BE,max}}{I_{BE,0}} \cdot \frac{\Gamma^2_{eff,dc}}{\Gamma^2_{eff,rms}} = f_{c,1/f} \cdot \frac{I_{BE,max}}{I_{BE,0}} \cdot \frac{\Gamma^2_{eff,dc}}{\Gamma^2_{eff,rms}}. \quad (6.8)$$

The relationship between $f_{c,offset}$ and $f_{c,1/f}$ is not clear to us when the cyclostationary model is applied because $I_{BE,max} > I_{BE,0}$, while $\Gamma_{eff,dc} < \Gamma_{eff,rms}$. Despite the uncertainty, we find for all oscillators we investigated, $f_{c,offset} < f_{c,1/f}$ holds. Therefore we conclude that $f_{c,1/f}$ should not be used alone to evaluate the importance of $1/f$ noise for oscillator phase noise.

We now examine the relationship between $f_{c,offset}$ resulted from *dc* only model and cyclostationary model. Comparing (6.7) and (6.8), the relationship between $f_{c,offset}$ from the *dc* only model and

cyclostationary model becomes clear if we can evaluate quantitatively the magnitude of

$$\frac{I_{BE,0}^2}{I_{BE,max}^2} \frac{\Gamma_{dc}^2}{\Gamma_{eff,dc}^2}$$

compared to unity. It is without doubt that $I_{BE,max} > I_{BE,0}$, the relationship between Γ_{dc} and $\Gamma_{eff,dc}$ is not so obvious. In typical oscillators, The absolute magnitude of Γ of $1/f$ noise is small during off-state, at least compared to the on-state Γ value. The absolute magnitude of Γ reduces to zero after modulation. The change in the dc component of the ISF is generally quite small compared to the difference in $I_{BE,0}$ and $I_{BE,max}$, as evidenced by our simulation results. Therefore $f_{c,offset}$ resulted from the cyclostationary model is generally larger than that from the dc only model.

6.5.2   Impact on System Phase Noise

Recall in Chapter 5, the $1/f$ noise K factor threshold is defined and identified for each technology with a loop bandwidth of 100 kHz. The actual K factor is below the K_{th} for all of the technologies. At that time, we used frequency sensitivity method in ADS which implements the dc only model. We have also shown that the $1/f^3$ phase noise resulted from the cyclostationary model is more than 10 dB higher than the phase noise from the dc only model. The next logical question is how $1/f$ noise modeling affects the threshold K factor and whether the actual K factor for the three technologies is still below the threshold K factor. Figure 6.18 shows $f_{c,offset}$ as a function of $1/f$ noise K factor. The loop bandwidth is still 100 kHz. K_{th} is determined from $f_{c,offset} = 10$ kHz. As we can see, the actual K factor for the 50 and 120 GHz HBTs is much higher than their respective K_{th}. The actual K factor for the 210 GHz HBT is almost the same as the K_{th}.

Table 6.4 compares the actual K factor, the K_{th} derived from the cyclostationary model and the K_{th} derived from dc only model for the three technologies. The difference between K_{th} derived from the two models is at least 300×. This emphasize the necessity of using the right model for $1/f$ noise. If the cyclostationary model is applied to $1/f$ noise, the $1/f$ noise is still a concern to frequency synthesizer phase noise. Using a larger device can help reducing $1/f^3$ phase noise. Like $f_{c,offset}$, K_{th} itself does not
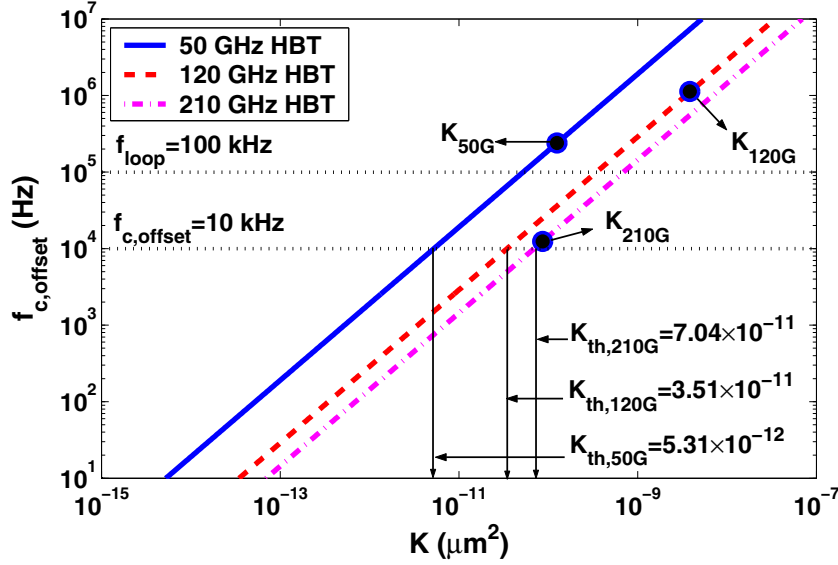
Figure 6.18: $f_{c,offset}$ versus K factor. K_{th} is determined for a loop bandwidth of 100 kHz. The actual K values are shown as circles. The cyclostationary model is used for $1/f$ noise upconversion.

Table 6.4: Comparison of the actual K factor, the threshold K derived from cyclostationary model (model A) and dc only model (model B) for the three technologies. The loop bandwidth is 100 kHz

technology	50 GHz	120 GHz	210 GHz
A_E (μm^2)	0.5×2.5×5	0.2×6.4×5	0.12×12×4
Actual K (μm^2)	1.25×10^{-10}	3.84×10^{-9}	8.64×10^{-11}
Model A K_{th} (μm^2)	5.31×10^{-12}	3.51×10^{-11}	7.04×10^{-11}
Model B K_{th} (μm^2)	1.64×10^{-8}	1.24×10^{-8}	2.11×10^{-8}

contain information on the absolute $1/f^2$ or $1/f^3$ phase noise. It only represents the maximum K factor that is "tolerable" to a frequency synthesizer. A higher $1/f^2$ phase noise level naturally increases K_{th}, other things being equal. Therefore a technology with lower $1/f^2$ phase noise challenges the process engineer for lower $1/f$ noise K factor. Despite the highest K factor in the 120 GHz HBT and the biggest difference between the actual K and K_{th} derived using the cyclostationary model, the far-off phase noise is the lowest in the 120 GHz HBT. Therefore one cannot disqualify this technology for low noise oscillator applications. As long as the loop bandwidth is no smaller than its $f_{c,offset}$ (24.3 kHz), the 120 GHz HBT leads to the smallest integrated frequency synthesizer phase noise.

Using the ISF method, we have investigated phase noise upconversion in SiGe HBTs as a function of transistor sizing, biasing, scaling and oscillation frequency using measured $1/f$ noise data. For optimal phase noise performance, a medium sized HBT should be used, and the maximum oscillating collector current should be kept below severe high-injection region where f_T and β are significantly degraded and quasi-saturation occurs. With scaling to 120 and 210 GHz, phase noises due to collector and base current shot noises decrease as a result of increased current gain and transistor speed, as well as the ability to operate at higher current density. Phase noise due to intrinsic base resistance thermal noise decreases naturally as a result of intrinsic base resistance reduction. Phase noise due to extrinsic base resistance thermal noise can also be reduced by using a relatively large device and improved extrinsic base structure. Phase noise due to collector current shot noise becomes the most dominant phase noise source with technology scaling. With increasing oscillation frequency, the output noise powers due to all noise sources decrease, except for the output noise power due to collector current shot noise, which becomes the ultimate phase noise limiter. The relevant importance of $1/f$ noise compared to collector current shot noise becomes less as well. Using a loop bandwidth of 100 kHz, the actual K factor for the three HBTs are found to be higher than their respective threshold K factor.

CHAPTER 7

CONCLUSION AND FUTURE WORK

7.1 Conclusions

We have investigated the modeling and scaling limitations of SiGe HBTs low-frequency noise and oscillator phase noise. Using inverse circuit simulation, base current noise spectrum is extracted much more accurately by accounting for higher order effects such as avalanche multiplication and self-heating. The utility of the method is demonstrated by examining the collector-base voltage and base transport current dependence of $1/f$ noise. The impact of CB junction traps on low-frequency noise in high breakdown voltage SiGe HBTs for a 50 GHz peak f_T technology is examined. The impact of series resistances on Gummel characteristics is eliminated by using the internal base-emitter voltage. The series resistance $1/f$ noise is found negligible. For SiGe HBTs exhibiting a larger CB junction traps induced recombination at low-injection, a larger difference in high-injection base current is observed between the standard and high breakdown voltage SiGe HBTs. This result suggests the necessity of modeling the recombination current due to the CB junction traps since it contributes significant amount of I_B when high-injection occurs. CB junction traps do not generate g-r noise, but contribute $1/f$ noise when high-injection occurs. The base current components due to hole injection into emitter and CB junction recombination, as well as their respective $1/f$ noises are separated. The noises generated from the EB and CB junctions are distinctive. However, the dependence of total base current $1/f$ noise on the total base current for the high breakdown voltage SiGe HBTs is found to be approximately the same at both low- and high-injections, and is nearly the same as that of the standard breakdown voltage SiGe HBTs, making modeling easier. The above conclusions are also verified using standard and high breakdown voltages HBTs from a 90 GHz peak f_T technology.

132

We examined the impact of SiGe HBT technology scaling on $1/f$ noise using experimental results. $1/f$ noise for a given base current is found to increase with scaling from 50 to 120 GHz peak f_T technology, then decrease with scaling from 50 to 210 GHz peak f_T technology. We then investigated the implications of scaling on oscillator phase noise using frequency sensitivity method in ADS. In ADS, $1/f$ noise is considered to depend on the *dc* component of the noise generating current only. The impact on overall phase noise with scaling to 120 GHz is a degradation of the close-in phase noise, but an improvement of the far-off phase noise. With scaling from 50 to 210 GHz, both the close-in and far-off phase noises decrease. A significant difference between the $1/f$ noise typically measured at the *dc* biasing current and the $1/f$ noise available for phase noise upconversion is identified using Verilog-A based circuit modeling.

The detailed upconversion process of transistor noise sources to oscillator phase noise is investigated using a time domain based impulse sensitivity function method, as a function of transistor sizing and biasing, technology scaling and the increase of oscillation frequency. The modulated cyclostationary noise model is applied to $1/f$ noise. The resulting phase noise is at least 10 dB higher than that simulated using *dc* current based $1/f$ noise model for oscillators, as found in ADS and SpectreRF. For optimal phase noise performance, a medium sized HBT should be used, and the maximum oscillating collector current should be kept below severe high-injection region where f_T and β are significantly degraded and quasi-saturation occurs. The combination of higher speed and the ability to operate at higher current density without severely degrading f_T and β help reducing the shot noise contribution to phase noise in scaled technologies. Phase noise due to intrinsic base resistance thermal noise decreases naturally as a result of intrinsic base resistance reduction. Phase noise due to extrinsic base resistance thermal noise can also be reduced by using a relative large device and improved extrinsic base structure. Phase noise due to collector current shot noise becomes the most dominant phase noise source with scaling. With increasing oscillation frequency, the output noise powers due to all noise sources decrease, except for the output noise power due to collector current shot noise, which becomes the ultimate phase noise limiter. The relevant importance of $1/f$ noise compared to collector current shot noise becomes less as well.

For a given process, the $1/f$ noise K factor only needs to be below certain threshold, and any further reduction of the K factor does not help reducing system phase noise. Such a threshold is defined and identified for each technology. The modeling of $1/f$ noise in oscillating transistors have significant impact on system phase noise. The MF approach (amplitude modulation followed by filtering) considers $1/f$ noise only a function of the dc component of the noise generating current. The FM approach (filtering followed by amplitude modulation) treats $1/f$ noise as modulated stationary noise. $1/f^3$ phase noise resulted from the MF approach is about 10 dB lower than the phase noise from the FM approach. Using the MF approach, the threshold K factor is *lower* than the actual K factor for all of the technologies under investigation, while the threshold K derived from the FM approach is *higher* than the actual K factor in all cases. This calls for accurate modeling of $1/f$ noise in large signal operation conditions. The threshold K itself does not indicates either the $1/f^3$ or the $1/f^2$ phase noise level. It is the K factor that makes $1/f$ noise "disappear" from the out-of-band frequency synthesizer phase noise. One can not disqualify a certain technology simply because the threshold K is below the actual K factor.

7.2 Future Work

Now we have come to the end of presenting the results of modeling and scaling limitations of SiGe HBTs low-frequency noise and oscillator phase noise investigation obtained from IBM's 50, 120 and 210 GHz technologies. We have answered many interesting and intriguing questions we asked at the beginning, and discovered several unknown issues in the process. The answers are often quite different from or even opposite to our initial expectations. Nevertheless, it is those questions that led us to the results, and here we ask a few more questions and suggest some topics for future investigation:

1. Experimental verification of the cyclostationary behavior of transistor $1/f$ noise under large signal oscillating condition. As we have already seen, phase noise resulting from cyclostationary model and dc model can easily vary by as much as 10 dB. This calls for accurate modeling of $1/f$ noise under large signal operating condition. This can be best investigated by comparing the experimental data with the theoretical calculation. Currently we are designing a single-ended

Colpitts oscillator using IBM's 60 GHz technology. Since $1/f$ noise level in SiGe HBT is quite low, by manually stressing the transistor inside the VCO, we expect to see observe $1/f^3$ phase noise even at a high offset frequency.

2. Experimental verification of the phase noise optimization results with respect to technology scaling, transistor sizing and biasing and oscillation frequency.

3. Extending the findings in phase noise upconversion mechanism to oscillators of different oscillator topologies. In this work, a single-end Colpitts oscillator is used. It is interesting to see whether the conclusions hold in other oscillator topologies, such as a differential Colpitts oscillator, or a cross coupled oscillator.

4. Derivation of accurate models which account for the scattering behavior of low-frequency noise in devices of small emitter areas. Currently low-frequency noise is modeled using

$$S_{I_B} = KF\frac{I_B^{AF}}{f^\gamma}, \tag{7.1}$$

with AF, KF and γ being the fitting parameters. The effect of the increasing dispersion in low-frequency noise with decreasing emitter areas requires a more systematic study. New models are needed to help circuit designers better predict the noise behavior when a small device is used.

5. Inclusion of recombination current due to CB junction traps into bipolar compact models. We have shown CB junction recombination current becomes significant when high-injection occurs. The accurate modeling of CB junction recombination current is necessary not only for the sake of base current modeling, but also for the base current $1/f$ noise. The method for extracting CB recombination current used in Chapter 3 is not convenient because it requires the existence of both high breakdown voltage device and high f_T device processed under identical condition. A better way is needed to extract the CB recombination current especially in highly scaled SiGe HBTs where the trap density is high and the operating current density is high.

BIBLIOGRAPHY

[1] D. L. Harame, D. C. Ahlgren, D. D. Coolbaugh, J. S. Dunn, G. Freeman, J. D. Gillis, R. A. Groves, F. N. Hendersen, R. A. Johnson, A. J. Joseph, S. Subbanna, A. M. Victor, K. M. Watson, C. S. Webster, and P. J. Zampardi, "Current status and future trends of SiGe BiCMOS Technology," *IEEE Trans. on Electron Devices*, vol. 48, no. 11, pp. 2575-2594, November 2001.

[2] L. S. Vempati, J. D. Cressler, J. A. Babcock, R. C. Jaeger, and D. L. Harame, "Low-frequency noise in UHV/CVD epitaxial Si and SiGe bipolar transistors," *IEEE Journal of Solid-State Circuits*, vol. 31, no. 10, pp. 1458-1467, October 1996.

[3] B. V. Haaren, M. Regis, O. Llopis, L. Escotte, A. Gruhle, C. Mahner, R. Plana, and J. Graffeuil, "Low-frequency noise properties of SiGe HBT's and application to ultra-low phase-noise oscillators," *IEEE Trans. on Microwave Theory and Techniques*, vol. 46, no. 5, pp. 647-652, May 1998.

[4] J. D. Cressler and G. Niu, *Silicon-Germanium Heterojunction Bipolar Transistors*, Artech House, 2003.

[5] D. J. Roulston, *Bipolar Semiconductor Devices*, McGraw Hill, 1990.

[6] B. S. Meyerson, "Low-temperature silicon epitaxy by ultrahigh vacuum/chemical vapor deposition," *Appl. Phys. Lett.*, vol. 48, pp. 797-799, 1986.

[7] T. O. Sedgwick, M. Berkenbilt, and T. S. Kuan, "Low-temperature selective epitaxial growth of silicon at atmospheric pressure," *Appl. Phys. Lett.*, vol. 54, pp. 2689-2691, 1989.

[8] D. C. Ahlgren, M. Gilbert, D. Greenberg, J. Jeng, J. Malinowski, D. Nguyen-Ngoc, K. Schonenberg, K. Stein, R. Groves, K. Walter, G. Hueckel, D. Colavito, G. Freeman, D. Sunderland, D. L. Harame, and B. Meyerson, "Manufacturability demonstration of an integrated SiGe HBT technology for the analog and wireless marketplace," *Tech. Dig. International Electron Devices Meeting*, pp. 859-862, 1996.

[9] D. C. Ahlgren, G. Freeman, S. Subbanna, R. Groves, D. Greenberg, J. Malinowski, D. Nguyen-Ngoc, S. J. Jeng, K. Stein, K. Schonenberg, D. Kiesling, B. Martin, S. Wu, D. L. Harame, and B. Meyerson, "A SiGe HBT BiCMOS technology for mixed signal RF applications," *Proc. IEEE Bipolar/BiCMOS Circuits and Technology Meeting*, pp. 195-197, 1997.

[10] L. Lanzerotti, J. Sturm, E. Stach, R. Hull, T. Buyuklimanli, and C. Magee, "Suppression of boron outdiffusion in SiGe HBTs with carbon incorporation," *Tech. Dig. International Electron Devices Meeting*, pp. 96-99, 1996.

[11] B. Jagannathan, M. Khater, F. Pagette, J. Rieh, D. Angell, H. Chen, J. Florkey, F. Golan, D. R. Greenberg, R. Groves, S. J. Jeng, J. Johnson, E. Mengistu, K. T. Schonenberg, C. M. Schnabel, P. Smith, A. Stricker, D. Ahlgren, G. Freeman, K. Stein, and A. Subbanna, "Self-aligned SiGe NPN

transistors with 285 GHz f_{MAX} and 207 GHz f_T in a manufacturable technology," *IEEE Electron Device Letters*, vol. 23, no. 5, pp. 258-260, May 2002.

[12] A. J. Joseph, D. Coolbaugh, M. Zierak, R. Wuthrich, P. Geiss, Z. He, X. Liu, B. Orner, J. Johnson, G. Freeman, D. Ahlgren, B. Jagannathan, L. Lanzerotti, V. Ramachandran, J. Malinowski, H. Chen, J. Chu, P. Gray, R. Johnson, J. Dunn, S. Subbanna, K. Schonenberg, D. Harame, R. Groves, K. Watson, D. Jadus, M. Meghelli, and A. Rylyakov, "A 0.18μm 120/100 GHz (f_T/f_{max}) HBT and ASIC-compatible CMOS using copper interconnect," *Proc. of IEEE Bipolar/BiCMOS Circuits and Technology*, pp. 143-146, 2001.

[13] P. F. Lu, "Low-frequency noise in self-aligned bipolar transistors," *Appl. Phys.*, vol. 62, pp. 1335-1339, 1987.

[14] L. K. J. Vandamme, "Noise as a diagnostic tool for quality and reliability of electronic devices," *IEEE Trans. Elect. Dev.*, vol. 41, no. 11, pp. 2176-2187, November 1994.

[15] M. J. Deen, J. I. Ilowski, and P. Yang, "Low frequency noise in polysilicon-emitter bipolar junction transistors," *J. Appl. Phys.*, vol. 77, pp. 6278-6285, 1995.

[16] H. A. W. Markus and T. G. M. Kleinpenning, "Low-frequency noise in polysilicon emitter bipolar transistors," *IEEE Trans. on Electron Devices*, vol. 42, no. 4, pp. 720-727, April 1995.

[17] A. L. McWhorter, "1/f noise and germanium surface properties," *Semiconductor Surface Physics*, p. 207, 1980.

[18] A. Hajimiri and T. H. Lee, "A general theory of phase noise in electrical oscillators," *IEEE Journal of Solid-State Circuits*, vol. 33, no. 2, pp. 179-194, February 1998.

[19] A. Demir, A. Mehrotra, and J. Roychowdhury, "Phase noise in oscillators: A unifying theory and numerical methods for characterization," *IEEE Trans. on Circuits and System - I: Fundamental Theory and Applications*, vol. 47, no. 5, pp. 655-674, May 2000.

[20] SpectreRF User Guide, Cadence, January 2003.

[21] C. C. McAndrew, D. F. Bowers, M. Dunn, M. Foisy, I. Getreu, M. McSwain, S. Moinian, J. Parker, D. J. Roulston, M. Schroter, P. van Wijnen, L. F. Wagner, "VBIC – the Vertical Bipolar Inter Company Model," *IEEE Journal of Solid-State Circuits*, vol. 31, no. 10, pp. 1476-1483, Oct. 1996.

[22] Verilog-A Language Reference Manual, Accellera, January 2003.

[23] Verilog-AMS Language Reference Manual, Accellera, November 2004.

[24] Affirma Verilog-A Language Reference, Cadence, July 2001.

[25] N. Bhandari, "A simple relationship between the transistor parameters h_{FE} and h_{fe}," *Proc. of the IEEE*, vol. 55, no. 6, pp. 1099 - 1099, June 1967.

[26] J. Tang, G. Niu, Z. Jin, J. D. Cressler, S. Zhang, A. J. Joseph, and D. L. Harame, "Modeling and characterization of SiGe HBT low-frequency noise figures-of-merit for RFIC applications," *IEEE Trans. Microwave Theory and Techniques*, vol. 50, no. 11, pp. 2467-2473, November 2002.

[27] J. Tang, G. Niu, A. Joseph, and D. Harame, "Impact of collector-base junction traps on low-frequency noise in high breakdown voltage SiGe HBTs," *IEEE Trans. on Electron Devices*, vol. 51, no. 9, pp. 1475-1482, September 2004.

[28] Theo G. M. Kleinpenning, "Location of Low-Frequency Noise Sources in Submicrometer Bipolar Transistors," *IEEE Trans. on Electron Devices*, vol. 39, no. 6, pp. 1501-1506, June 1992.

[29] G. Niu, S. Zhang, J. D. Cressler, A. J. Joseph, J. S. Fairbanks, L. E. Larson, C. S. Webster, W. E. Ansley, and D. L. Harame, "SiGe profile design tradeoffs for RF circuit applications," *Tech. Dig. International Electron Devices Meeting*, pp. 573-576, 1999.

[30] G. Niu, S. Zhang, J. D. Cressler, A. J. Joseph, J. S. Fairbanks, L. E. Larson, C. S. Webster, W. E. Ansley, and D. L. Harame, "Noise modeling and SiGe profile design tradeoffs for RF applications," *IEEE Trans. on Electron Devices*, vol. 47, no. 11, pp. 2037-2044, November 2000.

[31] G. Freeman, D. Ahlgren, D. R. Greenberg, R. Groves, F. Huang, G. Huge, B. Jagannathan, S. J. Jeng, J. Johnson, K. Schonenberg, K. Stein, R. Volant, and S. Subbanna, "A 0.18μm 90 GHz f_T SiGe HBT BiCMOS, ASIC compatible, copper interconnect technology for RF and microwave applications," *Tech. Dig. International Electron Devices Meeting*, pp. 569-572, 1999.

[32] Z. A. Shafi, C. J. Gibbings, P. Ashburn, I. R. C. Post, C. G. Tuppen, and D. J. Godfrey, "The importance of neutral base recombination in compromising the gain of Si/SiGe heterojunction bipolar transistors," *IEEE Trans. on Electron Devices*, vol. 38, pp. 1973-1976, August 1991.

[33] J. M. McGregor, D. J. Roulston, J. P. Noel, and D. C. Houghton, "Output conductance of bipolar transistors with large neutral base recombination current," *IEEE Trans. on Electron Devices*, vol. 39, pp. 2569-2575, November 1992.

[34] G. Niu, J. D. Cressler, and A. J. Joseph, "Quantifying Neutral Base Recombination and the Effects of Collector-base Junction Traps in UHV/CVD SiGe HBT's," *IEEE Trans. on Electron Devices*, vol. 45, no. 12, pp. 2499-2503, December 1998.

[35] M. Schroter, "Staying current with HICUM," *IEEE Circuits and Devices Magazine*, vol. 18, no. 3, pp. 16 -25, May 2002.

[36] J. C. J. Paasschens and R. v.d. Toorn, "Introduction to and usage of the transistor model mextram," *http://www.semiconductors.philips.com/acrobat/other/philipsmodels /bipolar/mextram/NLUR2002823.pdf*, August 2002.

[37] S. P. O. Bruce, L. K. J. Vandamme, and A. Rydberg, "Measurement of low-frequency base and collector current noise and coherence in SiGe heterojunction bipolar transistors using transimpedance amplifiers," *IEEE Trans. on Electron Devices*, vol. 46, no. 5, pp. 993-1000, May 1999.

[38] R. Plana, L. Escotte, J. P. Roux, J. Graffeuil, A. Gruhle, and H. Kibbel, "$1/f$ noise in self-aligned Si/SiGe heterojunction bipolar transistor," *IEEE Electron Device Letters*, vol. 16, no. 2, pp. 58-60, February 1995.

[39] A. van der Ziel, *Noise in Solid State Devices and Circuits*, John Wiley & Sons, 1986.

[40] F. Bonani and G. Ghione, *Noise in Semiconductor Devices. Modeling and Simulation*, Springer-Verlag, 2001.

[41] K. M. van Vliet, "Noise and admittance of the generation-recombination current involving SRH centers in the space-charge region of junction devices," *IEEE Trans. on Electron Devices*, vol. 23, no. 11, pp. 1236-1246, Nov. 1976.

[42] F. N. Hooge, "$1/f$ noise sources," *IEEE Trans. on Electron Devices*, vol. 41, no. 11 pp. 1926-11935, November 1994.

[43] Advanced Design System 2001 User's Guide, Agilent Technologies, September 2001.

[44] F. Bonani, S. D. Guerrieri, and G. Ghione, "Noise source modeling for cyclostationary noise analysis in large-signal device operation," *IEEE Trans. on Electron Devices*, vol. 49, no. 9, pp. 1640-1647, September 2002.

[45] C. Dragone, "Analysis of Thermal and Shot Noise in Pumped Resistive Diodes," *The Bell System Technical Journal*, pp. 1883-1902, November 1968.

[46] R. Poore, "Oscillator Phase Noise Simulation Using ADS, Including Flicker Noise Conversion," *MTT-S Workshop*, June 2003.

[47] A. Cappy, F. Danneville, G. Dambrine, and B. Tamen, "Noise analysis in devices under nonlinear operation," *Solid-state Electronics*, pp. 21-26, 1999.

[48] J. E. Sanchez, G. Bosman, and M. E. Law, "Two-dimensional semiconductor device simulation of trap-assisted generation- recombination noise under periodic large-signal conditions and its use for developing cyclostationary circuit simulation models," *IEEE Trans. on Electron Devices*, vol. 50, no. 5, pp. 1353-1362, May 2003.

[49] G. Niu, J. Tang, Z. Feng, A. Joseph, and D. Harame, "SiGe HBT scaling implications on $1/f$ noise and oscillator phase noise," *Tech. Dig. of IEEE Radio Frequency Integrated Circuit Symposium*, pp. 299-302, June 2004.

[50] J. W. M. Rogers and C. Plett, *Radio Frequency Integrated Circuit Design*, Artech House Publishers, 2003.

[51] B. Razavi, "Basic Concepts in RF Design," Chapter 2 - *RF Microelectronics*, Prentice Hall PTR, 1997.

[52] A. Kyranas and Y. Papananos, "A 5GHz fully integrated VCO in a SiGe bipolar technology," *IEEE International Symposium on Circuits and Systems*, pp. 193-196, 2000.

[53] X. Zhang and A. S. Daryoush, "Bias-dependent noise up-conversion factor in HBT oscillator," *IEEE Microwave and Guided Wave Letters*, vol. 4, no. 12, pp. 423-425, December 1994.

[54] G. Freeman, B. Jagannathan, S. Jeng, J. Rieh, A. D. Stricker, D. C. Ahlgren, and S. Subbanna, "Transistor design and application considerations for >200-GHz SiGe HBTs," *IEEE Trans. on Electron Devices*, vol. 50, no. 3, pp. 645-655, March 2003.

[55] I. Bietti, E. Temporiti, G. Albasini, and R. Castello, "An UMTS $\sum \Delta$ fractional synthesizer with 200kHz bandwidth and -128dBc/Hz @ 1MHz using spurs compensation and linearization techniques," *Proc. IEEE Custom Integrated Circuits Conference*, pp. 463-466, 2003.

[56] T. Morie, S. Dosho, K. Okamoto, Y. Yamada, and K. Sogawa, "A -90dBc@10kHz phase noise fractional-N frequency synthesizer with accurate loop bandwidth control circuit," *Symposium on VLSI Circuit Digest of Technical Paper*, pp. 52-55, 2005.

[57] S. L. J. Gierkink, D. Li, R. C. Frye, and V. Boccuzzi, "A 3.5-GHz PLL for fast low-IF/zero-IF LO switching in an 802.11 transceiver," *IEEE Journal of Solid-State Circuits*, vol. 40, no. 9, pp. 1909-1921, September 2005.

[58] W. Rhee, B. Bisanti, and A. Ali, "An 18-mW 2.5-GHz/900-MHz BiCMOS dual frequency synthesizer with < 10-Hz RF carrier modulation," *IEEE Journal of Solid-State Circuits*, vol. 27, no. 4, pp. 515-520, April 2002.

[59] P. Zhang, T. Nguyen, C. Lam, D. Gambetta, T. Soorapanth, B. Cheng, S. Hart, I. Sever, T. Bourdi, A. Tham, and B. Razavi, "A 5-GHz direct-conversion CMOS transceiver," *IEEE Journal of Solid-State Circuits*, vol. 38, no. 12, pp. 2232-2238, December 2003.

[60] B. Neurauter, G. Märzinger, T. Lüftner, R. Weigel, M. Scholz, V. Mutlu, and J. Fenk, "GSM 900/DCS 1800 fractional-N frequency synthesizer with very fast settling time," *Dig. IEEE Microwave Symposium*, pp. 705-708, 2001.

[61] A. Gilat, "MATLAB: An Introduction With Applications," *John Wiley & Sons*, 2004.

[62] A. Hajimiri and T. H. Lee, *The design of Low Noise Oscillators*, Kluwer Academic Publishers, 1997.

[63] Using Verilog-A in Advanced Design System, Agilent Technologies, August 2005.

[64] Verilog-A Reference Manual, Agilent Technologies, August 2005.

[65] G. B. Arfken, H. J. Weber, and H. Weber, "Mathematical Methods for Physicists," *Academic Press*, 1985.

[66] G. Niu, J. Tang, Z. Feng, A. Joseph and D. Harame, "Scaling and technological limitations of $1/f$ noise and oscillator phase noise in SiGe HBTs," *IEEE Trans. on Microwave Theory and Techniques*, vol. 53, no. 2, pp. 506-514, February 2005.

APPENDIX A

1/f Noise Measurement

This appendix describes measurement issues for low-frequency noise in typical BJTs.

A.1 Background

To measure the mathematically defined power spectral density (PSD), a waveform in the time domain is sampled (for example with an A/D-card, digital oscilloscope or a signal analyzer) and converted to a complex-valued spectrum using the fast Fourier transform (FFT). It is then possible to calculate the PSD. Two instrumental issues need to be addressed in order to have correct measurement. The first is the dynamic range of the measurement equipment. As the PSD spectrum contains a wide range of signal levels, it is important that the measurement equipment can resolve the lowest level in the presence of the highest level input to the equipment. Power line signals and their harmonics interfering with the measurements can create strong peaks in the frequency domain which can not be fully eliminated. The second issue of importance is the analog bandwidth of the measurement equipment. In order not to lose dynamic range in an offset of the input signal, the sampler should be put in an *ac* mode and thus an analog circuit is necessary.

A.2 Measurement Setup

Both the device under test (DUT) and the biasing circuit were well-shielded in metal boxes. The biasing circuit was enclosed in a HP 16808 Test Fixture and connected to the DUT using triaxial cables. The output from the test fixture was connected to the input of a low-noise pre-amplifier (EG&G 5113) from which it was fed into a HP 3561A Dynamic Signal Analyzer (DSA). The spectrum analyzer was controlled by a Labview program to process the data. The low-noise amplifier is necessary due to low

141
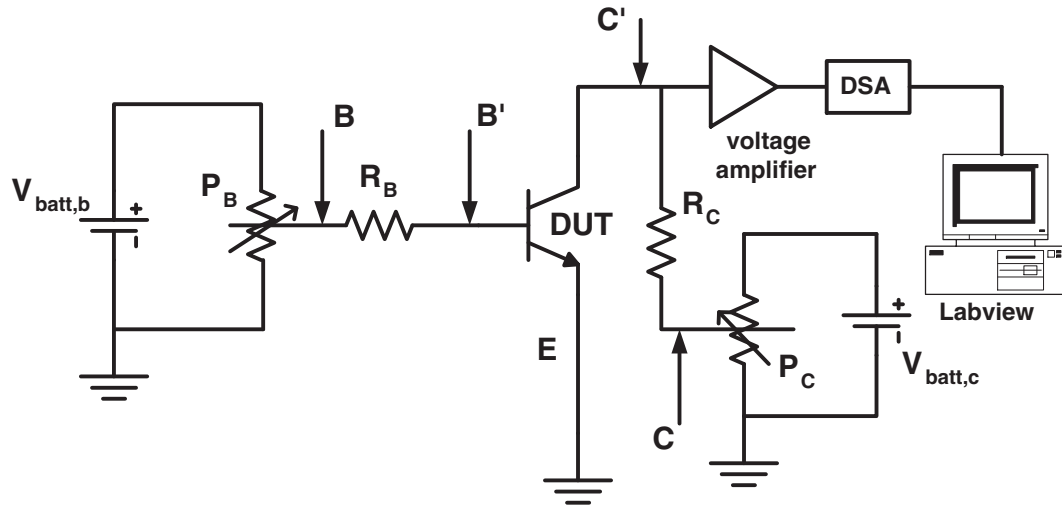
Figure A.1: Experimental setup used to measure the base current 1/f noise from the collector voltage fluctuation.

noise voltage level at the load resistance and the limited dynamic range of the spectrum analyzer. The measurement setup is shown in Figure A.1.

An oscilloscope is very helpful for monitoring the actual signal which is to be sampled by the signal analyzer. During probing and setting of correct bias point, the oscilloscope will give valuable information as to whether the measured signal indicates noise that possibly originates within the device or is only caused by external effects like power line interference or bad contacts. The oscilloscope is also very useful to monitor the signal throughout the measurement to see if the amplifier may saturate or the behavior of the signal changes. The former may result in a faulty spectrum and the latter indicates, e.g., a degrading contact between the device and the probe tips. The setting of the sweep time of the oscilloscope is of great importance when studying the measured signal. As there is no distinct frequency of the signal to observe, it is necessary to step through several sweep time settings in order to see if there are disturbances of, e.g. power line, seen at long sweep times. Possible oscillations within the DUT or the amplifiers may appear as noise if the sweep time is not set short enough for the oscilloscope to resolve the oscillating signal.

A.3   Importance of Averaging

Due to the random nature of noise, a power spectral density (PSD) based on a single measured time sequence will never give the expected spectral behavior. It is important to point out that the averaging is made of several subsequent sampled time sequences of the same signal. The averaging which is made assumes that the signal is stationary and that the spectrum from non-overlapping time sequences can be averaged as being independent and thus being considered as measured in parallel. The averaging process should not be confused with sampling a longer time sequence which only would give information about lower frequencies and consequently higher frequency resolution.

Although the averaging will improve the appearance of the PSD, caution is necessary when interpreting data at the lowest frequencies. Since the FFT is performed on a finite set of sampled data which has been assumed to repeat infinitely in time, PSD values at the lowest frequencies will correspond to very few samples within the sampled data. Averaging does somewhat help, but the amount of samples in each time sequence should be chosen so that the lowest two or three frequency points can be discarded.

A.4   Wide-band Measurement

To be able to distinguish slopes etc. in a PSD, measurements over several decades of frequencies are often necessary. The measurements should then be performed over several frequency bands. The total PSD is then constructed from the PSDs of the different frequency bands. When measuring over several sub-bands, it is possible to maintain a somewhat constant relative frequency resolution, i.e., the frequency resolution on a log-scale will remain fairly constant. If only one frequency band is chosen for the whole measurement, the majority of frequency points (90%) will be found in the top decade of the band.

An additional benefit when dividing the measurement into sub-bands is that an efficient analog filtering of the signal is possible before feeding it into the signal analyzer. As the low-frequency noise level has a tendency to decrease with increasing frequency, the highest power density will be found in the lowest frequency region. If the frequency band that is measured is too wide, the dynamic range

of the A/D converter in the signal analyzer may limit the ability to detect the levels of the PSD at the higher frequencies, i.e., the signal part with the lowest intensity. By passing the measured signal through a band-pass filter, the dynamic range of the A/D converter only needs to handle the different levels existing within the pass-band of the filter.
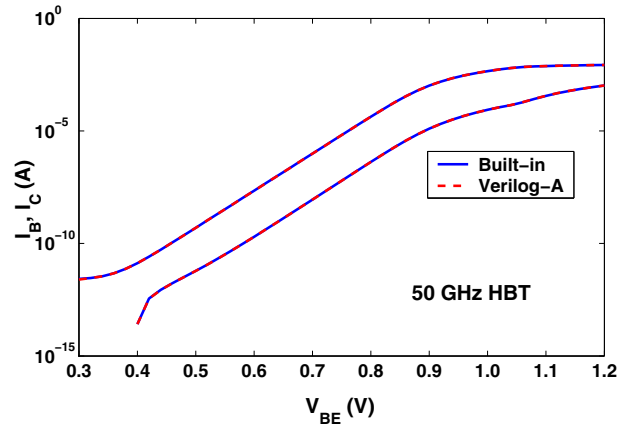
APPENDIX B

VERILOG-A IMPLEMENTATION OF VBIC MODEL

Verilog-A plays a crucial role is this work. In Chapter 2, we need to access the internal base-emitter junction to get the internal base-emitter transport current since it is the current that is responsible for base current $1/f$ noise generating. In Chapter 5, the waveforms of the internal base-emitter and collector-emitter transport currents are needed to better understand the upconversion of the cyclostationary shot noise. In chapter 6, we need to access the internal branches of a transistor where the noise source of interest are located for impulse sensitivity function calculation. However, neither ADS nor Cadence SpectreRF allows access of the internal nodes or branches when the built-in transistor VBIC (vertical bipolar inter-compnay) bipolar model is used. We therefore implement VBIC bipolar model using Verilog-A [22].

There are publicly available Verilog-A implementations of early VBIC models. However, when used in circuit simulation, these implementations give quite different results from the built-in VBIC model, for various reasons, including syntax differences between circuit simulators as well as bugs in the codes. To ensure accuracy and achieve consistency with the built-in VBIC model, we implemented exactly the same model equations giving in the user manual of the built-in VBIC model. For verification, extensive dc, ac, and noise simulation are performed using both the built-in VBIC model and our Verilog-A implementation. The VBIC model can be implemented using Affirma Verilog-A [24] in Cadence SpectreRF and Agilent ADS [63] [64]. Both are used in this work. Figure B.1 compares the simulated Gummel characteristics $\big[$Figure B.1 (a)$\big]$, output characteristics $\big[$Figure B.1 (b)$\big]$ and cut-off frequency (f_T) as a function of collector current (I_C) $\big[$Figure B.1 (c)$\big]$ between built-in VBIC model in Cadence spectreRF and Affirma Verilog-A. The 50 GHz HBT is used as an example. The emitter area is 0.5×2.5

145

μm^2. The results are identical within the error limits of the circuit simulator, conforming the validity of our Verilog-A implementation.
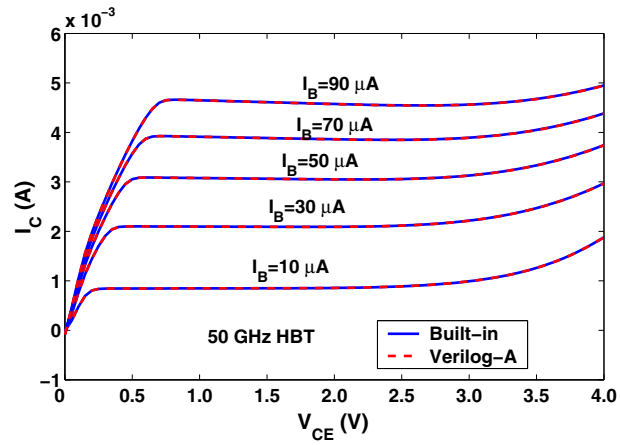
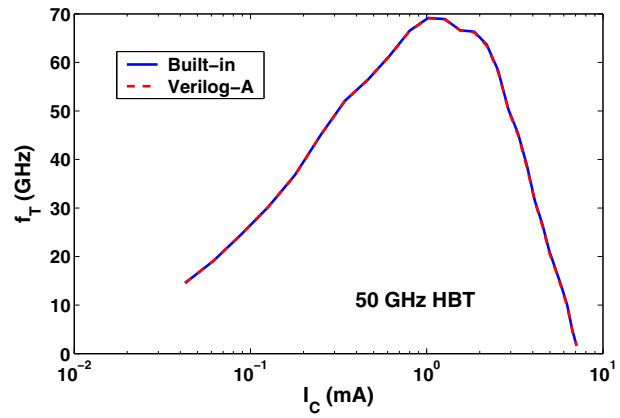Figure B.1: Comparison of simulated (a) Gummel characteristics, (b) output characteristics, and (c) f_T as a function of I_C using the built-in VBIC model in Cadence and Verilog-A implementation. The 50 GHz HBT is used. $A_E = 0.5 \times 2.5 \ \mu m^2$.

PHASE NOISE MODELING USING FREQUENCY SENSITIVITY METHOD

Frequency sensitivity method is used in ADS for phase noise simulation. It assumes that noise acts to randomly modulate the oscillation frequency. The change in oscillation frequency with respect to a noise current i_n at harmonic k, denoted as $\partial \omega_0 / \partial i_{n,k}$ with ω_0 being the oscillation frequency, is calculated for all harmonics. The frequency sensitivity can be viewed as the transfer function from the transistor noise to frequency noise.

Consider a noise current denoted as $\mathbb{I}_{\mathbb{N}}$ and the resultant noise in oscillation frequency denoted as $\mathbb{F}_{\mathbb{N}}$, $\mathbb{F}_{\mathbb{N}}$ relates to $\mathbb{I}_{\mathbb{N}}$ by the frequency sensitivity to the noise current, $\partial \mathbb{F}$. Using the frequency indexing presented in Section 4.3.2, the sideband noise current at $\widetilde{\omega}_k$ is written as

$$i_{n,k} = I_{n,k} \cos \widetilde{\omega}_k t, \tag{C.1}$$

where k is the harmonic index. $\mathbb{I}_{\mathbb{N}}$ consists of multiple sideband noise currents, it can be expressed using a vector

$$\mathbb{I}_{\mathbb{N}} = \begin{bmatrix} I_{n,0} I_{n,1} I_{n,2} \cdots I_{n,N} \end{bmatrix}^{\top} \tag{C.2}$$

with N being the highest harmonic index in question. $\top$ represents transpose. Each sideband noise current contributes to a frequency noise, the frequency sensitivity is also a vector

$$\partial \mathbb{F} = \begin{bmatrix} \dfrac{\partial \omega_0}{\partial i_{n,0}} & \dfrac{\partial \omega_0}{\partial i_{n,1}} & \dfrac{\partial \omega_0}{\partial i_{n,2}} & \cdots & \dfrac{\partial \omega_0}{\partial i_{n,l}} \end{bmatrix}. \tag{C.3}$$

The frequency noise $\mathbb{F}_{\mathbb{N}}$ is the product of $\mathbb{I}_{\mathbb{N}}$ and $\partial \mathbb{F}$

$$\mathbb{F}_{\mathbb{N}} = \partial \mathbb{F} \cdot \mathbb{I}_{\mathbb{N}}. \tag{C.4}$$

Frequency noise is usually expressed in the mean squared form

$$
\left\langle \mathbb{F}_\mathbb{N} \mathbb{F}_\mathbb{N}^* \right\rangle = \left\langle \partial \mathbb{F} \cdot \mathbb{I}_\mathbb{N} \left(\partial \mathbb{F} \cdot \mathbb{I}_\mathbb{N} \right)^{*\mathsf{T}} \right\rangle = \partial \mathbb{F} \left\langle \mathbb{I}_\mathbb{N} \mathbb{I}_\mathbb{N}^{*\mathsf{T}} \right\rangle \partial \mathbb{F}^{*\mathsf{T}}. \tag{C.5}
$$

$\langle \cdot \rangle$ represents statistical average. $*$ represents complex conjugate.

Bring (C.2) and (C.3) into (C.5), we get

$$
\left\langle \mathbb{F}_\mathbb{N} \mathbb{F}_\mathbb{N}^* \right\rangle
$$

$$
= \left[\frac{\partial \omega_0}{\partial i_{n,0}} \frac{\partial \omega_0}{\partial i_{n,1}} \cdots \frac{\partial \omega_0}{\partial i_{n,l}} \right]
\left\langle
\begin{bmatrix} I_{n,0} \\ I_{n,1} \\ \vdots \\ I_{n,l} \end{bmatrix}
\begin{bmatrix} I_{n,0}^* I_{n,1}^* \cdots I_{n,l}^* \end{bmatrix}
\right\rangle
\begin{bmatrix} \left(\frac{\partial \omega_0}{\partial i_{n,0}} \right)^* \\ \left(\frac{\partial \omega_0}{\partial i_{n,1}} \right)^* \\ \vdots \\ \left(\frac{\partial \omega_0}{\partial i_{n,l}} \right)^* \end{bmatrix}
$$

$$
= \left[\frac{\partial \omega_0}{\partial i_{n,0}} \frac{\partial \omega_0}{\partial i_{n,1}} \cdots \frac{\partial \omega_0}{\partial i_{n,l}} \right]
\begin{bmatrix}
\left\langle I_{n,0} I_{n,0}^* \right\rangle & \left\langle I_{n,0} I_{n,1}^* \right\rangle & \cdots & \left\langle I_{n,0} I_{n,l}^* \right\rangle \\
\left\langle I_{n,1} I_{n,0}^* \right\rangle & \left\langle I_{n,1} I_{n,1}^* \right\rangle & \cdots & \left\langle I_{n,1} I_{n,l}^* \right\rangle \\
\vdots & \vdots & \ddots & \vdots \\
\left\langle I_{n,l} I_{n,0}^* \right\rangle & \left\langle I_{n,l} I_{n,1}^* \right\rangle & \cdots & \left\langle I_{n,l} I_{n,l}^* \right\rangle
\end{bmatrix}
\begin{bmatrix} \left(\frac{\partial \omega_0}{\partial i_{n,0}} \right)^* \\ \left(\frac{\partial \omega_0}{\partial i_{n,1}} \right)^* \\ \vdots \\ \left(\frac{\partial \omega_0}{\partial i_{n,l}} \right)^* \end{bmatrix}
\tag{C.6}
$$

(C.6) can be simply written as

$$
\left\langle \mathbb{F}_\mathbb{N} \mathbb{F}_\mathbb{N}^* \right\rangle = \sum_{k=0}^{N} \sum_{l=0}^{N} \frac{\partial \omega_0}{\partial i_{n,k}} \left\langle I_{n,k} I_{n,l}^* \right\rangle \left(\frac{\partial \omega_0}{\partial i_{n,l}} \right)^*. \tag{C.7}
$$

The frequency fluctuations $\left\langle \mathbb{F}_\mathbb{N} \mathbb{F}_\mathbb{N}^* \right\rangle$ are then converted to the phase fluctuations and thus single-sideband (SSB) phase noise by:

$$
\mathscr{L}_{i_n}(\Delta \omega) = \frac{\left\langle \mathbb{F}_\mathbb{N} \mathbb{F}_\mathbb{N}^* \right\rangle}{2 \Delta \omega^2}. \tag{C.8}
$$

By dividing $\Delta \omega^2$, the noise in frequency is converted to noise in phase. Using the small phase modulation assumption, the phase noise is further converted to voltage noise by dividing by 2.

C.1   Thermal Noise

For thermal noise from a resistor R, the unilateral auto-correlation spectral density is simply

$$\left\langle I_{n,k} I_{n,l}^* \right\rangle = \begin{cases} \frac{4kT}{R} & k = l \\ \\ 0 & k \neq l \end{cases} \tag{C.9}$$

Since there is no correlation between noises at different frequencies, the total phase noise due to thermal noise is therefore

$$\mathscr{L}_{thermal}(\Delta\omega) = \frac{1}{2\Delta\omega^2} \sum_{k=0}^{N} \left| \frac{\partial\omega_0}{\partial i_{n,k}} \right|^2 \frac{4kT}{R}. \tag{C.10}$$

We further define thermal noise gain G_{r_b} for comparison of base resistance noise upconversion from different devices sizes or different technologies. G_{r_b} is the ratio of phase noise to thermal noise voltage $(4kTr_b)$

$$G_{r_b} = 2\Delta\omega^2 \frac{\mathscr{L}_{thermal}(\Delta\omega)}{4kTr_b} = \frac{\sum_{k=0}^{N} \left| \frac{\partial\omega_0}{\partial i_{n,k}} \right|^2}{r_b^2}. \tag{C.11}$$

C.2   Shot Noise

For shot noise, since the correlation time is typically much smaller than the oscillation period, the cyclostationary model discussed in Section 4.3.3 applies. The cross-correlation spectral density of the noise current at $\widetilde{\omega}_k$ and $\widetilde{\omega}_l$ are given by

$$\left\langle I_{n,l} I_{n,k}^* \right\rangle = 2q I_{l-k}, \tag{C.12}$$

where I_{k-l} is $k - l$ order Fourier coefficient of the noise generating current $i(t)$ (i_{BE} or i_{CE}) . All the noises at $\widetilde{\omega}_k$ contribute a phase noise at $\Delta\omega$. As these noises are correlated, the total phase noise is thus

given by

$$\mathscr{L}_{shot}(\Delta\omega) = \frac{1}{2\Delta\omega^2} \sum_{k=0}^{N} \sum_{l=0}^{N} \frac{\partial\omega_0}{\partial i_{n,k}} 2q I_{k-l} \left(\frac{\partial\omega_0}{\partial i_{n,l}} \right)^*. \tag{C.13}$$

C.3 $1/f$ Noise

$1/f$ noise is also a function of the oscillating current I. Under small signal operation condition, the power spectral density is given by

$$S_{1/f} = \frac{K_F I_{dc}^2}{f}. \tag{C.14}$$

I_{dc} is the dc biasing current in the small signal measurement. ADS assumes that phase noise due to $1/f$ noise at an offset angular frequency $\Delta\omega$ is from the dc component of instantaneous I only [46]. Therefore phase noise due to $1/f$ noise is calculated as:

$$\mathscr{L}_{1/f}(\Delta\omega) = \frac{1}{2\Delta\omega^2} 2 \left| \frac{\partial\omega_0}{\partial i_{n,0}} \right|^2 S_{1/f}(I_0) = \frac{1}{\Delta\omega^2} \left| \frac{\partial\omega_0}{\partial i_{n,0}} \right|^2 S_{1/f}(I_0), \tag{C.15}$$

where I_0 is the dc component of I, and $S_{1/f}(I_0)$ is the $1/f$ noise power spectral density at a biasing current equal to I_0.

PHASE NOISE MODELING USING IMPULSE SENSITIVITY FUNCTION

Impulse sensitivity function method is used in Chapter 6 to model oscillator phase noise. In this Appendix, the detailed derivations are presented. The derivation is based on [18].

D.1 Impulse Sensitivity Function

Impulse sensitivity function (ISF) method is a time domain based phase noise modeling method. Phase noise in the time domain can be viewed as random variations in the deviations of the zero crossing points from their ideal position along the time axis, as shown in Figure D.1. An ideal sinusoidal oscillator output is described by

$$v_{out}(t) = V_0 \cos(\omega_0 t + \phi_0). \tag{D.1}$$

Here, V_0 is the nominal amplitude of the signal, ω_0 is the nominal oscillation radian frequency, and ϕ_0 is the phase of the signal. ϕ_0 can be arbitrarily chosen, therefore we neglect ϕ_0 in the following discussion. The instantaneous output of an oscillator can be expressed by

$$v_{out}(t) = V_0 \left[1 + \Delta A(t)\right] \cos \left[\omega_0 t + \Delta \phi(t)\right], \tag{D.2}$$

where $\Delta A(t)$ and $\Delta \phi(t)$ represent the amplitude and phase fluctuations of the signal, respectively. The amplitude noise is not important because of the inherent amplitude stabilization mechanisms. Generally, $\Delta A(t) \ll 1$ is assumed, therefore in the following discussion $v_{out}(t)$ takes the form

$$v_{out}(t) = V_0 \cos \left[\omega_0 t + \Delta \phi(t)\right]. \tag{D.3}$$
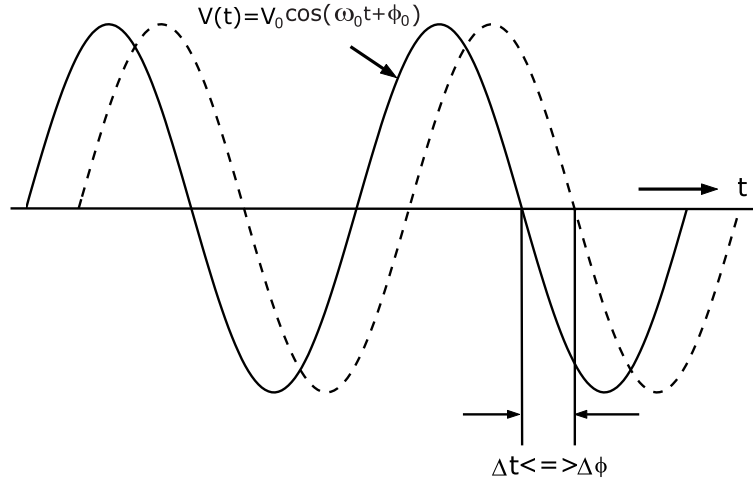
Figure D.1: Phase noise represented in the time domain.

Consider injecting an impulse perturbation current into an oscillator. The resulting amplitude shift dies away due to the built-in amplitude limiting mechanisms, while the phase shift remains as any time-shifted version of the solution remains a solution. The sensitivity of the phase response to the injected impulse perturbation is expressed using an impulse sensitivity function Γ, which can be defined as

$$\Gamma \triangleq \frac{\Delta\phi}{\Delta q}. \tag{D.4}$$

Here $\Delta\phi$ is the phase shift, Δq is the injected charge. $\Gamma(\omega_0 t)$ is periodic, and fundamentally characterizes phase noise upconversion. Note here the definition of Γ is different from that in [18], where $\Gamma \triangleq q_{max} \frac{\Delta\phi}{\Delta q}$ with q_{max} being the maximum charge swing. Neglecting any short term responses, the phase response to the impulse current can be modeled using a step-like function,

$$h_\phi(t, \tau) = \Gamma(\omega_0\tau)u(t - \tau), \tag{D.5}$$

where $u(t)$ is the unit step function. For an arbitrary noise $\mu(t)$, the accumulated phase shift is:

$$\Delta\phi(t) = \int_{-\infty}^{\infty} h_\phi(t, \tau)\mu(\tau)d\tau = \int_{-\infty}^{t} \Gamma(\omega_0\tau)\mu(\tau)d\tau. \tag{D.6}$$

153

$\Gamma(\omega_0 t)$ can be expanded into Fourier series as:

$$\Gamma(\omega_0 t) = \frac{c_0}{2} + \sum_{n=1}^{\infty} c_n \cos(n\omega_0 \tau + \theta_n). \tag{D.7}$$

Note $\Gamma_{dc} = c_0/2$. θ_n is the phase of the nth harmonic, which is not important for random input noise and is thus neglected in the following discussion. Replacing $\Gamma(\omega_0 t)$ in (D.6) with (D.7), we get

$$\Delta\phi(t) = \frac{c_0}{2} \int_{-\infty}^{t} \mu(\tau)d\tau + \sum_{n=1}^{\infty} \int_{-\infty}^{t} c_n \cos(n\omega_0 \tau)\mu(\tau)d\tau. \tag{D.8}$$

Consider a noise current at a frequency close to the harmonics of the oscillation frequency given by

$$i_n(t) = I_n \cos(n\omega_0 + \Delta\omega)\, t. \tag{D.9}$$

I_n is the magnitude of the unilateral noise spectrum at frequency $n\omega_0 + \Delta\omega$ where $\Delta\omega \ll \omega_0$. The phase shift due to i_n becomes

$\Delta\phi(t)$

$$= \frac{I_n c_0}{2} \int_{-\infty}^{t} \cos[(n\omega_0 + \Delta\omega)\tau]d\tau + \sum_{m=1}^{\infty} \int_{-\infty}^{t} I_n c_m \cos(m\omega_0 \tau)\cos[(n\omega_0 + \Delta\omega)\tau]d\tau$$

$$= \frac{I_n c_0}{2} \frac{\sin[(n\omega_0 + \Delta\omega)t]}{n\omega_0 + \Delta\omega} + \sum_{m=1}^{\infty} \frac{I_n c_m}{2} \int_{-\infty}^{t} \{\cos[(m+n)\omega_0 + \Delta\omega)]\tau + \cos[(m-n)\omega_0 + \Delta\omega]\tau\}\, d\tau$$

$$= \frac{I_n c_0}{2} \frac{\sin[(n\omega_0 + \Delta\omega)t]}{n\omega_0 + \Delta\omega} + \sum_{m=1}^{\infty} \frac{I_n c_m}{2} \left\{ \frac{\sin[(m+n)\omega_0 + \Delta\omega]t}{(m+n)\omega_0 + \Delta\omega} + \frac{\sin[(m-n)\omega_0 + \Delta\omega]t}{(m-n)\omega_0 + \Delta\omega} \right\} \tag{D.10}$$

Since $\Delta\omega \ll \omega_0$, the only significant term in (D.10) for $n \geq 1$ is the second term in the summation when $m = n$, which is

$$\Delta\phi(t) \approx \frac{I_n}{2} c_n \frac{\sin(\Delta\omega t)}{\Delta\omega} \quad (n \geq 1). \tag{D.11}$$

If the noise current is at a frequency close to dc ($n = 0$), the only significant term is the first term,

$$\Delta\phi(t) \approx \frac{I_0}{2}c_0\frac{\sin(\Delta\omega t)}{\Delta\omega} \quad (n = 0). \tag{D.12}$$

In general, the phase shift due to the impulse current injected at a frequency of $n\omega_0 + \Delta\omega$ ($n \geq 0$) takes the form

$$\Delta\phi(t) \approx \frac{I_n}{2}c_n\frac{\sin(\Delta\omega t)}{\Delta\omega} \quad (n \geq 0), \tag{D.13}$$

with c_n's defined in (D.7).

The phase shift resulted from noise current at $n\omega_0 - \Delta\omega$ can be derived in the same manner. Here $n \geq 1$ as we consider the unilateral noise spectrum only. The phase shift is written as

$$\begin{aligned}
\Delta\phi(t) &= \frac{I_n c_0}{2}\frac{\sin[(n\omega_0 - \Delta\omega)t]}{n\omega_0 - \Delta\omega} \\
&+ \sum_{m=1}^{\infty}\frac{I_n c_m}{2}\left\{\frac{\sin[(m+n)\omega_0 - \Delta\omega]t}{(m+n)\omega_0 - \Delta\omega} + \frac{\sin[(m-n)\omega_0 - \Delta\omega]t}{(m-n)\omega_0 - \Delta\omega}\right\}
\end{aligned} \tag{D.14}$$

The only significant term in (D.14) is the second term in the summation when $m = n$,

$$\Delta\phi(t) \approx \frac{I_n}{2}c_n\frac{\sin(-\Delta\omega t)}{-\Delta\omega} = \frac{I_n}{2}c_n\frac{\sin(\Delta\omega t)}{\Delta\omega} \quad (n \geq 1). \tag{D.15}$$

(D.15) is the same as (D.11), therefore phase shift due to impulse current injected at $n\omega_0 \pm \Delta\omega$ can be written as

$$\Delta\phi(t) \approx \frac{I_n}{2}c_n\frac{\sin(\Delta\omega t)}{\Delta\omega} \quad (n \geq 0). \tag{D.16}$$

To relate the phase variations to voltage variations, we substitute $\Delta\phi(t)$ in (D.3) with (D.16). Assuming small phase modulation $\left[\Delta\phi(t) \text{ is small}\right]$, $v_{out}(t)$ is written as

$$
\begin{aligned}
v_{out}(t) &= V_0 \cos\left[\omega_0 t + \phi_0 + \Delta\phi(t)\right] \\
&= V_0 \cos(\omega_0 t + \phi_0) \cos\left[\Delta\phi(t)\right] - V_0 \sin(\omega_0 t + \phi_0) \sin\left[\Delta\phi(t)\right] \\
&= V_0 \cos(\omega_0 t + \phi_0) - V_0 \Delta\phi(t) \sin(\omega_0 t + \phi_0) \\
&= V_0 \cos(\omega_0 t + \phi_0) - \frac{V_0 I_n c_n}{2\Delta\omega} \sin(\Delta\omega t) \sin(\omega_0 t + \phi_0) \\
&= V_0 \cos(\omega_0 t + \phi_0) - \frac{V_0 I_n c_n}{4\Delta\omega} \cos\left[(\omega_0 - \Delta\omega)t - \cos(\omega_0 + \Delta\omega)t\right].
\end{aligned}
\tag{D.17}
$$

The injected current at $n\omega_0 \pm \Delta\omega$ results in a pair of equal sidebands at $\omega_0 \pm \Delta\omega$ with a magnitude equal to $\frac{V_0 I_n c_n}{4\Delta\omega}$. The single-sideband (SSB) phase noise due to noise current at $n\omega_0 \pm \Delta\omega$ is calculated according to the $\mathscr{L}$ definition in Section 1.3:

$$
\mathscr{L}(\Delta\omega)\bigg|_n = \frac{\frac{1}{2}\left(\frac{V_0 I_n c_n}{4\Delta\omega}\right)^2}{\frac{1}{2}V_0{}^2} = \frac{I_n^2 c_n^2}{16\Delta\omega^2}.
\tag{D.18}
$$

The total phase noise at offset frequency $\Delta\omega$ is the sum of phase noises resulted from noise currents in the vicinity of the harmonics of ω_0, $n\omega_0 \pm \Delta\omega$.

$$
\begin{aligned}
\mathscr{L}(\Delta\omega) &= \mathscr{L}(\Delta\omega)\bigg|_0 + 2\sum_{n=1}^{\infty} \mathscr{L}(\Delta\omega)\bigg|_n \\
&= \frac{1}{16\Delta\omega^2}\left(I_0^2 c_0^2 + \sum_{n=1}^{\infty} I_n^2 c_n^2\right).
\end{aligned}
\tag{D.19}
$$

Note that the component at $-\Delta\omega$ does not exists since we are dealing with the unilateral noise spectrum. Figure D.2 illustrates the upconversion of phase noise from transistor physical noise sources. From (a) to (b), each noise current at $n\omega_0 \pm \Delta\omega$ translates to a phase noise at $\Delta\omega$, as shown in (D.16). The total phase noise at $\Delta\omega$ is the sum of all the contributions. From (b) to (c), phase noise is translated to voltage noise through phase modulation.
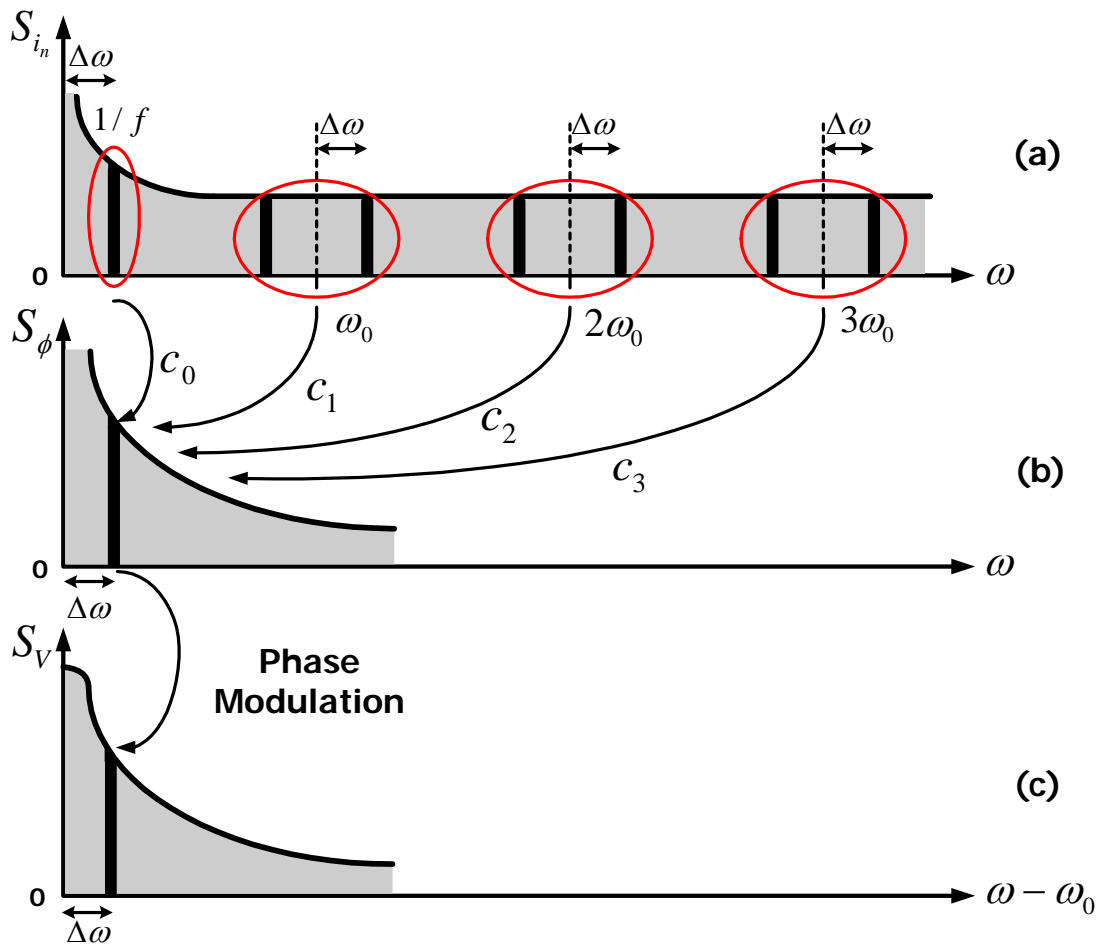
Figure D.2: Conversion of transistor noise to phase fluctuations and then to phase noise sideband.

If I_n ($n \geq 0$) is a constant, (D.19) can be written as

$$\mathscr{L}(\Delta\omega) = \frac{I_n^2}{16\Delta\omega^2}\left(c_0^2 + 2\sum_{n=1}^{\infty} c_n^2\right) = \frac{I_n^2}{4\Delta\omega^2}\Gamma_{rms}^2, \tag{D.20}$$

where we used Parseval's relation [65],

$$\Gamma_{rms}^2 = \frac{1}{T}\int_0^T \left|\Gamma(t)\right|^2 dt = \left(\frac{c_0}{2}\right)^2 + \frac{1}{2}\sum_{n=1}^{\infty} c_n^2 = \frac{1}{4}\left(c_0^2 + 2\sum_{n=1}^{\infty} c_n^2\right). \tag{D.21}$$

Γ_{rms} is the root-mean-squared (*rms*) value of the periodic Γ function. Phase noise due to stationary noise is determined by the *rms* value of the ISF function and the noise power. The equations above assume a stationary small signal noise source, and do not apply directly to noises with an oscillating current dependent power spectral density, such as the base or collector current shot noise, which we address below. The main noise sources of interest in a SiGe HBT are illustrated in Fig. 4.5 with a simplified VBIC model [21], including: 1) thermal noise due to intrinsic and extrinsic r_b, r_{b_i} and r_{b_x}, 2) base and collector current shot noise $i_{b,s}$, and $i_{c,s}$, and 3) base current $1/f$ noise $i_{b,1/f}$. We now discuss the upconversion of each type of noise.

D.2 Thermal Noise

For base resistance thermal noise, $I_n^2/2 = 4kT/r_b$. Substituting this into (D.20),

$$\mathscr{L}_{r_b}(\Delta\omega) = \frac{2kT}{r_b}\frac{\Gamma_{rms}^2}{\Delta\omega^2}. \tag{D.22}$$

For better insight, we define the base resistance thermal noise upconversion gain as the ratio of phase noise to thermal noise ($4kTr_b$)

$$G_{r_b} = 2\Delta\omega^2\frac{\mathscr{L}_{r_b}(\Delta\omega)}{4kTr_b} = \left(\frac{\Gamma_{rms}}{r_b}\right)^2, \tag{D.23}$$

which essentially represents the phase noise produced by one Ω base resistance. This is equivalent to replacing the Γ in (D.22) with Γ/R. This normalization by R physically makes sense. To first order, the voltage change Δv due to injected impulse current Δi is proportional to r_b. A higher r_b leads to larger Δv, and thus $\Delta \phi$, even if the Δi (Δq) is fixed. Since Γ is defined as the ratio of $\Delta \phi$ and Δq, Γ is also proportional to r_b. Γ/r_b eliminates the impact of r_b on Γ function, and is more suitable for comparing base resistance noise upconversion from different devices sizes or different technologies.

D.3 Shot Noise

For shot noise with a power spectral density of $2qI$, we need to account for the time-varying nature of the noise generating current I, by modulating a unity white stationary noise with a modulation function [45]. A convenient though arbitrary choice is to use the maximum $2qI$ as a reference, and modulate the reference noise with a function $\alpha_{shot}=\sqrt{|I(t)/I_{max}|}$, which varies between 0 and 1 [18]. Here I_{max} is the maximum of $I(t)$. We can then equivalently use a constant noise generating current I_{max}, but replace Γ with an effective ISF $\Gamma_{eff}(\omega_0 t)=\Gamma(\omega_0 t) \times \alpha_{shot}(\omega_0 t)$. (D.20) is then replaced by

$$\mathscr{L}_{shot}(\Delta\omega) = qI_{max}\frac{\Gamma^2_{eff,rms}}{\Delta\omega^2}, \tag{D.24}$$

where $\Gamma_{eff,rms}$ is the *rms* value of $\Gamma_{eff}(\omega_0 t)$.

D.4 $1/f$ Noise

For $1/f$ noise which is also a function of biasing current I in small signal measurements, it is often assumed that the $1/f$ noise in an oscillator is simply equal to the small signal $1/f$ noise one would measure at a biasing current equal to the *dc* component of $I(t)$, I_0 [18] [46] [47]. As $S_{1/f}=K_F I^2/f$, $S_{1/f}$ decreases rapidly with increasing frequency, and the most significant term in (D.18) is the first term. (D.18) can then be reduced to

$$\mathscr{L}_{1/f}(\Delta\omega) = \mathscr{L}(\Delta\omega)\Big|_0 = 2\pi K_F I_0^2 \frac{c_0^2}{8\Delta\omega^3} = \pi K_F I_0^2 \frac{\Gamma^2_{dc}}{\Delta\omega^3}. \tag{D.25}$$

The assumption above, however, does not consider the physical origin of $1/f$ noise, which is still being debated. As discussed in Section 4.3.4, the cyclostationary modulation model should be used for $1/f$ noise in the SiGe HBTs since superposition of GR fluctuations is the origin of $1/f$ noise. Using the maximum current as a reference, the modulation function for $1/f$ noise becomes $\alpha_{1/f} = I(t)/I_{max}$. The upconverted phase noise is then

$$\mathscr{L}_{1/f}(\Delta\omega) = 2\pi K_F I_{max}^2 \frac{c_{eff,0}^2}{8\Delta\omega^3} = \pi K_F I_{max}^2 \frac{\Gamma_{eff,dc}^2}{\Delta\omega^3}. \qquad (D.26)$$

It has been experimentally shown that the major $1/f$ noise in SiGe HBTs is in the base current. $1/f$ noise and base current shot noise therefore have the same Γ as the two noise sources are both located at the internal emitter-base junction, but different Γ_{eff} due to different α function. The modulated $1/f$ noise yields significantly higher phase noise than the dc component based model implemented in current CAD tools and used in [49] and [66], as we have shown in Appendix F. We also compare in Appendix F the phase noise simulated using ISF, ADS and Cadence, and the agreement is less than 1 dB in most cases for white noise.

SIMULATION OF IMPULSE SENSITIVITY FUNCTION

The way impulse sensitivity function (ISF) is calculated is based on direct injection of a current impulse of small area at a certain time and measurement of induced phase shift when the oscillation restablizes. ISF is defined as $\Delta\phi/\Delta q$ (rad/C), with Δq being the amount of charge injection, and $\Delta\phi$ being the phase shift. ISF is a periodic function, it can be found by repeating this process for injection times spanning one oscillation period. Transient analysis is required to solve ISF directly, for which we need direct access to the internal nodes of a transistor where the noise sources are located. Neither ADS nor Cadence SpectreRF allows access of the internal nodes when the build-in VBIC model is used. To solve this problem, we implemented the VBIC model using Verilog-A, the hardware description language.

E.1   Implementation of Verilog-A

To inject a current impulse where a noise source is located, the following code is added to the verilog-A source code:

```
if ($abstime<StartTime||$abstime>StartTime+5e-12)

begin

Ipulse=0;

end

else if ($abstime>=StartTime&&$abstime<(StartTime+2e-12))

begin

Ipulse=Imax*($abstime-StartTime)/2e-12;

end
```

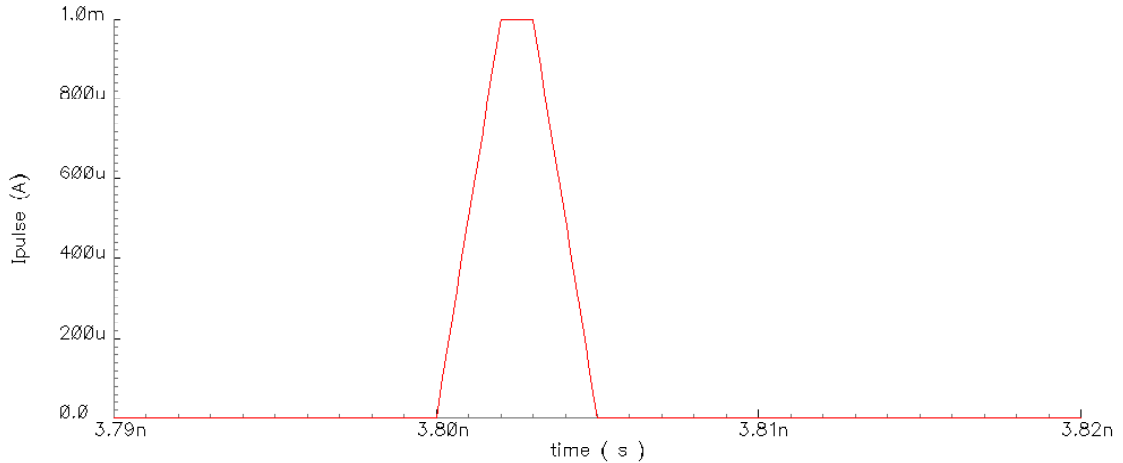Figure E.1: Cadence SpectreRF output from transient analysis: current impulse.

```
else if ($abstime>=(StartTime+2e-12)&&$abstime<(StartTime+3e-12))

begin

Ipulse=Imax;

end

else if ($abstime>=(StartTime+3e-12)&&$abstime<=(StartTime+5e-12))

begin

Ipulse=Imax*(StartTime+5e-12-$abstime)/2e-12;

end
```

In this code, `Ipulse` is defined as a function of `Imax`, `StartTime` and `$abstime`. `Imax` and `StartTime` are pre-defined as parameters, `$abstime` is an environment parameter function, returning the absolute time in second. After the `Ipulse` function is defined, adding the `Ipulse` to the branch where the noise source of interest is located. For example, to simulate the base current shot noise and $1/f$ noise, `I(b_bei) <+ Ipulse` is used which means injecting the `Ipulse` to the intrinsic base-emitter branch. Figure E.1 shows the simulated current impulse used in this work. The current impulse has a trapezoidal shape with a rising and fallen times of 2 ps each and an "on" time of 1 ps. `Imax` is 1 mA. Therefore the injected charge Δq is 3 fC. `StartTime` here is 3.8 ps.
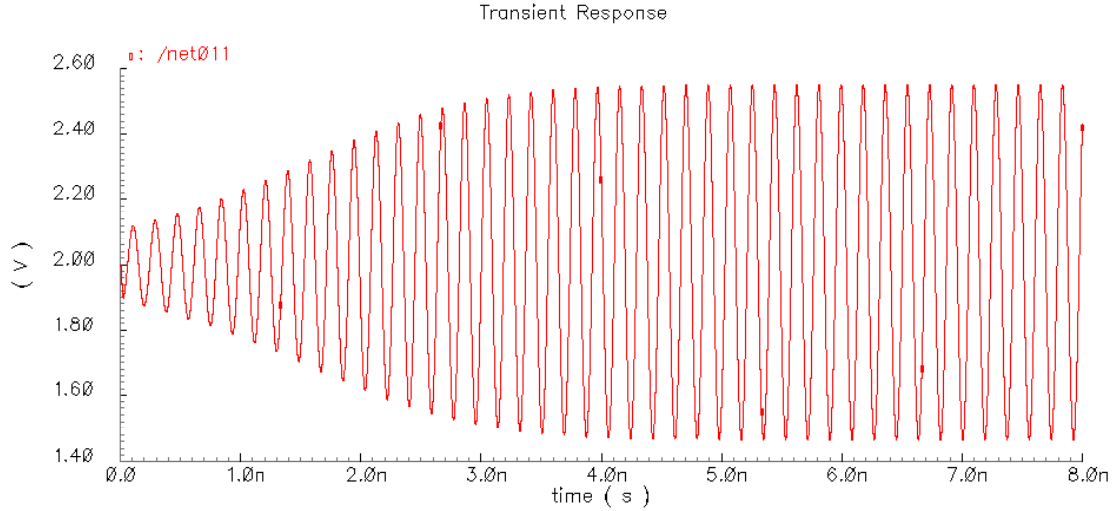
162

Figure E.2: Cadence SpectreRF output from transient analysis: oscillator output.

E.2 Simulation of ISF from Transient Analysis

ISF is a periodic function, therefore only ISF within one cycle is needed. Since a continuous ISF is impossible to get, it is important to decide the number of points that will be calculated. Based on our experience, 16 points are good enough. The next step in ISF calculation is to find a certain cycle during which multiple current impulses will be injected. Any cycle can be chosen as long as oscillation is stabilized. However since transient analysis is time-consuming especially when the time step is small, an earlier period is desired to reduce the simulation time. We do a rough transient simulation to find the wanted cycle. In this step, the time step is between 100 fs to 500 fs. Figure E.2 shows a simulated output from one of the 5.5 GHz oscillators discussed in Chapter 6. Although the oscillator seems to be stabilized when $t > 4.0$ ns. A period around $t = 6$ ns would be a safer choice. A finer transient simulation around $t = 6$ ns is then followed (as shown in Figure E.3) to find the exact time instants at which the current impulse should be injected. Since the oscillation frequency is about 5.5 GHz, the spacing between 16 equally separated points in one period is in the order of 10 ps. Therefore a time step of 10 fs is a maximum in this round in order to get accurate result.
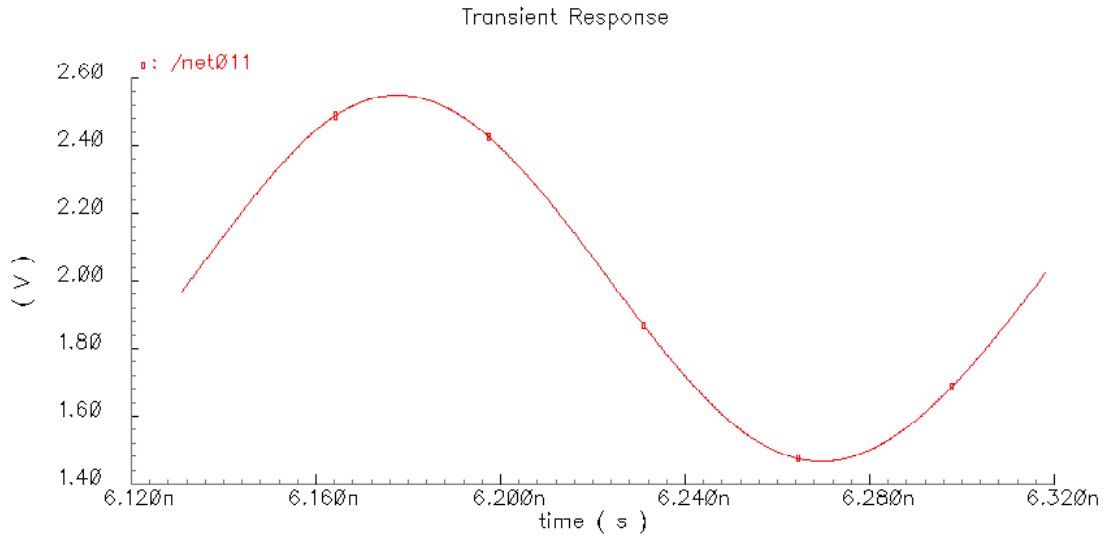
163

Figure E.3: Cadence SpectreRF output from transient analysis: oscillator output in a cycle.

The choice of the size of the current impulse is very important. In order for the linear current-to-phase transfer function assumption to hold, the injected current (representing noise) must be very small. If the current is too small, on the other hand, a much smaller time step in the transient analysis is needed in order to detect the tiny change in phase. Figure E.4 shows the simulated excess phase against the maximum of current impulse. The excess phase grows almost linearly with the increase of the impulse current. Note that the magnitude of the effective injected current due to actual noise sources are several orders lower than the magnitude of the injected current in Figure E.4. In this work, a maximum of 1 mA is used.

The last step is to calculated the induced excess phase for each injection. The excess phase is calculated from the deviations of the zero crossing points from the "ideal" position (no current impulse injection). One must wait several cycles for the oscillation to restabilize to calculate the difference in time (phase). The amount of time that is need to restore the oscillation is case-dependent. 5-6 cycles are usually the minimum. Figure E.5 shows an oscillator output when a current impulse is injected. The size of the current pulse is magnified for demonstration purpose. We see a sudden change in oscillation amplitude at roughly $t = 3.9$ ns when the current impulse is injected. The oscillation becomes stable
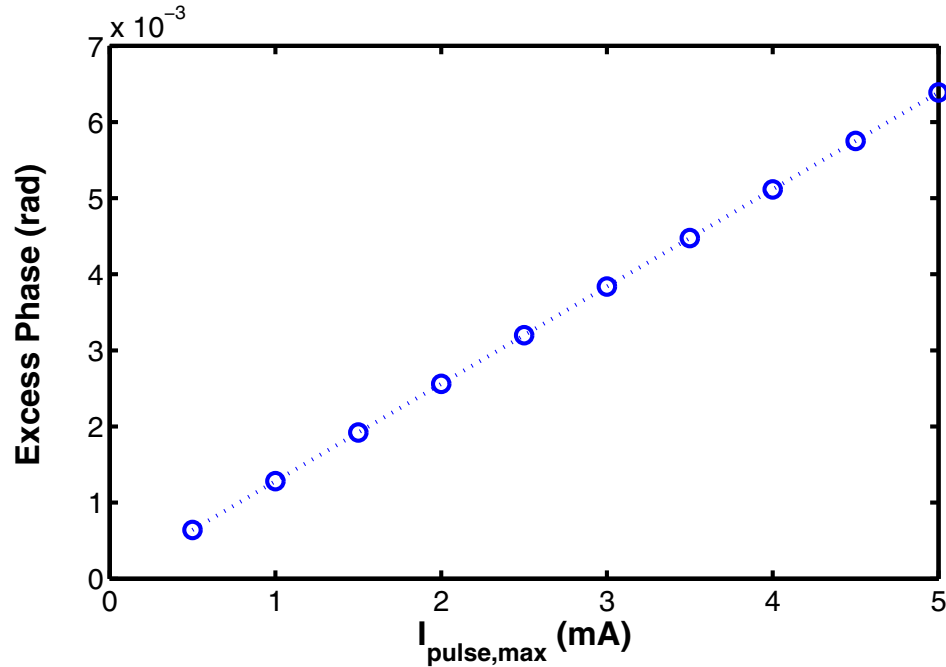
Figure E.4: Excess phase as a function of current impulse for one of the Colpitts oscillators used in this work.

after 6 cycles. Figure E.6 shows a calculated ISF for base current shot noise from one of the oscillators, together with the oscillator output. 32 points are used. The time step used for calculating the ISF is 1 fs.

E.3 Computation of Fourier Coefficient in MATLAB

Now we have the ISF waveform ready, the next step is to use this waveform to calculate the phase noise. According to (D.22) - (D.26), phase noise can be calculated as long as we have the c_n's or $c_{eff,n}$'s ready. This job can be done in MATLAB using the FFT function. `fft(X,N)` returns the discrete Fourier transform (DFT) of vector X, computed with a fast Fourier transform (FFT) algorithm. N means this is a N-point FFT. MATLAB makes taking an FFT easy: the only hard part comes in deciphering what the algorithm has given you back.

To demonstrate how to interpret the result given by FFT, we use an simple example. We type the following command in MATLAB prompt:
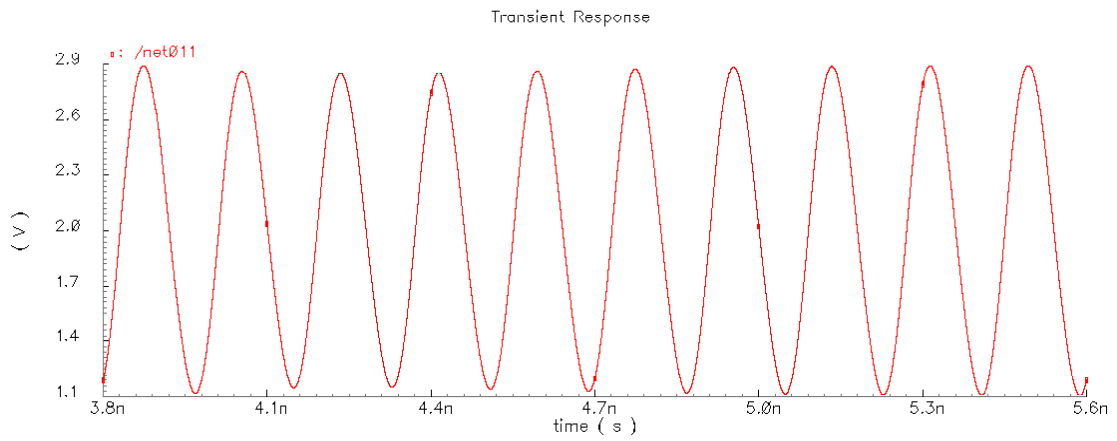
```
>>t=[0:7]'/8;
```

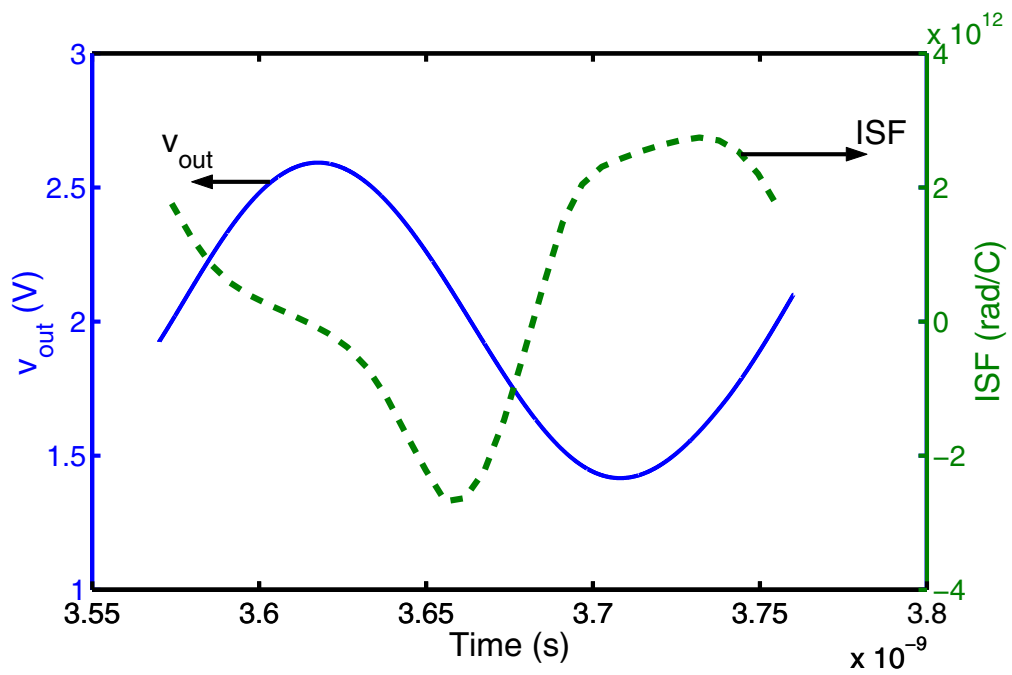Figure E.5: Simulated oscillator output with current impulse injected at $t = 3.89\ ns$.

Figure E.6: Oscillator output together with the ISF function for base current shot noise.

```
>>f=sin(2*pi*t);

>>fft(f)

0.0000

-0.0000 - 4.0000i

0.0000 - 0.0000i

0.0000 - 0.0000i

0.0000

0.0000 + 0.0000i

0.0000 + 0.0000i

-0.0000 + 4.0000i
```

The ordering of the frequencies is as follows [0 1 2 3 0 -3 -2 -1]. The first half of the list of numbers is the positive frequencies and the second half is the negative frequencies. Note that 8 discrete data points yields 8 Fourier coefficients and the highest frequency that will be resolved is $(N/2 - 1) \times f$, where f is the signal frequency. In our case, it is the oscillation frequency f_0. The real part of the FFT corresponds to the cosines series and the imaginary part corresponds to the sine. When taking an FFT of a real number data set (i.e. no complex numbers in the original data), the positive and negative frequencies turn out to be complex conjugates, as shown in the above example. Also, the MATLAB FFT returns data that needs to be divided by $N/2$ to get the coefficients that we used in the sin and cos series. To get the coefficient c_n, one need to convert the complex output to the absolute value and take the positive frequencies only:

```
p=abs(fft(X))/(N/2)

c=p(1:N/2)
```

Note that the last point of a periodic function should not be included based on the way the discrete FFT is defined. One need to be very careful about the points chosen spanning one period. The first point and the last point can not overlap, as illustrated in Figure E.7. Figure E.7 demonstrates how these 32 points (circles) should be chosen. The last point (square) should be omitted in the calculation.
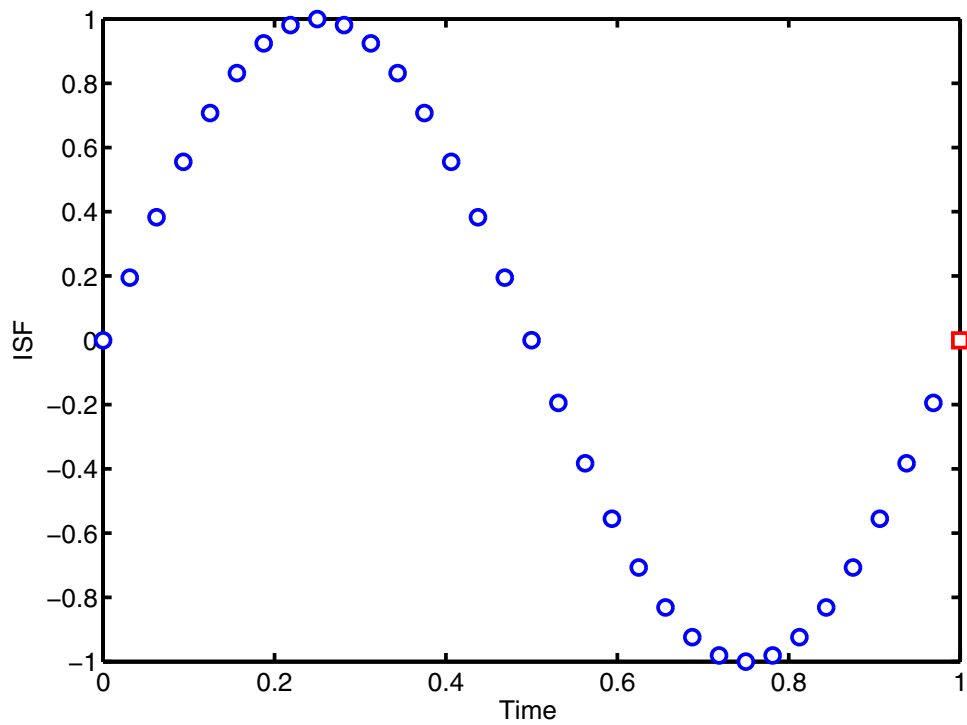
Figure E.7: Illustration of how to choose 32 points when using `fft(ISF,32)`.

COMPARISON OF PHASE NOISE SIMULATED USING ADS, CADENCE AND ISF METHOD

In this appendix, the individual phase noise simulated using ADS, Cadence and ISF method is compared. The three Colpitts oscillators used in Chapter 5 and Chapter 6 are used here. They are designed using the 50, 120 and 210 GHz HBTs. The schematic of the Colpitts oscillator is shown in Figure 5.3. The biasing current is 5 mA for all the oscillators. The emitter area is $0.5 \times 2.5 \times 5$ μm^2, $0.2 \times 6.4 \times 5$ μm^2 and $0.12 \times 12 \times 4$ μm^2 for the 50, 120 and 210 GHz HBTs, respectively. The Γ function is calculated from transient analysis in ADS and Cadence. The internal base-emitter transport current i_{BE} and collector-emitter transport current i_{CE} necessary for base and collector current shot noise calculation are obtained in Cadence using Verilog-A implementation. The *rms* value for Γ and Γ_{eff} is calculated in MATLAB.

F.1   Phase Noise due to White Noise

$1/f^2$ phase noise upconverted from white noise is dominated at large offset frequency. We compare the individual $1/f^2$ phase noise simulated using ADS, Cadence and ISF method in this section. Figure F.1 (a), Figure F.1 (b) and Figure F.1 (c) compares the white noise contributions for the 50, 120 and 210 GHz HBT oscillators, respectively. As we can see, phase noise obtained from different methods differs by less than 1 dB for most of the white noises. The r_{bi} noise contribution in the 50 GHz HBT oscillator is almost 3 dB less than the results from ADS and Cadence simulation, for the reason we do not understand yet. In general, an excellent agreement is achieved for phase noise simulated using the three methods.
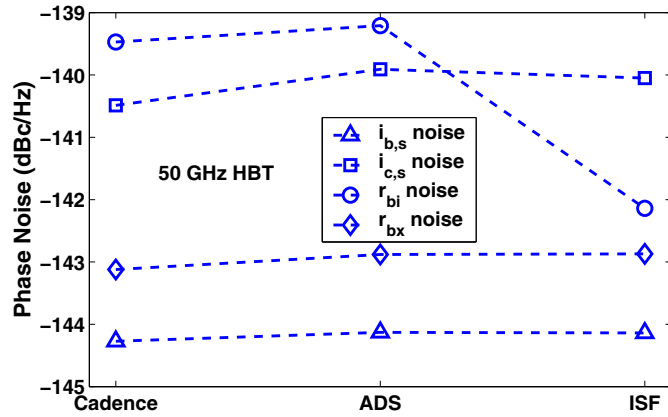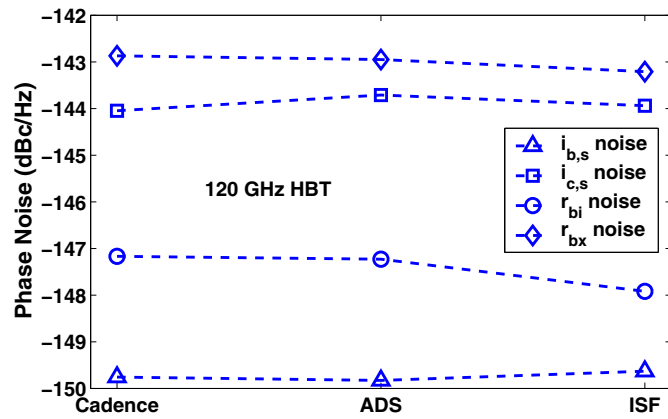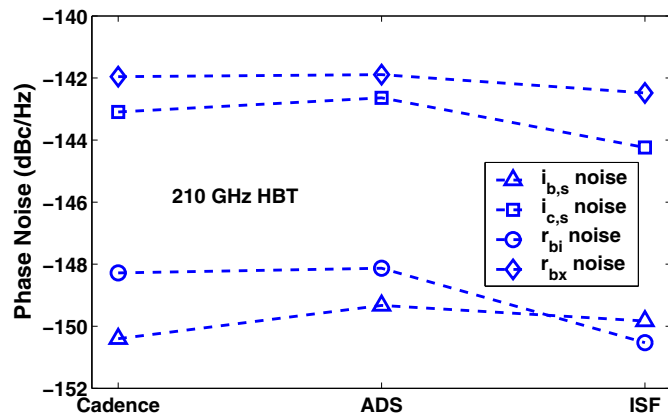
Figure F.1: Comparison of simulated white noise contributions to phase noise using ADS, Cadence and ISF method. (a) The 50 GHz HBT oscillator. (b) The 120 GHz HBT oscillator. (c) The 210 GHz HBT oscillator. Offset frequency is 10 MHz.
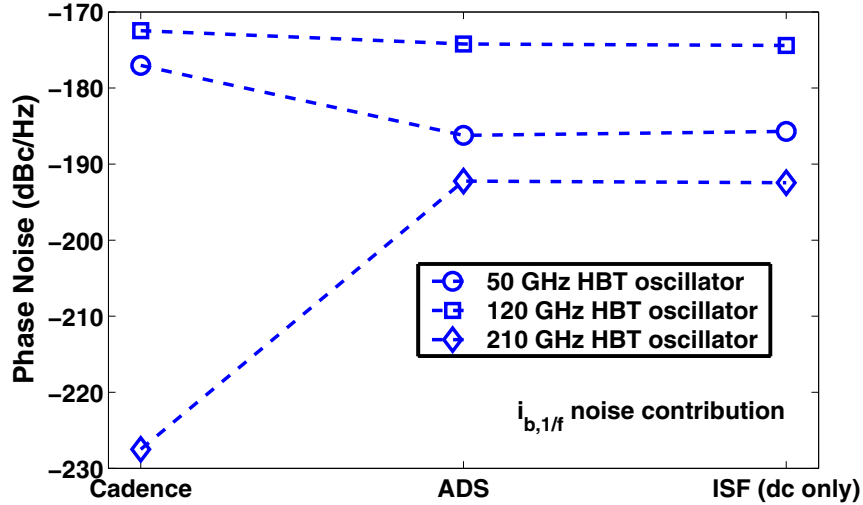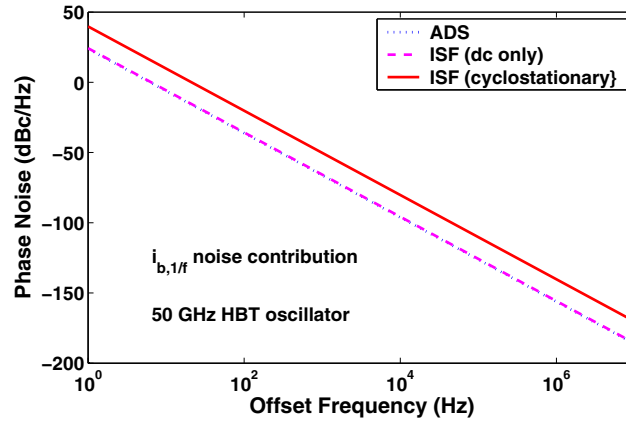
Figure F.2: Comparison of simulated $1/f$ noise contribution to phase noise using ADS, Cadence and ISF method implementing the *dc* only model. Offset frequency is 10 MHz.

F.2   Phase Noise due to $1/f$ Noise

Two models are available for $1/f$ noise treatment in oscillators; the *dc* only model and the cyclostationary model. Both ADS and Cadence use the *dc* only model. They assume that $1/f$ noise in oscillator is identical to the $1/f$ noise measured at a biasing current equal to the *dc* component of the oscillating current. Recent work, however, showed that $1/f$ noise in a oscillating transistor should also be treated as modulated stationary noise, in the same way shot noise is treated, if superposition of GR events is the origin for $1/f$ noise. The model is supported by the experimental results. In the ISF method, both the *dc* only model and cyclostationary model can be implemented. We compare the $1/f$ noise contribution to phase noise using ADS, Cadence and ISF method implementing *dc* only model. A comparison between the ISF method implementing cyclostationary model and the *dc* only model results is also made to understand the importance to use the right model for $1/f$ noise upconversion.

Figure F.2 compares the simulated $1/f^3$ phase noise using ADS, Cadence, and ISF method implementing the *dc* only model. An excellent agreement is achieved between the results simulated using ADS and ISF method. The difference is less than 0.5 dB for all of the cases. The results from Cadence simulation differs a lot in the 210 GHz HBT oscillator. Figure F.3 compares the simulated $1/f$ noise
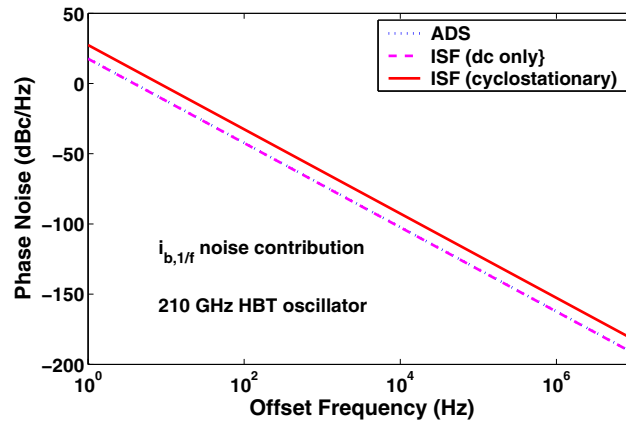
171

contribution using ADS, ISF method implementing the *dc* only model and ISF method implementing the cyclostationary model. The phase noise simulated using cyclostationary model is over 10 dB higher than the phase noise using *dc* only model. For the 50 GHz HBT oscillator, the difference is as much as 15 dB.
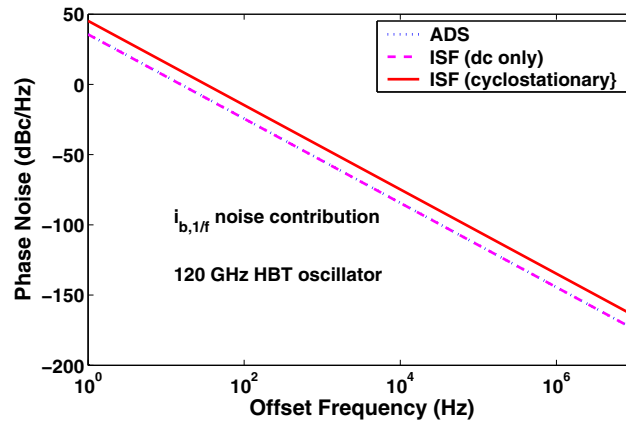
Figure F.3: Comparison of simulated $1/f$ contributions to phase noise using ADS, ISF method implementing the *dc* only model and ISF method implementing cyclostationary model. (a) The 50 GHz HBT oscillator. (b) The 120 GHz HBT oscillator. (c) The 210 GHz HBT oscillator.

AN OSCILLATOR DESIGNED FOR $1/f$ NOISE UPCONVERSION MECHANISM INVESTIGATION

In Chapter 5 and Chapter 6, we investigated the upconversion of individual phase noise sources in a bipolar junction transistor. Chapter 6 presents that the phase noise results from cyclostationary model and dc only model can easily varies by as much as 15 dB. This calls for accurate modeling of $1/f$ noise under large signal oscillating condition. This can be best investigated by comparing the experimental data with the theoretical calculation. We designed a 5.5 GHz single-ended Colpitts VCO using IBM's 60 GHz peak f_T SiGe technology. The schematic is identical to Figure 5.3. The frequency tuning is achieved by a MOS varactor. The VCO takes up 720×540 μm^2 area.

Since $1/f$ noise level in SiGe HBT is quite low, the $1/f^3$ phase noise can not always be observed in the measurement. It is well known that the post-stress transistors show a higher $1/f$ noise level. To manually increase the $1/f$ noise level, separate dc pads were layouted so that we can stress the transistor inside the VCO. After stress, we expect to observe the $1/f^3$ phase noise even at high offset frequency. The VCO layout is shown in Figure G.1.
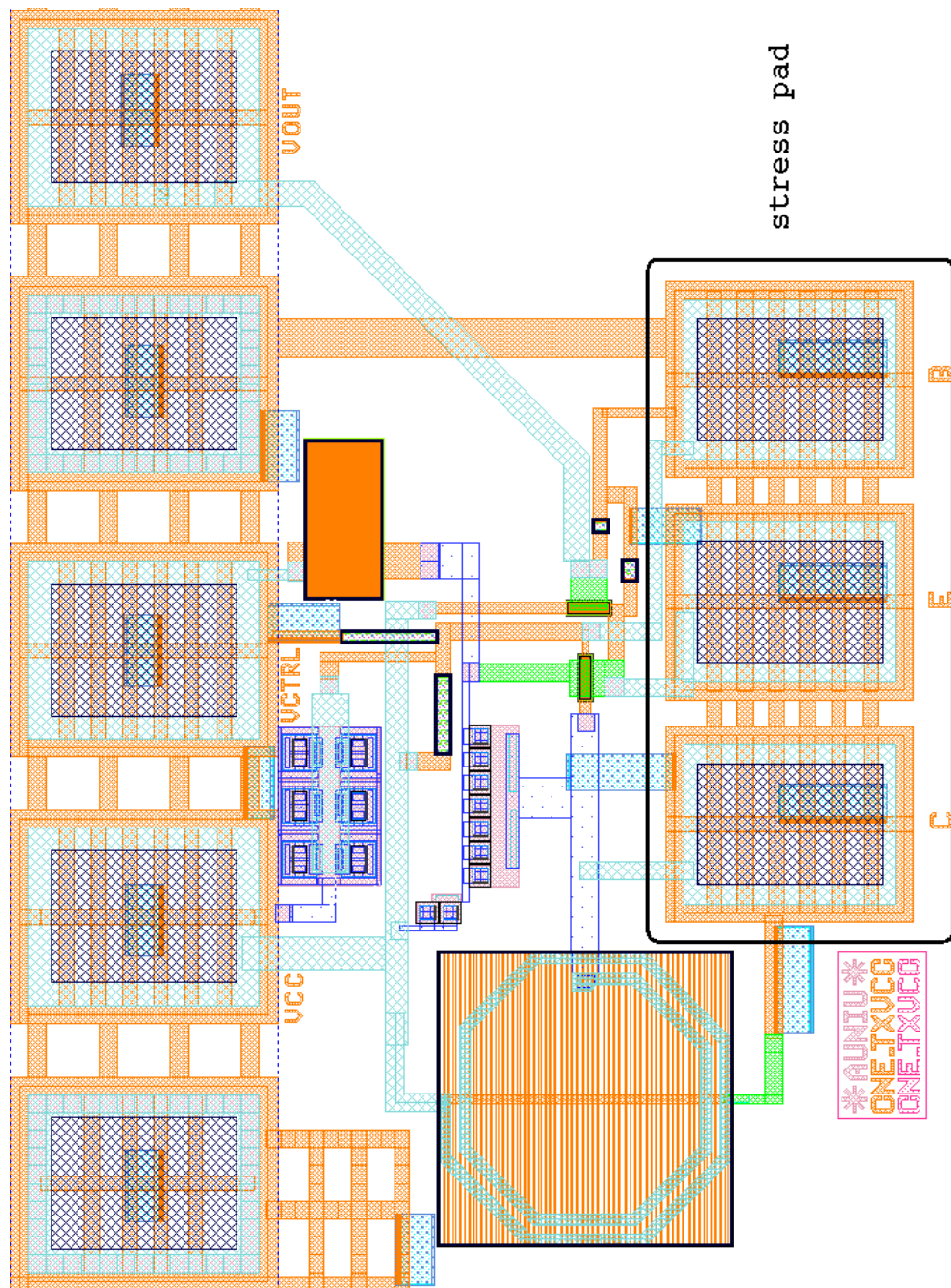
Figure G.1: Layout of the 5.5 GHz single-ended colpitts VCO. The 60 GHz peak f_T SiGe HBT is used.